

Technische Universität München
TUM School of Engineering and Design

Identification of Spatially Varying Elastic Material Properties with Modal Data

Karl-Alexander Hamilton Hoppe

Vollständiger Abdruck der von der TUM School of Engineering and Design der Technischen Universität München zur Erlangung eines

Doktors der Ingenieurwissenschaften (Dr.-Ing.)

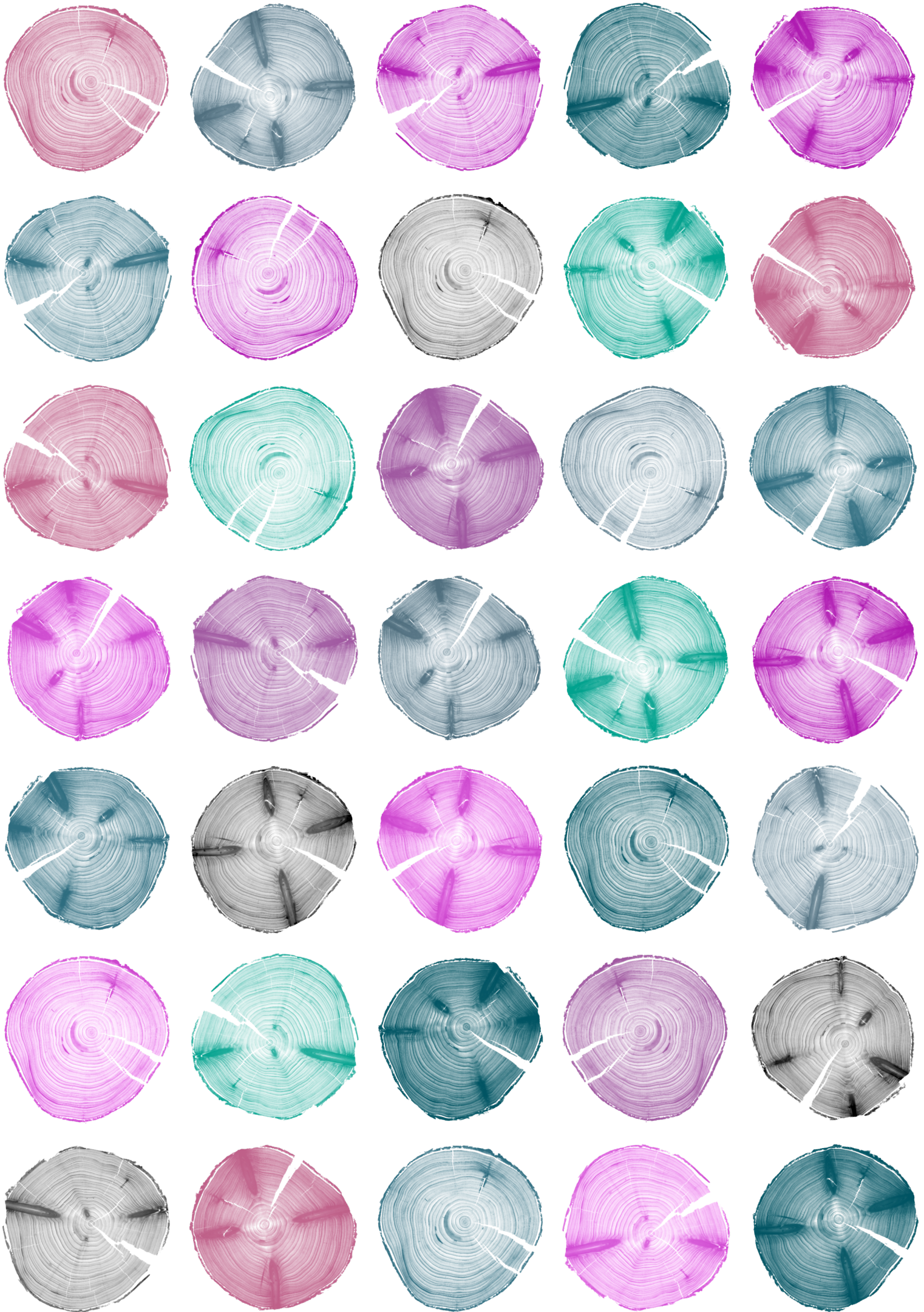
genehmigten Dissertation.

Vorsitz: Prof. Dr.-Ing. Christian U. Große

Prüfende der Dissertation:

1. Prof. Dr.-Ing. Steffen Marburg
2. Prof. Dr.-Ing. Jan-Willem G. van de Kuilen

Die Dissertation wurde am 1. August 2024 bei der Technischen Universität München eingereicht und durch die TUM School of Engineering and Design am 14. Januar 2025 angenommen.



Danksagung

Die vorliegende Arbeit ist zum Teil während meiner Tätigkeit als wissenschaftlicher Mitarbeiter am Lehrstuhl für Akustik mobiler Systeme an der School of Engineering and Design der Technischen Universität München entstanden, an dem ich mich zuvor schon als Student bei späteren Kolleg:innen engagierte. Ich danke Patrick Langer, Christian Geweth und Ferina Saati Khosroshahi für die Förderung und Einbindung gleich zu Beginn.

Mein Doktorvater ist Prof. Dr.-Ing. Steffen Marburg. Steffen, ich danke Dir für die Betreuung meines Promotionsvorhabens, für den großen Vertrauensvorschuss, den Du mir entgegenbrachtest und vor allem für die Freiheit, die Du mir gewährtest und die ich stets zu schätzen weiß. Neben Sorgfalt hast Du mir auch Klarheit und Selbstreflexion vermittelt.

Prof. Dr.-Ing. Jan-Willem G. van de Kuilen bin ich für die Übernahme des Zweitgutachtens, die konstruktive inhaltliche Rückmeldung und die angenehme mündliche Prüfung sehr dankbar. Prof. Dr.-Ing. habil. Dipl.-Geophys. Christian U. Große danke ich vielmals für den freundlichen Vorsitz der Promotionsprüfung.

Ein Großteil meiner fachlichen Arbeit geschah während der COVID-19-Pandemie, die ich hauptsächlich für mein Abweichen vom *geplanten* Aufstehen um 5 Uhr verantwortlich mache. Das Auf- und Abschwellen des Lebens in Folge der Pandemie ist in Retrospektive skurril. Allen Kolleg:innen am Lehrstuhl bin ich gerade deswegen verbunden für das beständige Aufrechterhalten von Perspektive und Hoffnung - trotz aller Unsicherheiten im außerberuflichen und beruflichen Leben. Danke an Ahmed Mostafa Shaaban Mohamed, Arne Hildenbrand, Bettina Chocholaty, Caglar Gürbüz, Christopher Jelich, Elke Reichardt, Felix Kronowetter, Johannes Schmid, Jonas Schmid, Kian Kheirollah Sepahvand, Martina Sommer, Magdalena Scholz, Martin Eser, Mert Dogu, Michael Buba, Monika Gatt, Marcus Mäder, Nishant Choudhary Singh, Sabine Crnjanowic, Semere Birhane Gebrekidan, Shivani Verma, Shuvajit Mukherjee, Simone Anna Preuss, Sourav Chandra, Suhaib Koji Baydoun-Hidding, Tao Yang, Xiaodong Sun, Yingxin Zhang und Zhe Liu. Die fortwährende kollegiale Heiterkeit werde ich vermissen, ebenso unsere gemeinsame Begeisterung für Musik, Sport, sowie das Philosophieren über große Pläne für *danach*.

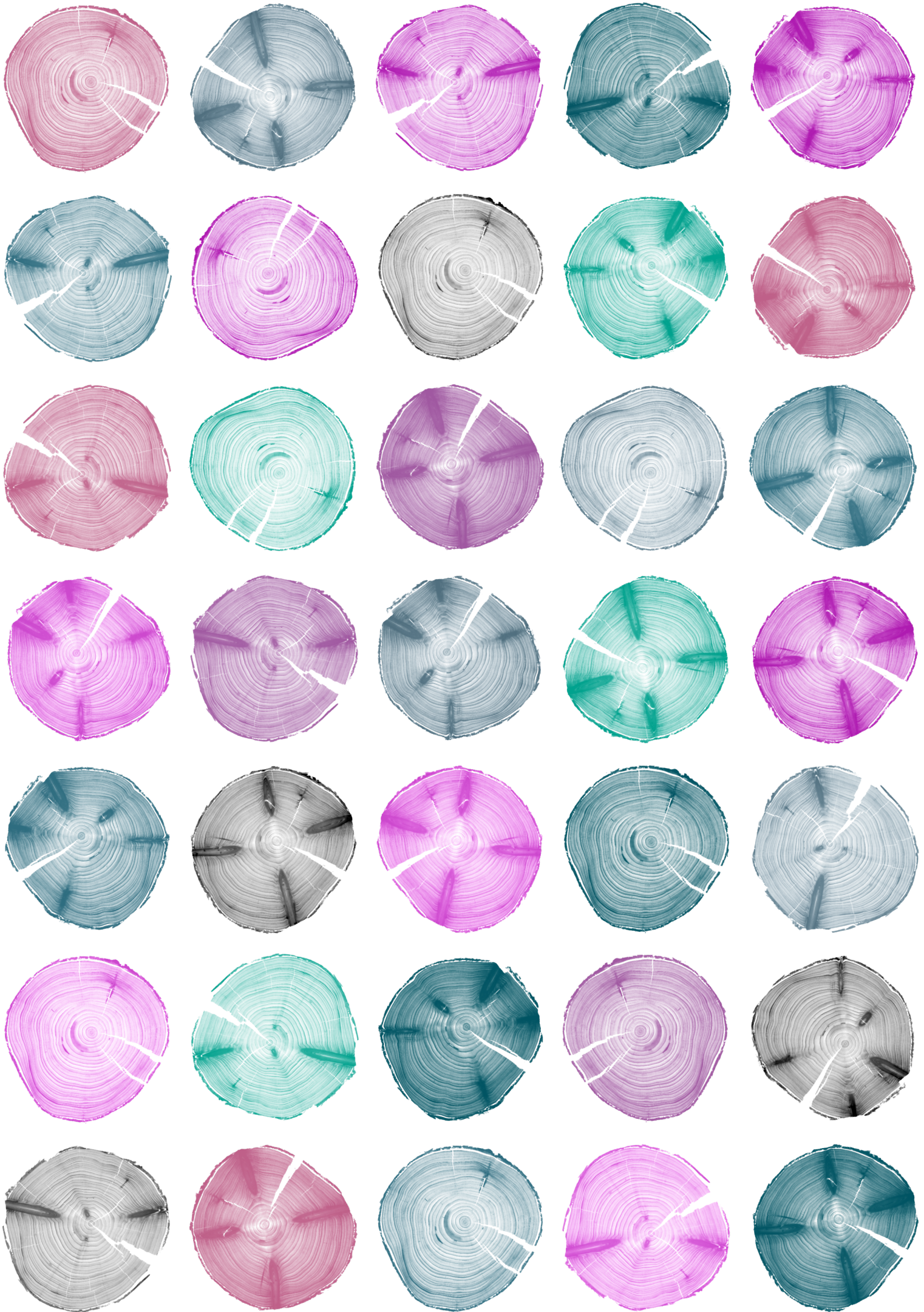
Jochen Kollofrath und Simon Schmid vom Lehrstuhl für Zerstörungsfreie Prüfung danke ich für die fruchtbare Zusammenarbeit. Dr.-Ing. Iason Papaioannou und meinem Mentor Dr. Dirk Porezag bin ich verbunden für ihre geduldige Auseinandersetzung mit meinen Ideen. Dankbar bin ich auch Kevin Josef Li, Lars Nockenberger, Martin Georg T. Kronthaler, Pablo Francisco Ramírez Hönack und Simon Mannhardt, die mich als wissenschaftliche Hilfskräfte oder über Studien- und Abschlussarbeiten tatkräftig unterstützten.

Meinen Freund:innen aus Schulzeiten danke ich, dass sie eine Konstante in meinem Leben bleiben. Die gemeinsame Reise an der TU München mit meinen Studienfreund:innen begann vor über einer Dekade - danke für eine unvergessliche Zeit.

An meine Eltern und meine Schwester: Liebevoll und sorgsam habt Ihr alles ermöglicht, was ich Heute lebe und erlebe. Für Eure bedingungslose Unterstützung bin ich zutiefst dankbar. Meinen Schwiegereltern gilt ein besonderer Dank für Ihren Beistand. Ich danke meiner Frau von Herzen. Ohne Deinen unermüdlichen Rückhalt hätte ich es nicht bis hierher geschafft.

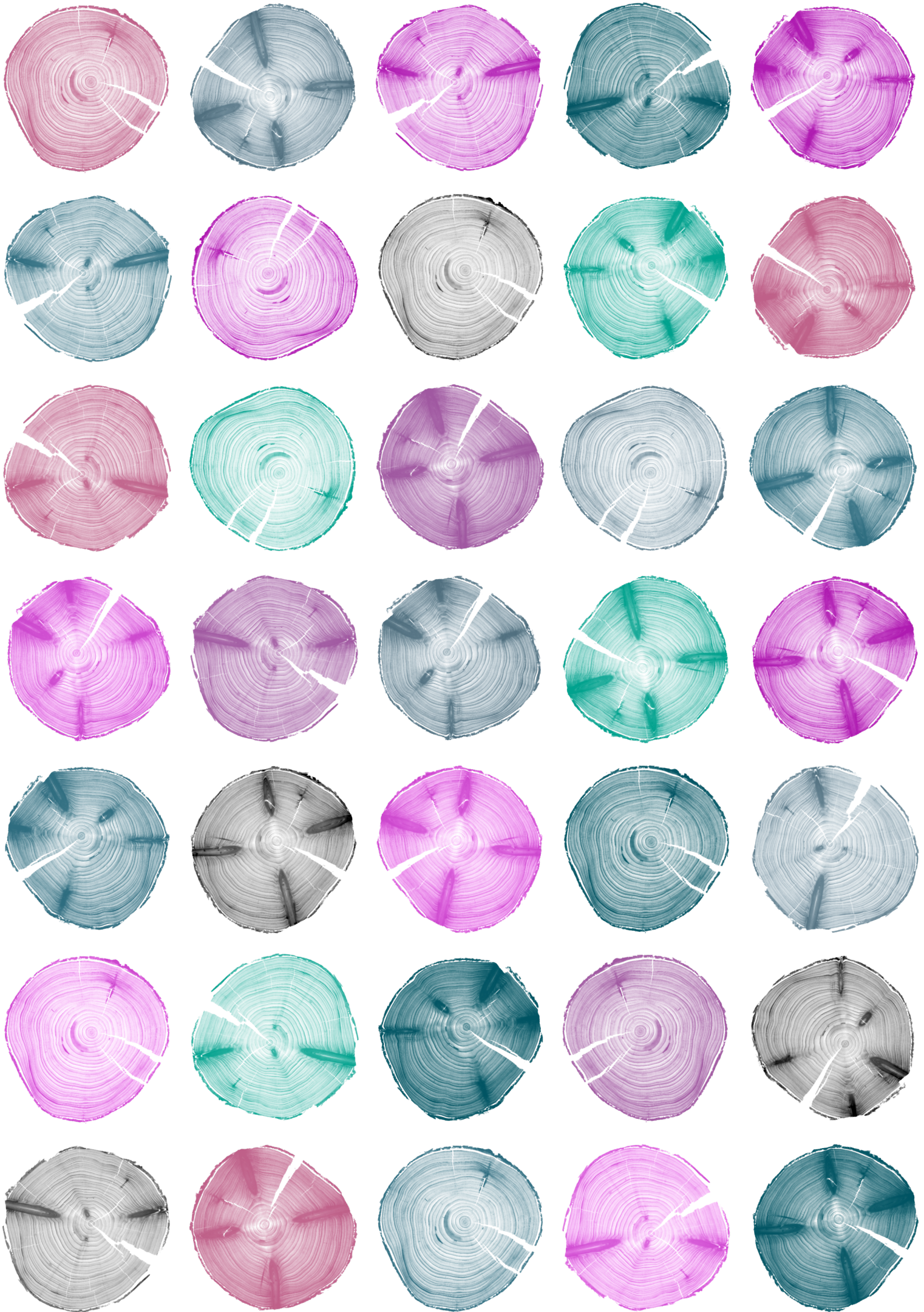
Garching, January 28, 2025

Karl-Alexander Hamilton Hoppe



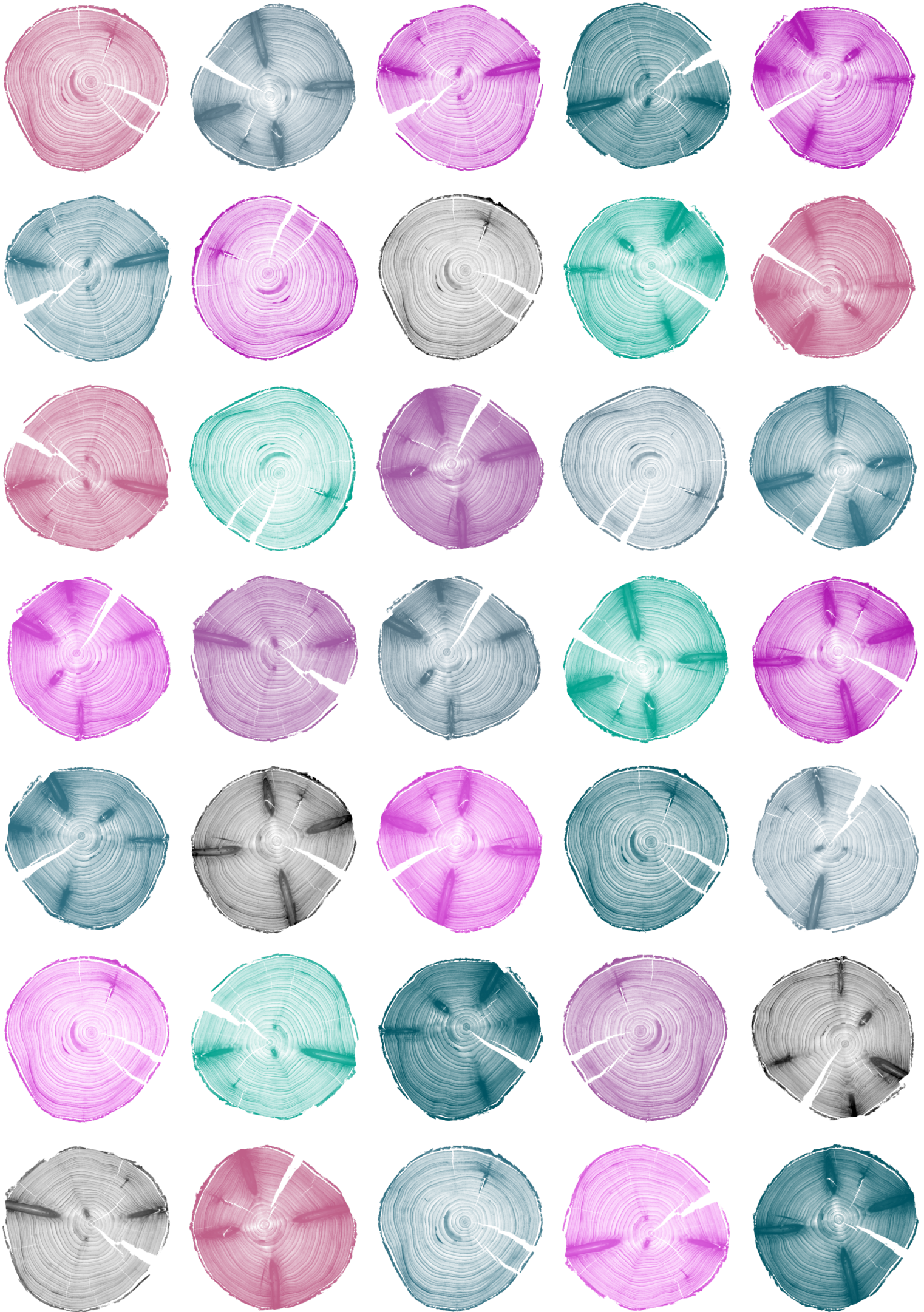
Abstract

The steady increase in computational power, on the one hand, and the advent of functionally graded materials, on the other hand, give rise to characterization methods for heterogeneous materials. Confining the context to non-destructive testing sets the stage for methods like digital image correlation or digital volume correlation. Next to these involved approaches, guided waves and data from modal analysis present fundamentally feasible approaches that are not mature yet in for functionally graded materials. This thesis develops a numerical method for identifying the spatially varying elastic material properties of a structure using modal data while considering uncertainty. This is achieved by using Bayesian inference, the finite element method, the generalized polynomial chaos expansion, and the Karhunen-Loève expansion. A modification accelerates the method, and a generalization of several quantities of interest is proposed alongside a stochastic material model for a softwood species. The acceleration of the procedure implies that once the generalized polynomial chaos surrogate is trained, it could potentially be applied to an unlimited number of altered configurations. Stumping intuition, further results show that providing the cross-correlation of multiple unknowns a priori is not necessarily beneficial. A realistic covariance model for describing wood by a random field is presented. Next to unlocking non-destructive testing for this application, it forms the basis for synthesizing wood at the macro-scale.



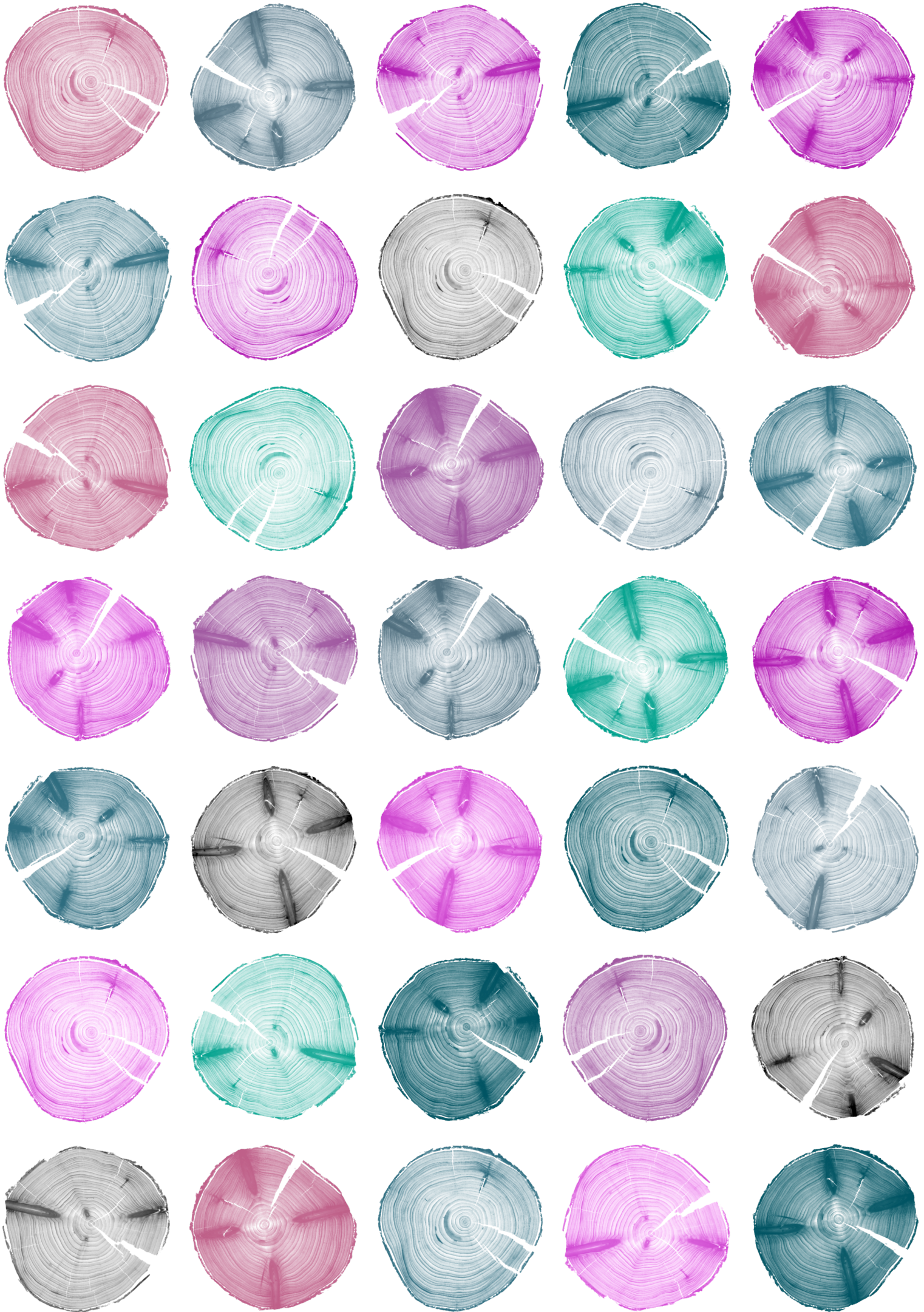
Zusammenfassung

Die kontinuierliche Steigerung der verfügbaren Rechenleistung sowie die Popularisierung von Werkstoffen mit funktionalen lokalen Eigenschaften kreieren Angebot und Nachfrage von Prüfverfahren für heterogene Materialien. Innerhalb der zerstörungsfreien Prüfung existieren Methoden wie die digitale Volumenkorrelation, die auf dem Vergleich von Daten aus der Computertomografie vor und nach dem Aufprägen einer Last auf die Struktur beruht. Neben diesen kostspieligen Ansätzen stellen der Einsatz von geführten Wellen und die Nutzung des Schwingungsverhaltens praktikable Alternativen dar. Allerdings ist die letztere im Kontext räumlich schwankender Materialeigenschaften noch nicht technisch ausgereift. Ziel dieser Arbeit ist es, ein numerisches Verfahren zu entwickeln, das das inhomogene linear-elastische Materialverhalten von Strukturen anhand von Eigenfrequenzen und Eigenschwingformen unter Berücksichtigung von Unsicherheiten bestimmt. Zu diesem Zweck wird Bayes'sche Inferenz unter Verwendung eines von der räumlichen Diskretisierung entkoppelten Ersatzmodells für die Finite-Elemente-Methode eingesetzt. Darauf bauen eine beschleunigte Variante sowie eine Erweiterung des Verfahrens für die gleichzeitige Bestimmung mehrerer korrelierter Zielgrößen auf. Das beschleunigte Verfahren impliziert, dass das Ersatzmodell nach seiner initialen Erstellung potenziell für beliebig viele weitere Einbausituationen des Bauteils wiederverwendet werden kann. Es wird gezeigt, dass die Berücksichtigung der Kreuzkorrelation mehrerer Unbekannter in der a priori Wahrscheinlichkeitsdichtefunktion nicht zwingend von Vorteil ist. Zur Erleichterung der Anwendung der entwickelten Methode wird ein stochastisches Materialmodell für Holz entwickelt. Dieses stellt sich als das erste realistische Kovarianzmodell zur Beschreibung der Materialeigenschaften von Holz durch Zufallsfelder heraus. Neben der Erschließung der zerstörungsfreien Prüfung für diesen Werkstoff, stellt das neue Modell die Grundlage für die Erzeugung realistischer Holzmuster auf der Makroskala dar.



Contents

1	Introduction	1
2	Methods	5
2.1	Problem Statement	5
2.1.1	Finite Element Method	5
2.1.2	Applied Bayesian Inference	6
2.2	Bayesian Inference	9
2.2.1	Sampling	10
2.2.2	Likelihood of Observed Data	11
2.3	Random Vectors and Random Fields	12
2.4	Random Field Description	13
2.4.1	Covariance Identification	17
2.4.2	Karhunen-Loève Expansion: Definitions and Numerical Treatment . . .	19
2.4.3	Generalized Karhunen-Loève Expansion: Cross-Correlated Random Fields	21
2.5	Acceleration	24
2.5.1	Generalized Karhunen-Loève Expansion: Acceleration by Transformation	24
2.5.2	Generalized Polynomial Chaos Expansion Surrogate Model	25
3	Summary of Publications	29
3.1	Paper A	30
3.2	Paper B	32
3.3	Paper C	34
3.4	Paper D	36
4	Discussion and Conclusions	39
	Bibliography	43
	Appendices	55
I	Parameter Studies on the Effect of Measurement Noise, Prior Cross-Correlation, and the Number of Observation Points Concerning Multivariate Identification Problems	55
II	Paper A	59
III	Paper B	77
IV	Paper C	97
V	Paper D	115



Chapter 1

Introduction

Functionally graded materials are currently being popularized [41, 131]. They represent a class of heterogeneous materials whose properties are deliberately varied over space to achieve a desired effect on the macro-scale. Testing such materials exhibits different requirements compared to the procedures used for homogeneous materials. For instance, volume effects and local deviations in the material properties both impact the procedures for static bending tests of wood. These protocols then differentiate between the determining the local and global modulus of elasticity. Suitable methods tailored to functionally graded materials currently do not exist yet. Hence, characterization methods for these new materials need to be developed. In principle, strategies for identifying the underlying material properties of a structure are available. These are mostly imaging methods that provide information on the local mass density of the subject, such as elastography in medicine applications [9, 43]. Not only locating stiff inclusions but also quantifying them corresponds to assessing Young's modulus. Two ways of determining a specimen's local elastic material properties at the surface are described in the literature [68]. Wood represents one application example for a heterogeneous material where such a procedure is commonly employed. Here, the tracheid effect, an interaction of light with the surface of an object, may be employed to measure the orientation of fibers [68]. While this allows for some predictions about the stiffness via a material model, it is susceptible to local imperfections in the material, and local strain imaging is more pertinent to the cause together with a beam theory [68]. The correlation of an image of the surface of a specimen that is endowed with a speckle pattern with an image of the identical surface after the application of an external load is termed digital image correlation [105, 135, 147]. Using this displacement information and subjecting the specimen to constant bending, a map of the underlying stiffness can be constructed using the constitutive equations for the case of linear elastic material after the intermediate derivation of the strains from the displacements [68]. An analogous procedure called digital volume correlation exists for the three-dimensional case in combination with X-ray computed tomography [38, 84, 156]. It enables strain imaging in the interior of a structure, but it suffers from a relevant drawback. Within the digital volume correlation method, the specimen can be investigated with a computed tomography scan at different stages of displacement. This entails packaging issues that render digital volume correlation unfeasible for quality control applications, as a rudimentary implementation of the principle would require the tensile testing setup of the specimen to fit in the scanning apparatus. Further, it is challenging to find features within non-homogeneous materials that could be correlated in the three-dimensional scanned volume.

This motivates the goal of developing a non-destructive and contactless characterization method for heterogeneous materials with elastodynamic behavior as described by a structure's modal data. In general, the aspiration of 'looking into the material' and imaging the quantity of interest there demands the solution of a localization problem [10, 165]. The latter is the counterpart to numerical homogenization approaches. Both of these are studied in the literature and considerable research efforts are being made to develop these hierarchical or multi-fidelity modeling approaches and establish linkages between homogenization

and localization [1, 4, 19, 103, 117, 125, 149]. These ambitions will benefit greatly from the advances in computational power [144]. The present localization approach is centered on interpreting the a priori unknown stiffness functions as realizations of random fields and representing the random fields with the Karhunen-Loève expansion, see Figure 1.1. Retaining the description of the unknowns as random variables and recognizing the presence of noise in any measured data, Bayesian inference solve the inverse problem posed by the localization problem. Bayesian inference is established as the current method of choice when measurement data are involved. Noteworthy applications in the fields of acoustics include the work by Xiang and Fackler [155] and the study by Bockman et al. [15]. The estimation of homogeneous elastic material parameters of isotropic and orthotropic plates by modal analysis or dispersion curves using the Bayesian approach is well researched [25, 40, 46, 102]. The combination of Bayesian inference with the Karhunen-Loève expansion is popular for the inference of permeability fields [140] and in the geotechnical engineering community [162]. Uribe et al. [146] apply this combination of methods to elastostatics. The following highlights the contributions to the state of the art.

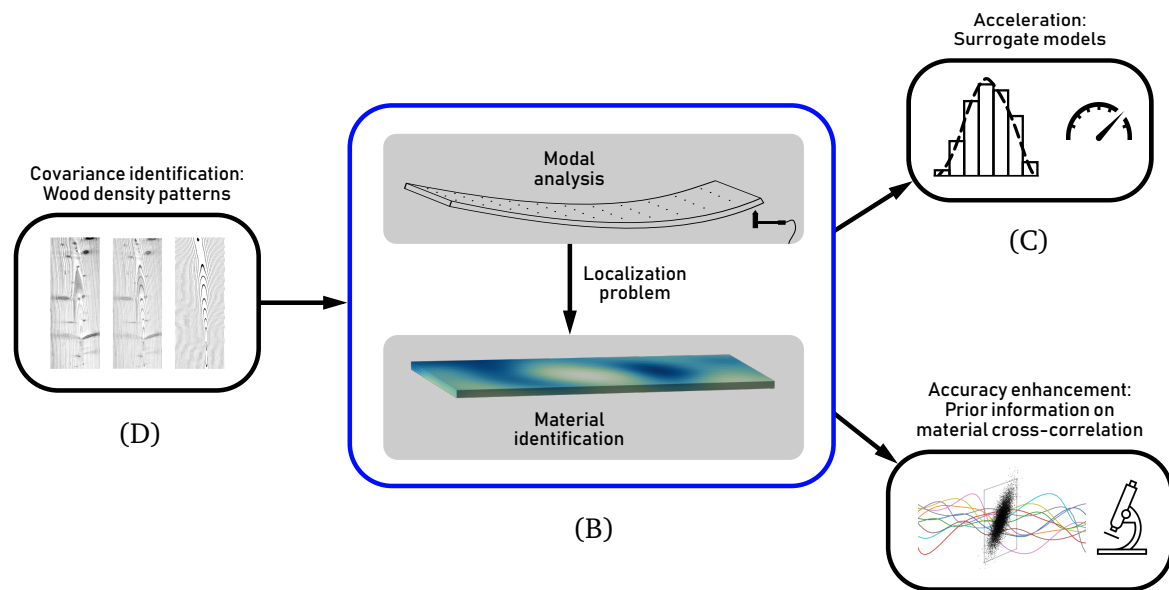


Figure 1.1: The developments of the state of the art connected to this dissertation consist of four modules. In the center lies the localization problem of identifying a structure’s spatially varying stiffness from its natural frequencies and mode shapes. In order to apply the random field description with the Karhunen-Loève expansion, the covariance of the material needs to be identified first. This is done for wood here. Based on this methodology, two improvements are presented on the right. They consist of an acceleration of the method using a generalized polynomial chaos expansion surrogate and a generalization to the simultaneous recovery of multiple correlated stiffness functions. The latter entails the potential for further acceleration and an improvement of the estimation accuracy by the consideration of the cross-correlation coefficient of the quantities of interest.

Contributions and Accomplishments The present dissertation manuscript represents a cumulative thesis in the field of non-destructive material characterization of heterogeneous materials subject to elastodynamics [60]. Thus, the aim of this document is not to provide exhaustive explanations concerning the accomplishments. In contrast to this, the achievements and contributions to the state of the art are condensed in publications in peer-reviewed scientific journals. Namely, these are [Paper A](#) [62], [Paper B](#) [57], [Paper C](#) [58], and [Paper D](#) [56]. The noteworthy accomplishments are summarized below.

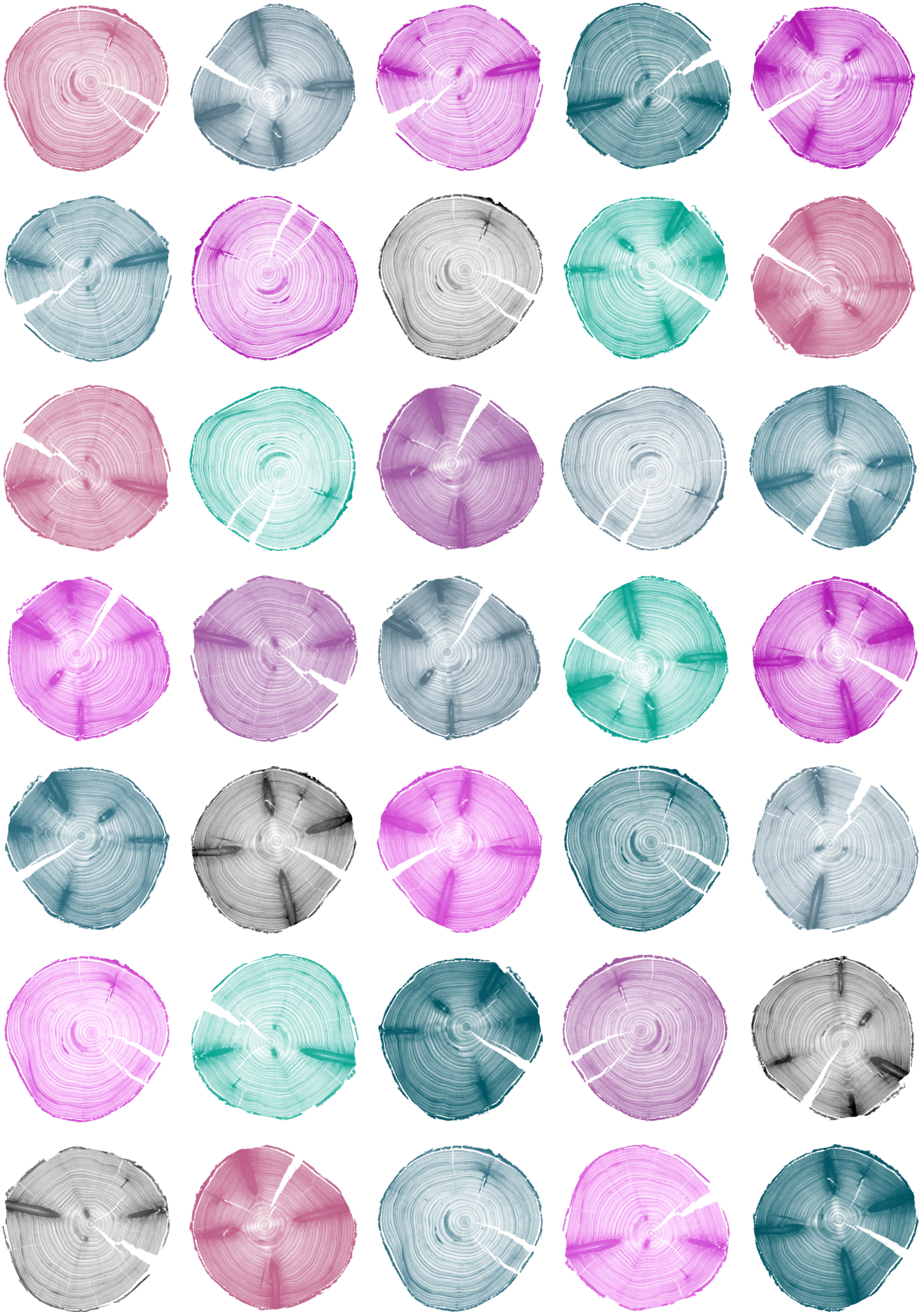
- Firstly, the suitability of natural frequencies for detecting defects in homogeneous plates is assessed in [Paper A](#). A comparison with the use of guided waves, which presents the

current method of choice, discovers that employing resonance frequency data offers some advantages. In fact, it leads to smoother objective functions that facilitate using gradient-based optimization procedures. However, it entails symmetry problems concerning defect localization.

- A solution to the stiffness localization problem within a cantilever beam from its natural frequencies is presented in [Paper B](#). This approach describes the structural flexibility using the Karhunen-Loève expansion and embeds this description into a Bayesian inference formulation, which allows for an estimate of the solution uncertainty. The study shows that basing the inference on modal data does not fall victim to error propagation, unlike an inversion procedure from the literature that uses deflection data, and it considers the effects of the stiffness length scale and the signal quality on performance.
- [Paper C](#) develops a method for reusing surrogate models mapping from Karhunen-Loève coefficients to the mode shapes of a structure. This improvement accelerates the procedure presented in [Paper B](#) significantly. This is demonstrated numerically for a functionally graded material application. Here, three structural beams with respectively changing application purposes are chosen for the demonstration of the method. Ultimately, the length scale corresponding to the original surrogate model should be chosen as small as possible.
- [Paper D](#) proposes a model for the elastic material properties of wood based on a compact morphological description. This model consists of a density model and a model for the fiber directions. These computational models are validated experimentally using computed tomography and modal analysis of a spruce trunk. Further, a generalization and quantification of formerly qualitatively described wood defects is achieved. The formulation a stochastic model for the heterogeneous material and quantify the uncertainty in Young's modulus due to the natural morphological variability of wood marks the final step.

Chapter 3 covers the key aspects of each paper, including novelty and results, the authors' contributions, and the citation reference in greater detail. Full-text reprints of the papers are provided in [Appendix II](#), [III](#), [IV](#), and [V](#).

This thesis is structured as follows: Chapter 2 describes the methods necessary for reproducing the results of this thesis. The latter are concentrated in publications that are summarized and put into a more general perspective in Chapter 3. Chapter 4 scrutinizes the results while relating them to results from the literature and draws the major conclusions to this dissertation. Finally, reprints of the publications are given in [Appendix II](#), [III](#), [IV](#), and [V](#).



Chapter 2

Methods

2.1 Problem Statement

2.1.1 Finite Element Method

Elastostatics for Spatially Varying Elasticity Finite element method models are routinely employed for tasks such as elastography [86], where the elasticity of a probe is to be mapped, and, in some applications, stiff inclusions such as cancer tissue shall be detected. The most pertinent information in this regard is delivered by strain gauges [146]. The generalized case of identifying the spatially varying stiffness of a sample receives significant attention in the literature [79]. Finding a local field from a global quantity is termed localization and is described in detail by Yvonnet [164]. Within solid mechanics, modeling the elastostatics of the system offers one basis for the aforementioned procedures. Koutsourelakis [79] formulates the corresponding equilibrium equations as

$$\nabla \cdot \hat{\sigma}(x) + \mathbf{b}(x) = \mathbf{0}, \quad \forall x \in \Omega, \quad (2.1)$$

where $\hat{\sigma}(x)$ represents the stress tensor and \mathbf{b} are body forces. The constitutive relations are

$$\boldsymbol{\sigma}(x) = \mathbf{D}(x)\boldsymbol{\varepsilon}(x), \quad (2.2)$$

where $\boldsymbol{\sigma}(x)$ is the stress vector, $\mathbf{D}(x)$ is the elasticity tensor, and $\boldsymbol{\varepsilon}(x)$ is the vector of strains. The local constitutive matrix \mathbf{D}_e satisfies $\boldsymbol{\sigma}_e = \mathbf{D}_e \boldsymbol{\varepsilon}_e$ [79]. The strains can be obtained from the displacements $\mathbf{u}(x)$ as

$$\boldsymbol{\varepsilon}(x) = \mathcal{S}\mathbf{u}(x), \quad (2.3)$$

where the differential operator \mathcal{S} is the strain-displacement matrix [79]. Refer to the literature (see Zienkiewicz [166]) for defining boundary conditions. The local elasticity may be modeled as constant over each finite element, discretized at the mesh nodes, or assigned at the quadrature points of each element [79]. Paper B evaluates the spatially varying flexibility at the mentioned integration points. Finally, Zienkiewicz [166] gives the standard form of the assembled finite element method equations as

$$\mathbf{K}\tilde{\mathbf{u}} + \mathbf{f} = \mathbf{0}, \quad (2.4)$$

where \mathbf{K} is the stiffness matrix, $\tilde{\mathbf{u}}$ are nodal displacements and \mathbf{f} is the load term.

Numerical Homogenization Having obtained the finite element method formulation that only departs from the standard formulation in terms of the explicit notation of the spatial dependence, homogenization approaches that play the counterpart to localization can be explored. Usually, numerical homogenization is employed for materials with multiple discrete

phases at the micro-scale [112]. For this case, approaches based on periodic unit cells and representative volume elements exist [164]. The following connects to the representative volume element branch. Consider the stress tensor component results on a small scale $\tilde{\sigma}_{\zeta,ij}$ from a static analysis based on Eq. (2.4) on a domain with volume $|V|$. Now, the homogenized stress component $\tilde{\sigma}_{h,ij}$ can be obtained using these stresses as

$$\tilde{\sigma}_{h,ij} = \frac{1}{|V|} \int \tilde{\sigma}_{\zeta,ij} d\zeta, \quad (2.5)$$

and the homogenized strain $\varepsilon_{h,ij}$ is computed analogously as

$$\varepsilon_{h,ij} = \frac{1}{|V|} \int \varepsilon_{\zeta,ij} d\zeta, \quad (2.6)$$

where ζ refers to the small scale, see Charalambakis [21]. Finally, the homogenized stiffness E_h reads as

$$E_h = \frac{\tilde{\sigma}_h}{\varepsilon_h}. \quad (2.7)$$

Elastodynamics Consider a matrix eigenvalue problem corresponding to the assembled finite element method formulation for the case of no damping as [166]

$$(\mathbf{K} - \varpi^2 \mathbf{M}) \hat{\mathbf{u}} = \mathbf{0}. \quad (2.8)$$

Here, \mathbf{M} is the system's global mass matrix. The eigenvectors $\hat{\mathbf{u}}$ and the angular eigenfrequencies ϖ present the solutions to this eigenvalue problem. The i^{th} natural frequency may then be found as $\varpi_i/2\pi$. Further, a structure's general frequency response may be constructed by modal superposition [34].

This thesis uses modal data resulting from the dynamic behavior of elastic structures as input data for the characterization of the local stiffness. Paper B solves the localization problem of identifying the spatially varying structural flexibility from natural frequency measurements. In contrast, Paper C uses information about the eigenvectors.

2.1.2 Applied Bayesian Inference

Overview of Approach The methods from the following sections can be employed for the Bayesian inference of a parameter that exhibits spatial dependence, which lies at the core of this thesis, see Figure 2.1, and is published in Paper B. The most important use case within this dissertation is identifying the Young's modulus function $E(x)$ of a structure. Measurements \mathbf{d} of the mode shapes $\hat{\mathbf{u}}$ or natural frequencies of the structure represent the data for the inference here. The numerical model consists of a finite element method implementation of the elastodynamic behavior resulting in Eq. (2.8). To evaluate Eq. (2.11), the prior and likelihood functions need to be chosen. The measurement noise model is application-specific and should be chosen according to one of the equations presented in Section 2.2.2. All elastic material properties are inherently stochastic and non-homogeneous. Typical simplifications that prescribe a homogeneous and deterministic material, as is often the case for steel, are merely modeling assumptions that discard the variability based on claims of negligible influence. For cases where this influence is not negligible, the stiffness shall be considered as a random field $E(x, \omega)$ represented by the Karhunen-Loève expansion in Eq. (2.50). Consider a stationary mean function $\mu(x) = \mu$ and an appropriate truncation [70] to K that is

independent of the spatial discretization of the Karhunen-Loève expansion. This leads to a description of $E(x, \omega)$ by θ , a collection of parameters $\{\mu, \eta_1, \eta_2, \dots, \eta_K\}$. The evaluation of the finite element method model G based on this yields the response $v = G(\theta)$. Finally, the underlying $E(x)$ can be inferred by updating the joint distribution of θ from Eq. (2.11) [92].

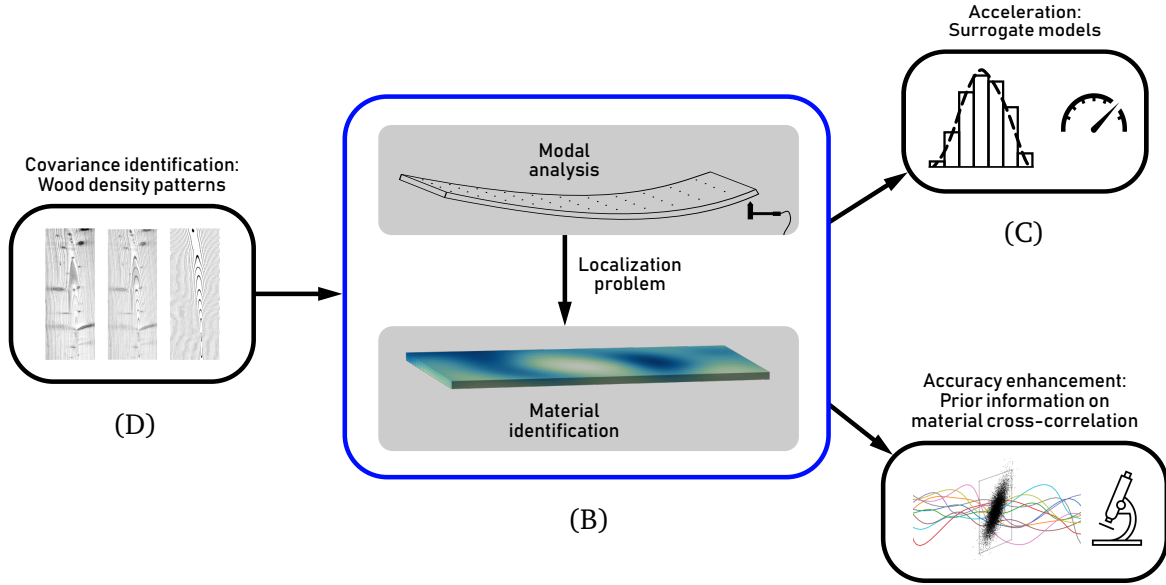


Figure 2.1: This figure constitutes a repetition of Figure 1.1 for the reader's convenience. The Bayesian inference of a Young's modulus function $E(x)$ given modal data shown in pictogram (B) represents the choice of application for this dissertation and is published in [Paper B](#).

Acceleration The Karhunen-Loève expansion possesses some characteristics that affect the solution of the inverse problem. There are fewer parameters to identify than when $E(x)$ is modeled with one random variable per node of the spatial discretization in the finite element method. This can be applied using Eq. (2.39). On the one hand, this is detrimental to the well-posedness of the problem. In a continuous and deterministic setting, the uniqueness of the problem is still given, as the Karhunen-Loève bases ϕ_i are orthogonal. But as soon as the spatial domain is discretized, it is possible to present the same $E(x)$ using two different sets of Karhunen-Loève coordinates η_i . This worsens when errors such as noise are introduced to d . On the other hand, the dimension of the posterior from Eq. (2.11) is reduced to the length of θ . This facilitates its exploration by the sampling algorithm or the mode identification in the case of maximum a posteriori estimation.

A compelling argument for using the Karhunen-Loève expansion in Bayesian inference arises when the likelihood is costly and sampling is done using Markov chains. This motivates constructing a surrogate of the finite element method model that is cheaper to evaluate. Obtaining the generalized polynomial chaos coefficients, see Section 2.5.2, becomes expensive with a growing number of input parameters. It suffers from the curse of dimensionality as expressed by Eq. (2.82). This can cause the generalized polynomial chaos expansion to become unfeasible for approximating parameters with spatial dependence. The Karhunen-Loève expansion solves this problem by decoupling the dimension of the random space from the spatial grid. Marzouk and Najm [92] pioneer its usage for Bayesian inference applications alongside generalized polynomial chaos.

Here, the generalized polynomial chaos expansion is used instead of the finite element method for the likelihood evaluation, see Eq. (2.18). To this aim, a model output v is ex-

panded according to Eq. (2.82). The Karhunen-Loève coefficients η_i that represent the model inputs are standard normal random variables in the case of a Gaussian $E(x, \omega)$. Thus, Hermite polynomials may be chosen as the polynomial basis [92].

The generalized polynomial chaos coefficients must be determined again once a different prior covariance is imposed on $E(x, \omega)$ within the framework proposed in [92], as the generalized polynomial chaos expansion formulates the surrogate based on the Karhunen-Loève coefficients. To decouple the surrogate from changes in the covariance hyper-parameters, two extensions of the framework are developed in the literature to allow for uncertain \mathbf{q} [138, 142]. One of these extensions is presented in detail in Section 2.5.1. Here, Eq. (2.79) delivers an approximate description of a Karhunen-Loève expansion endowed with arbitrary hyper-parameters based on a transformation of the covariance that is used for the original construction of the surrogate. Following this, the new surrogate is found without new finite element method evaluations with Eq. (2.86). These methods are integrated into the baseline procedure and are applied to accelerate the identification of the Young's modulus function $E(x)$, see pictogram (C) in Figure 2.1, which is published in Paper C.

Optimal Choice of Prior Distributions for the Bayesian Inference of Multi-Correlated Random Fields

The following covers the accuracy enhancement of the Bayesian inference using information about the cross-correlation of two or more spatially varying quantities of interest. The relation of this investigation to the other considerations within this dissertation is illustrated in the lower-right pictogram within Figure 2.1. There are often several quantities of interest with spatial dependence that shall be identified simultaneously. If they exhibit a cross-correlation, the prior distribution on θ may reflect this cross-correlation. One way this may be achieved is by modeling the quantities of interest as simply cross-correlated random fields. This type of approach is best suited to empirical studies. Generally, inferring local operating conditions along with the main quantity of interest is a perspective that is valuable to any researcher seeking to achieve reproducible results. In the context of solid mechanics, the task of identifying the full elasticity tensor $\mathbf{D}(x)$ comes to mind. Hooke's law provides the basis for the correlation assumption between its components, while the inherent randomness commands the emergence of covariances.¹ No authoritative study on the effect of reflecting the cross-correlation in the prior distribution exists in the literature. This motivates a corresponding investigation here, presenting an extension to [92]. As causality becomes harder to identify for complex systems, a very simple, even trivial, problem statement is formulated here.

Consider two simply cross-correlated random fields M_1 and M_2 that are represented by Eq. (2.65)² with $H = 1$ m evaluated at $n = 50$ nodes. They exhibit a linear coefficient of cross-correlation of $\rho = 0.9$. All kernels are chosen as the squared exponential kernel in Eq. (2.30) with $L = 1$ m and auto-covariance $\sigma^2 = 1$ (-), while the cross-correlation kernels are expressed in terms of the auto-correlation kernels using $\rho = 0.9$. A visualization of samples from a cross-correlated bi-variate field is provided in Figure 2.6.

Now, the task is to reconstruct ground truth samples from M_1 and M_2 given their noisy observations \mathbf{d} . While this problem can be solved using Gaussian process regression, the aspiration is to arrive at conclusions that can be generalized when any forward operator G is used. To this aim, the Bayesian inference formulation from Eq. (2.11) is employed. The likelihood function is adopted from Eq. (2.15) such that each noise component ϵ_j possesses

¹The real and imaginary parts of the acoustic boundary admittance also possess a cross-correlation for the case of granular porous materials. Identifying these while accounting for the cross-correlation in the prior for the Bayesian inference based on sound pressure evaluations in proximity to the boundary is studied by Hoppe et al. [59].

²Gratitude is expressed towards Heyrim Cho for providing their source code from [22] for validating the simply cross-correlated Karhunen-Loève expansion implementation.

the noise standard deviation γ . The decomposition of the block covariance matrix satisfying $\rho = \rho_{\text{rec}}$ in Eq. (2.66) as formulated by Eq. (2.73) generates the samples within the updating procedure to evade an inverse crime. The coefficients ζ representing θ are endowed with mutually uncorrelated zero-mean, unit-variance Gaussian prior distributions. This setup implicitly encodes the reconstruction cross-correlation coefficient ρ_{rec} of the random fields via the prior of the Bayesian inference, whose posterior is explored using slice sampling, see Section 2.2.

Two parameter studies exploring the effect of measurement noise, the reconstruction cross-correlation coefficient, and the number of observation points are presented in Appendix A.

2.2 Bayesian Inference

Model updating procedures attempt to identify the parameterization of a system [143]. This is usually performed iteratively until the output produced by the simulation model matches the measurement data. This procedure is relevant for a quantity of interest that is not directly observable or when the measurement is time- or cost-intensive. The Bayesian approach to inverse problems integrates uncertainty into the procedure. Refer to the literature for introductions to Bayesian inference [23, 85, 89, 97, 104]. Considering uncertainty instead of modeling a system as deterministic represents a generalization from the engineering perspective. Many elements in a typical engineering system are fraught with uncertainty. Consider data \mathbf{d} that are subject to additive measurement noise ϵ [140]

$$\mathbf{d} = G(\theta) + \epsilon. \quad (2.9)$$

Here, the data shall be described using the parameters θ to a model G yielding the noise-free model predictions $\mathbf{v} = G(\theta)$. All models are mere approximations of reality, which brings the concept of model uncertainty. Also, assuming the data is uncertain accounts for measurement errors. Lastly, the parameters θ can only be determined with finite accuracy, and therefore, they should also be considered as uncertain. These considerations support modeling each component of the system as uncertain. Eq. (2.9) assumes a perfect model G , which is just a mathematical depiction of the real physical system [7, 143]. Solving the connected inverse problem is then to

$$\text{find } \theta : \mathbf{v} = G(\theta) \text{ given } \mathbf{d}. \quad (2.10)$$

Bayes' Theorem This task of identifying the true model parameters θ from noisy observations of the system output may be formulated accounting for the sources of uncertainty listed above. Employing Bayes' theorem, the conditional probability density of the parameters θ given that their evaluation within the model yields the observed data \mathbf{d} reads as [140]

$$P(\theta | G(\theta) + \epsilon = \mathbf{d}) = \frac{P(\mathbf{d} | \theta) P(\theta)}{P(\mathbf{d})}. \quad (2.11)$$

Typical terminology refers to the marginal distribution $P(\theta)$ as the prior probability distribution, the conditional distribution $P(\mathbf{d} | \theta)$ as the likelihood, the marginal distribution $P(\mathbf{d})$ as the evidence, and to the conditional distribution $P(\theta | \mathbf{d})$ as the posterior [82]. Essentially, Bayes' rule treats all parameters as random variables and describes how novel data change prior assumptions on any quantity of interest [7]. The prior offers a way of incorporating experience and information from previous measurement campaigns [7]. The distribution

$P(\mathbf{d}|\boldsymbol{\theta})$ expresses the likelihood that evaluating the model with $\boldsymbol{\theta}$ yields the observation of \mathbf{d} and represents the increase of knowledge by new data [116]. As the factors in the denominator can be small floating point numbers, it is advisable to operate on the logarithm of Eq. (2.11) to avoid numerical complications during their multiplication [116]. Because $P(\mathbf{d})$ is not tangible in the Bayesian inference context, it is usually chosen as a normalizing term, such that the theorem reads as

$$P(\boldsymbol{\theta}|G(\boldsymbol{\theta}) + \epsilon = \mathbf{d}) \propto P(\mathbf{d}|\boldsymbol{\theta})P(\boldsymbol{\theta}). \quad (2.12)$$

Challenges A mathematical problem is considered well-posed when its solution exists, is unique, and changes continuously with respect to the inputs [50]. This definition can be equally applied to inverse problems [12]. In contrast to this, if no set of parameters $\boldsymbol{\theta}$ suffices to describe the data, several parameter combinations yield the same output, or if small data discrepancies propagate to a comparatively large parameter variation, the problem is called ill-posed [33]. While regularization or constraints are used in traditional optimization to enforce physically sensible parameter values [7, 47], similar effects in Bayesian inference may be achieved by choosing appropriate prior distributions. One general concept to remember when the data stems from a computational model instead of experimental measurement is to coarsen the discretization during the inversion with respect to the computation of the ground truth. Neglecting this results in an inverse crime, yielding an overestimation of the method's accuracy [76].

2.2.1 Sampling

Closed-form solutions for $P(\boldsymbol{\theta}|\mathbf{d})$ in Eq. (2.11) only exist when conjugacy is present in special cases with linear forward models [146]. For all other cases, the posterior distribution must be approximated by random sampling [76]. Exploration algorithms based on Markov chain Monte Carlo methods present one option [106]. Here, approaches that neglect [119] and consider the gradient [54] exist.

The following provides a selection of Markov chain Monte Carlo sampling methods. The Gibbs procedure samples separately from each component of the quantity of interest [94, 163].

The Metropolis-Hastings algorithm generates candidate samples within each step of the chain from a proposal distribution [106]. If the acceptance probability of the candidates does not satisfy a threshold, they are rejected, and the samples from the previous step are retained [94, 115]. On the one hand, the acceptance probability is sensitive towards the proposal covariance, while a too-small choice of the latter yields a poor exploration of the posterior [106]. On the other hand, the acceptance ratio is low for strongly correlated components of the quantity of interest. One of the remedies [123] is found in Metropolis-within-Gibbs sampling [82]. Many improvements of the highly influential base algorithm exist [98, 106, 145].

Slice sampling is applied individually to each component, where it uniformly draws samples based on intervals [100]. While there is no adaptive component involved after the preparatory tuning, several posterior evaluations are required to produce a sample, which is especially detrimental for computationally expensive models [96]. Postprocessing the results of the mentioned sampling procedures yields statistical sample moments of the Markov chain [163].

Falling back to the maximum a posteriori estimate of $\boldsymbol{\theta}$ strays from the intended path of Bayesian inference and sacrifices the latter's main advantages. The maximum a posteriori estimate identifies the mode of the posterior, which is not equal to the expected value for

skewed data. Though it is computationally cheap as merely an optimization problem needs to be solved instead of the construction of a Markov chain, applying the maximum a posteriori estimate entails abandoning the shape of the posterior or even its higher order moments [151]. Refer to the literature for further reading on Bayesian inference [94, 123].

2.2.2 Likelihood of Observed Data

This section inspects the likelihood introduced in Section 2.2 in greater detail. The likelihood integrates measurement data into Bayes' theorem and is the conditional probability that this data is observed using one set of θ [116]. Essentially, it answers how likely a measurement of the data is when certain model parameters are used. Consider the noise-free output of the numerical model as $v = G(\theta)$ and consider the random additive noise ϵ as normally distributed. This implies that the investigated scenarios are based on normal or multivariate normal distributions.

For one measurement data point d and the corresponding model prediction v , the Gaussian likelihood with standard deviation γ reads as [85]

$$\mathcal{L}(d|\theta) = \frac{1}{\gamma\sqrt{2\pi}} \exp\left(-\frac{1}{2} \frac{(d-v)^2}{\gamma^2}\right). \quad (2.13)$$

Countless application-specific modifications can be made to this normal likelihood to correctly accommodate the properties of the data. Some items that mandate customization of Eq. (2.13) are the repeated acquisition of data, simultaneous measurements of several quantities of interest, and recording vector-valued data points. The following first provides the appropriate formula for each of these cases and finally presents the generalized equation that encompasses all of these scenarios.

If one scalar variable d is observed repeatedly, say n times, a suitable likelihood reads as

$$\mathcal{L}(d|\theta) = \frac{1}{\gamma\sqrt{2\pi}} \exp\left(-\frac{1}{2\gamma^2} \sum_{i=1}^n (d_i - v_i)^2\right). \quad (2.14)$$

This model for the measurement error is valid for multiple measurements of the system response with constant independent variables at the same location under identical environmental conditions. Note that γ is assumed to be stationary here.

Considering, say, m dependent variables is a common challenge. Some examples include the simultaneous measurement of several natural frequencies or observing a field quantity at a grid of locations. For scalar measurements of the specimen, the suitable likelihood [85, 116, 118]

$$\mathcal{L}(d|\theta) = \prod_{j=1}^m \frac{1}{\gamma_j\sqrt{2\pi}} \exp\left(-\frac{1}{2} \frac{(d_j - v_j)^2}{\gamma_j^2}\right) \quad (2.15)$$

is found by multiplying the individual marginal likelihoods. The characteristic here is that the noise standard deviation components γ_j corresponding to each of the set of observed variables are mutually independent. However, the noise components retain the flexibility of exhibiting different variances [85, 116]. As such, this represents a generalization of Eq. (2.14).

When the variable becomes vector-valued as d with dimension κ , the noise variability is now given by the noise covariance matrix

$$\Gamma_{ij} = C(\epsilon_i, \epsilon_j), \quad (2.16)$$

such that the now multi-dimensional measurement noise is distributed as $\epsilon \sim \mathcal{N}(\mathbf{0}, \mathbf{\Gamma})$ [146]. The likelihood becomes [146]

$$\mathcal{L}(\mathbf{d}|\boldsymbol{\theta}) = \frac{1}{\sqrt{(2\pi)^\kappa |\mathbf{\Gamma}|}} \exp\left(-\frac{1}{2}(\mathbf{d} - \mathbf{v})^\top \mathbf{\Gamma}^{-1}(\mathbf{d} - \mathbf{v})\right) \text{ with } \mathbf{d}, \mathbf{v} \in \mathbb{R}^\kappa. \quad (2.17)$$

One practical example is the measurement of the phase and amplitude of a quantity. For this case, $\kappa = 2$.

Generalized Case Finally, the superposition of the abovementioned cases yields a general likelihood. This general likelihood³

$$\mathcal{L}(\mathbf{d}|\boldsymbol{\theta}) = \prod_{j=1}^m (2\pi)^{-\frac{\kappa}{2}} (\det(\mathbf{\Gamma}_j))^{-\frac{1}{2}} \exp\left(-\frac{1}{2} \sum_{i=1}^n (\mathbf{d}_{ji} - \mathbf{v}_{ji})^\top \mathbf{\Gamma}_j^{-1}(\mathbf{d}_{ji} - \mathbf{v}_{ji})\right) \quad (2.18)$$

suits repeated measurements of several vector-valued quantities of interest whose noise components are mutually uncorrelated but individually described by a covariance matrix. Here, the i^{th} measurement of the j^{th} dependent vector-valued variable \mathbf{d} is denoted as \mathbf{d}_{ji} . The concept of composite likelihood functions is studied in the literature [139].

2.3 Random Vectors and Random Fields

When the uncertainty of the elastic material properties belonging to homogeneous materials are identified, these properties can be modeled as stochastic. The material properties can be modeled as random functions that live on the structure's geometry for heterogeneous materials. The corresponding discrete case is considered a random vector. The following elaborates on the theory of random vectors and fields, while Section 2.4 treats possible parameterizations, their identification, and representations. Note that these definitions of the statistical moments are agnostic to the probability density function, whose special cases are treated later in this thesis.

Random variables are commonly described by probability density functions, which are characterized by statistical moments [110]. The expected value μ of a random variable $M(\omega)$ reads as [20]

$$\mu = \mathbb{E}[M(\omega)]. \quad (2.19)$$

Here, ω corresponds to the random space, and a realization of ω leads to a realization of M [2]. The variance, the squared standard deviation σ , is denoted as

$$\sigma^2 = \mathbb{E}[(M(\omega) - \mu)^2]. \quad (2.20)$$

Some higher-order statistical central moments describe skewness and kurtosis [110]. Note that symmetrical distributions possess no skewness. Minimizing the deviation of the statistical moments of two distributions as a means of fitting one to the other is called the moments-matching approach [83]. Recently, minimizing the Kullback-Leibler divergence between two distributions, a generalization of the squared distance between the probability distributions [83] is being favored over the moments-matching approach.

A collection of random variables becomes a random vector of length n [106]

$$\mathbf{M}(\omega) = [M_1(\omega), M_2(\omega), \dots, M_n(\omega)]^\top. \quad (2.21)$$

³This composite likelihood formulation was developed together with Martin Eser.

The corresponding collection of mean values becomes a vector as well [20]

$$\boldsymbol{\mu} = [\mu_1, \mu_2, \dots, \mu_n]^T. \quad (2.22)$$

Several random variables are now considered jointly, and while their individual variance persists, their relationship can be described using a covariance matrix \mathbf{C} with the entries C_{ij} [106]

$$C_{ij} = \mathbb{E}[(M_i(\omega) - \mu_i)(M_j(\omega) - \mu_j)], \quad \text{with } i, j \in 1, 2, \dots, n. \quad (2.23)$$

The designation of the random vector changes based on the index set. If the indices refer to discrete locations in space, the generalized continuous function is called a random field, and one may write $M(x, \omega)$ [82]. For temporal dependence, the discrete random sequence [20] can be generalized to the concept of a random process $M(t, \omega)$ [106], and combined dependence results in the use of mixed nomenclature, see Carlton and Devore [20]. Alternative naming conventions exist [2, 82]. Random fields possess a mean function $\mu(x)$ and a covariance function $C(x, x')$ [20]. The expectation yields the average of a sample ensemble of realizations at x [20]. The remainder of this thesis will use the terminology related to random fields. However, all concepts apply equally to the random process case.

If the probability distribution of $M(x, \omega)$ does not change over the domain it is defined on, that is $M(x, \omega)$ and $M(x + \Delta x, \omega)$ share the identical distribution for any Δx [67], Marzouk and Najm [92] consider the random field as stationary. In greater detail, Carlton and Devore [20] term a random field strict-sense stationary if its statistical properties are invariant within the domain. Wide-sense stationarity is given for a constant mean function $\mu(x)$, finite variance σ^2 , and for a covariance $C(x, x')$ that is only a function of the distance between x and x' . Any wide-sense stationary random field is implicitly strict-sense stationary; see Hsu [67]. When the ensemble of realizations from a random field is the same as the sample average of one single sample, then this random field is called ergodic.

2.4 Random Field Description

Probability Distributions Consider the normal distribution over ζ of a random variable [20]

$$\mathcal{N}(\mu, \sigma^2) = \frac{1}{\sigma\sqrt{2\pi}} \exp\left(-\frac{1}{2} \frac{(\zeta - \mu)^2}{\sigma^2}\right). \quad (2.24)$$

The corresponding function for the n -dimensional multivariate case over ζ , implying a number of n random variables, reads as [106]

$$\mathcal{N}(\boldsymbol{\mu}, \mathbf{C}) = \frac{1}{(2\pi)^{n/2} |\mathbf{C}|^{1/2}} \exp\left(-\frac{1}{2} (\zeta - \boldsymbol{\mu})^T \mathbf{C}^{-1} (\zeta - \boldsymbol{\mu})\right), \quad (2.25)$$

where $|\boxtimes|$ denotes the determinant of any matrix that is symbolized using the placeholder \boxtimes here. If the probability density of all subsets of the underlying non-degenerate random field follows such a multivariate Gaussian distribution, it is called a Gaussian random field [2, 92]. A Gaussian random field is a second-order random field and is completely described by its mean and covariance [2].

If a non-Gaussian distribution is appropriate for any specific application, it can be convenient to begin with the Gaussian case and the desired correlation structure. This could be the

case if, say, non-negative material properties are modeled. It is then possible to obtain a random field exhibiting arbitrary marginal distributions while conserving the correlation structure through a transformation approach described by Vořechovský [148]. The remainder of this paragraph describes this procedure. Samples from $\mathbf{M}(\omega) \sim \mathcal{N}(\boldsymbol{\mu}, \mathbf{C})$ can be transformed to lie within the interval $[0, 1]$ using

$$\tilde{\mathbf{M}}(\omega) = \frac{1}{2} \left(1 - \operatorname{erf} \left(\frac{-\mathbf{M}(\omega)}{\sqrt{2}} \right) \right) \quad (2.26)$$

with the Gaussian error function erf . Having obtained cumulative distribution function percentiles, an inverse cumulative distribution function converts the former back to samples in the domain of the probability density function. Applying the Gaussian inverse cumulative distribution function yields the original samples of $\mathbf{M}(\omega)$. But applying, say the inverse cumulative distribution function of the two-parameter beta distribution equipped with the shape parameters $\boldsymbol{\alpha}$ and $\boldsymbol{\beta}$ yields

$$\hat{\mathbf{M}}(\omega) = I_M^{-1}(\boldsymbol{\alpha}, \boldsymbol{\beta}), \quad (2.27)$$

where I is the regularized incomplete beta function. Now, the marginals of $\hat{\mathbf{M}}$ are distributed according to the two-parameter beta distribution β , that is

$$\hat{M}_i(\omega) \sim \beta(\alpha_i, \beta_i) \quad \forall i \in 1, 2, \dots, n. \quad (2.28)$$

Covariance Kernels The following predominantly confines itself to second-order random fields, and adopting the corresponding notation $\mathcal{GP}(\boldsymbol{\mu}(x), C(x, x'))$ from Williams and Rasmussen [154] improves the readability here. This notation implies a Gaussian random field that exhibits mean $\boldsymbol{\mu}(x)$ and covariance $C(x, x')$. The covariance function $C(x, x') = \sigma^2 r(x, x')$ can be interpreted as the product of variance σ^2 and a correlation kernel $r(x, x')$. More precisely, the normalization of the covariance by the product of the variances at the respective coordinates $\sigma(x)$ and $\sigma(x')$ results in the correlation kernel [106]

$$r(x, x') = \frac{C(x, x')}{\sigma(x)\sigma(x')}. \quad (2.29)$$

By definition [2], the correlation at two identical coordinates $r(x, x)$ evaluates to 1, and it follows that $|r| \leq 1$, given that $\sigma(x) > 0 \forall x$ [2].

Correlation kernels are studied extensively in the literature [2, 31, 87]. All parameters of correlation functions apart from the points in the domain are termed hyper-parameters and gathered in \mathbf{q} such that $r(x, x', \mathbf{q})$. A specific \mathbf{q} results in choosing a correlation kernel from such a parameterized family of kernel functions. Many correlation kernels use a length scale parameter L on which the correlation at two locations is normalized. In this case, \mathbf{q} is simply $\mathbf{q} = \{L\}$. An example of this is the squared exponential kernel, which is widely used and describes the correlation based on the Euclidean distance $|x - x'|$ of the coordinates of two points. This stationary kernel reads as [154]

$$r(x, x', \mathbf{q} = \{L\}) = r(x, x') = \exp \left(-\frac{|x - x'|^2}{2L^2} \right) \quad \text{with } 0 < L. \quad (2.30)$$

This kernel is convenient for numerical implementations of series expansion methods that leverage eigenvalue decompositions of the covariance to sample from the random field. This is because analytical solutions to the eigenvalue problem of the corresponding covariance operator are available that serve as a reference for the quality of the numerical solution [74]. For the sake of simpler notation, the dependence on \mathbf{q} is not explicitly noted during

the remainder of the text. Refer to Figure 2.2 for a visualization of the effect of varying correlation lengths on the sample paths of a random field with otherwise identical covariance. Observe that a growing correlation length L increases the similarity between two points at a fixed distance. An infinite L would yield constant random field samples across all spatial points, while $L = 0$ would produce uncorrelated noise.

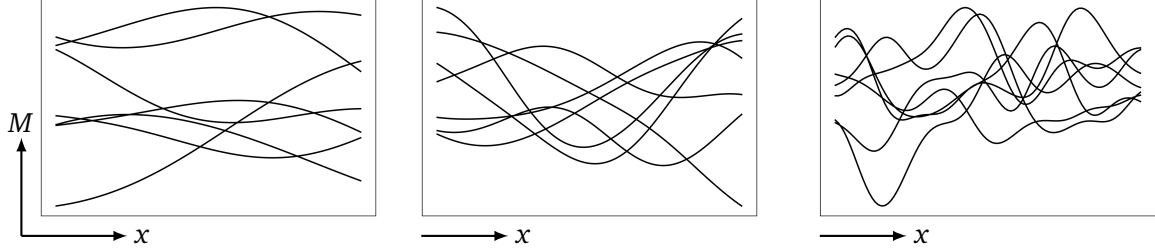


Figure 2.2: The effect of varying correlation length on the random field samples on the domain $[0, H]$. The left graph shows the case of $L = 0.6H$, the middle graph shows the $L = 0.3H$ case, and the plot on the right depicts the scenario $L = 0.1H$.

The Whittle-Matérn class of correlation kernels exhibits flexibility in terms of the roughness of the described random fields while maintaining differentiability for special cases. It incorporates a smoothing parameter ν , yielding $\mathbf{q} = \{L, \nu\}$. This kernel reads as [146]

$$r(x, x') = \frac{2^{1-\nu}}{\Gamma_G(\nu)} \left(\frac{\sqrt{2\nu}|x-x'|}{L} \right)^\nu K_\nu \left(\frac{\sqrt{2\nu}|x-x'|}{L} \right) \quad \text{with } \nu > 0. \quad (2.31)$$

Here, Γ_G is the gamma function, and K_ν is the modified Bessel function of the second kind. The expression simplifies when ν assumes half-integer values, and naturally, the resulting compact versions are most often used. This kernel models the material resulting from additive manufacturing in Paper C.

It turns out that combinations of correlation functions can again produce valid kernels; see Duvenaud et al. [31]. In fact, if r_1 and r_2 are positive-definite kernels, then

- $r_1 + r_2$
- and $r_1 \cdot r_2$

constitute positive-definite kernels as well, see Hofmann et al. [55]. One intuitive use of this property is the construction of multi-dimensional kernels that consist of the multiplication of basic kernels. This facilitates the synthesizing of random fields in several spatial dimensions. Consider a two-dimensional squared exponential kernel for two points with Cartesian coordinates (x, y) and (x', y') as [30]

$$r(x, y, x', y') = \exp \left(-\frac{(x-x')^2 + (y-y')^2}{2L^2} \right). \quad (2.32)$$

Anisotropic in this context implies that a distinct correlation function is applied for each Cartesian orientation. A two-dimensional an-isotropic squared exponential kernel with different correlation lengths L_x and L_y for the spatial dimensions x and y reads as [31]

$$r(x, x')r(y, y') = \exp \left(-\frac{(x-x')^2}{2L_x^2} \right) \exp \left(-\frac{(y-y')^2}{2L_y^2} \right). \quad (2.33)$$

Using multiplicative kernels for each spatial dimension as in Eq. (2.33) with $L_x = L_y = L$ is equivalent to the representation with a single isotropic kernel in Eq. (2.32). Figure 2.3

illustrates an exemplary realization of a zero-mean unit-variance Gaussian random field with isotropic covariance; see Eq. (2.32). In contrast, consider the visible difference given by the length scale directivity shown in Figure 2.4, which is related to the anisotropic case of the covariance in Eq. (2.33). The three-dimensional representation is analogous to the two-dimensional case, see Eq. (2.33), and reads as

$$r(x, x')r(y, y')r(z, z') = \exp\left(-\frac{(x-x')^2}{2L_x^2}\right)\exp\left(-\frac{(y-y')^2}{2L_y^2}\right)\exp\left(-\frac{(z-z')^2}{2L_z^2}\right). \quad (2.34)$$



Figure 2.3: The graph illustrates an exemplary realization of a two-dimensional zero-mean unit-variance Gaussian random field with isotropic covariance.



Figure 2.4: The graph shows a sample of a two-dimensional zero-mean unit-variance Gaussian random field for the case of $L_x > L_y$. As $L_x \neq L_y$, this represents an anisotropic covariance.

Preparing to generate samples from a random field with any certain covariance and noting the necessary properties of the used kernels invites the consideration of Mercer's theorem [159]. This theorem permits an eigendecomposition

$$C(x, x') = \sum_{i=1}^{\infty} \lambda_i \phi_i(x) \phi_i(x'), \quad (2.35)$$

with eigenvalues λ_i and normalized eigenfunctions ϕ_i , given that C is a Mercer kernel [49, 95], which then allows for the application of methods based on principal component analysis [55]. Any kernel that is continuous, symmetric, as in

$$C(x, x') = C(x', x) \quad \forall x, x', \quad (2.36)$$

and whose Gram matrix results in the covariance matrix

$$\mathbf{C} = \begin{bmatrix} C(x_1, x_1) & C(x_1, x_2) & \dots & C(x_1, x_n) \\ C(x_2, x_1) & C(x_2, x_2) & \dots & C(x_2, x_n) \\ \vdots & \vdots & \ddots & \vdots \\ C(x_n, x_1) & C(x_n, x_2) & \dots & C(x_n, x_n) \end{bmatrix} \quad (2.37)$$

is positive semi-definite, qualifies as a Mercer kernel [141].

Sampling Numerical methods for generating realizations of random fields are abundant. Several of these are listed in the literature (see [35]). The most popular of these consist of employing the Cholesky decomposition of the covariance or using the Karhunen-Loève expansion of the random field, while the moving average method, the circulant embedding

method [48], the local average subdivision method, and the turning bands method present alternatives [36]. The Cholesky decomposition of the covariance matrix is finding a lower diagonal matrix L such that

$$\mathbf{C} = \mathbf{L}\mathbf{L}^T. \quad (2.38)$$

holds for the symmetric positive semi-definite \mathbf{C} [152]. Now, a random vector \mathbf{z} with mean $\boldsymbol{\mu}$ that follows the covariance \mathbf{C} can be generated as

$$\mathbf{z} = \boldsymbol{\mu} + \mathbf{L}\boldsymbol{\zeta} \quad (2.39)$$

using a column vector $\boldsymbol{\zeta}$ of independent standard normal random numbers $\zeta_j \sim \mathcal{N}(0, 1)$ [106]. Note that this procedure using the Cholesky decomposition is the multi-dimensional equivalent to sampling from $z \sim \mathcal{N}(\mu, \sigma^2)$ by the linear transformation operation $z = \mu + \sigma\zeta$. Implementations of the numerical routine for any spatial dimension of the random field involve creating a list of discretization points, the construction of their distance matrix, the latter's evaluation to the covariance matrix, and finally, the remapping of the sample vector to the original sorting of the points.

2.4.1 Covariance Identification

This section covers the methods for identifying the underlying covariance of a random field whose realization is subject to Bayesian inference. Its relation to the other motifs explored in this thesis is expressed by Figure 2.5. Essentially, knowing the covariance of the latent random field is a prerequisite for the localization framework. These methods present a valuable resource in the context of Bayesian material discovery applications [5]. They are used to identify the variability of the material properties of wood due to natural growth in Paper D.

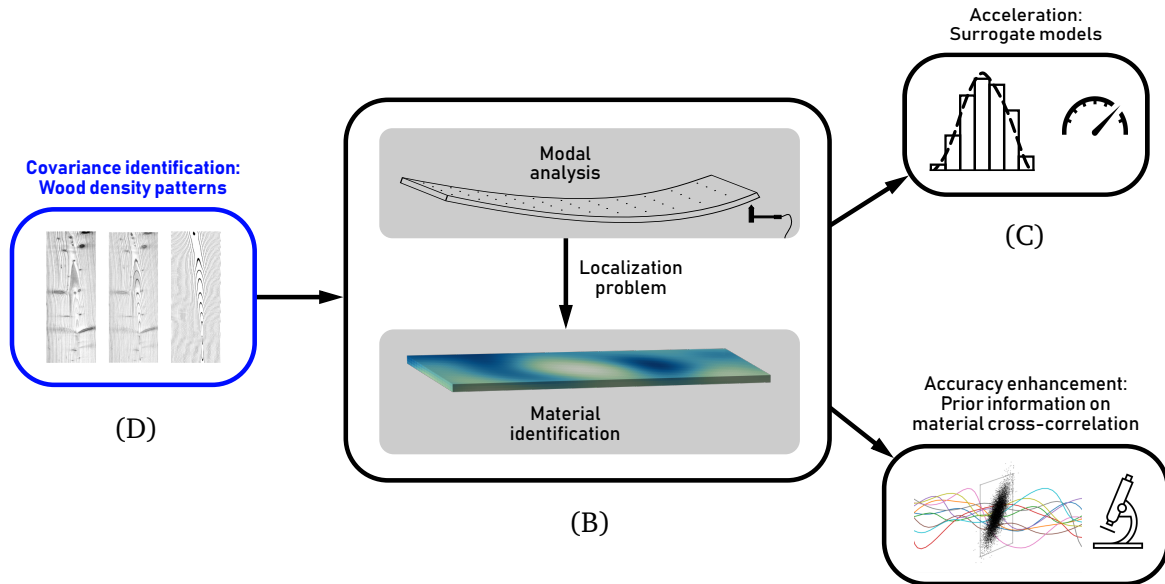


Figure 2.5: This section covers the methods related to pictogram (D) for identifying the underlying covariance of a random field whose realization is subject to Bayesian inference.

Bayesian Linear Regression Consider a data set \mathbf{d} consisting of n_d observations that shall be modeled using n_p predictor variables $\boldsymbol{\vartheta}$. The corresponding design matrix \mathbf{X} has the dimensions $n_p \times n_d$. Now consider the simple linear regression approach with input vector \mathbf{x} [154]

$$\mathbf{d} = \mathbf{x}^T \boldsymbol{\vartheta} + \epsilon. \quad (2.40)$$

Here, the independent Gaussian noise is assumed as $\epsilon \sim \mathcal{N}(0, \sigma_\epsilon^2)$. The prior $\boldsymbol{\vartheta} \sim \mathcal{N}(\mathbf{0}, \mathbf{B})$ with mean $\mathbf{0}$ and a standard deviation of σ_p employs a diagonal covariance matrix \mathbf{B} of [154]

$$\mathbf{B} = \sigma_p \mathbf{I}, \quad \text{where } \mathbf{I} \in \mathbb{R}^{n_p \times n_p}. \quad (2.41)$$

The covariance matrix of the posterior is derived as \mathbf{A}^{-1} , the inverse of [154]

$$\mathbf{A} = \frac{1}{\sigma_\epsilon^2} \mathbf{X}\mathbf{X}^T + \mathbf{B}^{-1}. \quad (2.42)$$

Finally, the mean of the posterior or maximum a posteriori estimate reads as [154]

$$\bar{\boldsymbol{\vartheta}} = \frac{1}{\sigma_\epsilon^2} \mathbf{A}^{-1} \mathbf{X}\mathbf{d}. \quad (2.43)$$

Gaussian Process Regression The above approach can readily be extended to the generalized polynomial regression. In this context, and assuming that the complete model exhibits a \mathcal{GP} component next to the polynomial global function or trend component, the expected value for the design parameters is obtained as [107]

$$\bar{\boldsymbol{\vartheta}} = (\mathbf{X}\mathbf{R}^{-1}\mathbf{X}^T)^{-1} (\mathbf{X}\mathbf{R}^{-1}\mathbf{d}), \quad (2.44)$$

with the correlation matrix \mathbf{R} and when using an uninformative prior on the parameters [107]

$$\mathbf{B}^{-1} = \mathbf{0}. \quad (2.45)$$

Gaussian process regression is synonymous with Kriging [90, 132], where the Gaussian random field model is employed to interpolate between data points and cover local changes. Consider a collection of $n + n_*$ points $\hat{\mathbf{x}} = [x_1, x_2, \dots, x_n, x_{*,1}, x_{*,2}, \dots, x_{*,n_*}]$, where x_1 denotes the first of n training points and $x_{*,1}$ represents the first of n_* test points. The Gram matrix corresponding to $C(\hat{x}, \hat{x}')$, see Eq. (2.37), is written as $\hat{\mathbf{C}}$. Rasmussen and Williams [154] employ a prior $(\hat{\mathbf{C}}_{ij})_{\substack{1 \leq i \leq n \\ 1 \leq j \leq n}} + \sigma_\epsilon^2 \mathbf{I}$ on noisy observations of a \mathcal{GP} to obtain the joint density of the data \mathbf{y} and function evaluations \mathbf{f}_* at the test points as

$$\begin{bmatrix} \mathbf{d} \\ \mathbf{f}_* \end{bmatrix} \sim \mathcal{N} \left(\mathbf{0}, \begin{bmatrix} (\hat{\mathbf{C}}_{ij})_{\substack{1 \leq i \leq n \\ 1 \leq j \leq n}} + \sigma_\epsilon^2 \mathbf{I} & (\hat{\mathbf{C}}_{ij})_{\substack{1 \leq i \leq n \\ n < j \leq n+n_*}} \\ (\hat{\mathbf{C}}_{ij})_{\substack{n < i \leq n+n_* \\ 1 \leq j \leq n}} & (\hat{\mathbf{C}}_{ij})_{\substack{n < i \leq n+n_* \\ n < j \leq n+n_*}} \end{bmatrix} \right). \quad (2.46)$$

In fact, the corresponding regression model evaluations are called predictions [132]. This usage as a surrogate⁴ is well-studied in the literature [78]. The expected predictive function values at the test points read as [154]

$$\bar{\mathbf{f}}_* = (\hat{\mathbf{C}}_{ij})_{\substack{n < i \leq n+n_* \\ 1 \leq j \leq n}} \left[(\hat{\mathbf{C}}_{ij})_{\substack{1 \leq i \leq n \\ 1 \leq j \leq n}} + \sigma_\epsilon^2 \mathbf{I} \right]^{-1} \mathbf{d}, \quad (2.47)$$

⁴One convenient application is the interpolation of acoustic absorption values between previously measured frequencies and thicknesses of the porous layer sample. This was studied by Kevin Josef Li within his student thesis *Gaussian Process Regression for Interpolation, Extrapolation and Noise Reduction in several Dimensions* that was handed in on November 5th of 2020 at the Chair of Vibroacoustics of Vehicles and Machines of TUM School of Engineering and Design.

while the predictive covariance is found as [154]

$$\mathbb{E}[(\mathbf{f}_{*,k} - \bar{\mathbf{f}}_{*,k})(\mathbf{f}_{*,l} - \bar{\mathbf{f}}_{*,l})] = \left(\hat{\mathbf{C}}_{ij} \right)_{\substack{n < i \leq n+n_* \\ n < j \leq n+n_*}} - \left(\hat{\mathbf{C}}_{ij} \right)_{\substack{n < i \leq n+n_* \\ 1 \leq j \leq n}} \left[\left(\hat{\mathbf{C}}_{ij} \right)_{\substack{1 \leq i \leq n \\ 1 \leq j \leq n}} + \sigma_\epsilon^2 \mathbf{I} \right] \left(\hat{\mathbf{C}}_{ij} \right)_{\substack{1 \leq i \leq n \\ n < j \leq n+n_*}} \quad (2.48)$$

with $k, l \in 1, \dots, n_*$. Evaluating the prediction error to identify regions where this error is disproportionately large should be followed by a local increase in the number of samples to reduce the uncertainty [37].

Maximum Likelihood Estimation of the Covariance The estimation quality of spatially varying material properties modeled as random field samples is dictated by the chosen covariance kernel. If there is a mismatch between the true kernel and the assumed kernel, the accuracy suffers. An easily visualized example is an ill-chosen length scale, where an underestimation thereof results in an over-fit and an overestimation yields a sluggish match. Hence, the covariance model needs to be fitted. Choosing one kernel or a combination of several kernels as described in Section 2.3 is a task that receives significant attention in the literature [87]. Once the covariance structure is fixed, its hyper-parameters \mathbf{q} need to be identified by the maximum likelihood estimation of the likelihood (Eq. (2.49)) of the data [132]. Here, the case of $\mathbf{q} = L$ is considered as

$$\mathcal{L}(\mathbf{d}|L, \sigma, \bar{\boldsymbol{\theta}}) = \frac{1}{(2\pi)^{n_d/2} (\sigma^2)^{n_d/2} (|\mathbf{R}(L)|)^{1/2}} \exp\left(-\frac{(\mathbf{d} - \mathbf{X}^T \bar{\boldsymbol{\theta}})^T \mathbf{R}(L)^{-1} (\mathbf{d} - \mathbf{X}^T \bar{\boldsymbol{\theta}})}{2\sigma^2}\right), \quad (2.49)$$

where the correlation matrix \mathbf{R} is the Gram matrix corresponding to Eq. (2.30) and where the absence of a trend component can be reflected by setting $\mathbf{X}^T \bar{\boldsymbol{\theta}} = \mathbf{0}$. [107]

2.4.2 Karhunen-Loève Expansion: Definitions and Numerical Treatment

Describing the quantity of interest with a large random vector complicates the inference, as the exploration algorithm now must travel through a high-dimensional posterior. Compressing this random space facilitates the solution of the inverse problem. This can be achieved by representing the material property random fields with the Karhunen-Loève expansion.

The Karhunen-Loève expansion utilizes the mean function and decomposition of the covariance to find a representation of the random field as

$$M(x, \omega) = \mu(x) + \sum_{i=1}^{\infty} \sqrt{\lambda_i} \phi_i(x) \eta_i(\omega) \approx \mu(x) + \sum_{i=1}^K \sqrt{\lambda_i} \phi_i(x) \eta_i(\omega), \quad (2.50)$$

where η_i are the Karhunen-Loève coefficients and where $(\lambda_i, \phi_i)_{i=1}^{\infty}$ are the eigenpairs associated with the covariance operator that comply with the Fredholm equation of the second kind [14]

$$\int_{\Omega} C(x, x') \phi_i(x') dx' = \lambda_i \phi_i(x) \quad \text{with } x \in \Omega, \quad (2.51)$$

see Marzouk and Najm [92]. Notably, the full series from Eq. (2.50) may be limited to K terms, which decouples the random dimensionality of the random field representation from its spatial discretization [14]. This allows for a more random dimension compared to the

spatial discretization [14]. The mode strengths $\eta_i(\omega)$ corresponding to a specific realization of the random field are found as [138]

$$\eta_i(\omega) = \frac{1}{\sqrt{\lambda_i}} \int_{\Omega} (M(x, \omega) - \mu(x)) \phi_i(x) dx. \quad (2.52)$$

The Karhunen-Loève expansion delivers the best random field representation with respect to the mean square error [14, 44]. If the underlying random field is Gaussian, the Karhunen-Loève coefficients $\eta_i(\omega)$ are uncorrelated standard normal random variables.

Numerical Treatment Betz et al. [14] review several numerical solution approaches to the integral eigenvalue problem in Eq. (2.51). One feasible approach they present is the Nyström method that approximates Eq. (2.51) by

$$\sum_{j=1}^s w_j C(x_n, x_j) \hat{\phi}_i(x_j) = \hat{\lambda}_i \hat{\phi}_i(x_n), \quad n \in 1, \dots, s, \quad (2.53)$$

where w_j represents the integration weights to the integration positions x_j . Here, $\hat{\lambda}_i$ is an approximation of the eigenvalue λ_i and $\hat{\phi}_i$ is the discrete eigenvector corresponding to ϕ_i . Eq. (2.53) can be expressed as a matrix eigenvalue problem with

$$\mathbf{C} \mathbf{W} \mathbf{v}_i = \hat{\lambda}_i \mathbf{v}_i, \quad (2.54)$$

where \mathbf{v}_i is a vector with length s whose n^{th} entry $v_{i,n}$ is $\hat{\phi}_i(x_n)$, \mathbf{W} is the diagonal weight matrix with the diagonal entries $W_{jj} = w_j$ [14]. Within this thesis, the integration weights are set to the volume enclosed by grid points adjacent to the integration point, thus yielding a piece-wise constant integration scheme. This satisfies the requirement of scaling the eigenvalues of the covariance matrix to reflect the true variance. An appropriately scaled identity matrix can approximate the matrix of integration weights when equidistant grid points are used. However, this introduces an error at the boundary, as the correct weight for a one-dimensional domain equals half of the weight corresponding to an interior grid point. Adjusting the weights at the boundaries is recommended.

The eigenvalue problem in Eq. (2.54) is readily solved with an eigensolver. Some minor steps are necessary after the solution to ensure a consistent treatment. Firstly, the eigenvalues and eigenvectors shall be ordered descendingly in compliance with $\lambda_1 \geq \lambda_2 \geq \lambda_3 \cdots \geq \lambda_K$. Secondly, the orientation of the eigenvectors must be consistent to create a unique description of any random field sample. This is necessary for the well-posedness of any inverse problem involving characterizing a random field sample represented by the Karhunen-Loève expansion. One strategy is to require the first entry of all eigenvectors to be positive

$$v_{i,1} \stackrel{!}{>} 0 \quad \forall i. \quad (2.55)$$

Finally, the length of the eigenvectors needs to be normalized to once again accurately account for the variance of the underlying random field, as Mercer's theorem requires [88]

$$\int_{\Omega} (\hat{\phi}_i(x))^2 dx = 1 \quad \forall i. \quad (2.56)$$

One way of obtaining normalized eigenvectors $\tilde{\mathbf{v}}$ is to compute [14]

$$\tilde{\mathbf{v}}_i = \mathbf{v}_i \sqrt{\sum_{j=1}^s w_j (v_{j,i})^2}. \quad (2.57)$$

Errors Truncating the series in Eq. (2.50) results, among other effects, in an approximation error of the random field variability. This truncation error depends on the expansion order K . In general, shorter correlation lengths and lower smoothness coefficients necessitate retaining more terms in the series. One way of choosing an appropriate expansion order is by evaluating how much of the variability the Karhunen-Loève expansion accounts for [70]. To this aim, the expectation for the field's energy can be compared to that of the truncated counterpart [70]. After evaluating

$$\int_{\Omega} C(x, x') dx = \sum_{i=1}^{\infty} \lambda_i \approx \sum_{i=1}^K \lambda_i, \quad (2.58)$$

the measure for the variance approximation error e by truncation reads as [70]

$$e = 1 - \frac{\sum_{i=1}^K \lambda_i}{\sum_{i=1}^{\infty} \lambda_i}. \quad (2.59)$$

Non-Gaussian Case If the random field is non-Gaussian, the generalization of the Karhunen-Loève expansion induces correlations between the coefficients $\eta_i(\omega)$. The extension to these cases is not straightforward [14]. An alternative is to perform an operation on the resulting Gaussian variates. While the normal distribution is retained for linear transformations, albeit with changed mean and standard deviation, other distribution types can be achieved using simple operations. If the desired random field shall possess a log-normal distribution, the exponential of the results from the standard Karhunen-Loève expansion may be utilized. Examples of plain operations that yield valid probability distributions include using the absolute value or square of the Gaussian random numbers. For more complex target marginal distributions and in the absence of closed-form transformations, the conversion by Eqs. (2.26) and (2.27) offers a solution. It consists of transforming the Gaussian random variables to a cumulative distribution function and then applying the desired inverse cumulative distribution function to maintain smooth sample paths that follow the original covariance [148].

Sampling To synthesize the random field using the Karhunen-Loève expansion, realizations of its stochastic coefficients $\eta_i(\omega)$ need to be generated. The coefficients $\eta_i(\omega)$ are uncorrelated standard normal variates for a Gaussian random field $M(x, \omega)$ [146]. Thus, drawing a sample $\eta_i \sim \mathcal{N}(0, 1) \forall i$ creates a sample of the field [92].

2.4.3 Generalized Karhunen-Loève Expansion: Cross-Correlated Random Fields

Several descriptions for cross-correlated random fields exist in the literature, where Vořechovský [148] demonstrates sampling from simply cross-correlated random fields. Papaioannou and Der Kiureghian [108] show how to generate realizations from such generalized Karhunen-Loève expansions and investigate their numerical treatment. Cho et al. [22] propose two methods of extending the classical Karhunen-Loève expansion to several correlated random fields. One of their methods minimizes the size of the assembled covariance matrices, while the other optimizes the dimension of the random space. The latter property represents a synergy with the generalized polynomial chaos expansion by mitigating the curse of dimensionality. In this context,

$$C_{ij}(x, x') \stackrel{\text{def}}{=} \mathbb{E}[M_i(x', \omega)M_j(x, \omega)], \quad 1 \leq i \leq j \leq m. \quad (2.60)$$

represents $m(m+1)/2$ covariance functions describing the correlation structure of m random fields that are each defined on $[0, H]$, where H is the length of the domain. One of the methods proposed by Cho et al. [22] correlates the random fields by imposing a correlation structure on the traditionally uncorrelated Karhunen-Loève coefficients. The second method employs uncorrelated Karhunen-Loève coefficients, while the cross-correlation is induced by the structure of a dedicated joint covariance. The following relates to the latter. Here, an assembled random field $\tilde{M}(x, \omega)$ is considered as

$$\tilde{M}(x, \omega) \stackrel{\text{def}}{=} M_i(x - H_{i-1}, \omega), \quad x \in \mathcal{I}_i, \quad (2.61)$$

a sub-field $M_i(x, \omega)$ of the assembled field is mapped to the interval \mathcal{I}_i of the total domain. Here, $H_i = iH$. The corresponding assembled covariance function reads as

$$\tilde{C}(x, x') \stackrel{\text{def}}{=} C_{ij}(x - H_{i-1}, x' - H_{j-1}), \quad x \in \mathcal{I}_i, \quad x' \in \mathcal{I}_j. \quad (2.62)$$

For n unique points in space within $[0, H]$, the discretized assembly of the covariance $\tilde{C}(x_i, x_j)$ becomes an $n \times n$ matrix. Now, the assembled field can be expanded into the series

$$\tilde{M}(x, \omega) = \sum_{k=1}^{\infty} \sqrt{\lambda_k} \tilde{M}_k(x) \eta_k(\omega), \quad (2.63)$$

where the Karhunen-Loève coefficients $\eta_k(\omega)$ are uncorrelated, and λ_k and $\tilde{M}_k(x)$ are the eigenvalues and eigenfunctions corresponding to the assembled covariance function. Note that $\tilde{M}_k(x)$ can be split into m parts that are associated with sub-fields $\phi_k^{(i)}(x)$ ($i = 1, \dots, m$). The latter can be extracted using [22]

$$\phi_k^{(i)}(x) \stackrel{\text{def}}{=} \tilde{M}_k(x + H_{i-1}) \mathcal{I}_{[0, H]}(x). \quad (2.64)$$

Finally,

$$M_i(x, \omega) = \sum_{k=1}^{\infty} \sqrt{\lambda_k} \phi_k^{(i)}(x) \eta_k(\omega) \quad (2.65)$$

represents the Karhunen-Loève expansion for the sub-field $M_i(x, \omega)$. [22]

To generate realizations of a sub-field within the method by Cho et al. [22], the uncorrelated coefficients η_k need to be sampled as standard Gaussian variables after the corresponding Karhunen-Loève expansion is truncated and discretized. Figure 2.6 depicts 10 realizations for the case of two one-dimensional sub-fields, whose cross-correlation kernel results in a Pearson coefficient of linear correlation [111] of 0.7. Here, the y direction corresponds to the first random field, and the z direction corresponds to the second random field. The three-dimensional plot is chosen to visualize the effect of the cross-correlation. Some 10 000 samples from a distribution marginalized at $x = H/2$ are shown with a scatter plot in the center. This joint density clearly shows the cross-correlation of the fields.

Special Case of Two Correlated Random Fields The signal processing community treats complex-valued signals in the time domain [127]. The term complex random field refers to a signal on such a domain within this thesis. A classification of such complex fields can be accomplished depending on the correlation of the real and the imaginary parts [101]. If the correlation between the components is zero, the intersection graph shows a symmetric circular joint distribution. For a non-zero correlation, an ellipse-shaped pattern can be observed [128]. Further narrowing of the classification depending on the degree of correlation

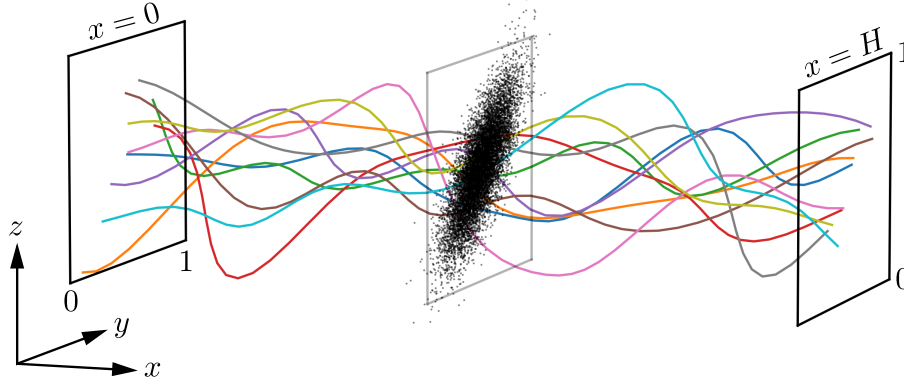


Figure 2.6: The figure shows 10 random samples of two one-dimensional squared exponential random fields that are correlated with a Pearson coefficient of linear correlation of 0.7. Evaluating the graph in the y direction yields the samples of the first random field while doing so for z yields those of the second. The y and z dimensions of the intersection planes are normalized on the 10 exemplary samples. The cutting plane in the center presents 10 000 samples and approximates the joint density of the fields there.

is not common. Note that the sample cross-correlation matrix is generally not equal to zero but tends to the latter for large sample sizes. Refer to the literature for more detailed information on complex random fields [16]. The insight gained from studying complex random fields can readily be applied to considering two one-dimensional real-valued random fields without losing generality. The following paragraphs formulate the complex-valued case. To treat the case of two real-valued fields, use the real and imaginary parts separately.

Special covariance kernels for complex fields are treated in the literature [17]. However, a block covariance matrix $\mathbf{C} \in \mathbb{R}^{2n \times 2n}$

$$\mathbf{C} = \begin{bmatrix} \mathbf{C}_{11} & \mathbf{C}_{12} \\ \mathbf{C}_{12}^T & \mathbf{C}_{22} \end{bmatrix} \quad (2.66)$$

can readily be constructed with the same effect. It consists of the auto-covariance matrices \mathbf{C}_{11} and \mathbf{C}_{22} that stem from conventional covariance kernels. The cross-covariance matrix \mathbf{C}_{12} may be found by applying the operation [127]

$$C_{12,ij} = \rho_{12} \sqrt{C_{11,ij}} \sqrt{C_{22,ij}} \quad \forall i, j = 1, \dots, n \quad (2.67)$$

on the auto-covariances utilizing a linear cross-correlation coefficient ρ_{12} . Naturally, \mathbf{C}_{11} and \mathbf{C}_{22} are symmetric and it follows that $\mathbf{C}_{12} = \mathbf{C}_{21}^T$ [18]. Schreier and Scharf [126, 128] develop special adaptations of the Karhunen-Loève expansion for such covariance structures [51, 127]. Full-dimensional approaches for representing two correlated random fields are available, such as the convolutional approach by Boloix-Tortosa et al. [16], which compares to the moving average method [35]. This thesis presents an alternative employing the complete random space by building on results obtained by Schreier and Scharf [127]. They find the eigendecomposition of the block covariance as

$$\mathbf{C} = \mathbf{U} \mathbf{\Lambda} \mathbf{U}^T. \quad (2.68)$$

Here, \mathbf{U} contains eigenvectors and

$$\mathbf{\Lambda} = \begin{bmatrix} \mathbf{\Lambda}^{(1)} & \mathbf{0} \\ \mathbf{0} & \mathbf{\Lambda}^{(2)} \end{bmatrix}, \quad (2.69)$$

where the diagonal matrices $\mathbf{\Lambda}^{(1)}$ and $\mathbf{\Lambda}^{(2)}$ contain the odd and even eigenvalues in decreasing order, respectively. Denoting the imaginary unit as j and the Hermitian transpose with \boxtimes^H ,

Schreier and Scharf [128] define the unitary transformation

$$T = \frac{1}{\sqrt{2}} \begin{bmatrix} I & jI \\ I & -jI \end{bmatrix}, \quad TT^H = T^HT = I. \quad (2.70)$$

Using this yields⁵

$$\underline{\mathbf{L}} = \underline{\mathbf{U}}T\Lambda^{\frac{1}{2}}T^H\underline{\mathbf{U}}^H, \quad (2.71)$$

where $\underline{\mathbf{x}}$ denotes the augmentation by the complex conjugate of a quantity. This leads to a representation of complex random fields

$$\mathbf{z} = \boldsymbol{\mu} + \left(\underline{\mathbf{L}}_{ij} \right)_{\substack{1 \leq i \leq n \\ 1 \leq j \leq n}} \boldsymbol{\zeta} + \left(\underline{\mathbf{L}}_{ij} \right)_{\substack{1 \leq i \leq n \\ n < j \leq 2n}} \boldsymbol{\zeta}^H \quad (2.72)$$

that resembles a generalization of Eq. (2.38). Corresponding realizations of two cross-correlated one-dimensional random fields are obtained by sampling

$$\boldsymbol{\zeta} \sim \mathcal{N}(0, \mathbf{I} \in \mathbb{R}^n) + j\mathcal{N}(0, \mathbf{I} \in \mathbb{R}^n). \quad (2.73)$$

2.5 Acceleration

Employing the Karhunen-Loève expansion has a second benefit next to the simplification of the posterior space that the Bayesian inference exploration algorithm traverses. Surrogate models represent a popular way of accelerating the solution time and are especially beneficial when a computationally expensive forward model needs to be repeatedly evaluated. Notably, surrogate modeling techniques such as the generalized polynomial chaos expansion suffer from the curse of dimensionality. Employing generalized polynomial chaos to connect material properties described by a random vector to the stochastic system outputs offers diminishing time savings when the spatial discretization of the material properties is increasingly refined. The Karhunen-Loève expansion preserves the advantages of surrogate models such as generalized polynomial chaos by decoupling the spatial discretization from the random space.

2.5.1 Generalized Karhunen-Loève Expansion: Acceleration by Transformation

One drawback when using the standard Karhunen-Loève expansion and generalized polynomial chaos expansion in conjunction is that the generalized polynomial chaos surrogate needs to be updated every time the covariance of the latent field is modified. This is because the eigenvectors and eigenvalues of the covariance simultaneously change. Consequently, the Karhunen-Loève coefficients need to be updated. Finally, this calls for adapting the generalized polynomial chaos surrogate that expands these coefficients.

Sraj et al. [138] formulate a parameterized generalization of the Karhunen-Loève expansion. Motivated by the elusiveness of hyper-parameters of random fields in many engineering applications, they alter the Karhunen-Loève expansion to accommodate for changes in covariance hyper-parameters \mathbf{q} . Any covariance kernel such as Eq. (2.30) is subject to such hyper-parameters, whose notation is introduced in Section 2.3. The following reproduces the

⁵Simon Mannhardt developed this decomposition and the connected sampling procedure while he was a student research assistant at the Chair of Vibroacoustics of Vehicles and Machines of TUM School of Engineering and Design.

equations related to the core of their method that is provided in [138], as it is not well-known within the community. Instead of the usual implicit dependence of the Karhunen-Loève expansion on \mathbf{q} in Eq. (2.50), they introduce such a dependence explicitly as

$$M_K(x, \omega, \mathbf{q}) = \mu(x) + \sum_{i=1}^K \sqrt{\lambda_i(\mathbf{q})} \phi_i(x, \mathbf{q}) \eta_i(\omega). \quad (2.74)$$

The remaining text passages covering this generalized version of the Karhunen-Loève expansion refrain from explicitly mentioning the spatial dependence on x for brevity. [133, 138]

A Karhunen-Loève expansion with covariance reference $C(\mathbf{q}^r)$ endowed with reference hyper-parameters \mathbf{q}^r marks the start of their procedure. This basis is morphed into a Karhunen-Loève expansion characterized by target hyper-parameters \mathbf{q} . To achieve this, Sraj et al. [138] leverage the similarity of the connected eigenvectors. The product of the square root of the eigenvalues and the eigenfunctions of the target covariance yields the scaled eigenfunctions

$$\Phi_i(\mathbf{q}) = \sqrt{\lambda_i(\mathbf{q})} \phi_i(\mathbf{q}). \quad (2.75)$$

They express these scaled eigenfunctions $\Phi_i(\mathbf{q})$ in terms of the reference eigenfunctions $\phi_i^r(\mathbf{q})$ by means of projection coefficients $b_{ii'}$ as obtained by the inner product $(\boxtimes, \boxtimes)_X$ of any function symbolized by \boxtimes as

$$\Phi_i(\mathbf{q}) = \sum_{i'=1}^K b_{ii'}(\mathbf{q}) \phi_{i'}^r \quad \text{with} \quad b_{ii'} = (\phi_i^r, \Phi_{i'}(\mathbf{q}))_X. \quad (2.76)$$

Using these projection coefficients $b_{ii'}$, transformed Karhunen-Loève coefficients may be found as

$$\hat{\eta}_i(\omega, \mathbf{q}) = \sum_{i'=1}^K b_{ii'}(\mathbf{q}) \eta_{i'}(\omega), \quad (2.77)$$

or using matrix notation as

$$\hat{\boldsymbol{\eta}}(\omega, \mathbf{q}) = \mathcal{B}(\mathbf{q}) \boldsymbol{\eta}(\omega). \quad (2.78)$$

With this transformation, the dependence on \mathbf{q} may be moved to the Karhunen-Loève coordinates $\hat{\eta}_i(\omega, \mathbf{q})$ from the scaled eigenfunctions Φ_i . Finally, the Karhunen-Loève expansion of a centered random field with the target covariance is formulated using the reference eigenfunctions as

$$M_K(\omega, \mathbf{q}) = \sum_{i=1}^K \Phi_i(\mathbf{q}) \eta_i(\omega) \approx \hat{M}_K(\omega, \mathbf{q}) = \sum_{i=1}^K \left(\sum_{i'=1}^K b_{ii'}(\mathbf{q}) \phi_{i'}^r \right) \eta_i(\omega) = \sum_{i=1}^K \phi_i^r \hat{\eta}_i(\omega, \mathbf{q}). \quad (2.79)$$

The minimally possible transformation error is achieved when choosing \mathbf{q}^r as equal to the true target hyper-parameters. For an extensive investigation of the approximation error between the transformed and non-truncated field, refer to the work by Sraj et al. [138].

2.5.2 Generalized Polynomial Chaos Expansion Surrogate Model

Methods like the finite element method for solving partial differential equations represent the overwhelmingly dominant choice of engineers. In its traditional form, the finite element method is a deterministic method reporting a deterministic system response to an equally deterministic excitation and boundary conditions. Evaluating involved finite element method

models is computationally expensive. Monte Carlo sampling of the inputs of such a model presents a popular method within uncertainty quantification. This assesses how input uncertainties propagate to the outputs by repeatedly drawing samples from the input distributions and subsequently evaluating the forward model. Naturally, a computationally expensive forward model does not bode well for Monte Carlo sampling. Hence, constructing a computationally cheap surrogate model is desirable. Indeed, a compromise between accuracy and efficiency exists. Koziel and Pietrenko-Dabrowska [80] state that surrogate models, or meta-models, present such a trade-off. Physics-based surrogates rely on simplifications, while data-driven ones are purely mathematical. The generalized polynomial chaos expansion falls within the latter while approximating the outputs of the high-fidelity model G as random variables. The notion of polynomial chaos is coined by Wiener [153], where chaos refers to randomness or uncertainty. Ghanem and Spanos [44] apply the original idea of projecting a deterministic quantity onto a stochastic space spanned by polynomials Ψ to solid mechanics. Xiu and Karnidakis [160] generalize this concept beyond the Gaussian case to polynomials belonging to the Askey scheme [6]. The result is called the generalized polynomial chaos expansion [157].

The polynomials used in this context are functions of the random vector $\xi = [\xi_1, \xi_2, \dots, \xi_n]$ [160]. Sepahvand et al. [130] provide detailed explanations concerning generalized polynomial chaos. Consider the expansion of an uncertain parameter v as [130]

$$v = a_0 \Psi_0 + \sum_{i_1=1}^{\infty} a_{i_1} \Psi_1(\xi_{i_1}) + \sum_{i_1=1}^{\infty} \sum_{i_2=1}^{i_1} a_{i_1 i_2} \Psi_2(\xi_{i_1}, \xi_{i_2}) + \sum_{i_1=1}^{\infty} \sum_{i_2=1}^{i_1} \sum_{i_3=1}^{i_2} a_{i_1 i_2 i_3} \Psi_3(\xi_{i_1}, \xi_{i_2}, \xi_{i_3}) + \dots \quad (2.80)$$

which reads as [130]

$$v = \sum_{i=0}^{\infty} a_i \Psi_i(\xi) \quad (2.81)$$

in compact notation, where a_i are initially unknown deterministic coefficients. The truncation of the series to $N + 1$ terms yields

$$v \approx \sum_{i=0}^N a_i \Psi_i(\xi) \quad \text{with} \quad N + 1 = \frac{(n+p)!}{n!p!}, \quad (2.82)$$

where p is the expansion order and n represents the dimensionality of the random input vector ξ [130]. The base functions Ψ_i possess a mutual orthogonality property [160]. The distribution type of ξ dictates the optimal choice for Ψ_i , which consists of Hermite polynomials for Gaussian ξ [160].

Computation of Coefficients If the system equations are accessible, the coefficients a_i can be obtained by a Galerkin projection [137]. This approach results in the optimal error and is termed an intrusive method [92]. If the model G is a black box, stochastic collocation offers an alternative [72]. The coefficients may be estimated by minimizing the error between v and its representation by the truncated expansion representation using least square minimization [91]. For the special case of one input random variable ξ , consider n realizations of it as $\{\xi^{(1)}, \xi^{(2)}, \dots, \xi^{(n)}\}$ and the corresponding observed data points as $\{v^{(1)}, v^{(2)}, \dots, v^{(n)}\}$ [130].

Then, solving the linear equation system

$$\begin{bmatrix} \sum_{j=0}^N \Psi_0(\xi^{(1)})\Psi_0(\xi^{(1)}) & \cdots & \sum_{j=0}^N \Psi_0(\xi^{(n)})\Psi_n(\xi^{(n)}) \\ \vdots & \ddots & \vdots \\ \sum_{j=0}^N \Psi_n(\xi^{(1)})\Psi_0(\xi^{(1)}) & \cdots & \sum_{j=0}^N \Psi_n(\xi^{(n)})\Psi_n(\xi^{(n)}) \end{bmatrix} \begin{bmatrix} a_0 \\ \vdots \\ a_n \end{bmatrix} = \begin{bmatrix} \sum_{j=0}^N v^{(0)}\Psi_0(\xi^{(0)}) \\ \vdots \\ \sum_{j=0}^N v^{(n)}\Psi_n(\xi^{(n)}) \end{bmatrix} \quad (2.83)$$

yields the coefficients a_i [130]. Instead of random samples, the collocation points can be strategically chosen. One strategy is to utilize the roots of basis polynomials of the degree $p+1$ [130]. The next step is to sort the resulting collocation points based on their L^2 norm and to arrange the equation system in Eq. (2.83) such that each entry within the model response $v^{(i)}$ is correctly assigned to the corresponding collocation point $\xi^{(i)}$. Sparse collocation point grids reduce computational effort here [124]. However, it is generally advisable to employ an over-determined system of equations. For a higher dimensionality, all possible combinations of terms must be expanded using the tensor product on the polynomial bases [158].

Non-optimal Expansions If the distribution type of the random variable ξ does not align with the polynomial, the above procedure turns into a non-optimal generalized polynomial chaos expansion. Now, the series expansion does not necessarily converge. This challenge can be overcome by transforming the respective probability spaces associated with ξ and v to common ground [29, 130].

Sampling To sample from the generalized polynomial chaos surrogate, one may generate realizations of ξ and evaluate Eq. (2.82) to obtain the approximated system response. Statistical moments of v follow directly from its generalized polynomial chaos coefficients a_i with no dependence on preceding sampling. The first coefficient is synonymous with the expected value [73]

$$\mu \approx a_0, \quad (2.84)$$

and a compact expression for the variance reads as [73]

$$\sigma^2 \approx \sum_{i=0}^N h_i^2 a_i^2, \quad (2.85)$$

where h_i is the norm of the basis polynomials [130]. These and higher order normalized central moments can be computed by additionally using the basis polynomials and the probability density of ξ ; however, this also necessitates higher expansion orders, where the convergence of the approximation is not guaranteed [130].

Coefficient Transformation Traditionally, the covariance of the quantity of interest must be known for the prior within the Bayesian inference to provide accurate results. The corresponding hyper-parameters can be identified using Gaussian process regression if sufficient data is available. If this is not possible, a flexible description that does not require new forward model evaluations is valuable. Such a description is available in the literature [138]. Note that this method is valid when the hyper-parameters connected to the chosen kernel change but does not account for a change of kernel or of the kernel structure in the case of composite kernels.

The generalization of the Karhunen-Loève expansion by Sraj et al. [138] (see Section 2.5.1) is conceptualized with a link to the generalized polynomial chaos expansion in mind. They free the generalized polynomial chaos coefficients a_i from the dependence on the hyper-parameters \mathbf{q} and cast it on ξ instead. In fact, a_i must only be computed once with the

input of the model G being described by the reference covariance $C(\mathbf{q}^r)$. Now, the surrogate for a model G whose inputs are connected to the Karhunen-Loève expansion of a different covariance reads as [138]

$$v(\boldsymbol{\eta}, \mathbf{q}) \approx \tilde{v}(\boldsymbol{\xi}(\boldsymbol{\eta}, \mathbf{q})) = \sum_{i=0}^N a_i \Psi_i(\boldsymbol{\xi}(\boldsymbol{\eta}, \mathbf{q})) \quad \text{with} \quad \boldsymbol{\xi}(\boldsymbol{\eta}, \mathbf{q}) = \hat{\mathcal{B}}(\mathbf{q})\boldsymbol{\eta}, \quad (2.86)$$

where $\hat{\mathcal{B}}$ is defined as

$$\hat{\mathcal{B}}_{kl}(\mathbf{q}) = \begin{cases} \frac{\mathcal{B}_{kl}(\mathbf{q})}{\sqrt{\lambda_k^r}} & \text{if } \frac{\lambda_k^r}{\lambda_1^r} > 1 \times 10^{-12}, \\ 0 & \text{otherwise.} \end{cases} \quad (2.87)$$

Here, the eigenvalues of the reference covariance operator λ_k^r shall be arranged to steadily shrink. The threshold enforces a good condition number of $\hat{\mathcal{B}}$ [138].

Chapter 3

Summary of Publications

This chapter summarizes the publications [Paper A \[62\]](#), [Paper B \[57\]](#), [Paper C \[58\]](#), and [Paper D \[56\]](#). It covers the key aspects of each paper, including novelty and results, the authors' contributions, and the citation reference. Full-text reprints are provided in Appendix [II](#), [III](#), [IV](#), and [V](#).

3.1 Paper A

Evaluation of inversion approaches for plates based on guided waves and modal analysis

Karl-Alexander Hoppe, Simon Schmid, Jochen Kollofrath, Steffen Marburg, and Christian U. Grosse

Summary Recent developments in regression pave the way for the simultaneous employment of two simulation models to characterize a quantity of interest [109]. Within the so-called multi-fidelity Gaussian process regression, the designated low-fidelity model is comparatively cheap in a computational sense. Its results are comparatively less accurate than those stemming from the so-called high-fidelity model. Evaluations of this model are costly but yield superior results. On the one hand, such a setup can be achieved using a fine-grained and a coarse discretization of the identical model. On the other hand, this could be set up at two different scales, which offers some new perspectives for computational multi-scale approaches [24, 39, 42, 161]. Finally, the multi-fidelity regression could also be used with two models that operate on the same scale but portray different physics. This motivates a study that presents a preparatory investigation in this regard [61]. The information content delivered by both modal analysis simulations using the finite element method and guided wave propagation as implemented by the spectral element method [3] is considered.

The effect of a continuous circular defect in a square aluminum plate on its natural frequencies and the propagation of lamb waves within the plate is investigated [62]. At the time of writing this manuscript, the author is not aware of any published research that addresses which method is better suited for the identification of such a defect. To advance here, it is assumed that a classical optimization task shall be solved to characterize the defect based on the minimization of an objective function. A set of four objective functions is constructed. The first results from the full time-domain response represented by the ultrasonic waveform as it is employed in full waveform inversion [114]. The second is based on the velocity of the first antisymmetric Lamb wave mode [52, 71] as identified by the peak of the Hilbert envelope [122] around the waveform. Refer to the literature for the fundamentals of elastic waves [8, 81]. The third and fourth are based on the first and second natural frequencies of the plate, respectively. The plate is modeled with free-free boundary conditions here [62]. This is reflected in the validation by experimental modal analysis, where the rigid body modes are sufficiently separated from the first natural frequency by suspension on strings when excited with the modal hammer. The laser Doppler vibrometer is also used for the experimental validation of the guided wave simulation, where the response is evaluated on a grid surrounding the source, a shear wave transducer. After evaluating the effect of the position of the defect and its geometry on the objective functions via numerical parameter studies, clear advantages and drawbacks can be associated with each trial method. [62] While the utilized modal data produces ambiguous objective functions due to symmetry in the investigated modes, the obtained objective functions are smooth over both the defect position and its size. [62] This renders modal data suitable for applying a gradient-based optimization procedure. The optima resulting from guided wave data are comparatively compact and free from ambiguity; however, the objective surface is rough. These findings support employing both lamb waves and modal data jointly, either with a two-step procedure beginning with natural frequency data or by integrating the approaches into multi-fidelity Gaussian process regression frameworks.

Contributions Karl-Alexander Hoppe: Conceptualization, Methodology, Software, Validation, Formal Analysis, Measurements, Investigation, Visualization, Writing - Original draft, Writing - Review and Editing, Project Administration. Simon Schmid: Conceptualization, Methodology, Software, Validation, Formal Analysis, Measurements, Investigation, Data Curation, Visualization, Resources, Writing - Original Draft, Writing - Review and Editing, Project Administration. Jochen Kollofrath: Conceptualization, Methodology, Software, Validation, Formal Analysis, Measurements, Investigation, Writing - Review and Editing. Steffen Marburg: Supervision, Resources, Writing - Review and Editing. Christian U. Grosse: Supervision, Resources, Writing - Review and Editing.

Reference Hoppe, K.-A., Schmid, S., Kollofrath, J., Marburg, S., and Grosse, C. U. "Evaluation of inversion approaches for plates based on guided waves and modal analysis". In: *Discover Applied Sciences* 6.5 (2024), p. 258. DOI: [10.1007/s42452-024-05912-3](https://doi.org/10.1007/s42452-024-05912-3). URL: <https://doi.org/10.1007/s42452-024-05912-3>

3.2 Paper B

Identification of a cantilever beam's spatially uncertain stiffness

Karl-Alexander Hoppe, Martin G. T. Kronthaler, Kian Sepahvand, and Steffen Marburg

Summary This publication presents the core of this thesis, see Figure 2.1, that all other efforts are centered on. It should be thus understood as a baseline framework that is complemented and expanded by the other contributions. The non-destructive characterization of the spatially varying elastic material properties from vibration measurements while incorporating uncertainty constitutes the engineering application. In the literature, this is done employing the generalized polynomial chaos expansion or Karhunen-Loève expansion of the stiffness and using frequency response functions or mode shape data [11, 26, 28, 93].

To the best of the author's knowledge at the time of submitting the paper, it is the first work to apply Bayesian inference to the identification of the spatially uncertain structural flexibility of a beam by a resonance frequency method together with the Karhunen-Loève expansion. This task can also be interpreted as a localization problem from the macro- to the meso-scale, as the natural frequency belongs to the structure globally, while the elasticity tensor possesses a spatial dependence at the meso-scale. To create a frame of reference, the model is compared closely to a recent result from the literature, where Uribe et al. [146] study the identification of the non-homogeneous stiffness of a cantilever beam under static loading given noisy deflection observations. To ensure comparability, their problem setting is reproduced in proprietary implementations for the finite element method and the Karhunen-Loève expansion. Additionally, the Bayesian inference is executed identically using slice sampling; see Section 2.2. The likelihood is chosen as given by Eq. (2.15) for both application cases. The choice of γ_j reflects that higher natural frequencies are harder to determine by increasing together with the eigenfrequency number.

To gain insight into the performance of both approaches, the inversion is applied for a range of signal-to-noise ratios and a range of correlation lengths L of the underlying random flexibility fields. The errors are interpreted in a mean sense over 100 ground truth realizations. The characterization based on static deflection data generally results in lower errors. This can be explained by the fact that, while using deflection data does suffer from error propagation, it is not a localization problem, as the deflection data probe positions live on the same scale as the a priori unknown elastic material properties. Thus, this approach has an easier time identifying the quantity of interest, much like using mode shape data. The error propagation in the static case leads to a widening confidence interval with increasing distance from the support. This is not the case when natural frequencies are used; the estimation uncertainty remains roughly constant over the problem domain here. Common observations for both approaches include that higher signal-to-noise ratios improve the accuracy, and an improved reconstruction can be achieved when L is large relative to the domain's size. [57]

Contributions Karl-Alexander Hoppe: Conceptualization, Methodology, Software, Validation, Formal Analysis, Investigation, Resources, Writing - Original Draft, Writing - Review and Editing, Visualization, Supervision, Project Administration. Martin G. T. Kronthaler: Methodology, Software, Validation, Formal Analysis, Investigation, Data Curation, Writing - Original Draft, Visualization. Kian Sepahvand: Writing - Review and Editing. Steffen Marburg: Supervision, Writing - Review and Editing.

Reference Hoppe, K.-A., Kronthaler, M. G. T., Sepahvand, K., and Marburg, S. "Identification of a cantilever beam's spatially uncertain stiffness". In: *Scientific Reports* 13, 1169

(2023), 1169:1–1169:13. DOI: [10.1038/s41598-023-27755-5](https://doi.org/10.1038/s41598-023-27755-5). URL: <https://doi.org/10.1038/s41598-023-27755-5>

3.3 Paper C

Surrogate recycling for structures with spatially uncertain stiffness

Karl-Alexander Hoppe, Kevin Josef Li, Bettina Chocholaty, Johannes D. Schmid, Kian Kheirollah Sepahvand, and Steffen Marburg

Summary This publication corresponds to the decrease in terms of the computational cost of the Bayesian inference framework as shown in pictogram (C) within Figure 2.1. It follows the paragraphs referring to acceleration within Section 2.1.2.

Marzouk and Najm [92] are the first to combine the generalized polynomial chaos expansion with the Karhunen-Loève expansion in the context of Bayesian inference of spatially varying quantities of interest. [58] The generalized polynomial chaos expansion suffers from the curse of dimensionality when a random field makes up the inputs. This is why the Karhunen-Loève expansion is necessary here: to decouple the generalized polynomial chaos dimensionality from the spatial discretization of the random field. In the original methodology, a change in the hyper-parameters of the covariance function of the underlying random field necessitates recomputing the generalized polynomial chaos surrogate models. The extension by Sraj et al. [138] to the original methodology offers an approximate alternative that is flexible in terms of the hyper-parameters and can retain the surrogate after they change.

In fact, the length scale of the elastic material properties may be a priori known for functionally graded materials. This link is based on process-structure-property relations, which are extensively studied in the literature [53]. The implication of the knowledge of the correlation length is that once a generalized polynomial chaos surrogate is computed, it can be reused an arbitrary number of times, leveraging the transformation proposed by Sraj et al. [138]. To explore the value of this insight, the study treats the non-destructive identification of the stiffness of structural beams. This study employs mode shape data instead of natural frequencies, drastically improving characterization accuracy. A functionally graded materials application serves to judge the performance of the method. Three parts based on a beam with identical geometry shall be designed to offer the largest possible failure safety while subjected to changing boundary conditions. This is achieved by building a material whose yield strength is the highest in regions of high stress due to the loads. The functionally graded parts indeed exhibit an improved minimum safety. Now, a generalized polynomial chaos surrogate is trained on a correlation length corresponding to one of the beam configurations, and the same surrogate is recycled for the remaining configurations. For the base case, the procedure yields an excellent location-independent identification of the stiffness complemented by a relevant workflow acceleration. In fact, the quality of the results remains excellent for recycled surrogates and scales fantastically with the number of process parameter length scales. A recommendation is that the length scale of the reference surrogate model should be set to the minimum possible length that is feasible in the light of computational resources.

Contributions Karl-Alexander Hoppe: Conceptualization, Methodology, Software, Validation, Formal Analysis, Investigation, Resources, Writing - Original Draft, Writing - Review & Editing, Visualization, Supervision, Project Administration. Kevin Josef Li: Methodology, Software, Formal Analysis, Investigation, Data Curation, Visualization. Bettina Chocholaty: Resources, Writing - Review & Editing. Johannes Schmid: Resources, Writing - Review & Editing. Kian Kheirollah Sepahvand: Validation. Steffen Marburg: Writing - Review & Editing, Supervision, Funding acquisition.

Reference Hoppe, K.-A., Li, K. J., Chocholaty, B., Schmid, J. D., Schmid, S., Sepahvand, K., and Marburg, S. “Surrogate recycling for structures with spatially uncertain stiffness”. In: *Journal of Sound and Vibration* 570 (2024), p. 117997. ISSN: 0022-460X. DOI: [10.1016/j.jsv.2023.117997](https://doi.org/10.1016/j.jsv.2023.117997). URL: <https://www.sciencedirect.com/science/article/pii/S0022460X23004467>

3.4 Paper D

Predicting the elastic properties of Norway spruce by its morphology

Karl-Alexander Hoppe, Pablo Francisco Ramírez Hönack, Simon Schmid, Jochen Kollofrath, Bettina Chocholaty, Iason Papaioannou, and Steffen Marburg

Summary While the requirement of knowing the covariance hyper-parameters a priori to the inference may be relaxed in selected cases when using an extension to the traditional procedure [138], the covariance kernel itself must always be known for the description with the Karhunen-Loève expansion. In this regard, the identification of the covariance, see Figure 2.5, can be interpreted as a mandatory preliminary for the Bayesian inference of local elastic material properties. When samples of a random field are available, this can readily be achieved using Gaussian process regression as described in Section 2.4.1.

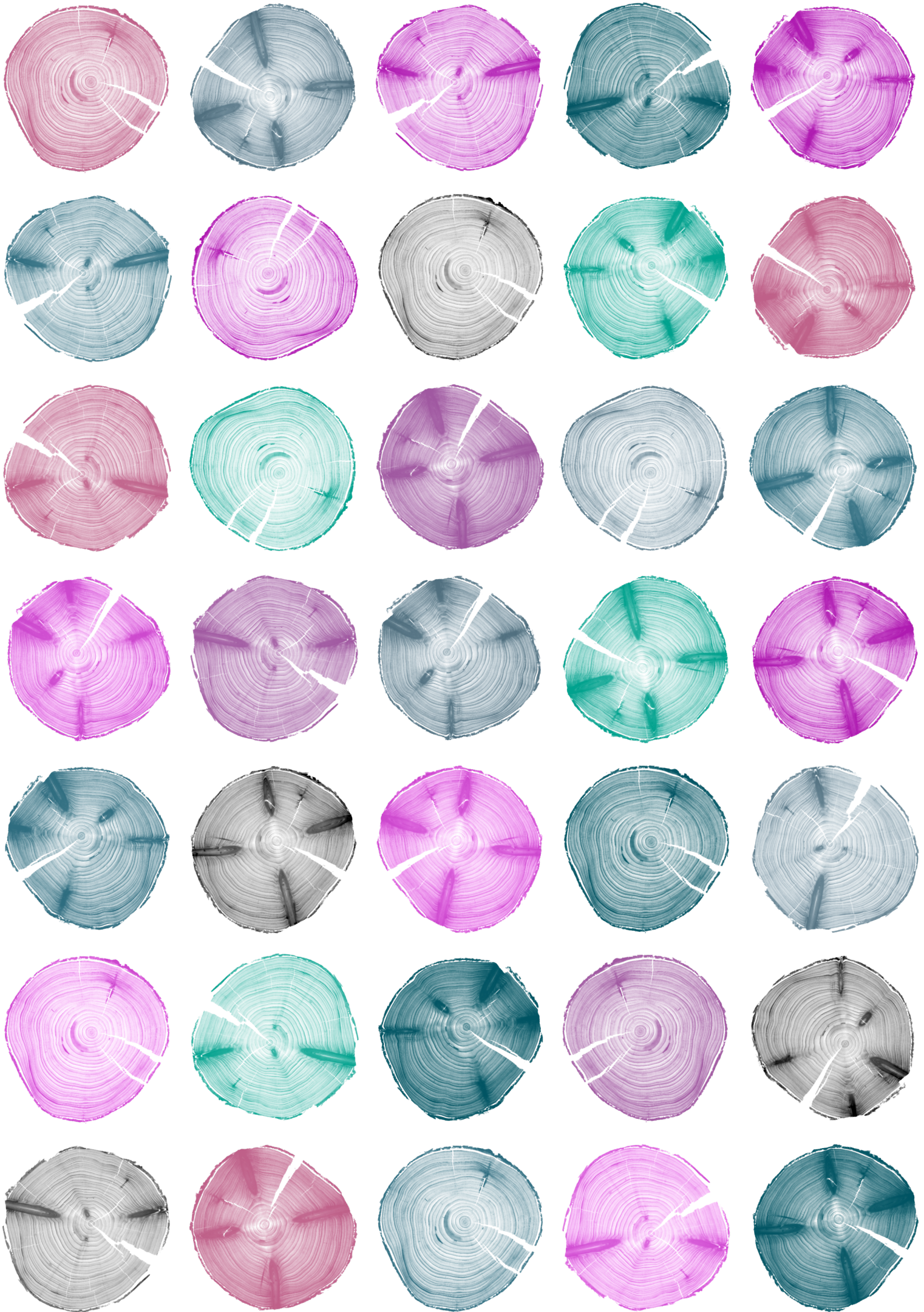
The formulation of a covariance model turns out to be an enticing research opportunity in comparison with the fitting of an existing covariance kernel. Precisely this is accomplished in this paper for the material wood, whose properties are scarcely considered as random fields in the literature [77]. Due to restrictions on the amount of necessary computational memory, the natural variability of wood is condensed to five one-dimensional random functions over a tree's growth direction instead of formulating the full three-dimensional covariance. These random functions correspond to the morphology of the tree cross-section by a simple sinusoidal annual ring model, which possesses a correlation with the mass density of wood. The morphological parameters are captured from the computed tomography scans of a spruce trunk, and it turns out that the model delivers an accurate approximation of the annual ring pattern. The derivation of a complementary model of the fiber directions from the density model that allows for an evaluation of the full heterogeneous and orthotropic elasticity validates the morphological model. The validation of the stiffness model via experimental modal analysis of the trunk shows an excellent agreement with its numerical counterpart. [56]

With uncertainty quantification in mind, the parameters of a stochastic variant of the new models that now include a model for knots and branches are identified. A comparison with bow height, taper, and spiral grain values from the literature confirms that the new data falls within a reasonable range for the regarded wood species. This comparison produces a useful result by delivering a generalized quantitative description of wood curvature in terms of random fields, while curvature manifestations are traditionally categorized using qualitative descriptors. Next, each Monte Carlo sample of the stochastic model is subjected to a numerical homogenization routine yielding the homogenized elasticity modulus E_h . The final result is a distribution of E_h that reflects the effect of the local fiber directions when considering a deterministic orthotropic base modulus of elasticity. Note that, among other effects, especially the variability originating from the naturally uncertain modulus of elasticity in the local longitudinal, radial, and tangential directions is not covered here. These findings are valuable for both sustainability and economic efficiency, as less of the raw material needs to be discarded with confidence intervals that can be readily computed from the uncertainty quantification procedure. [56]

Contributions Karl-Alexander Hoppe: Conceptualization, Methodology, Software, Validation, Formal Analysis, Investigation, Data Curation, Writing - Original Draft, Writing - Review & Editing, Visualization, Supervision, Project Administration. Pablo Francisco Ramírez Hönack: Software, Validation, Formal Analysis, Data Curation, Visualization. Simon Schmid: Measurements, Writing - Review & Editing. Jochen Kollofrath: Measurements. Bettina Chocholaty: Measurements, Writing - Review & Editing. Iason Papaioannou: Conceptualization,

Formal Analysis, Writing - Review & Editing, Supervision. Steffen Marburg: Resources, Writing - Review & Editing, Supervision.

Reference Hoppe, K.-A., Hönack, P. F. R., Schmid, S., Kollofrath, J., Chocholaty, B., Papaioannou, I., and Marburg, S. “Predicting the elastic properties of Norway spruce by its morphology”. In: *International Journal of Mechanical Sciences* 282 (2024), p. 109570. ISSN: 0020-7403. DOI: <https://doi.org/10.1016/j.ijmecsci.2024.109570>. URL: <https://www.sciencedirect.com/science/article/pii/S0020740324006118>



Chapter 4

Discussion and Conclusions

The goal of this doctoral project is the development of a method for non-destructively identifying the spatially varying elastic material properties of engineering structures using modal data [58]. The first step is accomplished by carrying out a preliminary study to confirm that resonance frequencies deliver sufficient information to detect defects in plates, see [Paper A](#). With this preparation, the main goal is achieved for the localization problem of characterizing the structural flexibility of a beam from noisy measurements of its natural frequencies. The procedure developed in [Paper B](#) interprets the a priori unknown spatially varying elastic properties as random fields and solves the inverse problem using Bayesian inference such that an estimate on the solution's uncertainty is available. The acceleration of the base procedure is presented in [Paper C](#). Here, generalized polynomial chaos expansion surrogate models describing a beam's mode shapes based on the Karhunen-Loève coefficients of the functionally graded Young's modulus are recycled. This reuse of the surrogates implies that costly finite element method models need only be evaluated for the initial surrogate. The only on-line computational overhead consists of constructing the Karhunen-Loève expansion for the proper correlation length of the part subject to non-destructive testing. Aiming to enhance the method's accuracy after its acceleration and simultaneously generalize it to estimate two or more unknown spatial functions, the ground truth cross-correlation is incorporated in the prior for the Bayesian inference as described in Section 2.1.2. It turns out that prescribing the cross-correlation is not uniformly beneficial [57]. Conversely, it is only advantageous when the cross-correlation of the quantities of interest is high, the signal-to-noise ratio is low, and few spatial observation points of the data are available. To provide a basis for the practical application of the novel method, a stochastic model for the natural variability for the example of the elastic material properties of wood is identified in [Paper D](#). This model is based on the models for the local density and the local grain angle. The validated models serve to provide an estimate of the uncertainty of the Young's modulus in the longitudinal direction due to morphological variability while providing an intermediary result by the quantitative generalization of previously qualitatively described wood defects.

The following paragraphs evaluate the consistency of the results with those from other studies. Inconclusive results and limitations of the research are then reviewed. Finally, the implications of the work are highlighted, and sensible future studies are suggested.

Consistency with Literature Results Uribe et al. [146] arrive at tighter confidence intervals for their estimation of the cantilever beam flexibility from deflection data compared to the results from [Paper B](#). This can be explained by differences in the numerical setup. They use a closed-form solution to the posterior, and the present study employs slice sampling. Additionally, different covariance functions and measurement noise characteristics are used in these two studies.

The bow height and spiral grain angle results reported in [Paper D](#) exceed the average values reported in the literature [32, 45, 75, 120, 121, 136, 150]. However, they still fall

within the overall range of these literature values. A possible explanation is that the investigated spruce trunk exhibits particularly prominent growth variability in comparison with statistically expected growth defects of this wood species. Studying inter-specimen variability should prove insightful here.

Inconclusive Results It may prove interesting to scrutinize the findings on prescribing the cross-correlation belonging to two or more unknown random fields presented in Section 2.1.2. It is possible that the choice of sampling algorithm for the Bayesian inference, the choice of likelihood, and most importantly, the forward model related to the specific application have a significant impact on the benefit of including the cross-correlation in the prior distribution. Especially gradient-based samplers, which are known for their superior performance when sampling from strongly correlated distributions [54], or recently emerging non-sampling approaches [129, 134] could react differently to the new prior formulations presented here.

Limitations The baseline procedure from Paper B demands that the intrinsic covariance function of the quantity of interest be known. Incorrect judgment of the covariance incurs several problems. If the correlation length is overestimated, the seemingly appropriate truncation order of the Karhunen-Loève expansion is insufficient. Moreover, the sampling performance suffers, as the priors on the Karhunen-Loève coefficients are now ill-fitting, and new samples must be drawn in regions of low prior probability.

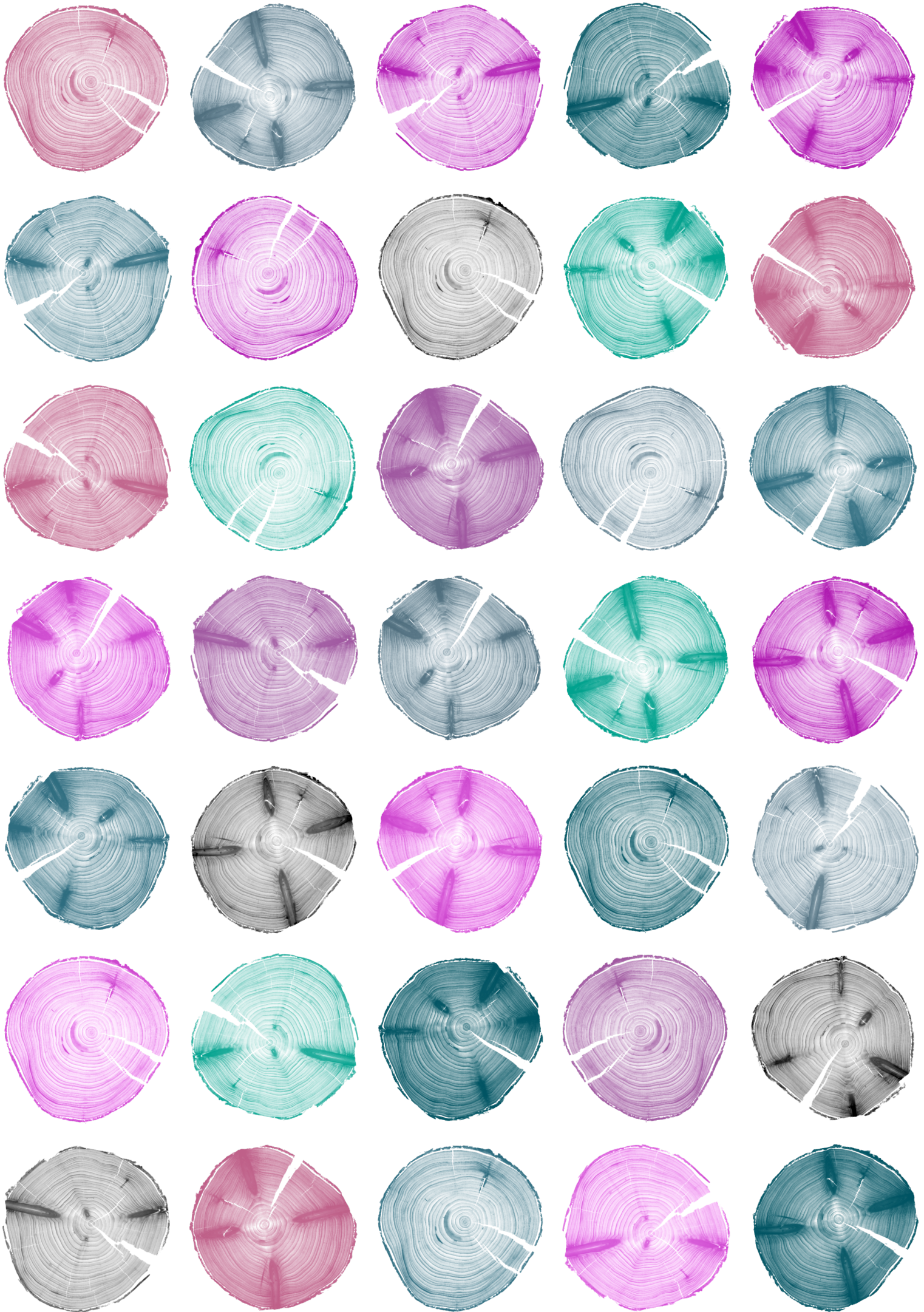
While two approaches from the literature [138, 142] relieve the methodology developed by Marzouk and Najm [92] of its reliance on the prior knowledge of the correct covariance kernel hyper-parameters, the restriction on the covariance function itself persists. Note that the procedure for surrogate recycling proposed in Paper C is only valid when the geometry of the structure and the boundary conditions remain unchanged. An argument can be made for the latter, as parts are commonly tested in quality control under identical conditions before ultimately being integrated into their application-specific environment. However, the restriction on the geometry is intractable. It is sensible for functionally graded materials, where the potential for saving costs is found in designing a part with a common geometry for several load cases by retaining the interface to other parts in the assembly and compensating for the varying loading conditions with a yield strength grading by design. Ultimately, tying in with neural networks that consider the underlying partial differential equations could offer a remedy, as they allow for the flexible modeling of real-world boundary conditions [113].

Implications and Applications The findings from Paper A can be used to fuse data from guided wave propagation and modal data into a multi-fidelity Gaussian process regression scheme for an efficient defect characterization [109]. The results from Paper B and especially the powerful procedure proposed in Paper C may be employed to satisfy the growing demand for non-destructive testing of functionally graded materials. The models in Paper D are simultaneously simpler and more holistic than typical material models for wood. It is desirable that they be employed for strength grading based on computed tomography or surface scan data of logs. The stochastic version of these models shall be extended and parameterized for different wood species to facilitate uncertainty quantification of their load-bearing capacity. Lastly, the stochastic model possesses the capacity to generate images that realistically mimic wood patterns. Synthetic wood flooring or paneling represent applications that immediately jump to mind.

Potential Future Studies A validation of the wood fiber direction model using a finer grid would be favorable. This could be achieved by applying automatic fiber tracing algorithms on

higher resolution computed tomography data than that available during this doctoral project [69]. The methods proposed in [Paper B](#) and [Paper C](#) could be tested numerically against step function profiles instead of smooth functions; they could be applied to different material classes such as carbon-fiber-reinforced polymers, and they could be validated experimentally on a functionally graded structure investigated with digital volume correlation, which is outside of the scope for this doctoral project. Further research developing additional generalizations of the Karhunen-Loève expansion to acquire the flexibility to account for different covariance structures instead of merely different sets of hyper-parameters is desirable for the generalized application of the methods. Such an approach may be inspired by the work by Lloyd et al. [87]. Significant research effort is still needed to develop a database of covariance functions describing the variability of material properties. The present research contributes an initial covariance model for wood. Ontologies such as the European Materials & Modelling Ontology [27, 63–65, 99] that make use of a taxonomy of materials could be used as a starting point here. Note that a preparatory step of identifying those material classes that exhibit heterogeneous material properties with a significant impact at the scale of interest should be completed first. Currently, numerical homogenization methods and multi-scale methods specified in frameworks like the Integrated Computational Materials Engineering [66] can be used for this purpose. Ultimately, model order reduction methods [13] or the advance of computational power [144] may render the aforementioned restrictions obsolete.

In conclusion, the value of modal analysis of structures for characterizing their non-homogeneous material is recognized. A potent method is developed for identifying the spatially varying stiffness as represented by the Karhunen-Loève expansion via Bayesian inference and by employing a generalized polynomial chaos surrogate. Including prior knowledge on the cross-correlation of multiple quantities of interest is not always useful. Finally, this work proposes a stochastic meso-scale material model for wood based on its morphological traits.



Bibliography

- [1] Aagesen, L., Adams, J., Allison, J., Andrews, W., Araullo-Peters, V., Berman, T., Chen, Z., Daly, S., Das, S., DeWitt, S., Ganesan, S., Garikipati, K., Gavini, V., Githens, A., Hedstrom, M., Huang, Z., Jagadish, H., Jones, J., Luce, J., Marquis, E., Misra, A., Montiel, D., Motamarri, P., Murphy, A., Natarajan, A., Panwar, S., Puchala, B., Qi, L., Rudraraju, S., Sagiyama, K., Solomon, E., Sundararaghavan, V., Tarcea, G., Teichert, G., Thomas, J., Thornton, K., Van der Ven, A., Wang, Z., Weymouth, T., and Yang, C. “PRISMS: An Integrated, Open-Source Framework for Accelerating Predictive Structural Materials Science”. In: *JOM* 70.10 (2018), pp. 2298–2314. ISSN: 10474838. DOI: [10.1007/s11837-018-3079-6](https://doi.org/10.1007/s11837-018-3079-6).
- [2] Abrahamsen, P. *A review of Gaussian random fields and correlation functions*. Tech. rep. Oslo: Norsk Regnesentral/Norwegian Computing Center, 1997.
- [3] Afanasiev, M., Boehm, C., Driel, M. van, Krischer, L., Rietmann, M., May, D. A., Knepley, M. G., and Fichtner, A. “Modular and flexible spectral-element waveform modelling in two and three dimensions”. In: *Geophysical Journal International* 216.3 (2019), pp. 1675–1692. DOI: [10.1093/gji/ggy469](https://doi.org/10.1093/gji/ggy469).
- [4] Allison, J. “Integrated computational materials engineering: A perspective on progress and future steps”. In: *JOM* 63.4 (2011), pp. 15–18. ISSN: 15431851. DOI: [10.1007/s11837-011-0053-y](https://doi.org/10.1007/s11837-011-0053-y).
- [5] Arróyave, R., Khatamsaz, D., Vela, B., Couperthwaite, R., Molkeri, A., Singh, P., Johnson, D. D., Qian, X., Srivastava, A., and Allaire, D. “A perspective on Bayesian methods applied to materials discovery and design”. In: *MRS Communications* 12.6 (2022), pp. 1037–1049. ISSN: 21596859. DOI: [10.1557/s43579-022-00288-0](https://doi.org/10.1557/s43579-022-00288-0).
- [6] Askey, R. and Wilson, J. *Some basic hypergeometric polynomials that generalize Jacobi polynomials* *Memoirs Amer.* Vol. 54. Providence: American Mathematical Society, 1985.
- [7] Aster, R. C., Borchers, B., and Thurber, C. H. *Parameter Estimation and Inverse Problems*. Vol. 90. International Geophysics. Cambridge: Academic Press, 2005. DOI: [https://doi.org/10.1016/S0074-6142\(05\)80014-2](https://doi.org/10.1016/S0074-6142(05)80014-2). URL: <https://www.sciencedirect.com/science/article/pii/S0074614205800142>.
- [8] Auld, B. A. *Acoustic fields and waves in solids*. Malabar: Krieger Publishing Company, 1990.
- [9] Babich, J., Bamber, J., Bentley, R., Bradley, A., Brown, B., Castellano, E., Dance, D., Dobbs, J., Doran, S., Evans, S., Flower, M., Flux, G., Hall, A., Hebden, J., Hill, K., Jones, C., Leach, M., Marsden, P., Miller, N., Ott, B., Sassi, S., Skinner, C., Suckling, J., Tristram, M., and Webb, S. *Webb’s physics of medical imaging*. Ed. by Flower, M. A. 2nd ed. Boca Raton: CRC Press, 2012. ISBN: 978-0-7503-0573-0.

- [10] Balokhonov, R. and Romanova, V. “On the problem of strain localization and fracture site prediction in materials with irregular geometry of interfaces”. In: *Facta Universitatis, Series: Mechanical Engineering* 17.2 (2019), pp. 169–180. ISSN: 03542025. DOI: [10.22190/FUME190312023B](https://doi.org/10.22190/FUME190312023B).
- [11] Batou, A. and Soize, C. “Stochastic modeling and identification of an uncertain computational dynamical model with random fields properties and model uncertainties”. In: *Archive of Applied Mechanics* 83 (2013), pp. 831–848. DOI: [10.1007/s00419-012-0720-7](https://doi.org/10.1007/s00419-012-0720-7).
- [12] Bekey, G. A. and Kogan, B. Y., eds. *Modeling and simulation: theory and practice*. 1st ed. Boston: Springer Science+Business Media, 2003.
- [13] Benner, P., Gugercin, S., and Willcox, K. “A survey of projection-based model reduction methods for parametric dynamical systems”. In: *SIAM review* 57.4 (2015), pp. 483–531. DOI: [10.1137/130932715](https://doi.org/10.1137/130932715).
- [14] Betz, W., Papaioannou, I., and Straub, D. “Numerical methods for the discretization of random fields by means of the Karhunen–Loève expansion”. In: *Computer Methods in Applied Mechanics and Engineering* 271 (2014), pp. 109–129.
- [15] Bockman, A., Fackler, C., and Xiang, N. “Bayesian-based estimation of acoustic surface impedance: finite difference frequency domain approach”. In: *The Journal of the Acoustical Society of America* 133.5 (2013), p. 3576.
- [16] Boloix-Tortosa, R., Murillo-Fuentes, J. J., Payán-Somet, F. J., and Pérez-Cruz, F. “Complex Gaussian Processes for Regression”. In: *IEEE Transactions on Neural Networks and Learning Systems* 29.11 (2018), pp. 5499–5511. DOI: [10.1109/TNNLS.2018.2805019](https://doi.org/10.1109/TNNLS.2018.2805019).
- [17] Boloix-Tortosa, R., Murillo-Fuentes, J. J., and Tsaftaris, S. A. “The generalized complex kernel least-mean-square algorithm”. In: *IEEE Transactions on Signal Processing* 67.20 (2019), pp. 5213–5222.
- [18] Boloix-Tortosa, R., Payán-Somet, F. J., Arias-de-Reyna, E., and Murillo-Fuentes, J. J. *Proper Complex Gaussian Processes for Regression*. 2015. DOI: [10.48550/arXiv.1502.04868](https://doi.org/10.48550/arXiv.1502.04868). arXiv: [1502.04868](https://arxiv.org/abs/1502.04868) [cs.LG]. URL: <https://arxiv.org/pdf/1502.04868>.
- [19] Brough, D. B., Wheeler, D., and Kalidindi, S. R. “Materials Knowledge Systems in Python—a Data Science Framework for Accelerated Development of Hierarchical Materials”. In: *Integrating Materials and Manufacturing Innovation* 6.1 (2017), pp. 36–53. ISSN: 21939764. DOI: [10.1007/s40192-017-0089-0](https://doi.org/10.1007/s40192-017-0089-0).
- [20] Carlton, M. A. and Devore, J. L. *Probability with applications in engineering, science, and technology*. Cham: Springer, 2017.
- [21] Charalambakis, N. “Homogenization techniques and micromechanics. A survey and perspectives”. In: *Applied Mechanics Reviews* 63.3 (2010). DOI: [10.1115/1.4001911](https://doi.org/10.1115/1.4001911).
- [22] Cho, H., Venturi, D., and Karniadakis, G. “Karhunen–Loève expansion for multi-correlated stochastic processes”. In: *Probabilistic Engineering Mechanics* 34 (2013), pp. 157–167.
- [23] Coutant, O. *Bayesian Inversion*. Lecture notes. Grenoble, 2015. URL: <https://inv-conj-geophy.sciencesconf.org/conference/inv-conj-geophy/talkJointInversionCoutant.pdf>.
- [24] Cranford, S. W. and Buehler, M. J. “Shaky foundations of hierarchical biological materials”. In: *Nano Today* 6.4 (2011), pp. 332–338. DOI: [10.1016/j.nantod.2011.07.001](https://doi.org/10.1016/j.nantod.2011.07.001).

- [25] Daghia, F., Miranda, S. de, Ubertini, F., and Viola, E. “Estimation of elastic constants of thick laminated plates within a Bayesian framework”. In: *Composite Structures* 80.3 (2007), pp. 461–473.
- [26] Debryne, S., Vandepitte, D., and Moens, D. “Identification of design parameter variability of honeycomb sandwich beams from a study of limited available experimental dynamic structural response data”. In: *Computers & Structures* 146 (2015), pp. 197–213. DOI: [10.1016/j.compstruc.2013.09.004](https://doi.org/10.1016/j.compstruc.2013.09.004).
- [27] Del Nostro, P., Goldbeck, G., and Toti, D. “CHAMEO: An ontology for the harmonisation of materials characterisation methodologies”. In: *Applied Ontology* (2022), pp. 1–21. DOI: [10.3233/AO-220271](https://doi.org/10.3233/AO-220271).
- [28] Desceliers, C., Soize, C., and Ghanem, R. “Identification of Chaos Representations of Elastic Properties of Random Media Using Experimental Vibration Tests”. In: *Computational Mechanics* 39 (2006), pp. 831–838. DOI: [10.1007/s00466-006-0072-7](https://doi.org/10.1007/s00466-006-0072-7).
- [29] Devroye, L. *Non-Uniform Random Variate Generation*. New York: Springer, 1986.
- [30] Duvenaud, D. “Automatic model construction with Gaussian processes”. PhD thesis. University of Cambridge, 2014.
- [31] Duvenaud, D., Lloyd, J. R., Grosse, R., Tenenbaum, J. B., and Ghahramani, Z. *Structure Discovery in Nonparametric Regression through Compositional Kernel Search*. 2013. arXiv: [1302.4922](https://arxiv.org/abs/1302.4922) [stat.ML].
- [32] Edlund, J. and Warensjö, M. “Repeatability in automatic sorting of curved Norway spruce saw logs”. In: *Silva Fennica* 39.2 (2005), pp. 265–275. DOI: [10.14214/SF.388](https://doi.org/10.14214/SF.388).
- [33] Eriksson, K., Estep, D., and Johnson, C. *Applied mathematics: body and soul*. Heidelberg: Springer-Verlag Berlin, 2004.
- [34] Ewins, D. J. *Modal testing: theory, practice and application*. Philadelphia: Research Studies Press, 2009.
- [35] Fenton, G. A. *Simulation of random fields*. Lecture notes. Wrocław, 2008.
- [36] Fenton, G. A. and Griffiths, D. “Random field generation and the local average subdivision method”. In: *Probabilistic methods in geotechnical engineering*. Springer, 2007, pp. 201–223.
- [37] Forrester, A. I. and Keane, A. J. “Recent advances in surrogate-based optimization”. In: *Progress in aerospace sciences* 45.1-3 (2009), pp. 50–79. DOI: [10.1016/j.paerosci.2008.11.001](https://doi.org/10.1016/j.paerosci.2008.11.001).
- [38] Forsberg, F., Sjö Dahl, M., Mooser, R., Hack, E., and Wyss, P. “Full three-dimensional strain measurements on wood exposed to three-point bending: Analysis by use of digital volume correlation applied to synchrotron radiation micro-computed tomography image data”. In: *Strain* 46.1 (2010), pp. 47–60. ISSN: 14751305. DOI: [10.1111/j.1475-1305.2009.00687.x](https://doi.org/10.1111/j.1475-1305.2009.00687.x).
- [39] Fratzl, P. and Weinkamer, R. “Nature’s hierarchical materials”. In: *Progress in Materials Science* 52.8 (2007), pp. 1263–1334. DOI: [10.1016/j.pmatsci.2007.06.001](https://doi.org/10.1016/j.pmatsci.2007.06.001).
- [40] Gallina, A., Ambrozinski, L., Packo, P., Pieczonka, L., Uhl, T., and Staszewski, W. J. “Bayesian parameter identification of orthotropic composite materials using Lamb waves dispersion curves measurement”. In: *Journal of Vibration and Control* 23.16 (2017), pp. 2656–2671.
- [41] Garcia, D., Jones, M. E., Zhu, Y., and Hang, Z. Y. “Mesoscale design of heterogeneous material systems in multi-material additive manufacturing”. In: *Journal of Materials Research* 33.1 (2018), pp. 58–67. DOI: [10.1557/jmr.2017.328](https://doi.org/10.1557/jmr.2017.328).

- [42] Gatsos, T., Elsayed, K. A., Zhai, Y., and Lados, D. A. “Review on computational modeling of process–microstructure–property relationships in metal additive manufacturing”. In: *JOM* 72.1 (2020), pp. 403–419. DOI: [10.1007/s11837-019-03913-x](https://doi.org/10.1007/s11837-019-03913-x).
- [43] Gennisson, J.-L., Deffieux, T., Fink, M., and Tanter, M. “Ultrasound elastography: principles and techniques”. In: *Diagnostic and interventional imaging* 94.5 (2013), pp. 487–495. DOI: [10.1016/j.diii.2013.01.022](https://doi.org/10.1016/j.diii.2013.01.022).
- [44] Ghanem, R. G. and Spanos, P. D. *Stochastic Finite Elements: A Spectral Approach*. Berlin/Heidelberg: Springer Science & Business Media, 2012.
- [45] Gjerdrum, P. and Bernabei, M. “Three-dimensional spiral grain pattern in five large Norway spruce stems”. In: *Silva Fennica* 43.3 (2009), pp. 457–464. DOI: [10.14214/sf.200](https://doi.org/10.14214/sf.200).
- [46] Gogu, C., Yin, W., Haftka, R., Ifju, P., Molimard, J., Le Riche, R., and Vautrin, A. “Bayesian identification of elastic constants in multi-directional laminate from Moiré interferometry displacement fields”. In: *Experimental Mechanics* 53.4 (2013), pp. 635–648.
- [47] Goodwin, G. C. “Inverse Problems with Constraints”. In: *IFAC Proceedings Volumes* 35.1 (2002), pp. 35–48. DOI: [10.3182/20020721-6-ES-1901.01638](https://doi.org/10.3182/20020721-6-ES-1901.01638).
- [48] Graham, I. G., Kuo, F. Y., Nuyens, D., Scheichl, R., and Sloan, I. H. “Analysis of circulant embedding methods for sampling stationary random fields”. In: *SIAM Journal on Numerical Analysis* 56.3 (2018), pp. 1871–1895. DOI: [10.1137/17M114973](https://doi.org/10.1137/17M114973).
- [49] Grigoriu, M. *Stochastic Calculus Applications in Science and Engineering*. 1st ed. Boston, MA: Birkhäuser, 2002.
- [50] Hadamard, J. “Sur les problèmes aux dérivées partielles et leur signification physique”. In: *Princeton university bulletin* (1902), pp. 49–52.
- [51] Hambric, S. A., Sung, S. H., and Nefske, D. J., eds. *Engineering Vibroacoustic Analysis*. Chichester: John Wiley & Sons, 2016.
- [52] Harb, M. and Yuan, F. “Non-contact ultrasonic technique for Lamb wave characterization in composite plates”. In: *Ultrasonics* 64 (2016), pp. 162–169. DOI: [10.1016/j.ultras.2015.08.011](https://doi.org/10.1016/j.ultras.2015.08.011).
- [53] Hashemi, S. M., Parvizi, S., Baghbanijavid, H., Tan, A. T., Nematollahi, M., Ramazani, A., Fang, N. X., and Elahinia, M. “Computational modelling of process–structure–property–performance relationships in metal additive manufacturing: A review”. In: *International Materials Reviews* 67.1 (2022), pp. 1–46. DOI: [10.1080/09506608.2020.1868889](https://doi.org/10.1080/09506608.2020.1868889).
- [54] Hoffman, M. D. and Gelman, A. “The No-U-Turn Sampler: Adaptively Setting Path Lengths in Hamiltonian Monte Carlo”. In: *Journal of Machine Learning Research* 15.47 (2014), pp. 1593–1623. URL: <http://jmlr.org/papers/v15/hoffman14a.html>.
- [55] Hofmann, T., Schölkopf, B., and Smola, A. J. “Kernel methods in machine learning”. In: *The annals of statistics* (2008), pp. 1171–1220.
- [56] Hoppe, K.-A., Hönack, P. F. R., Schmid, S., Kollofrath, J., Chocholaty, B., Papaioannou, I., and Marburg, S. “Predicting the elastic properties of Norway spruce by its morphology”. In: *International Journal of Mechanical Sciences* 282 (2024), p. 109570. ISSN: 0020-7403. DOI: <https://doi.org/10.1016/j.ijmecsci.2024.109570>. URL: <https://www.sciencedirect.com/science/article/pii/S0020740324006118>.

- [57] Hoppe, K.-A., Kronthaler, M. G. T., Sepahvand, K., and Marburg, S. "Identification of a cantilever beam's spatially uncertain stiffness". In: *Scientific Reports* 13, 1169 (2023), 1169:1–1169:13. DOI: [10.1038/s41598-023-27755-5](https://doi.org/10.1038/s41598-023-27755-5). URL: <https://doi.org/10.1038/s41598-023-27755-5>.
- [58] Hoppe, K.-A., Li, K. J., Chocholaty, B., Schmid, J. D., Schmid, S., Sepahvand, K., and Marburg, S. "Surrogate recycling for structures with spatially uncertain stiffness". In: *Journal of Sound and Vibration* 570 (2024), p. 117997. ISSN: 0022-460X. DOI: [10.1016/j.jsv.2023.117997](https://www.sciencedirect.com/science/article/pii/S0022460X23004467). URL: <https://www.sciencedirect.com/science/article/pii/S0022460X23004467>.
- [59] Hoppe, K.-A., Mannhardt, S., and Marburg, S. "Bayesian Identification of Spatially Varying Impedance". In: *Fortschritte der Akustik - DAGA 2022, 48. Jahrestagung für Akustik, 21.-24. März 2022 in Stuttgart / online (hybrid)*. Ed. by Leistner, P. Stuttgart: Deutsche Gesellschaft für Akustik e.V. (DEGA), 2022, pp. 868–870. ISBN: 978-3-939296-20-1.
- [60] Hoppe, K.-A. and Marburg, S. "A Framework for the Identification of Spatially Varying Elastic Material Properties via Modal Data". In: *Fortschritte der Akustik - DAGA 2024, 50. Jahrestagung für Akustik, 18.-21. März 2023, Hannover*. Ed. by Peissig, J. and Rolfes, R. Berlin: Deutsche Gesellschaft für Akustik e.V. (DEGA), 2024, pp. 1062–1064. ISBN: 978-3-939296-22-5. URL: https://pub.dega-akustik.de/DAGA_2024.
- [61] Hoppe, K.-A., Schmid, S., Kollofrath, J., and Marburg, S. "Vergleich von Ansätzen zur Identifikation von Defekten an Homogenen Platten". In: *Fortschritte der Akustik - DAGA 2023, 49. Jahrestagung für Akustik, 06.-09. März 2023, Hamburg*. Ed. by Estorff, O. von and Lippert, S. Berlin: Deutsche Gesellschaft für Akustik e.V. (DEGA), 2023, pp. 1090–1093. ISBN: 978-3-939296-21-8. URL: https://pub.dega-akustik.de/DAGA_2023.
- [62] Hoppe, K.-A., Schmid, S., Kollofrath, J., Marburg, S., and Grosse, C. U. "Evaluation of inversion approaches for plates based on guided waves and modal analysis". In: *Discover Applied Sciences* 6.5 (2024), p. 258. DOI: [10.1007/s42452-024-05912-3](https://doi.org/10.1007/s42452-024-05912-3). URL: <https://doi.org/10.1007/s42452-024-05912-3>.
- [63] Horsch, M., Chiacchiera, S., Schembera, B., Seaton, M., and Todorov, I. "Semantic interoperability based on the European materials and Modelling Ontology and its ontological paradigm: Mereosemiotics". In: *World Congress in Computational Mechanics and ECCOMAS Congress*. Ed. by Chinesta, F., Abgrall, R., Allix, O., and Kaliske, M. Vol. 2100. 2021. DOI: [10.23967/wccm-eccomas.2020.297](https://doi.org/10.23967/wccm-eccomas.2020.297).
- [64] Horsch, M. T., Chiacchiera, S., Seaton, M. A., Todorov, I. T., Šindelka, K., Lísal, M., Andreon, B., Bayro Kaiser, E., Moggi, G., Goldbeck, G., Kunze, R., Summer, G., Fiseni, A., Brüning, H., Schiffels, P., and Cavalcanti, W. L. "Ontologies for the Virtual Materials Marketplace". In: *KI - Künstliche Intelligenz* 34.3 (2020), pp. 423–428. DOI: [10.1007/s13218-020-00648-9](https://doi.org/10.1007/s13218-020-00648-9).
- [65] Horsch, M. T., Schembera, B., and Preisig, H. A. "European standardization efforts from FAIR toward explainable-AI-ready data documentation in materials modelling". In: *2023 3rd International Conference on Applied Artificial Intelligence, ICAPAI 2023*. 2023. DOI: [10.1109/ICAPAI58366.2023.10193944](https://doi.org/10.1109/ICAPAI58366.2023.10193944).
- [66] Horstemeyer, M. F. and Sahay, S. *Integrated Computational Materials Engineering (ICME) for Metals*. Hoboken: John Wiley & Sons, Ltd, 2018. ISBN: 9781119018377. DOI: [10.1002/9781119018377](https://doi.org/10.1002/9781119018377).
- [67] Hsu, H. P. *Schaum's outline of theory and problems of probability, random variables, and random processes*. New York: McGraw-Hill, 1997.

- [68] Hu, M., Johansson, M., Olsson, A., Oscarsson, J., and Enquist, B. “Local variation of modulus of elasticity in timber determined on the basis of non-contact deformation measurement and scanned fibre orientation”. In: *European Journal of Wood and Wood Products* 73 (2015), pp. 17–27. DOI: [10.1007/s00107-014-0851-3](https://doi.org/10.1007/s00107-014-0851-3).
- [69] Hu, M., Olsson, A., Hall, S., and Seifert, T. “Fibre directions at a branch-stem junction in Norway spruce: a microscale investigation using X-ray computed tomography”. In: *Wood Science and Technology* 56.1 (2022), pp. 147–169. DOI: [10.1007/s00226-021-01353-y](https://doi.org/10.1007/s00226-021-01353-y).
- [70] Huang, S., Quek, S., and Phoon, K. “Convergence study of the truncated Karhunen–Loeve expansion for simulation of stochastic processes”. In: *International journal for numerical methods in engineering* 52.9 (2001), pp. 1029–1043.
- [71] Huthwaite, P. “Evaluation of inversion approaches for guided wave thickness mapping”. In: *Proceedings of the Royal Society A: Mathematical, Physical and Engineering Sciences* 470.2166 (2014), p. 20140063. DOI: [10.1098/rspa.2014.0063](https://doi.org/10.1098/rspa.2014.0063).
- [72] Isukapalli, S. S. “Uncertainty analysis of transport-transformation models”. PhD thesis. New Brunswick: The State University of New Jersey, 1999.
- [73] Jacquelin, E., Adhikari, S., Sinou, J.-J., and Friswell, M. I. “Polynomial chaos expansion in structural dynamics: Accelerating the convergence of the first two statistical moment sequences”. In: *Journal of sound and vibration* 356 (2015), pp. 144–154. DOI: [10.1016/j.jsv.2015.06.039](https://doi.org/10.1016/j.jsv.2015.06.039).
- [74] Jardak, M., Su, C.-H., and Karniadakis, G. E. “Spectral polynomial chaos solutions of the stochastic advection equation”. In: *Journal of Scientific Computing* 17 (2002), pp. 319–338.
- [75] Johansson, M. and Kliger, R. “Influence of Material Characteristics on Warp in Norway Spruce Studs”. In: *Wood and Fiber Science* 34.2 (Apr. 2002), pp. 325–336.
- [76] Kaipio, J. and Somersalo, E. *Statistical and Computational Inverse Problems*. New York: Springer Science+Business Media, 2005.
- [77] Kandler, G., Füssl, J., and Eberhardsteiner, J. “Stochastic finite element approaches for wood-based products: theoretical framework and review of methods”. In: *Wood science and technology* 49 (2015), pp. 1055–1097. DOI: [10.1007/s00226-015-0737-5](https://doi.org/10.1007/s00226-015-0737-5).
- [78] Kleijnen, J. P. “Kriging metamodeling in simulation: A review”. In: *European journal of operational research* 192.3 (2009), pp. 707–716. DOI: [10.1016/j.ejor.2007.10.013](https://doi.org/10.1016/j.ejor.2007.10.013).
- [79] Koutsourelakis, P.-S. “A novel Bayesian strategy for the identification of spatially varying material properties and model validation: an application to static elastography”. In: *International Journal for Numerical Methods in Engineering* 91.3 (2012), pp. 249–268. DOI: [10.1002/nme.4261](https://doi.org/10.1002/nme.4261).
- [80] Koziel, S. and Pietrenko-Dabrowska, A. *Performance-Driven Surrogate Modeling of High-Frequency Structures*. Cham: Springer Nature, 2020.
- [81] Krautkrämer, J. and Krautkrämer, H. *Ultrasonic testing of materials*. Heidelberg: Springer Verlag Berlin Heidelberg, 1990. DOI: [10.1007/978-3-662-10680-8](https://doi.org/10.1007/978-3-662-10680-8).
- [82] Latz, J., Eisenberger, M., and Ullmann, E. “Fast sampling of parameterised Gaussian random fields”. In: *Computer Methods in Applied Mechanics and Engineering* 348 (2019), pp. 978–1012.
- [83] Latz, J., Papaioannou, I., and Ullmann, E. “Multilevel sequential Monte Carlo for Bayesian inverse problems”. In: *Journal of Computational Physics* 368 (2018), pp. 154–178. DOI: [10.1016/j.jcp.2018.04.014](https://doi.org/10.1016/j.jcp.2018.04.014).

- [84] Leclerc, H., Périé, J.-N., Roux, S., and Hild, F. “Voxel-Scale Digital Volume Correlation”. In: *Experimental Mechanics* 51.4 (2011), pp. 479–490. ISSN: 17412765. DOI: [10.1007/s11340-010-9407-6](https://doi.org/10.1007/s11340-010-9407-6).
- [85] Lee, P. M. *Bayesian Statistics: an Introduction*. Chichester: Wiley, 2012.
- [86] Leonov, A. S., Sharov, A. N., and Yagola, A. G. “Solution of the three-dimensional inverse elastography problem for parametric classes of inclusions”. In: *Inverse Problems in Science and Engineering* 29.8 (2021), pp. 1055–1069.
- [87] Lloyd, J. R., Duvenaud, D., Grosse, R., Tenenbaum, J., and Ghahramani, Z. “Automatic construction and natural-language description of nonparametric regression models”. In: *Proceedings of the Twenty-eighth AAAI conference on artificial intelligence*. Ed. by Brodley, C. E. and Stone, P. 2014.
- [88] Loève, M. *Probability Theory II*. New York: Springer, 1978.
- [89] Mallick, B. *Bayesian Inference in Inverse Problems*. Lecture notes. College Station, 2011. URL: <http://www.stat.rice.edu/~jrojo/4th-Lehmann/slides/Mallick.pdf>.
- [90] Martin, J. D. and Simpson, T. W. “Use of kriging models to approximate deterministic computer models”. In: *AIAA journal* 43.4 (2005), pp. 853–863. DOI: [10.2514/1.8650](https://doi.org/10.2514/1.8650).
- [91] Marzouk, Y. and Xiu, D. “A stochastic collocation approach to Bayesian inference in inverse problems”. In: *Communications in computational physics* 6.4 (2009), pp. 826–847.
- [92] Marzouk, Y. M. and Najm, H. N. “Dimensionality reduction and polynomial chaos acceleration of Bayesian inference in inverse problems”. In: *Journal of Computational Physics* 228.6 (2009), pp. 1862–1902. DOI: [10.1016/j.jcp.2008.11.024](https://doi.org/10.1016/j.jcp.2008.11.024).
- [93] Mehrez, L., Doostan, A., Moens, D., and Vandepitte, D. “Stochastic identification of composite material properties from limited experimental databases, Part II: Uncertainty modelling”. In: *Mechanical Systems and Signal Processing* 27 (2012), pp. 484–498. DOI: [10.1016/j.ymssp.2011.09.001](https://doi.org/10.1016/j.ymssp.2011.09.001).
- [94] Miller, J. W. *Lecture Notes on Bayesian Statistics*. Lecture notes. Durham, 2015. URL: <https://jwmi.github.io/BMS/>.
- [95] Minh, H. Q., Niyogi, P., and Yao, Y. “Mercer’s theorem, feature maps, and smoothing”. In: *International Conference on Computational Learning Theory*. Pittsburgh: Springer, 2006, pp. 154–168.
- [96] Mira, A., Møller, J., and Roberts, G. O. “Perfect slice samplers”. In: *Journal of the Royal Statistical Society: Series B (Statistical Methodology)* 63.3 (2001), pp. 593–606. DOI: [10.1111/1467-9868.00301](https://doi.org/10.1111/1467-9868.00301).
- [97] Mohammad-Djafari, A. *Bayesian inference for inverse problems*. Lecture notes. Baltimore, 2001. DOI: <https://doi.org/10.48550/arXiv.physics/0110093>. URL: <https://cds.cern.ch/record/525032/files/0110093.pdf>.
- [98] Møller, J., Pettitt, A., Reeves, R., and Berthelsen, K. K. “An efficient Markov chain Monte Carlo method for distributions with intractable normalising constants”. In: *Biometrika* 93.2 (2006), pp. 451–458. DOI: [10.1093/biomet/93.2.451](https://doi.org/10.1093/biomet/93.2.451). URL: <https://eprints.qut.edu.au/7869/1/7869.pdf>.
- [99] Morgado, J. F., Ghedini, E., Goldbeck, G., Hashibon, A., Schmitz, G. J., Friis, J., and De Baas, A. F. “Mechanical testing ontology for digital-twins: A roadmap based on EMMO”. In: *CEUR Workshop Proceedings*. Ed. by Garcia-Castro, R., Davies, J., Antoniou, G., and Fortuna, C. Vol. 2615. 2020.

- [100] Neal, R. M. “Slice Sampling”. In: *The Annals of Statistics* 31.3 (2003), pp. 705–767. DOI: [10.1214/aos/1056562461](https://doi.org/10.1214/aos/1056562461). URL: https://projecteuclid.org/download/pdf_1/euclid.aos/1056562461.
- [101] Neeser, F. D. and Massey, J. L. “Proper Complex Random Processes with Applications to Information Theory”. In: *IEEE Transactions on Information Theory* 39.4 (1993), pp. 1293–1302. DOI: [10.1109/18.243446](https://doi.org/10.1109/18.243446).
- [102] Nichols, J., Moore, E., and Murphy, K. “Bayesian identification of a cracked plate using a population-based Markov Chain Monte Carlo method”. In: *Computers & structures* 89.13-14 (2011), pp. 1323–1332.
- [103] NRC. *Integrated Computational Materials Engineering: A Transformational Discipline for Improved Competitiveness and National Security*. Washington, DC: The National Academies Press, 2008. ISBN: 978-0-309-11999-3. DOI: [10.17226/12199](https://doi.org/10.17226/12199). URL: <https://nap.nationalacademies.org/catalog/12199/integrated-computational-materials-engineering-a-transformational-discipline-for-improved-competitiveness>.
- [104] Nychka, D. *The Likelihood, the prior and Bayes’ Theorem*. Lecture notes for the NCAR / IMAGE summer school. 2007. URL: <https://www.image.ucar.edu/pub/TOY07.4/nychka2a.pdf>.
- [105] Olsson, A., Oscarsson, J., Serrano, E., Källsner, B., Johansson, M., and Enquist, B. “Prediction of timber bending strength and in-member cross-sectional stiffness variation on the basis of local wood fibre orientation”. In: *European Journal of Wood and Wood Products* 71.3 (2013), pp. 319–333. ISSN: 1436736X. DOI: [10.1007/s00107-013-0684-5](https://doi.org/10.1007/s00107-013-0684-5).
- [106] Papadopoulos, V. and Giovanis, D. G. *Stochastic Finite Element Methods*. Cham: Springer, 2018.
- [107] Papaioannou, I. *Data-driven prognostics*. Lecture notes. Munich, 2022.
- [108] Papaioannou, I. and Der Kiureghian, A. “EOLE for discretization of multivariate random fields”. In: *Proc. Computational Stochastic Mechanics, CSM 7, Santorini, Greece*. 2014.
- [109] Parussini, L., Venturi, D., Perdikaris, P., and Karniadakis, G. E. “Multi-fidelity Gaussian process regression for prediction of random fields”. In: *Journal of Computational Physics* 336 (2017), pp. 36–50. DOI: [10.1016/j.jcp.2017.01.047](https://doi.org/10.1016/j.jcp.2017.01.047).
- [110] Pearson, E. S. “Some problems arising in approximating to probability distributions, using moments”. In: *Biometrika* 50.1/2 (1963), pp. 95–112.
- [111] Pearson, K. “VII. Contributions to the Mathematical Theory of Evolution.—III. Regression, Heredity, and Panmixia”. In: *Proceedings of the Royal Society of London* 59 (1896), pp. 253–318.
- [112] Pindera, M.-J., Khatam, H., Drago, A. S., and Bansal, Y. “Micromechanics of spatially uniform heterogeneous media: A critical review and emerging approaches”. In: *Composites Part B: Engineering* 40.5 (2009), pp. 349–378. DOI: [10.1016/j.compositesb.2009.03.007](https://doi.org/10.1016/j.compositesb.2009.03.007).
- [113] Raissi, M., Perdikaris, P., and Karniadakis, G. E. “Physics-informed neural networks: A deep learning framework for solving forward and inverse problems involving nonlinear partial differential equations”. In: *Journal of Computational physics* 378 (2019), pp. 686–707. DOI: [10.1016/j.jcp.2018.10.045](https://doi.org/10.1016/j.jcp.2018.10.045).
- [114] Rao, J., Ratasapp, M., and Fan, Z. “Guided wave tomography based on full waveform inversion”. In: *IEEE transactions on ultrasonics, ferroelectrics, and frequency control* 63.5 (2016), pp. 737–745. DOI: [10.1109/TUFFC.2016.2536144](https://doi.org/10.1109/TUFFC.2016.2536144).

- [115] Robert, C. P. and Casella, G. *Monte Carlo Statistical Methods*. New York: Springer Science+Business Media, 1999.
- [116] Robinson, E. L. *Data analysis for scientists and engineers*. Princeton: Princeton University Press, 2016. ISBN: 9780691169927.
- [117] Robinson, L. “TMS Study Charts a Course to Successful ICME Implementation”. In: *JOM* 65.9 (2013), pp. 1087–1091. DOI: [10.1007/s11837-013-0722-0](https://doi.org/10.1007/s11837-013-0722-0).
- [118] Roncen, R., Fella, Z. E. A., and Ogam, E. “Bayesian inference of human bone sample properties using ultrasonic reflected signals”. In: *The Journal of the Acoustical Society of America* 148.6 (2020), pp. 3797–3808. DOI: [10.1121/10.0002878](https://doi.org/10.1121/10.0002878). eprint: <https://doi.org/10.1121/10.0002878>. URL: <https://doi.org/10.1121/10.0002878>.
- [119] Rudolf, D. and Ullrich, M. “Comparison of Hit-and-Run, Slice Sampler and Random Walk Metropolis”. In: *Journal of Applied Probability* 55 (2018), pp. 1186–1202. DOI: [10.1017/jpr.2018.78](https://doi.org/10.1017/jpr.2018.78).
- [120] Saint-André, L., Hervé, J.-C., and Leban, J.-M. “Modelling the number of rings in individual logs of Norway spruce”. In: *Scandinavian Journal of Forest Research* 15.1 (2000), pp. 135–143. DOI: [10.1080/02827580050160574](https://doi.org/10.1080/02827580050160574).
- [121] Säll, H. “Spiral grain in Norway spruce”. PhD thesis. Växjö University Press, 2002. ISBN: 91-7636-356-2.
- [122] Savitzky, A. and Golay, M. J. “Smoothing and differentiation of data by simplified least squares procedures.” In: *Analytical chemistry* 36.8 (1964), pp. 1627–1639. DOI: [10.1021/ac60214a047](https://doi.org/10.1021/ac60214a047).
- [123] Scerri, K. *MCMC Methods for data modeling*. Lecture notes. 2007. URL: https://www.sheffield.ac.uk/polopoly_fs/1.60510!/file/MCMC.pdf.
- [124] Schillings, C. and Schwab, C. “Sparse, adaptive Smolyak quadratures for Bayesian inverse problems”. In: *Inverse Problems* 29.6 (2013), p. 065011. DOI: [10.1088/0266-5611/29/6/065011](https://doi.org/10.1088/0266-5611/29/6/065011).
- [125] Schmitz, G. J. and Prahl, U. *Integrative Computational Materials Engineering: Concepts and Applications of a Modular Simulation Platform*. Wiley-VCH, 2012. ISBN: 978-352733081-2. DOI: [10.1002/9783527646098](https://doi.org/10.1002/9783527646098).
- [126] Schreier, P. J. and Scharf, L. L. “The Karhunen-Loève expansion of improper complex random signals with applications in detection”. In: *2003 IEEE International Conference on Acoustics, Speech, and Signal Processing, 2003. Proceedings. (ICASSP'03)*. Vol. 6. IEEE. 2003, pp. 717–720.
- [127] Schreier, P. J. and Scharf, L. L. *Statistical Signal Processing of Complex-Valued Data - The Theory of Improper and Noncircular Signals*. Cambridge university press, 2010.
- [128] Schreier, P. J. and Scharf, L. L. “Second-Order Analysis of Improper Complex Random Vectors and Processes”. In: *IEEE Transactions on Signal Processing* 51.3 (2003), pp. 714–725. DOI: [10.1109/TSP.2002.808085](https://doi.org/10.1109/TSP.2002.808085).
- [129] Seeger, M. W. and Wipf, D. P. “Variational Bayesian inference techniques”. In: *IEEE Signal Processing Magazine* 27.6 (2010), pp. 81–91. DOI: [10.1109/MSP.2010.938082](https://doi.org/10.1109/MSP.2010.938082).
- [130] Sepahvand, K., Marburg, S., and Hardtke, H.-J. “Uncertainty quantification in stochastic systems using polynomial chaos expansion”. In: *International Journal of Applied Mechanics* 2.2 (2010), pp. 305–353. DOI: [10.1142/S1758825110000524](https://doi.org/10.1142/S1758825110000524).

- [131] Setter, R., Hafenecker, J., Rothfelder, R., Kopp, S.-P., Roth, S., Schmidt, M., Merklein, M., and Wudy, K. “Innovative Process Strategies in Powder-Based Multi-Material Additive Manufacturing”. In: *Journal of Manufacturing and Materials Processing* 7.4 (2023), p. 133. DOI: [10.3390/jmmp7040133](https://doi.org/10.3390/jmmp7040133).
- [132] Simpson, T. W., Poplinski, J., Koch, P. N., and Allen, J. K. “Metamodels for computer-based engineering design: survey and recommendations”. In: *Engineering with computers* 17.2 (2001), pp. 129–150. DOI: [10.1007/PL00007198](https://doi.org/10.1007/PL00007198).
- [133] Siripatana, A., Le Maitre, O., Knio, O., Dawson, C., and Hoteit, I. “Bayesian inference of spatially varying Manning’sn coefficients in an idealized coastal ocean model using a generalized Karhunen-Loève expansion and polynomial chaos”. In: *Ocean Dynamics* 70 (2020), pp. 1103–1127. DOI: [10.1007/s10236-020-01382-4](https://doi.org/10.1007/s10236-020-01382-4).
- [134] Sisson, S. A., Fan, Y., and Tanaka, M. M. “Sequential Monte Carlo without likelihoods”. In: *Proceedings of the National Academy of Sciences* 104.6 (2007), pp. 1760–1765. DOI: [10.1073/pnas.0607208104](https://doi.org/10.1073/pnas.0607208104).
- [135] Sjödin, J., Enquist, B., and Serrano, E. “Contact-free measurements and numerical analyses of the strain distribution in the joint area of steel-to-timber dowel joints”. In: *Holz als Roh - und Werkstoff* 64.6 (2006), pp. 497–506. ISSN: 1436736X. DOI: [10.1007/s00107-006-0112-1](https://doi.org/10.1007/s00107-006-0112-1).
- [136] Socha, J. “A taper model for Norway spruce (*Picea abies* (L.) Karst.)” In: *Electronic Journal of Polish Agricultural Universities* 5.2 (2002), p. 3. ISSN: 1505-0297. URL: www.ejpau.media.pl/volume5/issue2/forestry/art-03.html.
- [137] Son, J. and Du, Y. “Comparison of intrusive and nonintrusive polynomial chaos expansion-based approaches for high dimensional parametric uncertainty quantification and propagation”. In: *Computers & Chemical Engineering* 134 (2020), p. 106685. DOI: [10.1016/j.compchemeng.2019.106685](https://doi.org/10.1016/j.compchemeng.2019.106685).
- [138] Sraj, I., Le Maître, O. P., Knio, O. M., and Hoteit, I. “Coordinate transformation and polynomial chaos for the Bayesian inference of a Gaussian process with parametrized prior covariance function”. In: *Computer Methods in Applied Mechanics and Engineering* 298 (2016), pp. 205–228. DOI: [10.1016/j.cma.2015.10.002](https://doi.org/10.1016/j.cma.2015.10.002).
- [139] Stoehr, J. and Friel, N. “Calibration of conditional composite likelihood for Bayesian inference on Gibbs random fields”. In: *Artificial Intelligence and Statistics*. PMLR. 2015, pp. 921–929.
- [140] Stuart, A. M. “Inverse problems: a Bayesian perspective”. In: *Acta numerica* 19 (2010), pp. 451–559.
- [141] Sullivan, T. J. *Introduction to uncertainty quantification*. Vol. 63. Cham: Springer, 2015.
- [142] Tagade, P. M. and Choi, H.-L. “A generalized polynomial chaos-based method for efficient Bayesian calibration of uncertain computational models”. In: *Inverse Problems in Science and Engineering* 22.4 (2014), pp. 602–624. DOI: [10.1080/17415977.2013.823411](https://doi.org/10.1080/17415977.2013.823411).
- [143] Tarantola, A. *Inverse problem theory and methods for model parameter estimation*. Philadelphia: SIAM, 2005.
- [144] Thornton, K., Qi, L., Uberuaga, B. P., and Van der Ven, A. “Recent advances and future needs in computational approaches for materials discovery and development”. In: *MRS Communications* 12.6 (2022), pp. 989–990. DOI: [10.1557/s43579-022-00289-z](https://doi.org/10.1557/s43579-022-00289-z).

- [145] Titsias, M. K., Lawrence, N. D., and Rattray, M. “Efficient Sampling for Gaussian Process Inference using Control Variables”. In: *Advances in neural information processing systems* 21 (2008), pp. 1681–1688. URL: <https://pdfs.semanticscholar.org/3713/dc6877d4fce0c6635fcf222f11751d7e0ccf.pdf>.
- [146] Uribe, F., Papaioannou, I., Betz, W., and Straub, D. “Bayesian inference of random fields represented with the Karhunen–Loève expansion”. In: *Computer Methods in Applied Mechanics and Engineering* 358 (2020), p. 112632.
- [147] Vessby, J., Serrano, E., and Enquist, B. “Contact-free measurement and numerical and analytical evaluation of the strain distribution in a wood-FRP lap-joint”. In: *Materials and Structures/Materiaux et Constructions* 43.8 (2010), pp. 1085–1095. ISSN: 13595997. DOI: [10.1617/s11527-009-9568-x](https://doi.org/10.1617/s11527-009-9568-x).
- [148] Vořechovský, M. “Simulation of simply cross correlated random fields by series expansion methods”. In: *Structural Safety* 30.4 (2008), pp. 337–363. ISSN: 0167-4730. DOI: <https://doi.org/10.1016/j.strusafe.2007.05.002>. URL: <https://www.sciencedirect.com/science/article/pii/S0167473007000422>.
- [149] Ward, C. “Materials genome initiative for global competitiveness”. In: *23rd Advanced Aerospace Materials and Processes (AeroMat) Conference and Exposition*. Vol. 202. OH: ASM International, June 2012.
- [150] Warensjö, M. “Compression wood in Scots pine and Norway spruce - Distribution in relation to external geometry and the impact on the dimensional stability in sawn wood”. PhD thesis. Swedish University of Agricultural Sciences, 2003. ISBN: 91-576-6532-X. URL: <http://res.slu.se/id/publ/11791>.
- [151] Watanabe, S. *Mathematical theory of Bayesian statistics*. Boca Raton: CRC Press, 2018.
- [152] Weisstein, E. W. *Cholesky decomposition*. Tech. rep. Last viewed 2020-07-18, 2020. URL: <https://mathworld.wolfram.com/CholeskyDecomposition.html>.
- [153] Wiener, N. “The homogeneous chaos”. In: *American Journal of Mathematics* 60.4 (1938), pp. 897–936. DOI: [10.2307/2371268](https://doi.org/10.2307/2371268).
- [154] Williams, C. K. and Rasmussen, C. E. *Gaussian processes for machine learning*. Vol. 2. 3. MIT press Cambridge, MA, 2006.
- [155] Xiang, N. and Fackler, C. “Objective Bayesian analysis in acoustics”. In: *Acoust. Today* 11.2 (2015), pp. 54–61.
- [156] Xiao, C., Sun, R., Adrien, J., Lachambre, J., Nadot, Y., Weck, A., and Buffière, J.-Y. “3D characterization of closure of surface and internal fatigue cracks in nodular cast iron using Digital Volume Correlation of laboratory X-ray tomography images”. In: *International Journal of Fatigue* 182 (2024). ISSN: 01421123. DOI: [10.1016/j.ijfatigue.2024.108226](https://doi.org/10.1016/j.ijfatigue.2024.108226).
- [157] Xiu, D. “Generalized (Wiener-Askey) Polynomial Chaos”. PhD thesis. Ann Arbor: Brown University, 2004.
- [158] Xiu, D. “Efficient collocational approach for parametric uncertainty analysis”. In: *Communications in computational physics* 2.2 (2007), pp. 293–309. URL: <https://api.semanticscholar.org/CorpusID:1227029>.
- [159] Xiu, D. *Numerical Methods for Stochastic Computations*. Princeton: Princeton University Press, 2010.
- [160] Xiu, D. and Karniadakis, G. E. “The Wiener–Askey polynomial chaos for stochastic differential equations”. In: *SIAM journal on scientific computing* 24.2 (2002), pp. 619–644. DOI: [10.1137/S1064827501387826](https://doi.org/10.1137/S1064827501387826).

- [161] Yan, W., Lin, S., Kafka, O. L., Lian, Y., Yu, C., Liu, Z., Yan, J., Wolff, S., Wu, H., Ndip-Agbor, E., et al. “Data-driven multi-scale multi-physics models to derive process–structure–property relationships for additive manufacturing”. In: *Computational Mechanics* 61.5 (2018), pp. 521–541. DOI: [10.1007/s00466-018-1539-z](https://doi.org/10.1007/s00466-018-1539-z).
- [162] Yang, K., Guha, N., Efendiev, Y., and Mallick, B. K. “Bayesian and variational Bayesian approaches for flows in heterogeneous random media”. In: *Journal of Computational Physics* 345 (2017), pp. 275–293.
- [163] Yildirim, I. *Bayesian Inference: Gibbs Sampling*. Lecture notes. 2012. URL: <http://www.mit.edu/~ilkery/papers/GibbsSampling.pdf>.
- [164] Yvonnet, J. *Computational homogenization of heterogeneous materials with finite elements*. Vol. 258. Solid Mechanics and Its Applications. Cham: Springer, 2019. DOI: [10.1007/978-3-030-18383-7](https://doi.org/10.1007/978-3-030-18383-7).
- [165] Zienkiewicz, O., Huang, M., and Pastor, M. “Localization problems in plasticity using finite elements with adaptive remeshing”. In: *International Journal for Numerical and Analytical Methods in Geomechanics* 19.2 (1995), pp. 127–148. ISSN: 03639061. DOI: [10.1002/nag.1610190205](https://doi.org/10.1002/nag.1610190205).
- [166] Zienkiewicz, O. C., Taylor, R. L., and Zhu, J. Z. *The finite element method: its basis and fundamentals*. 6th ed. Oxford: Elsevier, 2005. ISBN: 0750663200.

Appendix I

Parameter Studies on the Effect of Measurement Noise, Prior Cross-Correlation, and the Number of Observation Points Concerning Multivariate Identification Problems

Measurement Noise and Reconstruction Cross-Correlation Parameter Study Several configurations serve to investigate the effect of incorporating knowledge about the cross-correlation of the underlying random fields into their inference. Specifically, consider a range of synthetic measurement noise standard deviations γ and a range of cross-correlation coefficients ρ_{rec} . The error obtained by setting ρ_{rec} to the respective sweep value is denoted as $e_{\rho_{\text{rec}}}$. The method must be compared against the standard procedure to judge its efficacy. To this aim, the base-case reconstruction method is set up such that each of the unknown functions obtains its own Gaussian random field prior that is independent of the other. Setting $\rho_{\text{rec}} = 0$ achieves this. The error obtained by this benchmark procedure reads as $e_{\rho=0}$. Figure I.1 shows the parameter study results that are based on 29 random samples for the ground truth.

Parameter Study of the Number of Observation Points A second parameter study looks into the number of observation points n_{obs} .¹ This is done by performing a random choice of n_{obs} observation points out of the 50 available nodes. In this context, the values $\{0.01, 0.1, 0.2, 0.3, 0.4, 0.5, 0.6, 0.7, 0.8, 0.9, 1\}$ (-) represent the measurement noise standard deviation γ . The unit-less set $\{0.375, 0.5, 0.625, 0.75, 0.875, 0.925\}$ is used for the square root of ρ_{rec} within the reconstruction. Figure I.2 shows the corresponding results for 11 realizations of the random fields. Note that these results are reported in an average sense over the range of γ and ρ_{rec} .

Insights Surprisingly, including prior knowledge on the cross-correlation of two a priori unknown functions is not uniformly beneficial here. Conversely, accounting for cross-correlation only outperforms the independent model for a certain combination of the reconstruction cross-correlation coefficient, measurement noise, and observation scarcity characteristics. The results for a ground truth correlation of $\rho = 0.9$ demonstrate an advantage of prescribing cross-correlation in the prior when both the synthesized measurement noise standard deviation γ and the cross-correlation coefficient within the reconstruction ρ_{rec} are comparatively high, see Figure I.1. This result can be explained by a flexibility trade-off. Setting ρ_{rec} to a high value inhibits the flexibility of the model. The restriction by essentially coupling the two quantities of interest leads to comparatively worse performance as the exploration

¹The author would like to thank Dr. Jonas Latz and Dr.-Ing. Iason Papaioannou for their encouragement and several fruitful discussions that led to these results.

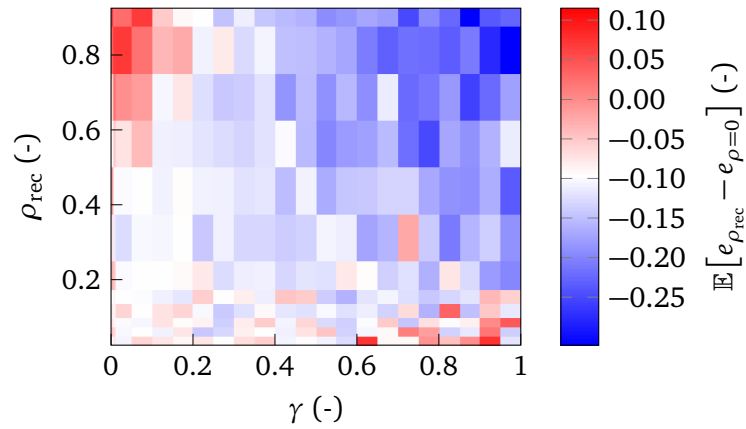


Figure I.1: Comparison of inference of two random fields simply cross-correlated with $\rho = 0.9$ using independent representations and using a representation with prescribed cross-correlation. The respective errors are averaged over 29 ground truth realizations of both fields. Using prior knowledge on the cross-correlation improves the results in the blue regions.

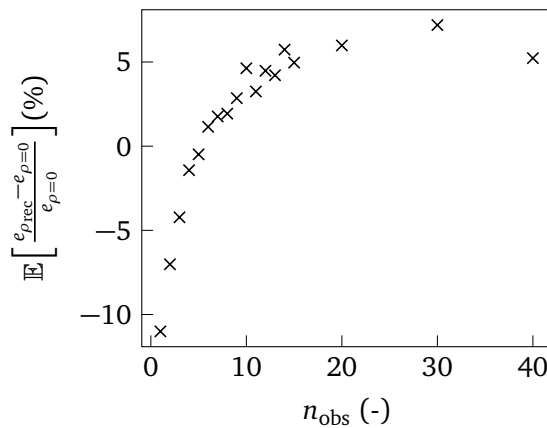
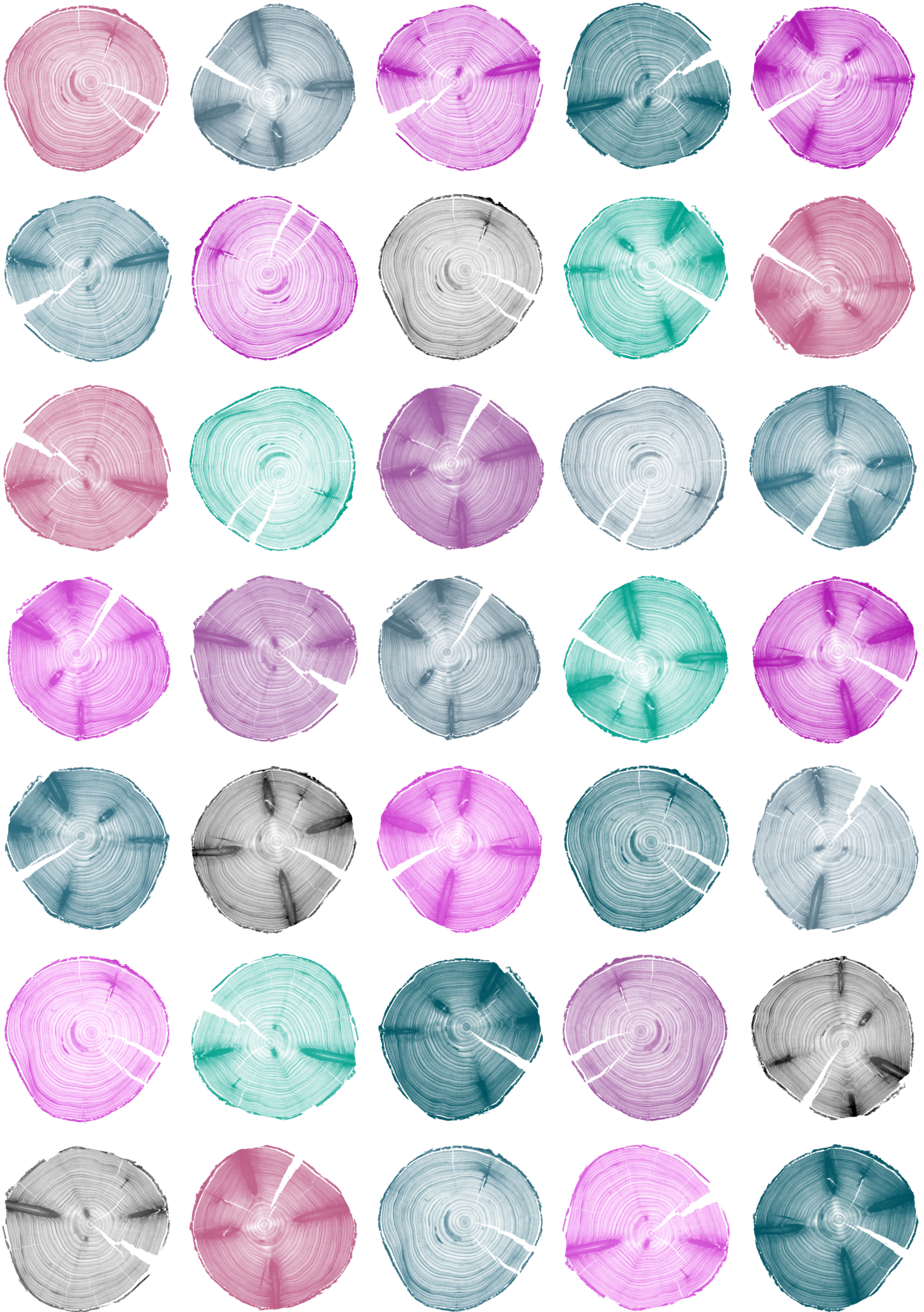


Figure I.2: The figure shows the comparison of the inference of two random fields simply cross-correlated with $\rho = 0.9$ using independent representations and using a representation with prescribed cross-correlation. The influence of the number of observation points n_{obs} is investigated. The inference is carried out for 11 realizations of the fields for each combination of measurement noise and inference cross-correlation kernel. Negative values for $\mathbb{E}\left[\frac{e_{\rho_{rec}} - e_{\rho=0}}{e_{\rho=0}}\right]$ suggest that making use of the cross-correlation offers an advantage.

algorithm needs to traverse a more constricted posterior solution space. However, the information about the correlation benefits the inference for noisy observations; see Figure I.1. Obviously, a mismatch between ρ_{rec} and the true ρ diminishes this advantage. The results on the number of observation points n_{obs} from Figure I.2 suggest that when a random choice of up to 5 of the nodes is observable, leveraging ρ_{prior} benefits the procedure. However, when a random choice of more than 5 of the 50 nodes is available, the independent model performs better. Analogously to the effect of excessive measurement noise masking the information, the information on the correlation is useful as soon as the information content within the data drops below a certain threshold.



Appendix II

Paper A

Evaluation of inversion approaches for plates based on guided waves and modal analysis

Karl-Alexander Hoppe^{*}, Simon Schmid, Jochen Kollofrath, Steffen Marburg, and Christian U. Grosse

This publication is reprinted in accordance with its open access license [CC BY 4.0](#).

^{*}orcid.org/0000-0002-3048-8284

Research

Evaluation of inversion approaches for plates based on guided waves and modal analysisKarl-Alexander Hoppe¹ · Simon Schmid² · Jochen Kollofrath² · Steffen Marburg¹ · Christian U. Grosse²

Received: 27 November 2023 / Accepted: 24 April 2024

Published online: 09 May 2024

© The Author(s) 2024 **OPEN****Abstract**

The identification of defects in plate-like structures has been successfully treated using both local guided ultrasonic waves and global modal quantities. Although there are many papers on these techniques, a lack of comparability between the two methods persists. This makes it difficult for users to identify the most appropriate method for the defect in question. This paper examines the effect of different parameterizations of a circular defect in a square aluminum plate on the system response in a case study. The measured local ultrasound signal from a propagating guided wave makes up the initial data set. The first method uses the entire waveform for the objective function of the optimization problem, while the second considers the velocity of the A_0 mode. In the third and fourth methods, the first and second global natural frequencies of the plate modeled with free-free boundary conditions are investigated. The numerical models are validated experimentally through measurements with a laser Doppler vibrometer. This results in the qualitative and quantitative evaluation of the objective functions for all parameter combinations of the defect. The recommendation to sequentially employ modal analysis and then the ultrasound procedure is made for the defect type used in this study. The data gathered on the objective functions suggests that potential joint employment of the natural frequency and ultrasound methods may increase computational efficiency. For a specific case, the methods could also complement each other in terms of challenges such as local minima.

Highlights

- Comparison of defect detection methods for plate-like structures using guided waves and global structural modes.
- Identification of advantages and limitations from the objective function values related to defect size and position.
- Modal data provides ambiguous but smooth estimates of defect properties; ultrasound yields narrowly localized minima.

Keywords Guided waves · Ultrasound · Lamb waves · Modal analysis · Optimization · Defect detection

✉ Karl-Alexander Hoppe, alexander.hoppe@tum.de; Simon Schmid, sim.schmid@tum.de | ¹Technical University of Munich, TUM School of Engineering and Design, Department of Engineering Physics and Computation, Chair of Vibroacoustics of Vehicles and Machines, Boltzmannstr. 15, 85748 Garching bei München, Bavaria, Germany. ²Technical University of Munich, TUM School of Engineering and Design, Department of Materials Engineering, Chair of Non-destructive Testing, Franz-Langinger-Str. 10, 81245 Munich, Bavaria, Germany.



1 Introduction

Determining the position and size of defects by imaging constitutes one of the challenges in non-destructive testing (NDT) and structural health monitoring (SHM) [1]. Corrosion presents a common defect type that leads to a local change in the wall thickness of metal pipes and pressure vessels. Conventionally, the remaining wall thickness is determined with time-of-flight measurements of ultrasonic bulk waves. Since this is time-consuming and the structure is not always fully accessible, there is a need for more efficient approaches, see [2]. Guided waves, especially Lamb waves, are efficient approaches to both structural health monitoring [3] and non-destructive testing [4]. With guided wave tomography, the dispersion characteristics of the ultrasonic waves are utilized in order to reconstruct defects such as the change in wall thickness or delaminations in composite structures [5, 6]. Different approaches for guided wave tomography exist in the literature. They use the travel time [1] or diffraction [7] of the ultrasonic wave. Also, a hybrid approach of the previous two, called the Hybrid Algorithm for Robust Breast Ultrasound Tomography (HARBUT), exists [8]. He et al. [9] make use of the full waveform with reverse time migration. Further, the full waveform inversion (FWI) method is utilized for guided wave tomography [10]. This method is intended for imaging problems in seismic applications in geophysics. With this method, an objective function is calculated based on the whole captured signal. With this objective function, an optimization problem is solved by updating the material model [10]. In order to map the calculated velocity image to the plate thickness, dispersion thickness mapping is used for all the previously introduced methods [8].

Another method for defect detection consists of using modal parameters like eigenfrequencies. This technique is applied successfully to characterize cracks in slender structures [11]. But changes in the resonance frequencies are also linked to the thickness change in plates [12]. If the mode shapes are available as data, they offer a precise identification of the elastic material of structures such as plates [13]. In [14], strain mode shapes are used to calculate the sensitivity indices of defects in plates. When using more than one mode shape, the locations of the defects are accurately identified. In [15], defects are detected with modal analysis. A rectangular area at a fixed position with a reduced thickness serves as a defect. They investigate the relationship between the mass change through the defect and the eigenfrequencies. The authors assume that corrosion could be detected through the deduced relation. Modal analysis plays an important role in structural health monitoring. Le et al. [16] employ the modal strain energy method based on modal data to identify damage to an aluminum plate and identify mode numbers relevant to the inverse problem. Hou et al. [17] locally add mass to their structure to gain insight into the local resonance frequencies for health monitoring purposes of a truss. Park et al. [18] accomplish health monitoring of bridges experimentally by fusing local and global acceleration data. Sun et al. [19] consider the numerically obtained natural frequencies and modes of a planar structure and a truss in a Bayesian damage detection scheme. Frequency response functions are suitable for identifying the piece-wise heterogeneous Young's modulus of composite structures [20, 21]. This procedure is extended to account for continuously heterogeneous materials, which may be regarded as a generalized defect in [22].

Reviewing the literature reveals that only limited efforts have been made so far to set ultrasonic and modal approaches in relation to each other. Mengelkamp and Fritzen [23] classify plates into damaged and non-damaged using a global vibration-based method and conditionally localize the damage with ultrasonic guided waves. The considered damage categories are cracks and delaminations. Fritzen and Mengelkamp [24] perform a similar study on artificial cracks in stiffened plates. Wang and Hao [25] employ guided wave and structural vibration tests of steel beams experimentally and numerically. They find that a shared objective function is not expedient and recommend a procedure consisting of two steps, one for each testing method. Claiming to bridge between modal analysis and guided waves, Yan and Rose [26] develop a damage identification method based on operating deflection shape analysis of the steady-state response to ultrasonic excitation of an aluminum plate in the kHz order of magnitude. Ahmed et al. [27] propose the usage of a guided wave method within a global method considering structural vibrations. They study its application to identify defects in a composite wing structure using regression models.

To the authors' knowledge, methods based on guided waves and modal parameters for defect detection in plate-like structures have not yet been compared in the context of optimization problems. Furthermore, the current methods for guided wave tomography are based on the reconstruction of a velocity image and use a dispersion thickness mapping in order to calculate the plate thickness. This study introduces a method that directly changes the topography of the mesh. We focus on the advantages and restrictions of the four methods and investigate the objective function values over the defect parameters range. The results are based on simulations, while our measurements

Fig. 1 Schematic display of the antisymmetric A_0 and symmetric S_0 Lamb wave modes

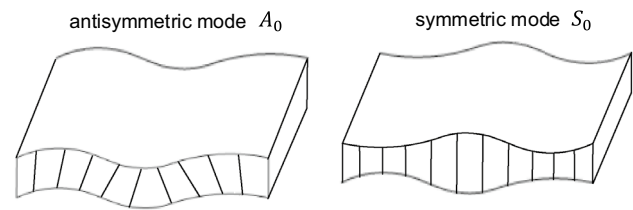
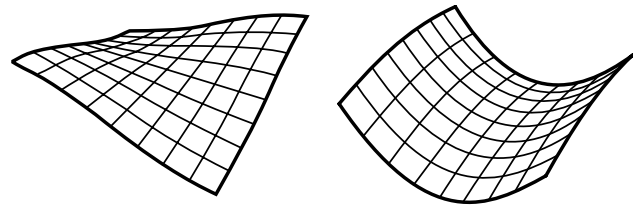


Fig. 2 A schematic of the first vibrational mode shape of the square plate is shown on the left, while the second mode shape is sketched on the right



serve to calibrate the simulation models. The subsequent application of an optimization algorithm should be pursued in future research. Our conclusions apply to the case study and any generalizations to other simulation setups or experimental ones with real transducers shall be conducted with care.

This paper is organized as follows: Sect. 2 covers the propagation of ultrasonic waves in plates and the latter's modal analysis. Section 3 details the simulation models and their calibration using measurements. Section 4 presents the objective functions for all methods and a strategic variation of the defect parameters. Finally, we draw some conclusions in Sect. 5.

2 Theoretical background

This section introduces the relevant basics of guided ultrasonic waves (Sect. 2.1) and modal parameters (Sect. 2.2).

2.1 Propagation of ultrasonic waves in plates

Lamb waves are guided waves propagating between two parallel boundaries [28]. They solely exhibit displacements along the propagation direction and the direction perpendicular to the plate. Waves featuring displacements in the remaining direction are referred to as shear-horizontal. In this study, only Lamb waves, where displacement is measured perpendicular to the propagation direction, are observed. For that reason, only Lamb waves will be further explained in this subsection. Lamb waves occur when longitudinal (p-) and transversal (s-) waves superimpose. Based on the boundary position (e.g. thickness of the plate) and the frequency of the ultrasonic wave, several characteristic modes occur [29]. The modes are distinguished as symmetric S_i and antisymmetric A_i modes [30]. Figure 1 displays the A_0 and S_0 modes schematically. Lamb waves are dispersive waves and therefore, their velocity varies with the frequency. With the assumption of slowly varying plate thickness, the velocities change either with the frequency or the plate thickness. This can be seen in so-called dispersion curves, which can be obtained with the open-source software 'Dispersion Calculator' [31], as also used in [32].

2.2 Modal parameters of plates

Within structural dynamics, the finite element method serves to predict a structure's vibration behavior in response to dynamic excitation. This method becomes increasingly expensive in terms of computational cost for higher frequencies, as a minimum number of elements per wavelength is necessary for accurate results [33]. The vibrational response across the frequency spectrum may be expressed as a superposition of the structure's modes connected to the respective natural frequencies [34]. Consider the eigenvalue problem resulting from the finite element method as described in the literature [35]. The eigenfrequencies and eigenvectors are the solutions to this eigenvalue problem. Figure 2 shows the mode shape connected to the first natural frequency f_1 of a square plate with free-free boundary conditions on the left and the second mode shape on the right.

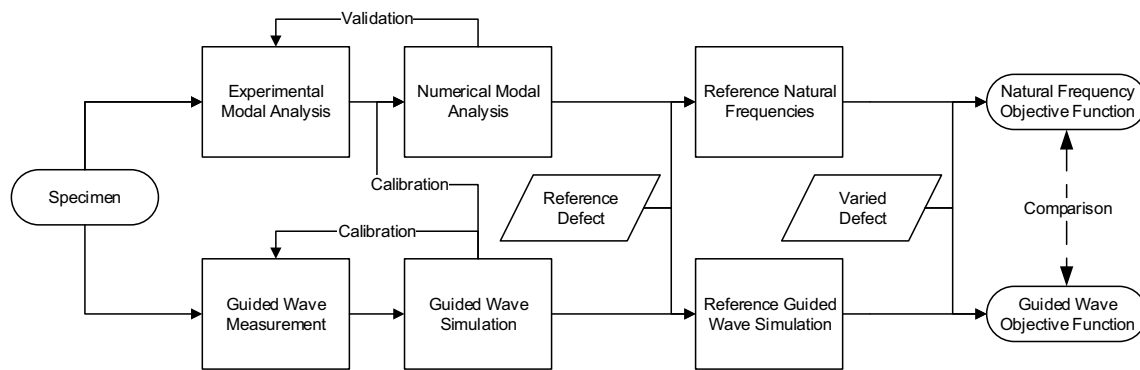


Fig. 3 A diagram encompassing the entire methodical procedure, whose components are described by the following subsections

Table 1 Material parameters of the aluminum plate

E	67.9 GPa
ρ	2,675 kg m ⁻³
ν	0.277
v_s	3,155 m s ⁻¹
v_p	5,682 m s ⁻¹

3 Experimental setup and numerical model

This section introduces the investigated specimens with artificial defects (Sect. 3.1). Additionally, the experimental and simulation setups for the measurement of the modal parameters and the guided waves are introduced (Sects. 3.2 and 3.3). Next, the procedures for evaluating the response of guided waves and modal features after changes in the defect parameters are explained in Sect. 3.4. Refer to Fig. 3 for a visual representation of the entire scope of this study.

3.1 Specimens with artificial defects

This study investigates an aluminum plate made of the AlMg3 alloy. The plate is square with a side length of 40 cm and a thickness of 1 cm. The density ρ is calculated by weighing the specimen and measuring its dimensions. Furthermore, the time-of-flight for the p- and s-waves is measured using the OmniScan MX2 ultrasonic device from the company Olympus (Evident) with a 2.25 MHz p-wave transducer (V104-RM) and a 5 MHz s-wave transducer (V157-RM) in a pulse-echo configuration. With the time-of-flight and the measured plate thickness, the longitudinal v_p and transversal v_s ultrasonic wave speeds are calculated. Young’s modulus E and Poisson’s ratio ν are derived from v_p , v_s , and ρ . The measured and derived material parameters of the plate are given in Table 1.

Using dispersion curves with the material parameters of AlMg3, it can be shown that around 70 kHz, the center frequency of the chosen transducer, the A_0 mode shows large changes in the velocity and is therefore sensitive towards plate thickness changes, see Fig. 4.

This study considers the influence of a defect on the ultrasound signals and modal parameters of the plate. A simple shape makes up the defect, which is described by the four parameters maximum depth D , diameter W , and the position of its center x_d and y_d . This is displayed in Figs. 5 and 6.

The defect depth profile, which is Hann-shaped, is calculated as

$$T(r) = \begin{cases} T_0 - \frac{D}{2} \left[1 + \cos\left(\frac{2\pi r}{W}\right) \right] & r < \frac{W}{2} \\ T_0 & r \geq \frac{W}{2} \end{cases} \quad (1)$$

Here, T_0 represents the nominal plate thickness and r is the radial coordinate centered at the defect. This function generates a smoothly varying shape. The defect shape is adopted from [29].

Fig. 4 Dispersion curves of the phase and group velocities for the $40 \times 40 \times 1$ cm plate using the aluminum material parameters given in Table 1

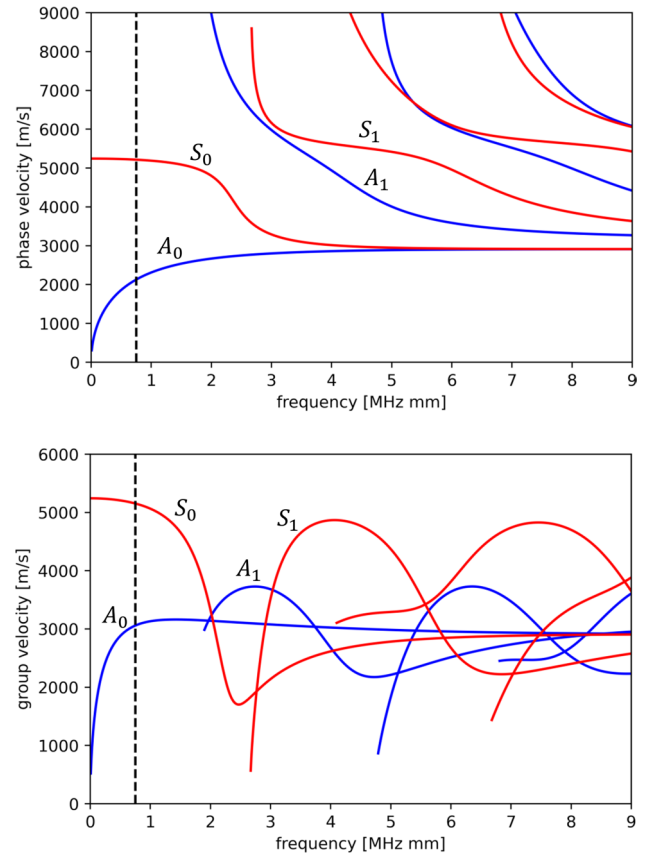


Fig. 5 Plate with defect, where W is the defect diameter at the surface and x_d and y_d mark the position of the circular defect's center

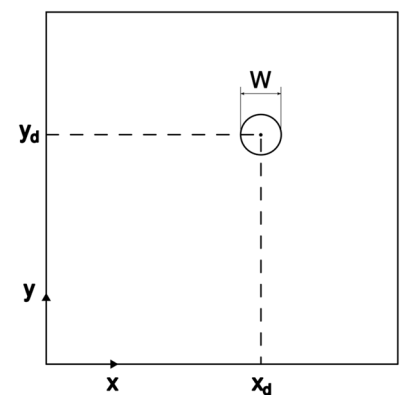
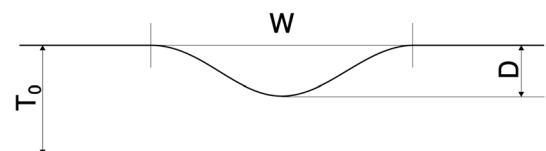


Fig. 6 Plate with defect, where W is the diameter, D represents the maximum depth, and T_0 is the plate thickness



3.2 Measurement setup for guided waves and calibration of the numerical model

To calibrate the guided wave simulations, measurements are conducted with a laser Doppler vibrometer (LDV) with an OFV-505 sensor head and the OFV-5000 controller manufactured by Polytec. The velocity decoder VD-O9 is used. The LDV is mounted on a robot (UR5 by Universal Robots) and pointed orthogonally at the surface of the plate. Therefore, the local particle velocity of the out-of-plane components of the Lamb wave modes is measured. A sine

signal with four bursts at 70 kHz (see Fig. 7) excites the shear wave transducer V151 by Panametrics. A TiePie HS5 generates the waveform. In order to capture the propagation of the Lamb wave in the x - and y -direction relative to the transducer position, several locations for the measurement points are investigated, see Fig. 7. Five measurement positions are staggered in the y -direction with 3 cm increments starting from the transducer. Three further measurement points are staggered in the x -direction using 3 cm increments. The latter corresponds to the horizontal line of measurement points in Fig. 7.

The simulation is conducted with the software Salvus by Mondaic AG [36]. Salvus is based on the spectral element method and is capable of conducting waveform simulations on the GPU. It furthermore offers a meshing routine for changing the topography of the mesh. In our study, a structured mesh is deformed in order to introduce the defect. The excitation wavelet used for the simulation is extracted from a measurement close to the transducer. The transducer is modeled as a point source with forces in the x -, y -, and z -direction. The magnitude of each force is calibrated by an optimization scheme using the Simplex algorithm. As an objective function, the least-square norm \mathcal{L} of the difference between the measured and the simulated signal's waveform is chosen (see Eq. 4). After the optimization of the three forces, a 3.2 times higher force in the x -direction than in the y -direction is identified. Here, the y -direction represents the direction of the polarization of the transducer. The remaining force in the x -direction could be explained by manufacturing inaccuracies of the transducer. With this procedure, the force in the z -direction converges to 0.

We further simulate a B-scan of two 2 m long measurement lines in the x - and y -directions to discern, which wave modes are present in the measured signal. Absorbing boundary conditions are applied to the sides of the plate. The resulting B-scans are given in Fig. 8. The negative slope of the phase fronts relating to the A_0 mode in Fig. 8 may be explained by the comparatively coarse spatial discretization chosen for this simulation. It can be seen that two distinct wave modes are present. By fitting a line through each respective wave mode, the velocities are determined as 3125.0 m s^{-1} and 5115.0 m s^{-1} . The velocities of the A_0 and S_0 modes are 3049.3 m s^{-1} and 5159.2 m s^{-1} based on the analytically determined values (see Fig. 4) and for the center frequency of the wavelet (see Fig. 7). It can be concluded that these modes are the A_0 and S_0 modes since no further modes are present. The A_0 mode is dominant within the signals compared with the S_0 mode, because the A_0 mode exhibits stronger out-of-plane components in comparison with S_0 . The modes are fully separated after 30 cm. A major contribution to the superimposed waveform stems from the A_0 mode, whose amplitude is approximately 6 times larger than that of the S_0 mode.

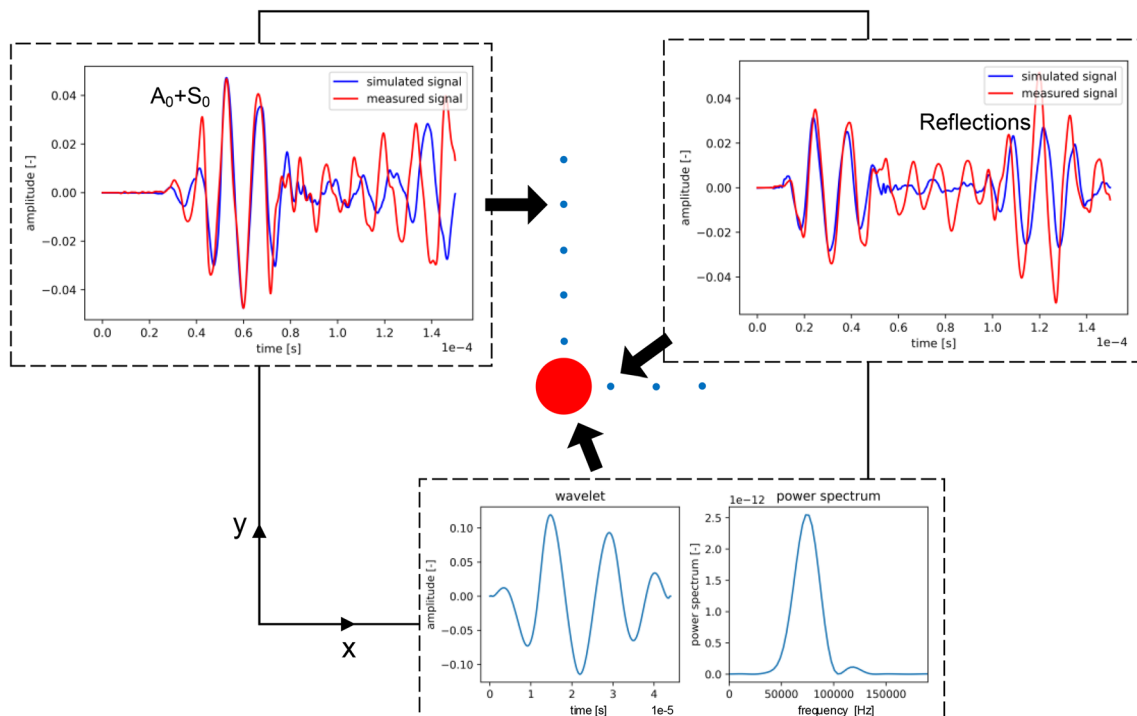
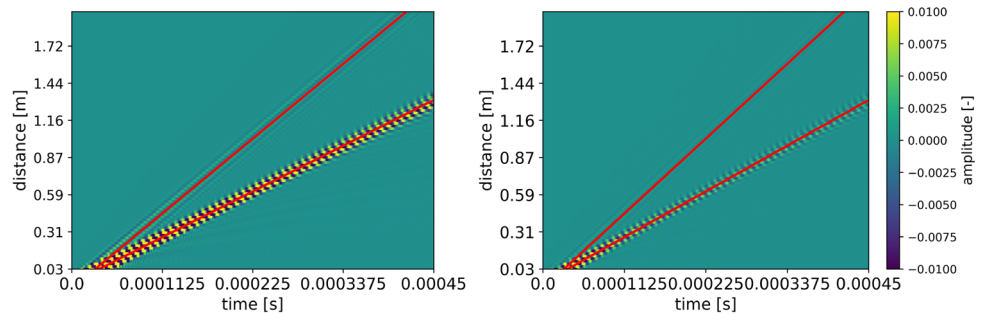


Fig. 7 Experimental setup for calibrating the waveform simulation: the red circle denotes the signal source, while the blue points indicate receiver locations used in the calibration process. For two selected receiver positions, the simulated and corresponding measured signals are shown. Additionally, the excitation waveform or wavelet is provided at the bottom

Fig. 8 A B-scan related to measurement lines in the x - and y -direction is shown on the left and right, respectively. Absorbing boundary conditions are applied to the plate's sides to eliminate side wall reflections. The color bar is clipped to make the S_0 mode visible



For the subsequent simulations, a denser receiver alignment is applied, leading to a total of 421 receivers. This is displayed in Fig. 9.

3.3 Measurement setup for modal parameters and calibration of the numerical model

Within the experimental modal analysis setup, the plate is suspended on two strings at intervals of thirds aligned in parallel to the plate edges, see Fig. 10. The plate is excited by the SAM Scalable Automatic Modal Hammer at the upper left corner.

Fig. 9 Receiver and source positions on the plate used for evaluation of the objective function for the waveform simulation. The red circle represents the source, and the blue points denote the receiver positions on the plate

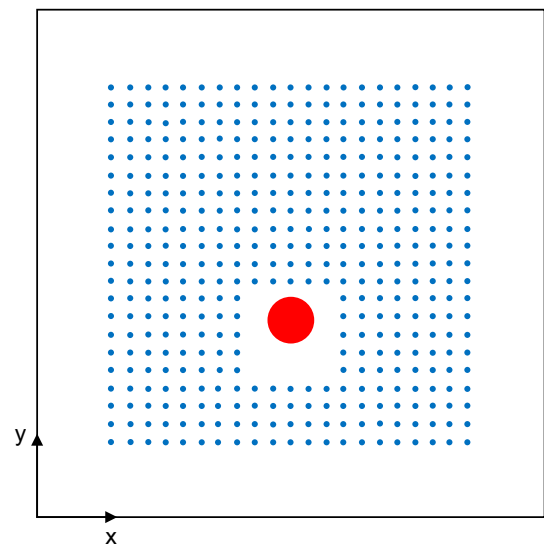
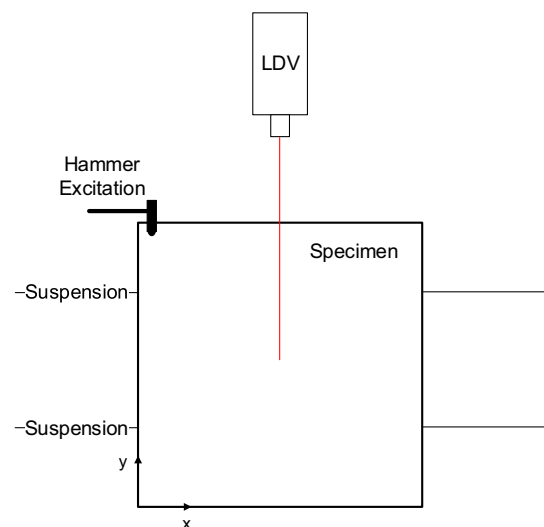


Fig. 10 A depiction of the experimental modal analysis measurement setup. The specimen is suspended by two strings, excited by a modal hammer, and the response is captured by an LDV aligned orthogonally to the surface of the plate



Using a Polytec LDV with a PSV-I-500 scanning head and a PSV-500-3D-H frontend, the structure’s velocities in z-direction at the top surface are captured on a regular 15 × 15 grid. The modal analysis is carried out based on these velocity data using MEscope for frequencies up to 1,100 Hz. This analysis results in the first natural frequency as 209 Hz.

The considered plate is modeled with the finite element method in COMSOL as a linear three-dimensional volume model with free-free boundary conditions. Quadratic serendipity polynomials serve as the shape functions for the weak form. The geometry is meshed with 1,096 tetrahedral elements yielding 15,405 degrees of freedom for the numerical modal analysis. The maximum element edge length of 2 cm results in at least 10 quadratic elements per wavelength when the first mode shape is considered.

This numerical model’s agreement with the measurements is evaluated based on the error ϵ defined in Eq. (2) with respect to the first natural frequency.

$$\epsilon = \frac{|f_{\text{num}} - f_{\text{exp}}|}{f_{\text{exp}}} \times 100\% \tag{2}$$

The density, Young’s modulus, and Poisson’s ratio for the numerical model are set in accordance with the experimentally determined values given in Table 1. Using these material parameters leads to an error of $\epsilon < 2\%$ in terms of the first natural frequency with respect to the experiment. This parameterization of the simulation model results in a consistent arrangement of the mode shapes in the considered frequency range between the experiment and simulation. The described frequency shift is readily explained by the non-perfect approximation of the ideal boundary conditions by the support chosen for the experimental setup. This is a well-known challenge in the literature; see, for instance, [37].

3.4 Change in guided wave and modal features after defect parameter variation

In this study, the simulation models for the modal and Lamb wave parameters are evaluated as a function of the defect parameters. To achieve this, the four parameters of the defect x_d , y_d , W , and D are varied. For this, two of the four parameters are varied in 51 steps in a full-factorial manner, while the remaining two are kept constant. This is done for all six parameter combinations. The range of the defect parameters’ values is given implicitly using the minimal and maximal values in Table 2.

The changes in the system response are investigated with respect to a reference parameterization considered as

$$\mathbf{m}_{\text{ref}} = \begin{Bmatrix} x_{d,\text{ref}} \\ y_{d,\text{ref}} \\ W_{\text{ref}} \\ D_{\text{ref}} \end{Bmatrix}. \tag{3}$$

We formulate the objective function \mathcal{L} in terms of the defect parameter vector \mathbf{m} and the system response vector \mathbf{q} as

$$\mathcal{L}(\mathbf{m}) = \|\mathbf{q} - \mathbf{q}_{\text{ref}}\|_2. \tag{4}$$

Here, the response \mathbf{q}_{ref} corresponds to the defect parameterization $\mathbf{m} = \mathbf{m}_{\text{ref}}$. Now, the optimization procedure aims to solve

$$\mathbf{m} = \arg \min \mathcal{L}(\mathbf{m}). \tag{5}$$

For the Lamb waves, changes in the full waveform and the A_0 group velocity ($\mathcal{L}(\mathbf{m}) = \|v_{A_0} - v_{A_0,\text{ref}}\|_2$) are investigated.

The group velocity is determined by truncating the signal around the expected arrival time of the A_0 mode and by picking the maximum of the Hilbert envelope [38] of the signal, where the A_0 mode makes up the strongest contribution. This method is referred to as the group velocity method within the remainder of the text. In order to get the velocity,

Table 2 Defect parameter ranges including reference configuration

Parameter	Minimum (cm)	Reference (cm) \boxtimes_{ref}	Maximum (cm)
x_d	5	$x_{d,\text{ref}} = 20$	35
y_d	5	$y_{d,\text{ref}} = 20$	35
W	1	$W_{\text{ref}} = 4.5$	9
D	0.1	$D_{\text{ref}} = 0.45$	0.9

the determined time point is divided by the distance from the source to the receiver. Further, the Hilbert envelope was smoothed using a Savitzky–Golay filter [39], which does not shift the position of the maximum. The smoothed Hilbert envelope of a signal can be seen in Fig. 11.

For the modal parameters, the first and second eigenfrequencies f_1 and f_2 are investigated individually. Here, \mathbf{q}_{ref} is set to $f_{1,\text{ref}}$ and $f_{2,\text{ref}}$, respectively.

4 Results and discussion

This section presents the objective function values obtained from the four methods. The objective functions are shown for the six unique pairings of the defect parameters (see Table 2). They are first evaluated separately for the guided wave-based approaches on the one hand, and the natural frequency-based approach on the other hand (Sect. 4.1), and subsequently compared (Sect. 4.2). Note that the results presented in this section stem from computer simulations, and the measurements described in Sect. 3 serve as the initial calibration of the simulation models.

4.1 Evaluation of the objective functions

The objective function results are grouped for pairs of defect parameters. Figure 12 shows the results as a function of the spatial defect coordinates x_d and y_d , and Fig. 13 shows the same results for an off-center reference defect position at $x = 10.49$ cm and $y = 11.86$ cm. Figure 14 depicts the results over varying defect dimensions D and W . The joint effects of x_d with D and x_d with W are displayed by Fig. 15 and Fig. 16, respectively. Figure 17 shows the objective function $\tilde{\mathcal{L}}$ as a function of y_d and D , and finally, Fig. 18 shows it as a function of y_d and W . Each figure contains four graphs, where the top left corresponds to the FWI results and the top right visualizes $\tilde{\mathcal{L}}$ using the group velocity of the A_0 mode. The bottom left and right graphs are connected to the first and second natural frequencies, respectively. The objective functions are normalized to the interval $[0, 1]$ as $\tilde{\mathcal{L}}$. This normalization makes the objective function evaluations qualitatively comparable in terms of measurement noise and error amplitude. Here, an error norm value of 0 indicates no deviation in the data observed from the reference configuration on the one hand and the modified configuration on the other hand. Following Eq. (4), a value of 1 indicates the maximum corresponding deviation.

4.1.1 Guided waves

For the normalized objective function $\tilde{\mathcal{L}}$ surfaces and the variation of the x - and y -position, the full waveform and the group velocity surfaces (Fig. 12 top left and right) show a maximum at the source position. The non-symmetry can be accounted for by using forces in the x - and y -direction for the source. The high objective function values close to the source can be explained on the one hand by the high ultrasound amplitudes in that region. Around the source, the FWI objective function shows rings, which can be explained by the so-called cycle-skipping. The reason for this is that the least squares objective function $\tilde{\mathcal{L}}$ only has a narrow parameter range where it is locally convex with respect to phase shifts in the signal [40]. Other error measures, such as cross-correlation, can mitigate this problem. The FWI $\tilde{\mathcal{L}}$ shows a non-smooth surface with local minima. For this reason, it is not suited for gradient-based optimization

Fig. 11 Procedure for the group velocity method via determining the group velocity of the A_0 mode by picking the time point at the maximum of the Hilbert envelope

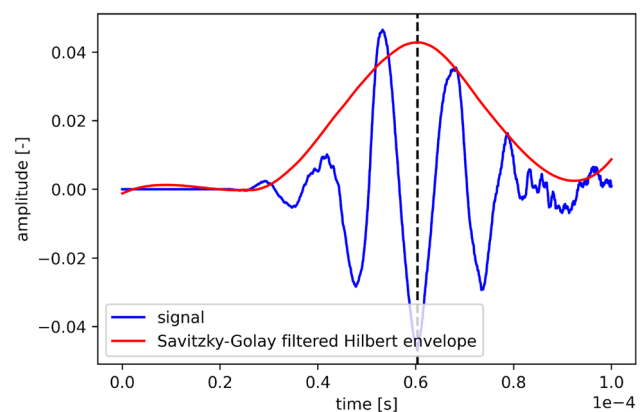


Fig. 12 $\tilde{\mathcal{L}}$ resulting from the reference defect parameters and a variation of its x- and y-position

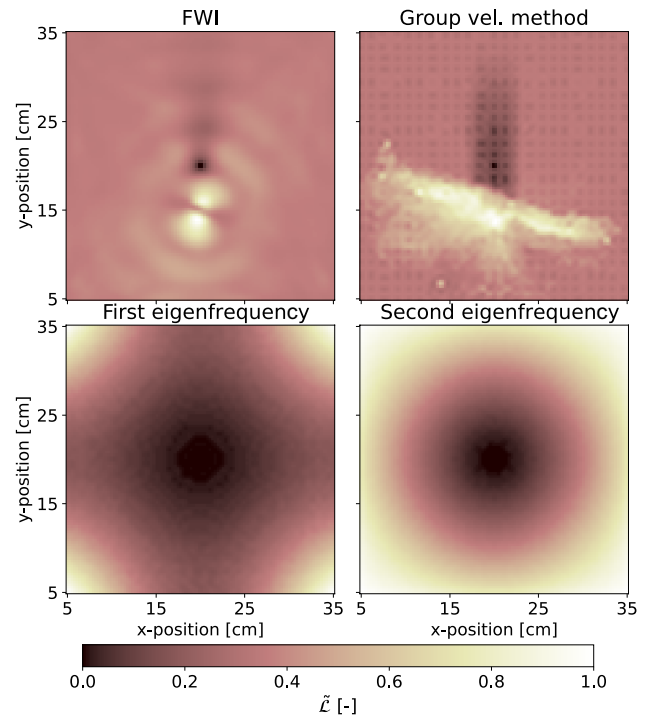
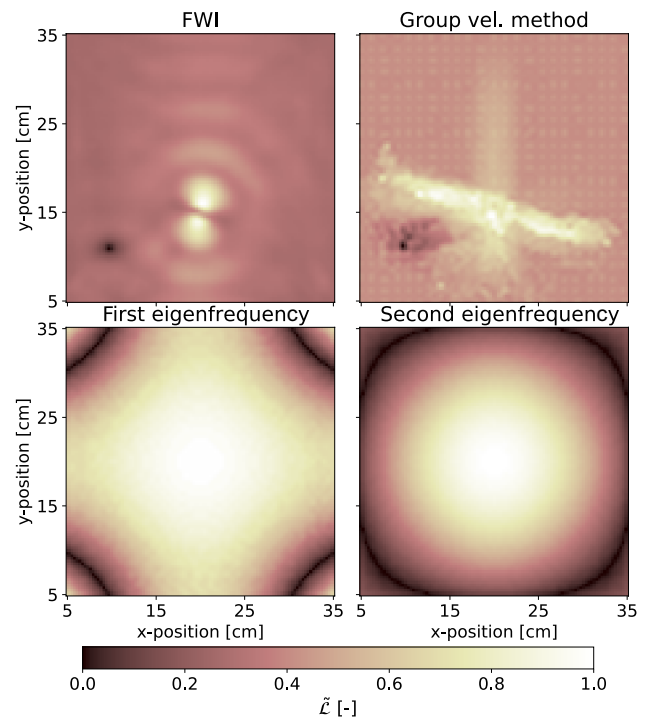


Fig. 13 $\tilde{\mathcal{L}}$ resulting from the reference defect parameters at $x = 10.49$ cm and $y = 11.86$ cm and a variation of its x- and y-position



algorithms or demands that the starting value be close to the true value. The objective function resulting from the A_0 mode shows a large cloud of local minima around the true defect position. With some smoothing within post-processing, this may yield a less steep global minimum. Further, the maximum at the source position is more pronounced in comparison to the FWI error, and at each receiver location, lower errors are reached. These effects around the source remain for the altered reference defect position, see Fig. 13. However, while the minimum connected to

Fig. 14 The figure shows \tilde{L} for a variation of D and W

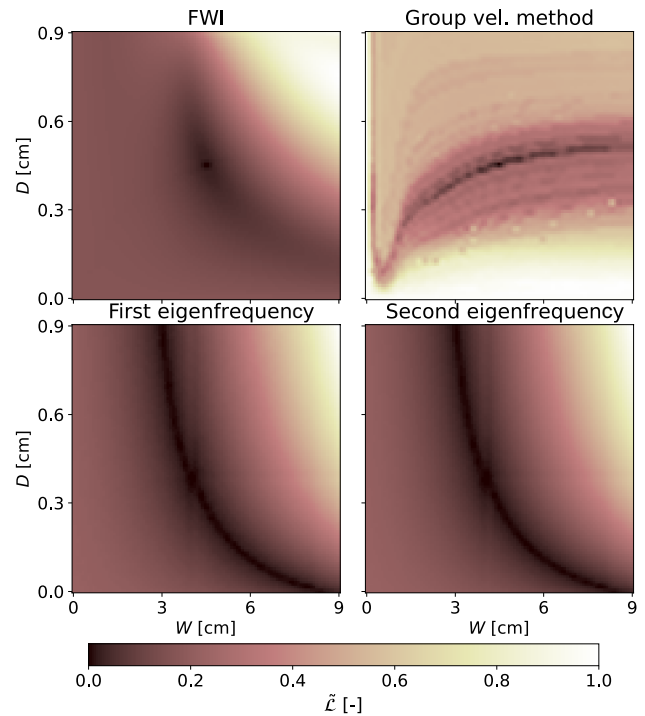
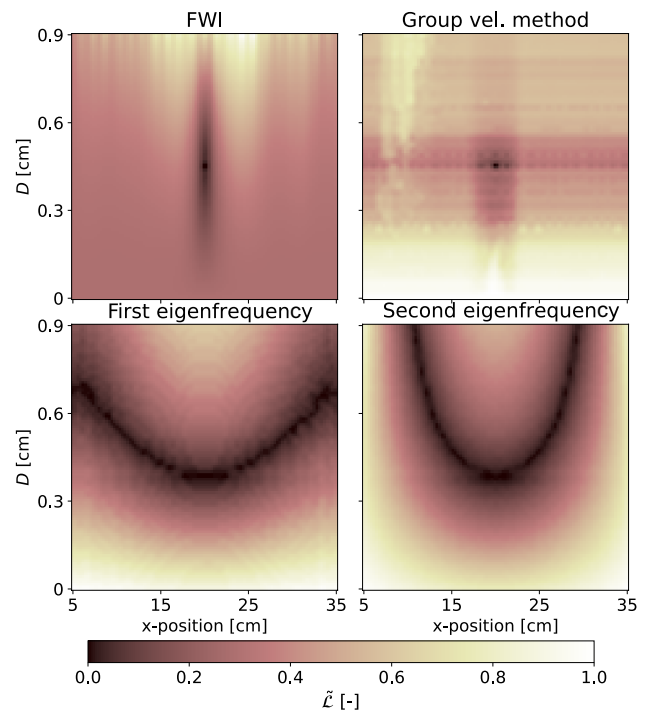


Fig. 15 The figure shows \tilde{L} , where D and x_d deviate from the reference configuration



FWI remains equally accurate, the minimum for the off-center defect position is less spread out when compared to the data from the centered position. The deviation of the diameter and maximum depth of the defects show a similar trend for the FWI objective function (see Fig. 14) as for the eigenfrequencies, where the minimum of the FWI error has the smallest area and is, therefore, the least ambiguous. The group velocity of the A_0 mode shows a different behavior. The reason for this can be the different slopes of the S_0 and A_0 modes within the dispersion curves at 70

Fig. 16 Here, $\tilde{\mathcal{L}}$ is shown for a variation of x_d and W

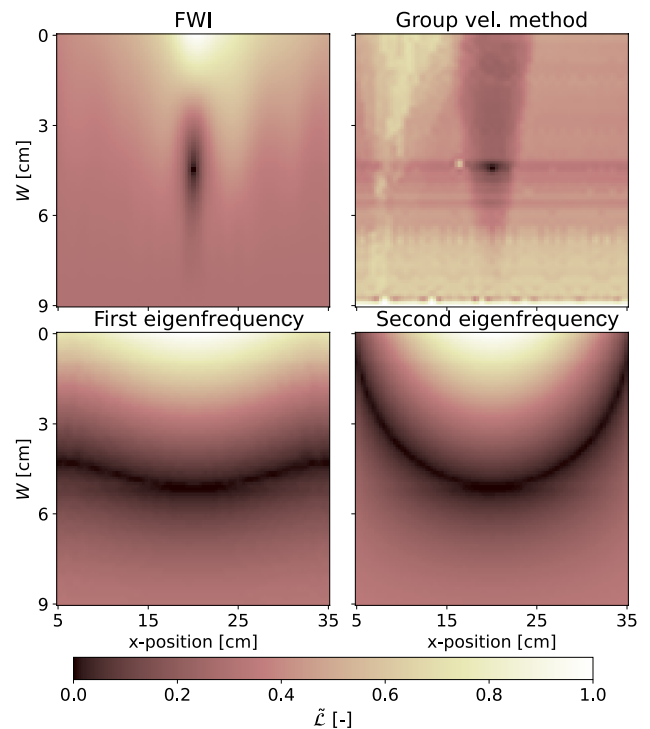
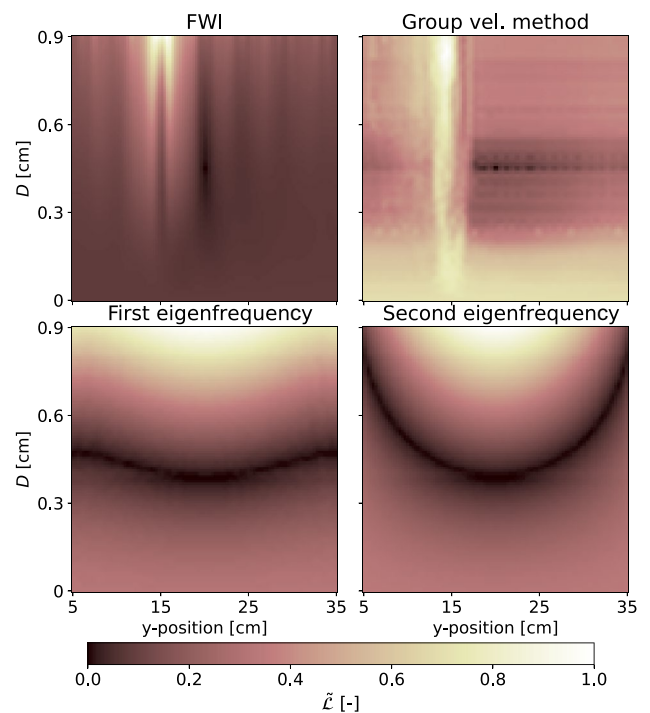
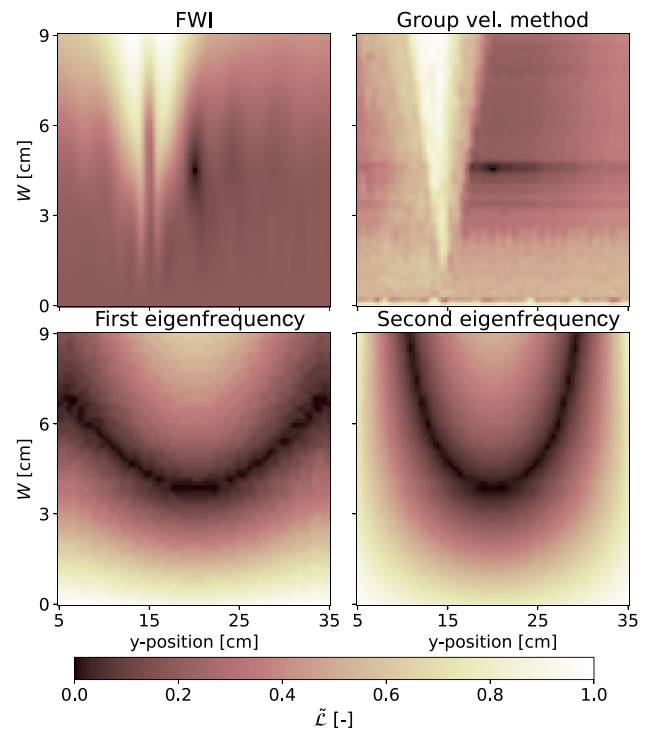


Fig. 17 The figure shows $\tilde{\mathcal{L}}$, where D and y_d deviate from the reference configuration



kHz. The A_0 group velocity is picked instead of that related to S_0 because the amplitude of the A_0 mode is significantly higher. Within the FWI $\tilde{\mathcal{L}}$, the S_0 and A_0 modes are included with their phase and group velocity. Through the consideration of all Lamb wave modes, using FWI may suppress some information within the data. When the y -position or the diameter of the defect leads to a defect close to the source, high $\tilde{\mathcal{L}}$ values are present for the group velocity of the A_0 and the FWI objective functions. Note that small errors in the objective functions belonging to the group velocity method are present close to the source position. This is due to the superposition of wave modes. However,

Fig. 18 Here, $\tilde{\mathcal{L}}$ is shown for a variation of y_d and W



this effect diminishes with growing distance from the source due to the faster velocity and the dominance in terms of the amplitude of the A_0 mode.

4.1.2 Modal

The subplots in the lower left quadrant refer to evaluating Eq. (4) for the first natural frequency, while those in the lower right quadrant are connected to the second natural frequency of the plate. The modal assurance criterion measures the degree of consistency between two vectors, see [41]. It is satisfied for all results, guaranteeing the correct sorting of modes.

Generally, we observe that the objective functions are smooth functions over all four defect parameters. This determines using natural frequency data as suitable when gradient-based optimization algorithms shall be employed.

The first mode shape for an ideal plate without defects, see Fig. 2, is point-symmetric with respect to the plate's center at $\{x, y\} = \{20 \text{ cm}, 20 \text{ cm}\}$. The second mode for an ideal plate without defects is axisymmetric with respect to both $x = 20 \text{ cm}$ and $y = 20 \text{ cm}$. This makes the change in natural frequency with respect to a perturbation in the defect position agnostic to the latter's quadrant within the plate. Axisymmetry of $\tilde{\mathcal{L}}$ with respect to the center lines of the plate is the result of this. In the present case, the error surfaces involving one spatial defect parameter develop single axisymmetry, while the objective function's surface over x_d and y_d shows twofold axisymmetry. To clearly show the latter and the resulting local minima, Fig. 13 is plotted. Our investigations show that neither using linear combinations of several natural frequencies within the objective function nor considering additional, higher natural frequencies can eliminate symmetry problems.

Furthermore, for the centered reference defect and the choice of the first two natural frequencies, all error surfaces show a single global minimum and, thus, the absence of local minima.

Considering the dimensionless gradient of the $\tilde{\mathcal{L}}$ surfaces reveals that the gradient exhibits a stronger sensitivity with respect to the defect position when the second natural frequency is used. This is attributed to the increased number of nodal line crossings in the x and y parameter space.

4.2 Comparison

Table 3 provides a summary of requirements for the measurement setups and the numerical simulations for each method. Additionally, it compares the properties of the resulting objective functions.

Table 3 Advantages and disadvantages of the methods

Criterion	Eigenfrequencies	FWI	Group velocity method
Necessary fidelity of the simulation	Low	High	Low
Necessary measurement point density	Low	High	High
Symmetry problems	Yes	No	No
Gradient around min	Shallow	Steep	Steep
Local minima	No	Yes	Yes

In general, the necessary fidelity of the simulation depends on the size of the defect and on the considered frequency range. However, FWI necessitates the highest measurement fidelity in comparison, as the signal must be represented accurately for time and space coordinates where the wave has been significantly attenuated. When the agreement of the investigated vibration mode can be guaranteed, a single observation point may suffice for the identification of the corresponding eigenfrequency, whereas ultrasound-based procedures rely on dense measurement points.

The minimum for the combined variation of x - and y -position and the diameter or maximum depth is less ambiguous for the Lamb waves than for the eigenfrequencies (see Figs. 15, 16, 17, and 18). Table 4 shows the minimum size relative to the regarded parameter area, determined by applying a threshold of 5% in relation to the respective maximum objective function values. Averaged over the parameter pairings, the minimum size lies in the same order of magnitude for both natural frequencies, while the Lamb wave data leads to minima smaller by orders of magnitude. The minima sizes for FWI and for the group velocity method are generally in the same order of magnitude. However, two irregularly large minima are present for the parameter combinations W and D as well as y and D when using FWI. These outliers lead to the minimum corresponding to the group velocity method objective function having the smallest area and, therefore, being the least ambiguous in this regard.

Further, shallow gradients surround the minimum for the eigenfrequency data. This also holds true when considering the variation of D and W using FWI (see Fig. 14). However, the gradients are steeper when compared to natural frequency data.

Additionally, positioning the reference defect off-center yields perfectly axisymmetric objective functions for natural frequency data, see Fig. 13. The natural frequencies alone do not encode the information to resolve this ambiguity as elaborated in Sect. 4.1. Partially due to the choice of the error norm for the objective function, the Lamb wave objective functions exhibit local minima. Using FWI exhibits less local minima than using the group velocity method does, where these minima mainly occur in proximity to the global minimum, while using the first two natural frequencies produces up to four local minima when the reference defect is not located at the center of the plate.

The influence of environmental conditions on the suitability of modal methods for the purpose of damage detection demands a brief discussion. A homogeneous temperature increment does not influence the mode shapes of a structure. For complex structures such as buildings or bridges, a change in ambient temperature may lead to a heterogeneous temperature field within the structure. The influence of temperature on the efficacy of employing modal methods for damage assessment to large structures has been studied in the literature, see [42]. For simple structures like the presently studied plate, the temperature is straightforward to determine. A change in temperature shifts the natural frequencies due to the temperature dependence of Young's modulus. Assuming an uncertainty in the temperature measurement of ± 1 K, the temperature-dependence of the material aluminum, see [43], leads

Table 4 Relative size of the optimum at a threshold of 5% of the maximum objective function value

Parameters	FWI	Group velocity method	f_1	f_2
x & y	0.04	0.05	11.51	4.07
W & D	1.94	0.07	14.03	13.96
x & D	0.08	0.04	7.83	6.63
x & W	0.08	0.08	9.54	10.26
y & D	1.86	0.07	9.57	10.34
y & W	0.16	0.12	7.98	6.64
Mean	0.46	0.07	10.18	8.31

to an uncertainty in the natural frequencies that amounts to two orders of magnitude less than the corresponding influence of the defects investigated in our study. Thus, it is deemed negligible here. The influence of uncertain mounting or boundary conditions remains significant, and the reader is referred to the pertinent literature, see [37].

5 Conclusions

In conclusion,

- The objective functions have been evaluated given the first and second natural frequency, the full waveform, and the group velocity of the A_0 mode.
- The effect of the defect position and geometry on the objective function has been studied.
- Advantages and drawbacks of using each simulation method have been obtained.

Using modal data yields ambiguous, albeit smooth estimates for both the defect position and size. Employing ultrasound methods provides compact objective function minima, but does not produce gradients pertinent to the global minimum when the initial guess for the unknown parameters deviates significantly from their true values. Therefore, we recommend a two-step procedure that begins with using eigenfrequency data and uses these results as the initial vector for an ultrasound procedure. These conclusions apply to the simulated case study with the specified defect and specimen configurations, and generalizations, especially those to equivalent experimental workflows with real transducers, need to be done with a lot of care.

Future research should investigate, whether the natural frequency and ultrasound methods could be employed simultaneously. The latter promises a decrease in solution time. To achieve this, suitable weighting factors for the methods shall be computed. Focusing on the defect's x - and y -position, our data suggest that the local minima produced by, say, FWI could be compensated through the natural frequency objective function's gradient, given an appropriate weighting. Further, the effect of different excitation frequencies on the objective function is an interesting future study. Finally, the effect of using mode shape data instead of natural frequencies should be studied, and different error norms should be investigated.

Author contributions K.-A.H.: conceptualization, methodology, software, validation, formal analysis, investigation, visualization, writing—original draft, writing—review and editing, project administration. S.S.: conceptualization, methodology, software, validation, formal analysis, investigation, data curation, visualization, resources, writing—original draft, writing—review and editing, project administration. J.K.: conceptualization, methodology, software, validation, formal analysis, investigation, writing—review and editing. S.M.: supervision, resources, writing—review and editing. C.U.G.: supervision, resources, writing—review and editing.

Funding Open Access funding enabled and organized by Projekt DEAL. No funding was received for conducting this study.

Data availability The raw data are available from the corresponding author upon reasonable request.

Code availability The code is available from the corresponding author upon reasonable request.

Declarations

Ethics approval and consent to participate Not applicable.

Consent for publication Not applicable.

Competing interests The authors declare that they have no competing interests.

Open Access This article is licensed under a Creative Commons Attribution 4.0 International License, which permits use, sharing, adaptation, distribution and reproduction in any medium or format, as long as you give appropriate credit to the original author(s) and the source, provide a link to the Creative Commons licence, and indicate if changes were made. The images or other third party material in this article are included in the article's Creative Commons licence, unless indicated otherwise in a credit line to the material. If material is not included in the article's Creative Commons licence and your intended use is not permitted by statutory regulation or exceeds the permitted use, you will need to obtain permission directly from the copyright holder. To view a copy of this licence, visit <http://creativecommons.org/licenses/by/4.0/>.

References

1. Zielińska M, Rucka M. Imaging of increasing damage in steel plates using lamb waves and ultrasound computed tomography. *Materials*. 2021;14(17):5114. <https://doi.org/10.3390/ma14175114>.
2. Krautkrämer J, Krautkrämer H. *Ultrasonic testing of materials*. Heidelberg: Springer; 1990. <https://doi.org/10.1007/978-3-662-10680-8>.
3. Zhao X, Royer RL, Owens SE, Rose JL. Ultrasonic lamb wave tomography in structural health monitoring. *Smart Mater Struct*. 2011;20(10):105002. <https://doi.org/10.1088/0964-1726/20/10/105002>.
4. Belanger P, Cawley P, Simonetti F. Guided wave diffraction tomography within the born approximation. *IEEE Trans Ultrason Ferroelectr Freq Control*. 2010;57(6):1405–18. <https://doi.org/10.1109/TUFFC.2010.1559>.
5. Guy P, Jayet Y, Goujon L. Guided-wave interaction with complex delaminations: application to damage detection in composite structures. In: *Smart nondestructive evaluation and health monitoring of structural and biological systems II*, vol. 5047, SPIE; 2003. p. 25–33. <https://doi.org/10.1117/12.483926>.
6. Tan K, Guo N, Wong B, Tui C. Experimental evaluation of delaminations in composite plates by the use of lamb waves. *Compos Sci Technol*. 1995;53(1):77–84. [https://doi.org/10.1016/0266-3538\(94\)00076-X](https://doi.org/10.1016/0266-3538(94)00076-X).
7. Maio L, Hervin F, Fromme P. Guided wave scattering analysis around a circular delamination in a quasi-isotropic fiber-composite laminate. In: *Health monitoring of structural and biological systems XIV*, vol. 11381. SPIE; 2020. p. 77–83. <https://doi.org/10.1117/12.2559125>.
8. Huthwaite P. Improving accuracy through density correction in guided wave tomography. *Proceed Royal Soci A: Math, Phys Eng Sci*. 2016;472(2186):20150832. <https://doi.org/10.1098/rspa.2015.0832>.
9. He J, Rocha DC, Leser PE, Sava P, Leser WP. Least-squares reverse time migration (lsrtm) for damage imaging using lamb waves. *Smart Mater Struct*. 2019;28(6):065010. <https://doi.org/10.1088/1361-665X/ab14b1>.
10. Rao J, Ratassepp M, Fan Z. Guided wave tomography based on full waveform inversion. *IEEE Trans Ultrason Ferroelectr Freq Control*. 2016;63(5):737–45. <https://doi.org/10.1109/TUFFC.2016.2536144>.
11. Stache M, Guettler M, Marburg S. A precise non-destructive damage identification technique of long and slender structures based on modal data. *J Sound Vib*. 2016;365:89–101. <https://doi.org/10.1016/j.jsv.2015.12.013>.
12. Rus J, Grosse CU. Thickness measurement via local ultrasonic resonance spectroscopy. *Ultrasonics*. 2021;109:106261. <https://doi.org/10.1016/j.ultras.2020.106261>.
13. Schneider F, Papaioannou I, Straub D, Winter C, Müller G. Bayesian parameter updating in linear structural dynamics with frequency transformed data using rational surrogate models. *Mech Syst Signal Process*. 2022;166:108407. <https://doi.org/10.1016/j.ymsp.2021.108407>.
14. Li Y, Cheng L, Yam L, Wong WO. Identification of damage locations for plate-like structures using damage sensitive indices: strain modal approach. *Comput Struct*. 2002;80(25):1881–94. [https://doi.org/10.1016/S0045-7949\(02\)00209-2](https://doi.org/10.1016/S0045-7949(02)00209-2).
15. Tufoi M, Gillich G, Mituletu I, Iancu V. Location of the corrosion damage in rectangular plates. In: *11th International Conference on Damage Assessment of Structures (DAMAS 2015)*. Journal of Physics: Conference Series, vol. 628. IOP Publishing; 2015. p. 012005. <https://doi.org/10.1088/1742-6596/628/1/012005>.
16. Le T-C, Ho D-D, Nguyen C-T, Huynh T-C. Structural damage localization in plates using global and local modal strain energy method. *Adv Civil Eng*. 2022;2022:4456439. <https://doi.org/10.1155/2022/4456439>.
17. Hou J, Jankowski Ł, Ou J. Structural health monitoring based on combined structural global and local frequencies. *Math Probl Eng*. 2014;2014:405784. <https://doi.org/10.1155/2014/405784>.
18. Park J-H, Kim J-T, Hong D-S, Mascarenas D, Peter Lynch J. Autonomous smart sensor nodes for global and local damage detection of prestressed concrete bridges based on accelerations and impedance measurements. *Smart Struct Syst*. 2010;6(5–6):711–30. https://doi.org/10.12989/sss.2010.6.5_6.711.
19. Sun XD, Sun XY, He J, Hou GL. Bayesian-based structural damage detection on the integration of global and local information. *Adv Struct Eng*. 2015;18(4):543–53. <https://doi.org/10.1260/1369-4332.18.4.543>.
20. Mehrez L, Doostan A, Moens D, Vandepitte D. Stochastic identification of composite material properties from limited experimental databases, part ii: Uncertainty modelling. *Mech Syst Signal Process*. 2012;27:484–98. <https://doi.org/10.1016/j.ymsp.2011.09.001>.
21. Debruyne S, Vandepitte D, Moens D. Identification of design parameter variability of honeycomb sandwich beams from a study of limited available experimental dynamic structural response data. *Comput Struct*. 2015;146:197–213. <https://doi.org/10.1016/j.compstruc.2013.09.004>.
22. Batou A, Soize C. Stochastic modeling and identification of an uncertain computational dynamical model with random fields properties and model uncertainties. *Arch Appl Mech*. 2013;83:831–48. <https://doi.org/10.1007/s00419-012-0720-7>.
23. Mengelkamp G, Fritzen C-P. Combination of global and local methods for structural health monitoring. In: *24th Conference and Exposition on Structural Dynamics 2006, IMAC-XXIV*. Springer Nature; 2006.
24. Fritzen C-P, Mengelkamp G. In-situ damage detection and localisation in stiffened structures. In: *23rd Conference and Exposition on Structural Dynamics 2005, IMAC-XXIII*. Springer Nature; 2005.
25. Wang Y, Hao H. Damage identification of steel beams using local and global methods. *Adv Struct Eng*. 2012;15(5):807–24. <https://doi.org/10.1260/1369-4332.15.5>.
26. Yan F, Rose JL. Defect detection using a new ultrasonic guided wave modal analysis technique (umat). In: *Health monitoring of structural and biological systems 2010*, vol. 7650. SPIE; 2010. p. 240–248. <https://doi.org/10.1117/12.847674>.
27. Ahmed S, Zhou P, Zager S, Kopsaftopoulos F. Local and global structural health monitoring via stochastic functional time series methods: a critical assessment and comparison; 2022. <https://doi.org/10.2514/6.2022-4001>.
28. Harb M, Yuan F. Non-contact ultrasonic technique for lamb wave characterization in composite plates. *Ultrasonics*. 2016;64:162–9. <https://doi.org/10.1016/j.ultras.2015.08.011>.
29. Huthwaite P. Evaluation of inversion approaches for guided wave thickness mapping. *Proceed Royal Soci A: Math, Phys Eng Sci*. 2014;470(2166):20140063. <https://doi.org/10.1098/rspa.2014.0063>.
30. Auld B. A: *Acoustic fields and waves in solids*. Malabar: Krieger Publishing Company; 1990.

31. Huber A. Dispersion calculator. Technical report, Deutsches Zentrum für Luft- und Raumfahrt, Augsburg; 2018. <https://elib.dlr.de/124561/>.
32. Huber A, Sause M. Classification of solutions for guided waves in anisotropic composites with large numbers of layers. *J Acoust Soci Am*. 2018;144(6):3236–51. <https://doi.org/10.1121/1.5082299>.
33. Langer P, Maeder M, Guist C, Krause M, Marburg S. More than six elements per wavelength: The practical use of structural finite element models and their accuracy in comparison with experimental results. *J Comput Acoust*. 2017;25(04):1750025. <https://doi.org/10.1142/S0218396X17500254>.
34. Ewins DJ. Modal testing: theory, practice and application. Philadelphia: Research Studies Press; 2009.
35. Bertolini AF. Review of eigensolution procedures for linear dynamic finite element analysis. *Appl Mech Rev*. 1998;10(1115/1):3098994.
36. Afanasiev M, Boehm C, van Driel M, Krischer L, Rietmann M, May DA, Knepley MG, Fichtner A. Modular and flexible spectral-element waveform modelling in two and three dimensions. *Geophys J Int*. 2019;216(3):1675–92. <https://doi.org/10.1093/gji/ggy469>.
37. Pavić G. Structure-borne energy flow. In: Crocker MJ, editor. Handbook of noise and vibration control. Hoboken, NJ: Wiley; 2007. p. 232–40. <https://doi.org/10.1002/9780470172520.CH74>.
38. Ulrich T. Envelope calculation from the hilbert transform. Technical report, Los Alamos National Laboratory, Los Alamos; 2006.
39. Savitzky A, Golay MJ. Smoothing and differentiation of data by simplified least squares procedures. *Anal Chem*. 1964;36(8):1627–39. <https://doi.org/10.1021/ac60214a047>.
40. Boehm C, Krischer L, Ulrich I, Marty P, Afanasiev M, Fichtner A. Using optimal transport to mitigate cycle-skipping in ultrasound computed tomography. *Medical Imaging 2022: ultrasonic imaging and tomography*. 2022;12038:48–57. <https://doi.org/10.1117/12.2605894>. SPIE.
41. Allemang RJ. The modal assurance criterion (mac): twenty years of use and abuse. In: IMAC-XX (Los Angeles CA, 4-7 February 2002) vol. 1. SPIE; 2002. p. 397–405. <http://pascal-francis.inist.fr/vibad/index.php?action=getRecordDetail &idt=14180753>.
42. Luo J, Huang M, Lei Y. Temperature effect on vibration properties and vibration-based damage identification of bridge structures: A literature review. *Buildings*. 2022;12(8):1209. <https://doi.org/10.3390/buildings12081209>.
43. Hopkins DC, Baltis T, Pitaress JM, Hazelmyer DR. Extreme thermal transient stress analysis with pre-stress in a metal matrix composite power package. Additional papers and presentations (HITEC); 2012. p. 000361–000372. <https://doi.org/10.4071/HITEC-2012-THA25>.

Publisher's Note Springer Nature remains neutral with regard to jurisdictional claims in published maps and institutional affiliations.

Appendix III

Paper B

Identification of a cantilever beam's spatially uncertain stiffness

Karl-Alexander Hoppe^{*}, Martin G. T. Kronthaler, Kian Sepahvand, and Steffen Marburg

This publication is reprinted in accordance with its open access license [CC BY 4.0](#).

^{*}orcid.org/0000-0002-3048-8284



OPEN

Identification of a cantilever beam's spatially uncertain stiffness

Karl-Alexander Hoppe¹✉, Martin G. T. Kronthaler, Kian Sepahvand¹ & Steffen Marburg¹

This study identifies non-homogeneous stiffnesses in a non-destructive manner from simulated noisy measurements of a structural response. The finite element method serves as a discretization for the respective cantilever beam example problems: static loading and modal analysis. Karhunen–Loève expansions represent the stiffness random fields. We solve the inverse problems using Bayesian inference on the Karhunen–Loève coefficients, hereby introducing a novel resonance frequency method. The flexible descriptions of both the structural stiffness uncertainty and the measurement noise characteristics allow for straightforward adoption to measurement setups and a range of non-homogeneous materials. Evaluating the inversion performance for varying stiffness covariance functions shows that the static analysis procedure outperforms the modal analysis procedure in a mean sense. However, the solution quality depends on the position within the beam for the static analysis approach, while the confidence interval height remains constant along the beam for the modal analysis. An investigation of the effect of the signal-to-noise ratio reveals that the static loading procedure yields lower errors than the dynamic procedure for the chosen configuration with ideal boundary conditions.

Material parameters may be identified in various ways. The established methods can be categorized as destructive and non-destructive methods¹. “Destructive” implies that the measurement specimen has, for example, experienced plastic deformations during tensile tests and thus fails to comply with the product requirements after the test, i.e. it can no longer fulfill the original purpose. Often, these tests are carried out until the specimen fails. Non-destructive testing methods offer a way to identify material parameters while the specimen retains its properties. Therefore, these methods are popular for quality control purposes after the manufacturing process in order to ensure certain requirements.

On the one hand, dynamic methods are popular for testing engineering materials. Impact-echo or transmission measurements using elastic waves present popular high-frequency regime methods that evaluate the wave onset². However, considering the individual modes of guided ultrasonic waves contains more information^{3–5}. In general, wave fitting approaches in the high-frequency regime continue to evolve⁶, where the utilization of the full waveform is noteworthy⁷. In lower frequency regimes, standing waves can be utilized. In this case, the resonance frequency method uses the eigenfrequencies connected to the eigenmodes for material parameter identification or defect detection⁸.

On the other hand, static methods may be considered as non-destructive when they are reversible and place the specimen in linear elastic loading conditions. Indentation tests and strain measurements with strain gauges are used in procedures that operate at the surface level, just as many displacement measurement techniques do. Within the latter, digital image correlation between a reference state and the deformed state of a specimen leads to a displacement field⁹, where several techniques can be used for capturing the respective images¹⁰.

Discontinuities like defects or cracks are typically the quantities of interest for nominally homogeneous materials¹¹. With non-homogeneous materials, local spatial variation of material properties is additionally introduced into the system¹². Depending on the severity of the non-homogeneity, it may have a relevant effect on the system response. This is certainly the case for engineering materials such as wood. The spatial variation of material properties has been quantified for individual specimens^{13,14}. Savvas et al.¹⁵ identify the mesoscale spatial variation of material properties given microscale information. However, rigorous descriptions of the spatial behavior are not readily available. Given this lack of data, the standard procedure is to assume a random spatial variation of the material properties. This spatial randomness of material properties can be described with the theory of random fields, which is extensively treated in the literature^{16,17}. Rasmussen and Williams¹⁸ popularize this theory for regression, which is generalized by Duvenaud¹⁹. The integration of spatial uncertainties with the finite element method (FEM) is covered in the literature^{20,21}.

TUM School of Engineering and Design, Department of Engineering Physics and Computation, Chair of Vibroacoustics of Vehicles and Machines, Technical University of Munich, 85748 Garching bei München, Germany.
✉ email: alexander.hoppe@tum.de

Spatial uncertainty is thus compatible with established uncertainty quantification practices²². Sepahvand and Marburg²³ demonstrate this for the forward propagation of uncertainty in structural dynamics by representing material properties as random fields.

Knowledge of the sensitivities of the system outputs with respect to the system inputs is valuable. However, many non-destructive testing methods involve an inverse problem, as for instance the study on elasticity imaging by Gokhale et al.²⁴. Since the quantities of interest as well as the measured parameters are fraught with uncertainties, a natural approach for the solution of the aforementioned inverse problems lies in Bayesian inference^{25–27}.

Parameter identification using the Bayesian framework holds two major advantages over other methods. Firstly, when limited test data on parameters exist, Bayesian methods provide us with an optimal tool to quantify uncertainty²⁸. This is crucial when one deals with expensive experiments in engineering. Using classical frequentist statistical models for such situations only yields reliable results when the number of data points is larger than a specific number, mostly 30, or when the data strictly follows a normal distribution²⁹. If these criteria are not met, the results generated with these methods either cannot be trusted to be valid or involve an increased level of uncertainty.

Secondly, the Bayesian framework involves available prior information about parameters that the statistical model considers³⁰. This prior information is then updated by information gained from observations. Available sources of prior information may include primary data, literature, online databases, and even the knowledge of experts. This is a substantial argument for using Bayesian methods in engineering applications, where data may be scarce but expertise on parameters is abundant.

Marzouk and Najm³¹ pioneer the application of Bayesian inference to spatially varying quantities of interest via dimensionality reduction achieved by the Karhunen-Loève (KL) expansion. They use a surrogate for the forward model to reduce computational cost that is based on generalized Polynomial Chaos (gPC)²¹. The decoupling of spatial discretization of the computational domain from the random dimensionality makes inverse problems involving larger systems accessible.

Sun and You³² provide an overview of sensitivities and damage features related to modal analysis in the context of non-destructive testing. Cugnoni et al.³³ perform a deterministic identification of a composite plate material model using the combined information of natural frequencies and mode shapes. Sepahvand and Marburg^{34,35} compute the homogeneous elastic parameters of composite plates while accounting for uncertainty using experimental data. Note the contribution by Desceliers et al.³⁶, who calculate the non-homogeneous beam stiffness from frequency response measurements using a maximum likelihood estimate. Batou and Soize³⁷ consider a random field material model employing model order reduction and maximum likelihood estimation given frequency response functions. Mehrez et al.³⁸ estimate the Young's modulus of a composite structure at a set of nodes with Bayesian inference and gPC using frequency response functions acquired at those nodes. Debruyne et al.³⁹ apply this general procedure to a honeycomb structure.

This study investigates the identification of spatially varying structural flexibility using both a dynamic and a static method. The dynamic method is a novel dimensionality-reduced Bayesian approach for identifying the elastic parameters of a structure using resonance frequency information. The static method follows a similar scheme as the research by Uribe et al.⁴⁰, who reconstruct the stiffness fields given deflection observations using a modified version of the framework by Marzouk and Najm³¹.

To provide comparability and insight into each method's respective advantages, both the dynamic and static method use the same setup, namely a cantilever beam with spatially varying structural flexibility. Eigenfrequencies mark the starting point for the flexibility identification within the dynamic method, while deflections connected to static loading serve as data for the static method. For each method, Bayesian updating is then performed on a finite element method model of the cantilever beam with unknown structural flexibility, which is considered as a sample of a Gaussian random field along the cantilever beam. The truncated KL expansion represents this spatially varying flexibility, resulting in a description with reduced random dimensionality. Owing to the Bayesian inference setup, the solution's uncertainty can then be compared between the dynamic and the static approach.

This paper is organized as follows: “[Methods](#)” introduces random fields and inverse problems, as well as the Bayesian inference setup shared between the dynamic and static approaches. “[Application of the procedure](#)” describes the integration of both the dynamic and static cantilever beam models into the inverse problem, and then the numeric results are presented in “[Results and discussion](#)”. Following the conclusion and an outlook on future research in “[Conclusion](#)”, we provide additional information in the Online appendix S1.

Methods

This study considers the spatially random fluctuation of material properties about a mean value. The connected covariance and the representation by the KL expansion are covered by “[Preliminary concepts](#)” alongside Bayes' theorem. “[Procedure](#)” treats the inverse problem formulation and the latter's integration into Bayesian updating by specifying the parametrization and measurement error model pertinent to the cantilever beam.

Preliminary concepts. Together with its mean value, a second-order random field is fully characterized by its covariance function. The covariance kernel $Cov(t, t')$ is a function of the coordinates of two points t, t' within the field's domain, the bounded interval $[0, L]$. This study considers continuous, symmetric, and positive semi-definite kernels such that the KL expansion can be used.

Several families of functions may be used as covariance functions. We adopt the isotropic exponential kernel from the literature¹⁷. It is a function of Euclidean distance r and the length scale parameter l as

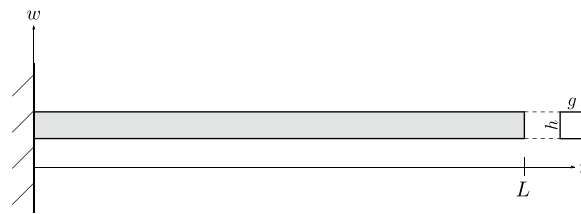


Figure 1. The figure shows a side view of the investigated cantilever beam model together with its profile and the coordinate system. The rectangular profile exhibits width g and height h . The beam length is L . Here, the beam coordinate is denoted as t , and the deflection coordinate reads as w .

$$\text{Cov}(t, t') = \sigma^2 \exp(-(|t - t'|/L)^2), \tag{1}$$

where σ^2 is the variance¹⁸. It is chosen because there exist analytical solutions to the connected eigenvalue problem that facilitate verifying the corresponding numerical implementations⁴¹.

Karhunen-Loève Expansion. The KL expansion represents a random field by taking into account the random field's mean $\mu(t)$ and decomposing its covariance function. This method utilizes deterministic spatial functions together with random coefficients ξ_i for the representation of the random field. Truncating the KL expansion after s summands yields an approximation of the field with a finite random space dimensionality⁴², such that

$$X(t, \xi) \approx \mu(t) + \sum_{i=1}^s \sqrt{\lambda_i} \varphi_i(t) \xi_i, \tag{2}$$

where λ_i are the eigenvalues and $\varphi_i(t)$ are the eigenfunctions of the corresponding covariance operator⁴². To obtain a sample path or realization of the random field, a sample of its parametrization ξ must be drawn.

If the considered material parameter follows a lognormal instead of a normal distribution, the generated samples may simply be exponentiated. However, the generalization of the KL expansion to non-Gaussian random fields is not straight-forward. Partially, this is due to correlations being induced between the random coefficients. When closed-form transformations are not readily available, a full-dimensional multivariate normal distribution may present a remedy. After transformation to $[0, 1]$ using the Gaussian error function, the inverse cumulative distribution function of a desired arbitrary distribution can be applied. The resulting marginal distributions follow the prescribed distributions and retain the sample smoothness over the domain inherent to the initial correlation structure, see Vofechovský⁴³.

Bayesian Inference. The above describes the quantity of interest, which is now declared as θ . The following introduces Bayesian inference, a method for estimating the quantity of interest using a model, data, and prior knowledge. Bayesian inference approaches attempt to solve the inverse problem while considering uncertainties along with prior knowledge about the quantities of interest and the likelihood of the observed data. Essentially, its outcome, the posterior, reflects how new data change our beliefs concerning the unknown quantities.

Using the logarithms of the probabilities to circumvent computational issues arising from the multiplication of small numbers and neglecting the normalizing constant that is the evidence, Bayes' theorem reads as

$$q(\theta|\mathbf{d}) \equiv l(\mathbf{d}|\theta) + p(\theta). \tag{3}$$

Here, q is the posterior distribution for θ given some data \mathbf{d} , l is the likelihood of observing the data \mathbf{d} given a model with parametrization θ , and lastly, p is the prior distribution on θ .

The reader is referred to the literature concerning the treatment of three major issues within the solutions of inverse problems: existence, non-uniqueness, and instability of the solution, with the latter also called ill-posedness⁴⁴.

Procedure. Consider a forward model, see Fig. 1, of a cantilever beam

$$\mathbf{d}_{true} = \mathcal{G}(C(t)). \tag{4}$$

Here, its structural flexibility $C(t)$ is considered as a function over the beam domain $[0, L]$. The operator \mathcal{G} is used to transform this function to an output \mathbf{d} . Static deflections and eigenfrequencies comprise \mathbf{d} for the static analysis and the modal analysis, respectively. The measured output

$$\mathbf{d}_{meas} = \mathbf{d}_{true} + \eta = \mathcal{G}(C(t)) + \eta \tag{5}$$

is subject to measurement noise η . Solving the inverse problem is then to

$$\text{find } C(t) \text{ s.t. } \mathbf{d}_{true} = \mathcal{G}(C(t)), \text{ given } \mathbf{d}_{meas}. \tag{6}$$

In practice, a finite-dimensional representation of the flexibility $C(t)$ based on the parameter vector θ made up of the KL parameters and the mean of the flexibility field reads as

$$\theta = \{\mu_C, \xi_1, \xi_2, \dots, \xi_s\}^T \in \mathbb{R}^{s+1}. \tag{7}$$

This leads to the discretized numerical forward model

$$\mathbf{d}_{meas} \approx \mathcal{G}(C(t, \theta)) + \eta = \widetilde{\mathcal{G}}(\theta) + \eta. \tag{8}$$

Now, Eq. (3) may be adopted to the problem at hand with $\mathbf{d} = \mathbf{d}_{meas}$, and the finite-dimensional parametrization θ given in Eq. (7). The necessary truncation order of the KL expansion depends on the covariance and is independent of the spatial discretization chosen within the forward model. To determine s , the ratio of the variance covered by the truncated KL expansion to that covered by the full expansion should be compared to recommended threshold ratios⁴⁵. Typically, s is less than 20, and is significantly smaller than the spatial discretization of the governing equations. This reduction in dimensionality from the spatial discretization to the number of KL coefficients is crucial for the efficiency of some Markov Chain Monte Carlo (MCMC) algorithms. Additionally, it allows for the use of surrogate model methods like gPC³¹.

Specifying the measurement noise model, a custom likelihood accommodates for flexible signal-to-noise ratios of the data components. This measurement error model assumes that the measurement vector \mathbf{d}_{meas} of dimension κ is perturbed by independent noise components

$$\eta_j \sim \mathcal{N}(0, \sigma_j^2) \tag{9}$$

with corresponding variances σ_j^2 . Now, for scalar-valued measurements at several frequencies or locations within the specimen and a single measurement run, the likelihood

$$\mathcal{L}(\mathbf{d}_{meas} | \theta) = \prod_{j=1}^{\kappa} \frac{1}{\sigma_j \sqrt{2\pi}} \exp\left(-\frac{1}{2} \frac{(\mathbf{d}_{meas,j} - \widetilde{\mathcal{G}}(\theta)_j)^2}{\sigma_j^2}\right) \tag{10}$$

becomes the product of the marginal likelihoods of its components. Vector-valued measurements as well as repeated measurements necessitate modifications of Eq. (10).

With fixed choices for the likelihood, the forward model, its parametrization and the latter's endowment with prior densities, the right hand side of Eq. (3) can be evaluated. However, closed form solutions for the posterior probability density function are only available for special cases involving conjugacy. This necessitates sampling from the posterior, which can be achieved using Markov Chain Monte Carlo (MCMC) algorithms. This study employs the single variable slice sampling method as formulated by Neal⁴⁶. It is applied to each parameter separately, while the other parameters are fixed.

Application of the procedure

This section describes the application of the methods presented in “Methods”. Specifically, “Cantilever beam model” introduces the used cantilever beam model, while “Modal analysis” describes the system’s modal analysis and “Static analysis” covers the system’s static analysis. After the explanations concerning these forward models, “Flexibility identification using eigenfrequency measurements from modal analysis” provides the solution procedure for the inverse problem based on modal data and “Flexibility identification using deflection measurements from static analysis” details the procedure when deflection data is given.

Cantilever beam model. Consider the Timoshenko cantilever beam model shown in Fig. 1, where the boundaries are clamped on the left side and free on the right side. The beam exhibits length L and a rectangular cross-section with an area of $A = g \cdot h$, where the cross-section width and height are denoted by g and h , respectively. The second moment of area is computed as $I = gh^3/12$, and the shear correction factor k_s for a rectangular cross-section is $k_s = 5/6$. The material of the beam is characterized by Young’s modulus E and the shear modulus G , while considering Hooke’s law.

This problem is implemented with the finite element method via the SfePy Python library⁴⁷. The discretization of the deflection w , the angle ψ , and the corresponding weighting functions is performed using 2nd order polynomials that are defined on each element.

To model the spatially varying elastic modulus E , it is assumed to vary randomly over the beam coordinate t . The inverse of the elastic modulus, i.e. the elastic flexibility $C = 1/E$, is then assumed to be a realization of a Gaussian random field, where the standard deviation is a fraction of the mean value. The covariance function for the random flexibility is defined on the domain $t \in [0, L]$ and an exponential kernel with arbitrarily chosen correlation length $l = L/5$, as defined in Eq. (1), is chosen. The covariance function is evaluated at the nodes of the finite element mesh, yielding piece-wise constant material properties as shown for a coarse exemplary discretization in Fig. 2.

The domain is discretized with 100 finite elements. This results in 201 nodes for the evaluation of the covariance function. The resulting 201×201 covariance matrix is used for synthesizing the reference flexibility vector. The Cholesky decomposition \mathbf{LL}^T of this covariance matrix achieves the realization of the reference flexibility²⁰. This alternative method is chosen for the reference model instead of the KL expansion to mitigate an inverse crime, as it is more accurate, albeit higher dimensional, than the KL expansion. With the prescribed mean bending flexibility $\mu_{C,true}$ and the lower triangular matrix \mathbf{L} resulting from the Cholesky decomposition, the flexibility field reads as

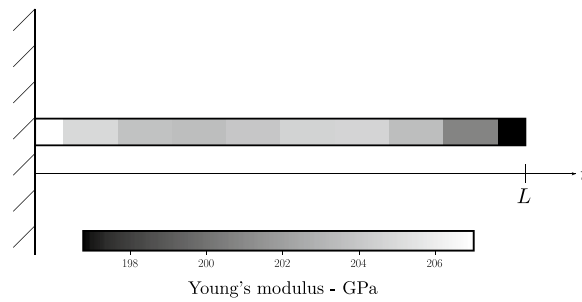


Figure 2. The graph shows an arbitrarily chosen stiffness distribution over the beam coordinate at ten discrete positions within the numerical model of the cantilever beam. The discretization is purposefully chosen as coarse for the illustration. Because the stiffness is assigned to nodes as opposed to elements, the stiffnesses at the bounds are half as wide compared with those assigned to interior elements.

$$C_{true} = \mu_{C,true} + L\xi, \tag{11}$$

where ξ is a vector of uncorrelated standard Gaussian random numbers. Realizing ξ yields the reference sample of the flexibility.

Modal analysis. On the one hand, we consider the modal analysis of the cantilever beam described in “Cantilever beam model”. Here, the first κ eigenfrequencies of the system $f_1, f_2, \dots, f_\kappa$ obtained via solving the system’s eigenvalue problem make up the response vector. Specifically, the reference flexibility C_{true} of the cantilever beam leads to the connected reference eigenfrequencies. A vector of independent Gaussian random variables is then superimposed on these eigenfrequencies to emulate measurement noise.

Static analysis. On the other hand, we consider the cantilever beam described in “Cantilever beam model” when subjected to static loading F at $t = L$. Here, κ equispaced static deflection measurements comprise the response vector. After applying the reference flexibility C_{true} to the cantilever beam model, we calculate the connected reference deflections. To simulate measurement noise, the static deflections are superimposed with independent and identically distributed Gaussian random variables.

Identification of spatially varying flexibility using synthetic noisy measurements. *Flexibility identification using eigenfrequency measurements from modal analysis.* Next, we use noisy measurements of the first 10 simulated eigenfrequencies of the cantilever beam with the reference flexibility vector. Then, the reference flexibility is estimated for all positions within the beam from these noisy eigenfrequency measurements. Note that the reference flexibility is unknown in the context of the inversion procedure.

Figure 4 shows a flowchart of the inference procedure, while the following paragraphs describe it in greater detail.

Reconstructing the unknown reference flexibility with the methods described in “Methods” necessitates the strong assumption of the flexibility mean being constant, that is stationary, and that of the flexibility covariance. We assume the same covariance, an exponential covariance kernel with correlation length $l = L/5$ and an exponent of $\gamma = 2$, as used for the reference model to maintain comparability of the flexibility parameterization. These assumptions may be relaxed by a parameterized family of kernels and an inference of their parameterization together with the KL parameters⁴⁸. The reconstruction FE model exhibits 50 quadratic elements leading to a spatial evaluation of the flexibility at 101 nodes. This coarser discretization in comparison with the reference model is once again chosen to avoid an inverse crime⁴⁹.

To reduce the random dimensionality, we discretize the unknown random field with the KL expansion from Eq. (2) truncated to $s = 6$ terms. Assuming a constant mean, this yields $s + 1$ unknown random variables that make up the discrete vector of unknowns θ , namely the mean and the s KL parameters. Following Huang et al.⁴⁵, this configuration accounts for $\alpha = 98\%$ of the variance of the random flexibility.

By using the KL expansion, we essentially apply a Gaussian process prior on the flexibility. Within this prior probability, the flexibility mean is distributed according to

$$\mu_C \sim \mathcal{N}\left(\mu = 5 \times 10^{-12} \frac{m^2}{N}, \sigma^2 = \left(1 \times 10^{-12} \frac{m^2}{N}\right)^2\right) \tag{12}$$

and the KL parameters are endowed with a normal prior:

$$\xi_{i-1} \sim \mathcal{N}\left(\mu = 0, \sigma^2 = \left(1 \times 10^{-11} \frac{m^2}{N}\right)^2\right) \quad \forall i > 1. \tag{13}$$

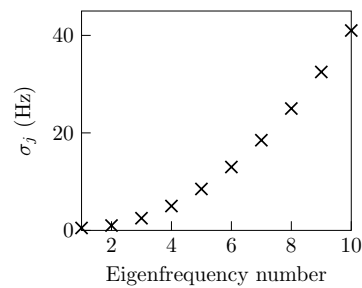


Figure 3. The measurement likelihood standard deviation is expressed as a function of the frequency. The graph shows the chosen quadratic increase of the measurement likelihood standard deviation σ_j over the number of the corresponding eigenfrequency. This weighting emphasizes the influence of the first few eigenfrequencies. The higher likelihood standard deviation for the higher eigenfrequencies reflects the expectation that measurement accuracy deteriorates with increasing frequency.

These prior distributions may be interpreted analogously to regularization in optimization. The chosen normal prior on the flexibility mean represents a weak assumption, while the prior on the KL coefficients encodes an assumption on the flexibility variance.

The real noise standard deviations present the ideal choice for the likelihoods standard deviations, because inaccurate measurements are not erroneously interpreted as accurate, and conversely, more accurate measurements are not assumed as excessively noisy, thus leading to a loss of information. In practice, the error or noise characteristics are unknown, but may be estimated from the statistical information gained from repeated measurements. We define the likelihoods with a higher standard deviation than that of the synthetic measurement noise used and thus underestimate the measurements' accuracy. The numerical values are compiled together with all parameters that are necessary for reproducing the results in the Online appendix S1. The likelihood function for vector-valued measurements in Eq. (10) implies that each eigenfrequency is measured only once and not repeatedly.

The likelihood's standard deviation increases quadratically with the number of the corresponding eigenfrequency, see Fig. 3. Matching low eigenfrequencies is thus given more importance.

The slice sampling algorithm generates samples $\theta^{(i)}$ from the posterior in Eq. (3). Multiple chains with different initial values help attenuate the influence of the initial value of the sampled Markov chain alongside the exclusion of burn-in samples from the number of samples used U . Evaluating the applied KL expansion at the posterior samples then produces the corresponding samples of the posterior random field.

Along with the flexibility's expected value,

$$\mu_{C,post}(t_j) = \frac{1}{U} \sum_{u=1}^U C^{(u)}(t_j), \quad (14)$$

we compute confidence intervals that contain 95% of the values of $C^{(u)}(t_j)$ for each position t_j . Finally, the root mean square percentage error (RMSPE) with respect to the reference flexibility is obtained as

$$\varepsilon_{RMSPE} = \sqrt{\frac{1}{k} \sum_{j=1}^k \left(\frac{\mu_{C,post}(t_j) - C_{true}(t_j)}{C_{true}(t_j)} \right)^2} \cdot 100\%. \quad (15)$$

Flexibility identification using deflection measurements from static analysis. The identification of the structural flexibility using static deflection data follows the same general procedure as described in “Flexibility identification using eigenfrequency measurements from modal analysis”. This section does not repeat the steps shared between the two procedures, it highlights the differences instead.

Here, noisy measurements of the simulated static deflections of the cantilever beam with the reference flexibility constitute the data. With these 10 equispaced static deflections, we estimate the unknown reference flexibility C_{true} .

Replacing modal with static analysis and eigenfrequencies with static deflections, respectively, in the procedure diagram, see Fig. 4, yields the inversion procedure using static analysis.

Contrary to inversion via modal analysis, we choose a constant likelihood standard deviation for the static analysis. The likelihood follows Eq. (10), where the static deflections are measured once at each equispaced position.

Results and discussion

This section presents the findings of the present study. “Modal analysis” and “Static analysis” consider the confidence interval of the solution over the beam coordinate and “The effects of signal-to-noise ratio and flexibility correlation length” explores the effects of signal-to-noise ratio as well as flexibility correlation length.

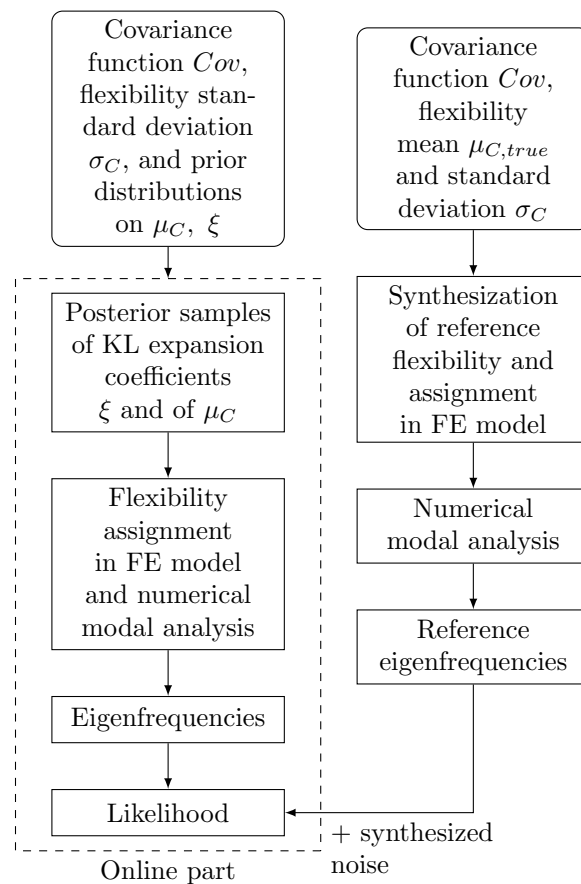


Figure 4. General procedure for reconstructing the reference random field given noisy eigenfrequencies and assuming the reference covariance, priors, and measurement noise characteristics with Bayesian inference. The top part refers to the calculation of the reference eigenfrequency from the reference flexibility. Given noisy observations of these reference frequencies, the aim of the procedure detailed at the bottom is to estimate the reference flexibility. Here, the dashed line marks the part of the inference that must be computed at every step in the chain.

Figure 5 shows the results of the procedure for one exemplary realization of the random flexibility. Here, the dashed-dotted lines mark the a priori unknown reference flexibility. Figure 5a shows the result using the dynamic method and Fig. 5b illustrates the result for the static deflection-based method for comparison. Note that the proposed Bayesian approach yields a chain of samples for θ_i . These samples can be used to estimate the posterior distribution's higher statistical moments in addition to mean and variance. Restricting the analysis of the results to mean and variance would disregard any skewness of the posterior at any location, which is visible in Fig. 5 through the asymmetrical confidence intervals. Additionally, note that the procedure has produced a non-stationary posterior random field as these moments are not constant over the beam length.

The following paragraphs interpret the confidence interval properties along the beam coordinate t based on a total of 100 realizations of the flexibility such that the interpretations are applicable in a general sense.

Modal analysis. With the eigenfrequency-based approach and with the chosen likelihood structure, the size of the confidence interval is roughly constant along the beam coordinate t . The present choice of the first 10 eigenfrequencies thus leads to a comparable amount of flexibility information for all spatial positions.

Avoiding non-physical signs of the flexibility is straightforward using the eigenfrequency-based model, since negative flexibility leads to a negative squared eigenfrequency. For this case, the likelihood of corresponding solution candidates is simply set to zero and we thus obtain a purely positive estimation of the flexibility here.

Static analysis. With the static deflection-based approach, the confidence interval increases as the distance from the clamping grows. This is consistent with the intuition that the bending moment within the beam varies linearly along the beam axis, with the maximum absolute value being at the clamping. Because the impact of flexibility fluctuations on the deflection depends directly on the bending moment, these fluctuations have

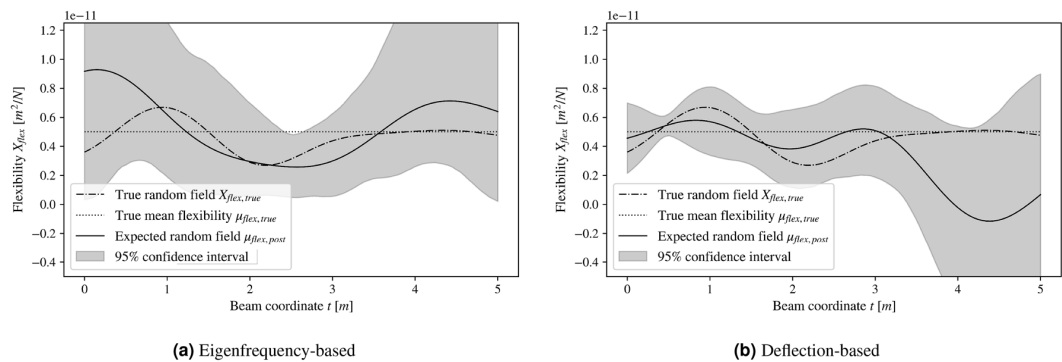
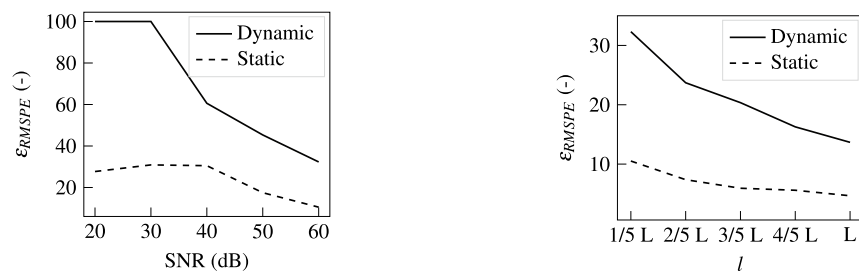


Figure 5. The figures show the results for the inference workflow for a specific reference flexibility. The left graph corresponds to the modal analysis, while the right figure is connected to the static analysis. The respective dashed-dotted lines show the reference flexibility, while the respective solid lines represent its estimated posterior mean. Low heights of the confidence intervals indicate a higher certainty of the inference results at the respective location.



(a) The strategic variation of the synthetic measurements' signal-to-noise ratio highlights the sensitivity of the inference performance with respect to the noise characteristics for $l = L/5$. The RMSPE between the reference and the identified flexibility measures the inference performance, where the dashed and solid lines correspond to the static and modal analysis, respectively. **(b)** A main finding of this study is the effect of the flexibility's correlation length l on the inference quality shown in the plot. The signal-to-noise ratio is set to 60 dB here. The dashed line shows the RMSPE between the reference flexibility and its estimation using static analysis, while the resonance frequency method results make up the solid line.

Figure 6. Comparison of the methods' performance influenced by changing inverse problem configurations. The left graph shows the effect of changing signal-to-noise ratios, while the right graph shows the impact of flexibility correlation length.

their biggest impact close to the clamped boundary. Conversely, the deflections contain proportionately more information about the flexibility on the left side than on the right side. This facilitates error propagation from the left to the right part of the domain and it finally leads to the narrow confidence interval in the left part and the wide confidence interval in the right part of the beam.

With the static deflection-based model, some issues may arise with the flexibility's sign, owing to the Gaussian random field's support $C(t_j) \in \mathbb{R}$ within the reconstruction. Here, the estimation violates the physical restriction of the flexibility being positive at some locations on the right side of the beam. The reason for this is a mixture of the characteristics of the beam and the assumed measurement noise. The cantilever beam exhibits a small bending moment on its right side, leading to a small curvature on this side. To simulate the deflection measurements, we add synthetic Gaussian noise to the deflections. In regions on the right side with a low reference curvature, the curvature of the noise is likely to dominate the total curvature within the simulated measurements. As the bending moment links the flexibility and the curvature, the reconstruction essentially estimates the curvature of the beam. This explains why the curvature component resulting from the synthetic measurement noise may propagate to the estimated flexibility and consequently lead to negative values for the flexibility in some cases.

The effects of signal-to-noise ratio and flexibility correlation length. This study focuses on investigating and comparing two non-destructive methods for material parameter identification. To study the efficacy of the dynamic and static method, we demonstrate the strategic variation of the inverse problem's configuration. Specifically, we expect both larger correlation lengths of the flexibility and larger signal-to-noise ratios to improve the inversion quality and did indeed obtain these expected results.

The effect of the signal-to-noise ratio (SNR) on the solution quality is investigated with a systematic variation of noise standard deviation, see Fig. 6a. To obtain representative results, the described procedure is carried out for 100 unique realizations of the reference flexibility per signal-to-noise ratio. The error described in Eq. (15) is then averaged over the 100 realizations. The error decreases non-linearly for the chosen SNR scale. Comparatively low signal-to-noise ratios produce a plateau in the error. After a kink in the curve, higher measurement noise entails

flattening error behavior. We observe a consistently lower RMSPE when employing the approach using static deflection measurements and a higher order of error convergence for the resonance frequency method. Note that more accurate measurements can be obtained in practice by averaging over several repeated measurement runs.

The variation of the flexibility correlation length shown in Fig. 6b exhibits the expected outcome. The error decreases non-linearly with increasing ground truth correlation lengths. The error gap between the static and dynamic methods narrows with growing correlation lengths. The comparatively large errors in the small correlation length regime result from the higher complexity of the unknown function. This in turn corresponds to an increasingly complex parameter space that the inference procedure needs to traverse. On the contrary, an infinitely large correlation length would correspond to a constant flexibility. This represents the simplest case and we expect the smallest errors here.

Concerning the static analysis, this study does not account for uncertainty in the load and its application to the specimen. These uncertainties propagate through the system to the deflections. Additionally, the measurement of the deflections is subject to measurement errors. Measurement noise challenges for micro-scale applications are linked to physical restrictions in optics⁵⁰. Macro-scale applications like the one studied in this paper on the one hand rely on methods such as digital image correlation⁵¹. On the other hand, they use optical active or passive marker systems that typically involve camera setups⁵². Here, a compromise must be found between the covered area and the camera distance, the two of which are coupled by the viewing angle. Maletsky et al.⁵³ report a non-linear relationship between camera distance and SNR and find an overall SNR of 45 dB for a generic setup. In fact, SNRs of higher than 60 dB are already achievable for dynamic response measurement setups⁵⁴. Accounting for this measurement accuracy of dynamic methods exceeding that of static methods⁸, an unfavorable light is cast on the modal analysis.

This study considers the modal and static analyses of an identically configured, clamped cantilever beam and does not account for uncertainty in the boundary conditions. However, an experimental modal analysis is typically conducted with free-free boundary conditions that are more accurately reproducible in practice than other mounting conditions⁵⁵. Here, this benefit of the method is traded for comparability with respect to the static analysis.

Debruyne et al.³⁹ find the usefulness of experimental modal analysis doubtful for their model updating procedure, when the measurement quality is not excellent. Their conclusion is confirmed by our results that stem from a setting with deterministically known modeling errors. Mehrez et al.³⁸ state that their number of data points prove suitable for their problem configuration. Our results complement this by setting the SNR and error into relationship, which enables an estimate for the required number of data points to achieve an error tolerance given the SNR of a single measurement. Their confidence region makes up for $\approx 30\%$ of the mean value. Our resonance frequency method matches this estimation accuracy for high signal-to-noise ratios and ground truth random field correlation lengths close to or greater than L . This is due to the gradient-agnostic sampling algorithm used in this study on the one hand and due to the difference in information provided to the method on the other hand, as local instead of global data is used in the study Mehrez et al.³⁸.

Conclusion

We develop a new Bayesian resonance frequency method with reduced stochastic dimensionality for identifying the spatially varying structural flexibility of a cantilever beam. It exhibits a major advantage compared to existing non-destructive methods for determining local macro-scale material properties using dynamic data. As it does not rely on local information as conventional methods do, it can operate without line-of-sight to the specimen. This is especially valuable in the context of the advent of functionally graded materials. The latter is furthering spatially varying material properties within geometrically complex assemblies. Here, our method enables non-destructive testing when undercuts are present.

We obtain results for the non-linear error characteristics with respect to SNR and the flexibility correlation length. Considering the influence of SNR highlights that a saturation of the error occurs at low signal-to-noise ratios. These results are set in relation to those obtained from applying the Bayesian procedure to the cantilever subjected to static linear elastic loading.

In conclusion, using identical noise and flexibility correlation length characteristics:

- inversion based on static deflections yields lower absolute errors.
- the confidence interval widens with growing distance from the clamping for the static approach.
- the confidence interval height using the dynamic approach stays constant along the beam.

We further conclude that, generally:

- larger flexibility correlation lengths lead to improved reconstruction.
- higher signal-to-noise ratios reduce the estimation error.

In practice, the choice of method should carefully consider the reproducibility of the real boundary conditions within the numerical models and especially the signal-to-noise ratios achievable by the experimental setups.

Currently, no reliable data describing the spatial randomness of material properties are available, and Matérn covariance models or special cases like isotropic exponential kernels are used as a fallback, see⁴⁸. Identifying the covariance from such data systematically for common material classes, the connected manufacturing processes, and engineering applications that introduce heterogeneity would eliminate the need for many assumptions that are currently necessary. Future research needs to study the influence of these identified covariance models and

their respective parameters on the efficacy of our method. This may include the construction of compound covariance kernels from base kernels, for example using addition or multiplication, see Hofmann et al.⁵⁶. This property could be used to combine kernels across spatial dimensions and model, among others, anisotropically heterogeneous materials.

This paper shows the solution of the inverse problem for a single quantity of interest that depends on a spatial coordinate. In practice, more than one parameter can be relevant. In the context of isotropic materials, the shear modulus or Poisson's ratio as well as the mass density may be relevant. For anisotropic materials, the spatial components of the elastic properties are additionally needed to fully characterize the material. This complicates the inverse problem. However, taking into account for additional information promises to mitigate these effects. For some material classes, the spatial components of the elastic properties are linearly correlated. Specifically for wood, the Young's modulus in a tree's growth direction correlates linearly with the Young's modulus in the radial direction orthogonal to the growth rings. Often, Pearson's coefficient for linear correlation exceeds $r = 0.5$ here. Preliminary investigations have shown that incorporating knowledge of the cross-correlation is not uniformly beneficial. Conversely, the method's success depends on the cross-correlation amplitude and the algorithm used to sample from the posterior distribution, among others. Future research needs to address this research gap and produce encompassing results that serve as a guideline for researchers.

Data availability

The raw data generated during the current study are available from the corresponding author on reasonable request.

Received: 4 October 2022; Accepted: 6 January 2023

Published online: 20 January 2023

References

- Schabowicz, K. Non-destructive testing of materials in civil engineering. *Materials* **12**, 3237. <https://doi.org/10.3390/ma12193237> (2019).
- Algernon, D., Gräfe, B., Mielentz, F., Köhler, B. & Schubert, F. Imaging of the elastic wave propagation in concrete using scanning techniques: Application for impact-echo and ultrasonic echo methods. *J. Nondestruct. Eval.* **27**, 83–97. <https://doi.org/10.1007/s10921-008-0034-4> (2008).
- Lugovtsova, Y., Bulling, J., Boller, C. & Prager, J. Analysis of guided wave propagation in a multi-layered structure in view of structural health monitoring. *Appl. Sci.* **9**, 4600. <https://doi.org/10.3390/app9214600> (2019).
- Gravenkamp, H., Prager, J., Saputra, A. A. & Song, C. The simulation of lamb waves in a cracked plate using the scaled boundary finite element method. *J. Acoust. Soc. Am.* **132**, 1358–1367. <https://doi.org/10.1121/1.4740478> (2012).
- Ratassepp, M., Rao, J. & Fan, Z. Quantitative imaging of young's modulus in plates using guided wave tomography. *NDT E Int.* **94**, 22–30. <https://doi.org/10.1016/j.ndteint.2017.09.016> (2018).
- Roosen, N., Leclere, Q., Ege, K. & Gerges, Y. Estimation of plate material properties by means of a complex wavenumber fit using hankel's functions and the image source method. *J. Sound Vib.* **390**, 257–271. <https://doi.org/10.1016/j.jsv.2016.11.037> (2017).
- Planès, T. & Larose, E. A review of ultrasonic coda wave interferometry in concrete. *Cem. Concr. Res.* **53**, 248–255. <https://doi.org/10.1016/j.cemconres.2013.07.009> (2013).
- Stache, M., Guettler, M. & Marburg, S. A precise non-destructive damage identification technique of long and slender structures based on modal data. *J. Sound Vib.* **365**, 89–101. <https://doi.org/10.1016/j.jsv.2015.12.013> (2016).
- Pan, B. Recent progress in digital image correlation. *Exp. Mech.* **51**, 1223–1235. <https://doi.org/10.1007/s11340-010-9418-3> (2011).
- Kwiatkowski, J., Anigacz, W. & Beben, D. Comparison of non-destructive techniques for technological bridge deflection testing. *Materials* **13**, 1908. <https://doi.org/10.3390/ma13081908> (2020).
- Leger, A. & Deschamps, M. *Ultrasonic wave propagation in non homogeneous media* vol. **128** (Springer Science & Business Media, 2009) <https://doi.org/10.1007/978-3-540-89105-5>.
- Ablitzer, F., Pézerat, C., Gènevaux, J.-M. & Bégué, J. Identification of stiffness and damping properties of plates by using the local equation of motion. *J. Sound Vib.* **333**, 2454–2468. <https://doi.org/10.1016/j.jsv.2013.12.013> (2014).
- Wassereau, T., Ablitzer, F., Pézerat, C. & Guyader, J.-L. Experimental identification of flexural and shear complex moduli by inverting the timoshenko beam problem. *J. Sound Vib.* **399**, 86–103. <https://doi.org/10.1016/j.jsv.2017.03.017> (2017).
- Latorre-Ossa, H., Gennisson, J.-L., De Broesses, E. & Tanter, M. Quantitative imaging of nonlinear shear modulus by combining static elastography and shear wave elastography. *IEEE Trans. Ultrason. Ferroelectr. Freq. Control* **59**, 833–839. <https://doi.org/10.1109/TUFFC.2012.2262> (2012).
- Savvas, D., Papaioannou, I. & Stefanou, G. Bayesian identification and model comparison for random property fields derived from material microstructure. *Comput. Methods Appl. Mech. Eng.* **365**, 113026. <https://doi.org/10.1016/j.cma.2020.113026> (2020).
- Guillemot, J., Soize, C. & Ghanem, R. G. Stochastic representation for anisotropic permeability tensor random fields. *Int. J. Numer. Anal. Meth. Geomech.* **36**, 1592–1608. <https://doi.org/10.1002/nag.1081> (2012).
- Abrahamsen, P. A review of gaussian random fields and correlation functions. Tech. Rep. Rapport 917, Norsk Regnesentral/Norwegian Computing Center, Oslo (1997). <https://doi.org/10.13140/RG.2.2.23937.20325>.
- Rasmussen, C. E. & Williams, C. K. I. *Gaussian Processes for Machine Learning*, (The MIT Press, Cambridge, 2006) <https://doi.org/10.7551/mitpress/3206.001.0001>.
- Duvenaud, D. K. *Automatic model construction with Gaussian processes*, (University of Cambridge, Cambridge, 2015) <https://doi.org/10.17863/CAM.14087>.
- Papadopoulos, V. & Giovanis, D. G. *Stochastic finite element methods: An introduction*, (Springer International Publishing AG, Cham, 2018) <https://doi.org/10.1007/978-3-319-64528-5>.
- Ghanem, R. G. & Spanos, P. D. *Stochastic finite elements: A spectral approach*, (Springer Science+Business Media, New York, 2012) <https://doi.org/10.1007/978-1-4612-3094-6>.
- Guillemot, J. & Soize, C. Itô sde-based generator for a class of non-gaussian vector-valued random fields in uncertainty quantification. *SIAM J. Sci. Comput.* **36**, A2763–A2786. <https://doi.org/10.1137/130948586> (2014).
- Sepahvand, K. & Marburg, S. Stochastic dynamic analysis of structures with spatially uncertain material parameters. *Int. J. Struct. Stab. Dyn.* **14**, 144029–1–144029–15. <https://doi.org/10.1142/S021945541440029X> (2014).
- Gokhale, N. H., Barbone, P. E. & Oberai, A. A. Solution of the nonlinear elasticity imaging inverse problem: the compressible case. *Inverse Prob.* **24**, 045010. <https://doi.org/10.1088/0266-5611/24/4/045010> (2008).
- Broemeling, L. D. *Bayesian Inference for Stochastic Processes*, (CRC Press, Boca Raton, 2018) <https://doi.org/10.1201/9781315303598>.

26. Papaioannou, I., Betz, W., Zwirgmaier, K. & Straub, D. Mcmc algorithms for subset simulation. *Probab. Eng. Mech.* **41**, 89–103. <https://doi.org/10.1016/j.probingmech.2015.06.006> (2015).
27. Gelman, A. et al. *Bayesian Data Analysis, Third Edition*, (CRC Press, Boca Raton, 2013) <https://doi.org/10.1201/9780429258411>.
28. Literature review and research trends. da Silva Hack, P. & Schwengber ten Caten, C. Measurement uncertainty. *IEEE Trans. Instrum. Meas.* **61**, 2116–2124. <https://doi.org/10.1109/TIM.2012.2193694> (2012).
29. Bárány, I. & Vu, V. Central limit theorems for Gaussian polytopes. *Ann. Probab.* **35**, 1593–1621. <https://doi.org/10.1214/009117906000000791> (2007).
30. Schneider, F., Papaioannou, I., Straub, D., Winter, C. & Müller, G. Bayesian parameter updating in linear structural dynamics with frequency transformed data using rational surrogate models. *Mech. Syst. Signal Process.* **166**, 108407. <https://doi.org/10.1016/j.ymsp.2021.108407> (2022).
31. Marzouk, Y. M. & Najm, H. N. Dimensionality reduction and polynomial chaos acceleration of Bayesian inference in inverse problems. *J. Comput. Phys.* **228**, 1862–1902. <https://doi.org/10.1016/j.jcp.2008.11.024> (2009).
32. Sun, H. C. & You, Y. C. Overview of the diagnostic methods of engineering components damage based on modal analysis. In *Mechanical and Electrical Technology IV*, vol. 229 of *Applied Mechanics and Materials*, 410–414. <https://doi.org/10.4028/www.scientific.net/AMM.229-231.410> (Trans Tech Publications Ltd, 2012).
33. Cugnoni, J., Gmür, T. & Schorderet, A. Inverse method based on modal analysis for characterizing the constitutive properties of thick composite plates. *Comput. Struct.* **85**, 1310–1320. <https://doi.org/10.1016/j.compstruc.2006.08.090> (2007).
34. Sepahvand, K. & Marburg, S. Identification of composite uncertain material parameters from experimental modal data. *Probab. Eng. Mech.* **37**, 148–153. <https://doi.org/10.1016/j.probingmech.2014.06.008> (2014).
35. Sepahvand, K. & Marburg, S. Non-sampling inverse stochastic numerical-experimental identification of random elastic material parameters in composite plates. *Mech. Syst. Signal Process.* **54**, 172–181. <https://doi.org/10.1016/j.ymsp.2014.09.011> (2015).
36. Desceliers, C., Soize, C. & Ghanem, R. Identification of chaos representations of elastic properties of random media using experimental vibration tests. *Comput. Mech.* **39**, 831–838. <https://doi.org/10.1007/s00466-006-0072-7> (2006).
37. Batou, A. & Soize, C. Stochastic modeling and identification of an uncertain computational dynamical model with random fields properties and model uncertainties. *Arch. Appl. Mech.* **83**, 831–848. <https://doi.org/10.1007/s00419-012-0720-7> (2013).
38. Mehrez, L., Doostan, A., Moens, D. & Vandepitte, D. Stochastic identification of composite material properties from limited experimental databases, part ii: Uncertainty modelling. *Mech. Syst. Signal Process.* **27**, 484–498. <https://doi.org/10.1016/j.ymsp.2011.09.001> (2012).
39. Debruyne, S., Vandepitte, D. & Moens, D. Identification of design parameter variability of honeycomb sandwich beams from a study of limited available experimental dynamic structural response data. *Comput. Struct.* **146**, 197–213. <https://doi.org/10.1016/j.compstruc.2013.09.004> (2015).
40. Uribe, F., Papaioannou, I., Betz, W. & Straub, D. Bayesian inference of random fields represented with the Karhunen-Loève expansion. *Comput. Methods Appl. Mech. Eng.* **358**, 112632. <https://doi.org/10.1016/j.cma.2019.112632> (2020).
41. Jardak, M., Su, C.-H. & Karniadakis, G. E. Spectral polynomial chaos solutions of the stochastic advection equation. *J. Sci. Comput.* **17**, 319–338. <https://doi.org/10.1023/A:1015125304044> (2002).
42. Betz, W., Papaioannou, I. & Straub, D. Numerical methods for the discretization of random fields by means of the Karhunen-Loève expansion. *Comput. Methods Appl. Mech. Eng.* **271**, 109–129. <https://doi.org/10.1016/j.cma.2013.12.010> (2014).
43. Vořechovský, M. Simulation of simply cross correlated random fields by series expansion methods. *Struct. Saf.* **30**, 337–363. <https://doi.org/10.1016/j.strusafe.2007.05.002> (2008).
44. Aster, R. C., Borchers, B. & Thurber, C. H. *Parameter Estimation and Inverse Problems*, vol. 90 of *International Geophysics*, (Academic Press, Cambridge, 2005) [https://doi.org/10.1016/S0074-6142\(05\)80014-2](https://doi.org/10.1016/S0074-6142(05)80014-2).
45. Huang, S. P., Quek, S. T. & Phoon, K. K. Convergence study of the truncated Karhunen-Loève expansion for simulation of stochastic processes. *Int. J. Numer. Meth. Eng.* **52**, 1029–1043. <https://doi.org/10.1002/nme.255> (2001).
46. Neal, R. M. Slice sampling. *Ann. Stat.* **31**, 705–767. <https://doi.org/10.1214/aos/1056562461> (2003).
47. Cimrman, R., Lukeš, V. & Rohan, E. Multiscale finite element calculations in python using sfepy. *Adv. Comput. Math.* **45**, 1897–1921. <https://doi.org/10.1007/s10444-019-09666-0> (2019).
48. Latz, J., Eisenberger, M. & Ullmann, E. Fast sampling of parameterised gaussian random fields. *Comput. Methods Appl. Mech. Eng.* **348**, 978–1012. <https://doi.org/10.1016/j.cma.2019.02.003> (2019).
49. Kaipio, J. & Somersalo, E. Statistical inverse problems: discretization, model reduction and inverse crimes. *J. Comput. Appl. Math.* **198**, 493–504. <https://doi.org/10.1016/j.cam.2005.09.027> (2007).
50. Schäffer, T. E. & Hansma, P. K. Characterization and optimization of the detection sensitivity of an atomic force microscope for small cantilevers. *J. Appl. Phys.* **84**, 4661–4666. <https://doi.org/10.1063/1.368707> (1998).
51. Hu, M., Johansson, M., Olsson, A., Oscarsson, J. & Enquist, B. Local variation of modulus of elasticity in timber determined on the basis of non-contact deformation measurement and scanned fibre orientation. *Eur. J. Wood Wood Prod.* **73**, 17–27. <https://doi.org/10.1007/s00107-014-0851-3> (2015).
52. Eberle, R. & Oberguggenberger, M. A new method for estimating the bending stiffness curve of non-uniform euler-bernoulli beams using static deflection data. *Appl. Math. Model.* **105**, 514–533. <https://doi.org/10.1016/j.apm.2021.12.042> (2022).
53. Maletsky, L. P., Sun, J. & Morton, N. A. Accuracy of an optical active-marker system to track the relative motion of rigid bodies. *J. Biomech.* **40**, 682–685. <https://doi.org/10.1016/j.jbiomech.2006.01.017> (2007).
54. Doughty, T. A., Davies, P. & Bajaj, A. A comparison of three techniques using steady state data to identify non-linear modal behavior of an externally excited cantilever beam. *J. Sound Vib.* **249**, 785–813. <https://doi.org/10.1006/jsvi.2001.3912> (2002).
55. Pavić, G. Structure-borne energy flow. In Crocker, M. J. (ed.) *Handbook of Noise and Vibration Control*, 232–240. <https://doi.org/10.1002/9780470172520.CH74> (John Wiley & Sons, Inc., Hoboken, New Jersey, 2007).
56. Hofmann, T., Schölkopf, B. & Smola, A. J. Kernel methods in machine learning. *The annals of statistics* 1171–1220. <https://doi.org/10.1214/009053607000000677> (2008).

Author contributions

K.-A.H.: conceptualization, methodology, software, validation, formal analysis, investigation, resources, writing—original draft, writing—review and editing, visualization, supervision, project administration. M.G.T.K.: methodology, software, validation, formal analysis, investigation, data curation, writing—original draft, visualization. K.S.: writing—review and editing. S.M.: supervision, writing—review and editing. Before submission, all authors agreed with the content and gave explicit consent to submit, they obtained consent from the responsible authorities at the institution listed under author affiliations.

Funding

Open Access funding enabled and organized by Projekt DEAL. Please verify relation to: Technische Universität München (1025).

Competing interests

The authors declare no competing interests.

Additional information

Supplementary Information The online version contains supplementary material available at <https://doi.org/10.1038/s41598-023-27755-5>.

Correspondence and requests for materials should be addressed to K.-A.H.

Reprints and permissions information is available at www.nature.com/reprints.

Publisher's note Springer Nature remains neutral with regard to jurisdictional claims in published maps and institutional affiliations.



Open Access This article is licensed under a Creative Commons Attribution 4.0 International License, which permits use, sharing, adaptation, distribution and reproduction in any medium or format, as long as you give appropriate credit to the original author(s) and the source, provide a link to the Creative Commons licence, and indicate if changes were made. The images or other third party material in this article are included in the article's Creative Commons licence, unless indicated otherwise in a credit line to the material. If material is not included in the article's Creative Commons licence and your intended use is not permitted by statutory regulation or exceeds the permitted use, you will need to obtain permission directly from the copyright holder. To view a copy of this licence, visit <http://creativecommons.org/licenses/by/4.0/>.

© The Author(s) 2023

Identification of a Cantilever Beam's Spatially Uncertain Stiffness

Karl-Alexander Hoppe, Martin G. T. Kronthaler, Kian
Sepahvand and Steffen Marburg

Identification of a Cantilever Beam's Spatially Uncertain Stiffness

A Static Analysis - Model Description

Consider a cantilever beam subjected to static loading F with the deflection response $w(t)$ at a specific position shown in Figure 7. This results in a linear

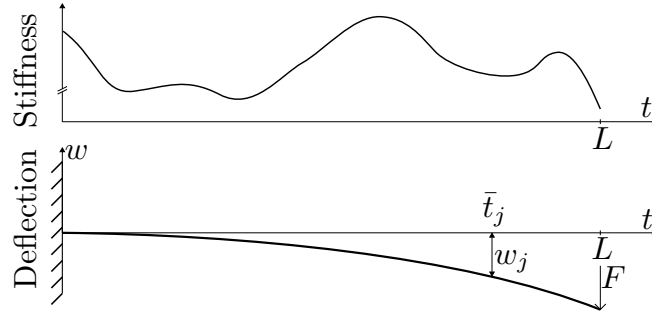


Fig. 7: The top graph shows an arbitrary exemplary stiffness curve of a cantilever beam and the lower graph shows the beam's static deflection when subjected to a load.

forward operator with analytical solutions, see [40].

B Parameters for the Example Calculations

Table 1: Beam properties

Length of beam L	5 m
Height h	0.1 m
Width g	0.1 m

Table 2: Reference random field properties

Mean Young's modulus $\mu_{E,true}$	$2 \times 10^{11} \text{ N/m}^2$
Mean material flexibility $\mu_{C,true}$	$5 \times 10^{-12} \text{ m}^2/\text{N}$
Dimensionality of discretized random field	100
Standard deviation to mean ratio (flexibility based) $\sigma_C/\mu_{C,true}$	0.2
Standard deviation for flexibility field σ_C	$1 \times 10^{-12} \text{ m}^2/\text{N}$
Correlation kernel type	exponential

*Identification of a Cantilever Beam's Spatially Uncertain Stiffness***Table 3:** Random field properties used for inversion

Number of KL Parameters s	6
Correlation kernel type	exponential
Minimum covered variance α for $l = 1$	98.13%

Table 4: Bayesian inversion parameters

Initial values	$\mu_C^{(0)} \sim \mathcal{N}\left(5 \times 10^{-12} \frac{m^2}{N}, (1 \times 10^{-14} \frac{m^2}{N})^2\right)$ $\xi_{d,i}^{(0)} \sim \mathcal{N}\left(0 \frac{m^2}{N}, (1 \times 10^{-15} \frac{m^2}{N})^2\right) \quad \forall i$
----------------	---

*Identification of a Cantilever Beam's Spatially Uncertain Stiffness***B.1 Static Analysis****Table 5:** General parameters

Discretization ground truth	400 integration points
Discretization reconstruction	115 integration points
Force	3,300 N
Maximal absolute deflection	7.21×10^{-2} m

Table 6: Bayesian inversion parameters

Number of chains	8
Total number of samples per chain	7,000
Number of burn-in samples	2,000
Total number of used samples U	40,000
Priors	$\mu_{prior,\mu} = 5 \times 10^{-12} \frac{m^2}{N}$ $\sigma_{prior,\mu} = 5 \times 10^{-13} \frac{m^2}{N}$ $\sigma_{prior,\xi_{i-1}} = 5 \times 10^{-12} \frac{m^2}{N} \quad \forall i > 1$

B.2 Modal Analysis**Table 7:** General parameters

Discretization ground true	100 quadratic elements 201 degrees of freedom for deflection
Discretization reconstruction	50 quadratic elements 101 degrees of freedom for deflection
Number of computed eigenvalues	10
Lowest computed eigenfrequency	3.625 Hz
Highest computed eigenfrequency	863.8 Hz

Table 8: Bayesian inversion parameters

Number of chains	4
Total number of samples per chain	3,500
Number of burn-in samples	1,000
Total number of used samples U	10,000
Priors	$\mu_{prior,\mu} = 5 \times 10^{-12} \frac{m^2}{N}$ $\sigma_{prior,\mu} = 1 \times 10^{-12} \frac{m^2}{N}$ $\sigma_{prior,\xi_{i-1}} = 1 \times 10^{-11} \frac{m^2}{N} \quad \forall i > 1$

C Methods for Second Order Random Fields

C.1 Multivariate Normal Distribution

The normal distribution can be generalized for random vectors x , leading to the multivariate Gaussian (or normal) distribution. Its probability density is defined as [20]:

$$f(\mathbf{x}) = \frac{1}{(2\pi)^{n/2} \cdot |\mathbf{\Gamma}|^{1/2}} \cdot \exp\left(-\frac{1}{2}(\mathbf{x} - \boldsymbol{\mu})^T \mathbf{\Gamma}^{-1}(\mathbf{x} - \boldsymbol{\mu})\right), \quad (16)$$

with $\boldsymbol{\mu}$ being the mean vector and $|\mathbf{\Gamma}|$ being the determinant of the covariance matrix $\mathbf{\Gamma}$.

C.2 Properties of the Covariance Function

The properties of the covariance functions considered here follow Abrahamson [17]: First,

$$Cov(t, t) = 1, \quad (17)$$

and it follows that

$$|Cov| \leq 1. \quad (18)$$

Second, it must be symmetric, meaning

$$Cov(t, t') = Cov(t', t) \quad \forall t, t', \quad (19)$$

and finally, the covariance must be positive semi-definite, meaning

$$\sum_{i=1}^k \sum_{j=1}^k c_i c_j Cov(t_i, t_j) \geq 0 \quad \forall k, \{t_1, \dots, t_k\}, \{c_1, \dots, c_k\}. \quad (20)$$

C.3 Numerical Treatment of the KL Expansion

The eigenvalues λ_i and the eigenfunctions $\varphi_i(t)$ from (2) are the solutions to a Fredholm integral equation of the second kind

$$\int_B Cov(t, t') \varphi_i(t') dt' = \lambda_i \varphi_i(t). \quad (21)$$

The eigenvalues λ_i and eigenfunctions φ_i are ordered as $\lambda_1 \geq \lambda_2 \geq \lambda_3 \dots$. For a Gaussian random field, the KL expansion leads to a representation of the field with uncorrelated ξ_i . Betz et al. [42] give an overview of the feasible methods for solving the integral eigenvalue problem numerically. Here, we use the Nyström method, where the integral in (21) is approximated by a numerical

Identification of a Cantilever Beam's Spatially Uncertain Stiffness

integration scheme. This leads to

$$\sum_{j=1}^k v_j \text{Cov}(t, t_j) \varphi_i(t_j) dt_2 = \lambda_i \varphi_i(t), \quad (22)$$

with the integration weights v_j , $j \in \{1, 2, \dots, k\}$. We use a piece-wise constant integration scheme with integration weights given as the length between the surrounding grid points

$$v_j = \begin{cases} \frac{t_2 - t_1}{2} & \text{if } j = 1 \\ \frac{t_k - t_{k-1}}{2} & \text{if } j = k \\ \frac{t_{j+1} - t_{j-1}}{2} & \text{else.} \end{cases}$$

This leads to the matrix eigenvalue problem

$$\mathbf{C}\mathbf{V}\mathbf{y}_i = \lambda_i \mathbf{y}_i, \quad (23)$$

with the covariance matrix

$$\mathbf{C} = C_{ij} = \text{Cov}(t_i, t_j), \quad (24)$$

and the matrix of integration weights

$$\mathbf{V} = \text{diag}(v_j), \quad (25)$$

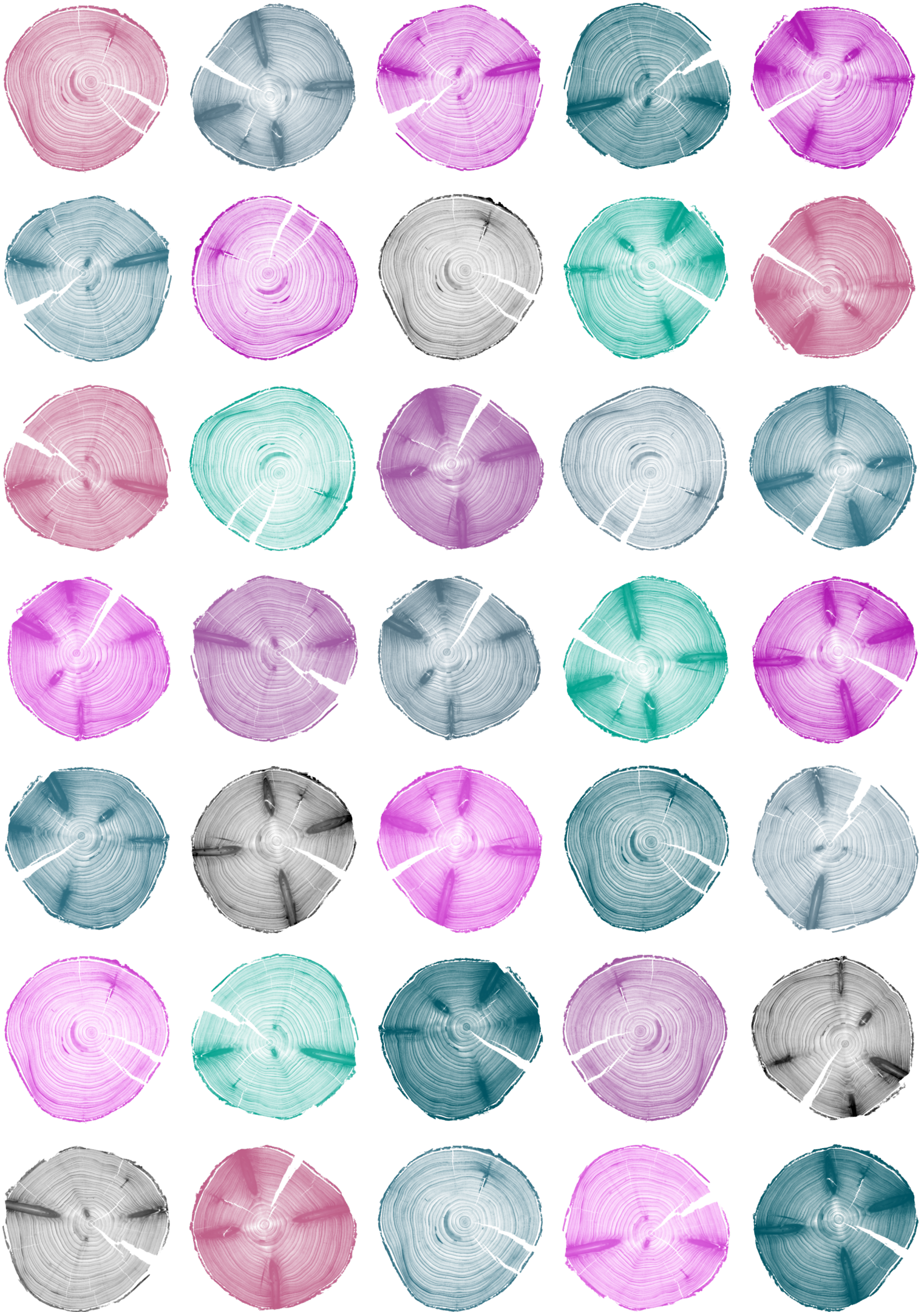
see [42]. The eigenvectors $\mathbf{y}_i = y_{ji} \approx \varphi_i(t_j)$ in Equation (23) approximate the eigenfunctions φ_i . For equidistant grid points t_i and neglecting boundary effects, a scaled identity matrix approximates the matrix of integration weights. The eigenvalues of the covariance matrix need to be scaled with the distance between the grid points for consistency with Equation (23). To consistently account for the random field variance as per Mercer's theorem, the eigenvectors $\hat{\mathbf{y}}_i$ are normalized as

$$\mathbf{y}_i = \frac{\hat{\mathbf{y}}_i}{l_i} \quad \text{with} \quad l_i = \sqrt{\sum_{j=1}^k v_j (y_{ji})^2}, \quad (26)$$

see [42]. The direction of the eigenvectors \mathbf{y}_i needs to be fixed in order for the KL expansion to be a unique representation of a random field in the context of the inverse problem. We prescribe a positive first element of each eigenvector

$$y_{i1} \stackrel{!}{>} 0 \quad \forall i \quad (27)$$

to fix the direction.



Appendix IV

Paper C

Surrogate recycling for structures with spatially uncertain stiffness

Karl-Alexander Hoppe^{*}, Kevin Josef Li, Bettina Chocholaty, Johannes D. Schmid, Kian Kheirollah Sepahvand, and Steffen Marburg

The author retains the right to include this article with the publisher Elsevier in this non-commercially published dissertation. The Journal of Sound and Vibration is the original source of publication for this article.

^{*}orcid.org/0000-0002-3048-8284



ELSEVIER

Contents lists available at ScienceDirect

Journal of Sound and Vibration

journal homepage: www.elsevier.com/locate/jsvi

Surrogate recycling for structures with spatially uncertain stiffness

Karl-Alexander Hoppe^{a,*}, Kevin Josef Li^{a,2}, Bettina Chocholaty^{a,3},
Johannes D. Schmid^{a,4}, Simon Schmid^{b,5}, Kian Sepahvand^{a,6}, Steffen Marburg^{a,7}^a Chair of Vibroacoustics of Vehicles and Machines, TUM School of Engineering and Design, Technical University of Munich, Boltzmannstraße 15, Garching bei München, 85748, Germany^b Chair of Non-Destructive Testing, TUM School of Engineering and Design, Technical University of Munich, Franz-Langinger-Straße 10, München, 81245, Germany

ARTICLE INFO

Keywords:

Material parameter identification
Modal analysis
Generalized polynomial chaos
Bayesian inference
Karhunen-Loève expansion
Functionally graded material

ABSTRACT

This study expands the existing methods for non-destructively identifying the spatially varying material properties of a structure using modal data. It continues a recently published approach to this inverse problem that employed Bayesian inference in conjunction with the Karhunen-Loève expansion to solve it. Here, we present two developments. Firstly, eigenvectors are used instead of eigenvalues, improving the results significantly. Secondly, a generalized polynomial chaos surrogate accelerates the inversion procedure. Finally, we develop a methodology for reusing the surrogate model across inversion tasks. We demonstrate the efficacy and efficiency of this methodology via the field of additive manufacturing and the fused deposition modeling process. The good results promise profound computational cost saving potential for large-scale applications.

1. Introduction

Non-homogeneous materials are receiving increasing attention from researchers. Owing to advances in computational power, naturally non-homogeneous materials and those, where the manufacturing process induces unintentional non-homogeneity, see Gupta and Gupta [1], are being regarded. On the other hand, functionally graded materials are being popularized, see Garcia et al. [2], which creates demand for corresponding testing methods. With functionally graded materials, the material parameters are varied spatially with intent. Marzouk and Najm [3] develop a method that is useful for characterizing such a material and Uribe et al. [4] apply a related method successfully to the identification of spatially varying stiffness using static deflection data of a structure.

Sundararajan et al. [5] report that the material non-homogeneity significantly influences the vibration behavior of functionally graded plates. As a response to this, Hoppe et al. [6] propose a non-destructive resonance frequency method for identifying the spatially varying stiffness of structures. Frequency response functions at several observation points improve the estimation of

* Corresponding author.

E-mail address: alexander.hoppe@tum.de (K.-A. Hoppe).1 <https://orcid.org/0000-0002-3048-8284>2 <https://orcid.org/0000-0002-5885-0863>3 <https://orcid.org/0000-0003-3840-5946>4 <https://orcid.org/0000-0002-7106-2407>5 <https://orcid.org/0000-0002-7509-6217>6 <https://orcid.org/0000-0001-6952-250X>7 <https://orcid.org/0000-0001-6464-8015><https://doi.org/10.1016/j.jsv.2023.117997>

Received 14 February 2023; Received in revised form 5 August 2023; Accepted 7 August 2023

Available online 9 August 2023

0022-460X/© 2023 Elsevier Ltd. All rights reserved.

the piece-wise non-homogeneous Young's modulus [7,8]. Batou and Soize [9] extend this procedure to account for continuously non-homogeneous materials in composite structures.

The framework by Marzouk and Najm [3] demands that the covariance of the spatially varying material property is known. Sraj et al. [10] propose a procedure that eliminates the requirement of having *a priori* knowledge of the covariance hyper-parameters using this established Bayesian inference framework in conjunction with the Karhunen-Loève expansion and generalized polynomial chaos expansion. Siripatana et al. [11] accelerate this procedure by adding a second, nested generalized polynomial chaos surrogate. However, these studies assume that the covariance hyper-parameters of the unknown spatially varying quantity are notoriously intangible.

Indeed, the linkage between manufacturing process parameters and the properties of the manufactured parts continues to elude researchers. The following paragraphs ponder why process-structure-property relations, that is the impact of process parameters on part properties, are so hard to identify within the scope of additive manufacturing.

Complexity must be mentioned as the first inhibitor. Hashemi et al. [12] stress that the knowledge of the underlying physics is incomplete. Non-linearity is notoriously hard to capture in the context of additive manufacturing, and excitation as well as boundary conditions are not approximated well enough, see Gatsos et al. [13]. Not only are the process-structure-property relations complex, so are the process parameters themselves [14–16]. On top of that, often more than 10 process parameters exhibit a relevant impact [12]. Models need to be harmonized across scales and time-scales [17]. In addition to being cost and time-intensive, the necessary experiment chains and cohesive multi-scale approaches [18,19] are prone to error propagation.

Secondly, the completeness and lack thereof present a recurring theme in the literature. A perpetual dichotomy seems to be present in the literature. It is often stated that a substantial amount of work has been completed, but that significant gaps remain [18,20]. Specifically, many physical phenomena have yet to be examined, more materials and manufacturing processes should be studied, and a broader range of process-structure-property relations are to be investigated, see Patham and Foss [21]. In general, more experimental and high-fidelity numerical data that are transparent and accessible are needed [21].

Finally, process-structure-property relations are plagued by uncertainties. The lack of deterministic process-structure-property relations stems from the aleatoric uncertainty that part properties entail and the epistemic uncertainty connected to physics-based models [22,23]. There exists considerable interest in the statistical information entailed by materials and their processing, where the correlations of the process-structure-property relations have yet to be established [24].

The integrated computational materials engineering framework proposed by Horstemeyer and Sahay [25] is a design approach that attempts to connect material models across different scales. Ghosh [26] predicts that multi-scale modeling will accelerate the discovery of the correlations of process-structure-property relations within the integrated computational materials engineering framework. They anticipate this to be achieved by the generation of large amounts of data and the subsequent completion of process-structure-property relations via data-driven methods.

We suggest an abstraction that may serve as a remedy. While process-structure-property relations continue developing, we instead consider the manufacturing process parameters as random processes and the material parameters of the manufactured part as random fields. Manufacturing process parameters such as feeding speeds or valve opening trajectories are not deterministic. Conversely, they are of stochastic nature due to closed-loop control and non-linearity among others and thus they are random processes. Similarly, the manufactured part exhibits inherently stochastic material properties that turn from random variables to random fields in the case of heterogeneity. A link between the random field length-scales of the process parameters and the material properties is significantly easier to establish than a direct one between the corresponding parameters. Especially when the material parameter exhibits a linear dependence on the process parameter, the length-scale of the latter as a Gaussian process propagates to the material parameter. We leverage this link to accelerate the inference of spatially varying material parameters of parts designed to meet different requirements that are configured similarly. For the additive manufacturing process fused deposition modeling [27–29], which uses plastics as a material, we train a surrogate for one set of hyper-parameters and then recycle this surrogate for modified configurations of the part.

This paper is organized as follows: Section 2 presents the theoretical preliminaries for our non-destructive material parameter identification workflow. These concepts are applied to the identification of spatially varying stiffness given a structure's modal data in Section 3. This section demonstrates the novel methodology, where the surrogate used for stiffness identification is trained using one configuration and recycled for the others. The results of this demonstrator are presented in Section 4 and discussed in Section 5, where we also draw conclusions from our findings.

2. Methods for inferring dimensionality-reduced random fields employing surrogate models

This section covers all relevant methods necessary for the generation of our results in Section 4. Section 2.1 formulates the Bayesian inverse problem setup, Section 2.2 describes the reduction of the random space via the Karhunen-Loève expansion, and Section 2.3 briefly covers how the generalized polynomial chaos surrogate is constructed on this dimensionality-reduced space. Finally, Section 2.4 details the transformation of the generalized polynomial chaos surrogate when the Karhunen-Loève expansion, whose coefficients are the surrogate inputs, changes.

2.1. Inverse problem setup using the Bayesian approach

Consider an ideal forward model \mathbf{G}

$$\mathbf{d} = \mathbf{G}(\mathbf{m}) + \epsilon, \quad (1)$$

where \mathbf{d} is the data, \mathbf{m} are the model parameters, and ϵ is independent and ideally distributed Gaussian measurement noise. Given the data \mathbf{d} and the forward model, solving the inverse problem is to estimate the unknown model parameters. One way of solving an inverse problem is the Bayesian approach. Bayes' rule reflects how new data updates our prior beliefs, formulated as the prior probability distribution $\rho(\mathbf{m})$, concerning the unknowns \mathbf{m} . Expressing these quantities in terms of probability densities produces Bayes' theorem

$$\pi_m(\mathbf{m}) = \rho(\mathbf{m}|\mathbf{d}) \propto \rho(\mathbf{d}|\mathbf{m})\rho(\mathbf{m}), \quad (2)$$

stating that the posterior probability density $\rho(\mathbf{m}|\mathbf{d})$ of the model parameters given the data is proportional to the product of the likelihood and prior probability density. The likelihood

$$\mathcal{L}(\mathbf{m}) = \rho(\mathbf{d}|\mathbf{m}) = \rho_\epsilon(\mathbf{d} - \mathbf{G}(\mathbf{m})) \quad (3)$$

measures how likely an observation of the data \mathbf{d} is, given the model parameters \mathbf{m} .

Sampling from the posterior distribution is often achieved with exploration algorithms. The samples approximate the true posterior density and allow for the calculation of statistical moments. A computationally cheaper strategy is finding the mode of the posterior probability density by solving an optimization problem. This approach, which explicitly does not estimate the expected value, is called the maximum a posteriori estimate:

$$\mathbf{m}_{\text{MAP}} = \arg \max \mathcal{L}(\mathbf{m})\rho(\mathbf{m}). \quad (4)$$

2.2. Karhunen-Loève expansion

When identifying the properties of homogeneous materials, the parameters are typically interpreted as random variables in the context of Bayesian inference. For non-homogeneous materials, the material parameters are spatially varying and are considered as functions that live on the spatial domain of the structure. Fine discretization of these functions yields a large number of unknowns that have to be identified in the inversion procedure. This collection of random variables can be described as a random field. Second order random fields are fully described by their mean and covariance functions. The covariance function of two points \mathbf{x} and \mathbf{x}' reads as

$$C(\mathbf{x}, \mathbf{x}') \approx \sum_{i=1}^K \lambda_i \phi_i(\mathbf{x})\phi_i(\mathbf{x}') \quad \text{with} \quad \|\phi_i\| = 1 \quad (5)$$

and is decomposable using its eigenvalues λ_i , eigenfunctions ϕ_i , and K terms.

Having to approximate a high-dimensional multi-variate distribution is detrimental to the inversion procedure, as the inference must then traverse this high-dimensional space. Mercer's theorem, see Eq. (5), is the basis for the Karhunen-Loève expansion [30], which offers a remedy. The Karhunen-Loève expansion of a random field coincides with a dimensionality reduction of the random space. Specifically, the random dimensionality is decoupled from the spatial discretization and reduced to the truncation order K . The truncated Karhunen-Loève expansion reads as

$$M_K(\mathbf{x}, \omega) = \boldsymbol{\mu}(\mathbf{x}) + \sum_{i=1}^K \sqrt{\lambda_i} \eta_i(\omega) \phi_i(\mathbf{x}). \quad (6)$$

Here, M is a Gaussian second order random field, $\boldsymbol{\mu}$ is the mean function, and η_i are the Karhunen-Loève coefficients. Now, η_i represent the new finite collection of random variables that encapsulate the random field's variability by means of the Karhunen-Loève expansion. They can be used to generate realizations of the random field when sampled from standard normal distributions.

2.3. Dimensionality-reduced generalized polynomial chaos

Marzouk and Najm [3] pioneer the combination of the Karhunen-Loève expansion with generalized polynomial chaos in the context of Bayesian inference. The use of generalized polynomial chaos as a surrogate is beneficial when forward model evaluations are computationally expensive. This is especially relevant for methods employing Markov chains for the posterior's exploration.

The goal of the generalized polynomial chaos expansion within this scope is to construct a computationally less expensive surrogate for the forward model $\mathbf{G}(\boldsymbol{\eta})$. This surrogate employs both, an expansion of the forward model inputs

$$\hat{\eta}_i = g_i(\boldsymbol{\xi}) = \sum_{k=0}^{N_{p1}} a_{ik} \Psi_k(\boldsymbol{\xi}) \quad (7)$$

and an expansion of the forward model outputs

$$\hat{G}_i = \sum_{k=0}^{N_{p2}} \beta_{ik} \Psi_k(\xi). \quad (8)$$

Here, the number of terms

$$N_p + 1 = \frac{(n+p)!}{n!p!} \quad (9)$$

depends on the polynomial order p and the number n of input random variables ξ . When the Karhunen-Loève coefficients comprise the model inputs, an optimal generalized polynomial chaos expansion can be achieved by using Hermite polynomials for the polynomial basis Ψ , as the Karhunen-Loève coefficients are standard normally distributed. After obtaining the generalized polynomial chaos coefficients \mathbf{a} and β using stochastic collocation, drawing samples from ξ and evaluating the generalized polynomial chaos surrogate $\hat{G}(\xi)$ accordingly yields response samples that approximate the true model response.

2.4. Removing the surrogate model's dependence on the random field hyper-parameters

A new generalized polynomial chaos surrogate must be computed, when the parametrization of the Gaussian process prior on the quantity of interest changes. When the covariance hyper-parameters of the random field change, so does its Karhunen-Loève expansion, as the eigenvalues and eigenvectors are updated. Because the generalized polynomial chaos surrogate utilizes an expansion of the Karhunen-Loève coefficients to construct the generalized polynomial chaos expansion of the model outputs, it must be trained anew. Srjaj et al. [10] resolve this dependency and develop a more flexible variant of the Karhunen-Loève expansion that need not be recomputed when the covariance hyper-parameters change. In the following paragraphs, we briefly summarize the study by Srjaj et al. [10], as it is not uniformly known within the community.

The transformation from one parametrization of a covariance function to another by leveraging the projection of their respective eigenfunctions onto each other lies at the core of their method. It is the aim to transform from a reference covariance $C(\mathbf{q}^r) = C^r$ with a set of reference hyper-parameters \mathbf{q}^r to a covariance endowed with different hyper-parameters. After being projected onto them, the new eigenfunctions $\Phi_i(\mathbf{q})$ can be expressed in terms of the reference eigenfunctions

$$\Phi_i(\mathbf{q}) = \sum_{i'=1}^{\infty} b_{ii'}(\mathbf{q}) \phi_{i'}^r \quad \text{with} \quad b_{ii'} = (\phi_{i'}^r, \Phi_i(\mathbf{q}))_X, \quad (10)$$

where $(U, U)_X$ denotes the inner product. These so-called scaled eigenfunctions are defined in the context of the target covariance as the product of its eigenvalues and eigenfunctions as

$$\Phi(\mathbf{q})_i = \sqrt{\lambda_i(\mathbf{q})} \phi_i(\mathbf{q}). \quad (11)$$

The Karhunen-Loève expansion corresponding to the target covariance can now be expressed in terms of the reference covariance as

$$M_K(\omega, \mathbf{q}) = \sum_{i=1}^K \Phi_i(\mathbf{q}) \eta_i(\omega) \approx \sum_{i=1}^K \left(\sum_{i'=1}^K b_{ii'}(\mathbf{q}) \phi_{i'}^r \right) \eta_i(\omega) = \sum_{i=1}^K \phi_i^r \eta_i^{\text{ct}}(\omega, \mathbf{q}). \quad (12)$$

The transformed Karhunen-Loève coefficients

$$\eta_i^{\text{ct}}(\omega, \mathbf{q}) = \sum_{i'=1}^K b_{i'i}(\mathbf{q}) \eta_{i'}(\omega) \quad (13)$$

are found using the reference Karhunen-Loève coefficients and the projection coefficients $b_{i'i}$. They read as

$$\boldsymbol{\eta}^{\text{ct}}(\omega, \mathbf{q}) = \mathcal{B}(\mathbf{q}) \boldsymbol{\eta}(\omega) \quad (14)$$

in matrix form. Finally, a transformed surrogate is obtained, where the generalized polynomial chaos expansion reads as

$$G_j(\boldsymbol{\eta}, \mathbf{q}) = G_j^r \approx \hat{G}_j^r(\boldsymbol{\xi}(\boldsymbol{\eta}, \mathbf{q})) = \sum_{i=0}^{N_{p2}} \beta_{ji} \Psi_i(\boldsymbol{\xi}(\boldsymbol{\eta}, \mathbf{q})) \quad \text{with} \quad \boldsymbol{\xi}(\boldsymbol{\eta}, \mathbf{q}) = \hat{\mathcal{B}}(\mathbf{q}) \boldsymbol{\eta}, \quad (15)$$

where the $\hat{\mathcal{B}}$ -matrix is defined as

$$\hat{\mathcal{B}}(\mathbf{q}) = \begin{cases} \frac{B_{ki}(\mathbf{q})}{\sqrt{\lambda_k^r}} & \text{if } \frac{\lambda_k^r}{\lambda_1^r} > \kappa \quad \text{with} \quad \kappa \approx 1 \times 10^{-12}, \\ 0 & \text{otherwise.} \end{cases} \quad (16)$$

This transformed surrogate is trained on the reference covariance, as it reuses the corresponding generalized polynomial chaos coefficients and applies a transformation to the input random variables $\boldsymbol{\eta}$. It may be used to approximate a system whose input random field is described by a different covariance function, termed the target covariance.

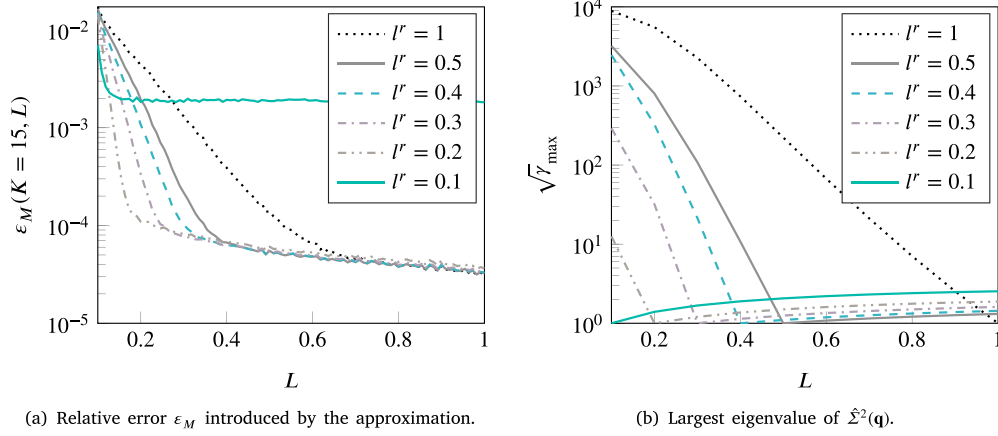


Fig. 1. Relative error ε_M and $\sqrt{\gamma_{\max}}$ for a range of ratios between reference and transformed random field, following Sraj et al. [10].

The relative error ε_M between a random field M and its transformed representation M_K^{ct} reads as

$$\varepsilon_M(K, \mathbf{q}) = \frac{\|M(\mathbf{q}) - M_K^{\text{ct}}(\mathbf{q})\|_{L^2}}{\|M(\mathbf{q})\|_{L^2}}, \quad (17)$$

where

$$\|U\|_{L^2}^2 \doteq \mathbb{E}[(U, U)_X]. \quad (18)$$

The left graph within Fig. 1 shows this error for $K = 15$, a squared exponential kernel with variance $\sigma^2 = 0.5$, and varying parametrization $\mathbf{q} = L$. The right graph shows the square root of $\gamma_{\max}(\mathbf{q})$, the largest eigenvalue of the covariance matrix $\hat{\Sigma}^2(\mathbf{q}) = \hat{B}^T(\mathbf{q})\hat{B}(\mathbf{q})$.

A pseudo-algorithm of our method for training a generalized polynomial chaos expansion surrogate model for one length-scale and then solving multiple inverse problems at different length-scales without having to train the surrogate anew for those cases is given in Algorithm 1. After a selection of the reference hyper-parameters and the decomposition of the corresponding covariance, the Karhunen-Loève coefficients represent the inputs to the model \mathbf{G} . The coefficients \mathbf{a} and β of the surrogate can then be obtained by means of least squares for model evaluations at collocation points of the inputs. Any required covariance distinct from the reference covariance may now be described by the Karhunen-Loève expansion. Using the inner product of its eigenfunctions with those of the reference covariance then serves to make the Karhunen-Loève coefficients suitable for use with the original surrogate by transformation. Finally, the posterior of the transformed coefficients can be evaluated.

Algorithm 1 Pseudo-algorithm for constructing a surrogate for the reference hyper-parameters and then transforming it to evaluate the posterior for other ground truth hyper-parameters.

```

1: procedure SURROGATE CONSTRUCTION FOLLOWING SRAJ ET AL. [10]
2:    $C^r \leftarrow \mathbf{q}^r$  ▷ Select reference hyper-parameters
3:    $(\lambda_i^r, \phi_i^r)_{i=1, \dots, K} \leftarrow C^r$  ▷ Decompose covariance
4:    $\mathbf{a}, \beta \leftarrow \mathbf{G}$  ▷ Solve generalized polynomial chaos collocation problem
5: end procedure
6: for  $\mathbf{q}_j$  in  $\{\mathbf{q}_1, \mathbf{q}_2, \dots, \mathbf{q}_n\}$  do ▷ Select desired target hyper-parameters for recycling
7:   procedure SURROGATE RECYCLING
8:      $C \leftarrow \mathbf{q}_j$ 
9:      $(\lambda_i, \phi_i)_{i=1, \dots, K} \leftarrow C$  ▷ Decompose covariance
10:     $M_K \leftarrow \sum_{i=1}^K \Phi_i \eta_i$ 
11:     $\hat{B}(\mathbf{q}_j) \leftarrow \Phi, \phi^r$  ▷ Transform coefficients
12:     $\xi \leftarrow \hat{B}(\mathbf{q}_j)\eta$ 
13:     $\mathbf{m}_{\text{MAP}} \leftarrow \mathcal{L}, \rho$  ▷ Evaluate posterior
14:   end procedure
15: end for

```

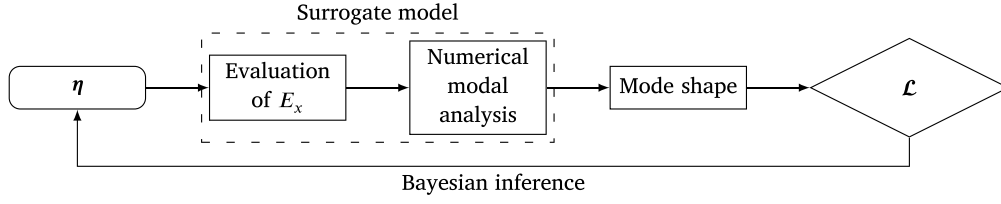


Fig. 2. General procedure for reconstructing the reference random field given a mode shape and assuming the covariance, priors, and measurement noise characteristics with Bayesian inference. The Karhunen-Loève coefficients η are the quantities of interest. Within each step of the Bayesian inference sequence, the evaluation of the Karhunen-Loève expansion with these coefficients yields E_x with the full spatial resolution. Numerical modal analysis is carried out using this E_x assigned within the finite element model, yielding the beam's first mode shape. The inference uses a generalized polynomial chaos surrogate here that connects η to a probe grid for the first mode shape. Upon comparison with the noisy measurement using the likelihood \mathcal{L} , this step within the Bayesian inference is complete and a new sample of η is drawn subsequently.

3. Procedure

3.1. Preliminary study and proof of concept: Dimensionality-reduced and generalized polynomial chaos accelerated inference of Young's modulus using mode shape data

In this section, we apply the accelerated and dimensionality-reduced inference procedure by Marzouk and Najm [3] to the non-destructive identification of spatially varying stiffness given mode shape information.

We present our application as a preliminary study and proof of concept for our methodology that will be introduced later. The quantity of interest is a random function defined on one spatial dimension. It represents the Young's modulus in x -direction $E_x(x)$ of a beam measuring $x \times y \times z = 450 \times 60 \times 9$ mm with free-free boundary conditions. The numerical modal analysis is carried out in a python-based finite element method software [31] with a structured mesh and 5472 quadratic elements. The first eigenvector of the structure obtained from performing numerical modal analysis given the ground truth Young's modulus makes up the synthesized measurement data. A signal-to-noise ratio of 60 dB describes the simulated independent and identically distributed Gaussian measurement noise. The reader is referred to Fig. 2 for a visual representation of our procedure and especially the scope of the surrogate model.

The material's statistical moments read as follows: The Young's modulus $E_x(x)$ is described by a mean \bar{E}_x of 3 MPa and a standard deviation of $\sigma_{E_x} = 1\% \times \bar{E}_x$. The material is modeled as a random field over x and endowed with a Gaussian process prior with a Matérn covariance kernel [32]

$$C(\mathbf{x}, \mathbf{x}') = \sigma^2 \frac{2^{1-\nu}}{\Gamma(\nu)} \left(\frac{\sqrt{2\nu} |\mathbf{x} - \mathbf{x}'|}{L} \right)^\nu K_\nu \left(\frac{\sqrt{2\nu} |\mathbf{x} - \mathbf{x}'|}{L} \right), \quad (19)$$

where $\Gamma(\nu)$ denotes the gamma function and K_ν is a modified Bessel function [33]. The smoothing parameter and correlation length are set to $\nu = 3/2$ and $L = L_2 = 450$ mm, respectively. The second order generalized polynomial chaos expansion is used in conjunction with a Karhunen-Loève expansion truncated to 5 terms. The Karhunen-Loève coefficients η are appropriately equipped with standard normal prior distributions, since $\eta \sim \mathcal{N}(0, 1)$. We use a non-normalized logarithmic likelihood $l(X_{\text{meas}}|\eta)$ of observing the displacements X_{meas} connected to the first eigenvector at the top of the geometry

$$l(X_{\text{meas}}|\eta) = -\frac{1}{2} \sum_{j=1}^N \frac{(X_{\text{meas}_j} - \hat{G}_j(\eta))^2}{\epsilon_j^2}, \quad (20)$$

where $N = 522$ is the number of evaluation points at the top of the geometry within the finite element model. Here, the likelihood variances are set equal to the measurement noise ϵ , which is obtained by applying the signal-to-noise ratio to the deterministic ground truth simulation mode shape data. The synthetic measurement is carried out 10 times in total.

3.2. Application of the methodology to material parameter identification for functionally graded fused deposition modeling parts

This section introduces the manufacturing process and the material models used in the academic example. It describes the chosen part configurations used in the example, see Section 3.2.1, and the process parameters together with the estimation of their length-scales, see Section 3.2.2. Finally, Section 3.2.3 introduces uncertainty into the material parameters.

In the following, we demonstrate how, given a correlation between process and part parameter length-scales, the knowledge of the former enables surrogate model recycling. By leveraging this link between the length-scales, this procedure exhibits significant computation cost improvements over existing procedures as soon as a part is designed for more than one configuration. It relies on the combination of the Karhunen-Loève expansion and generalized polynomial chaos within Bayesian inference. The novel interpretation of the coordinate transformation described in Section 2.4 makes it possible to reuse a surrogate for configurations other than the reference configuration. We demonstrate this for the acceleration of the inference of spatially varying material parameters, see Fig. 3. Here, the manufacturing parameters possess length-scale L_I , which is linked with the length-scale $L_{I'}$ of the functionally graded material. In a first step, the elastic material properties are identified from modal data, whereby a surrogate for the numerical model is employed to decrease computational cost. Now, the same surrogate can be recycled for parts, where the connected manufacturing process parameters possess length-scales $L_{II}, L_{III}, \dots, L_m$, owing to the coordinate transformation.

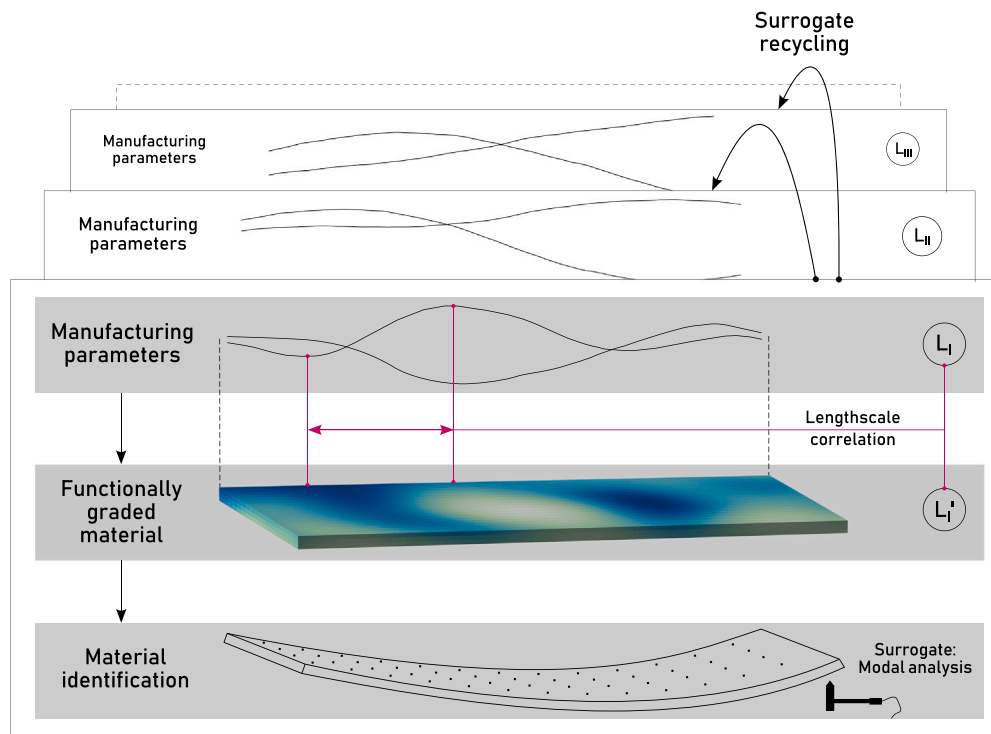


Fig. 3. The figure shows the proposed novel methodology for recycling surrogate models connecting spatially random materials to a structure's mode shape. The recycling is employed based on length-scale correlations between the manufacturing process parameters on the one hand and the resulting material properties on the other hand. This procedure is embedded into the non-destructive material parameter identification that uses a Bayesian approach for solving the inverse problem.

3.2.1. Part configurations

The goal for the considered manufacturing process is to produce three geometrically identical parts that are designed for distinct applications. In the context of large assemblies, interfaces dominate the development cost. If the production volume is high, the production cost is equally affected. The flexibility of application while maintaining the cost-sensitive compliance with interface requirements is enabled through the functional grading realized with the fused deposition modeling process and filaments A and B. The optimized, functionally graded parts offer surplus yield strength in regions with high equivalent stresses and reduce the yield stress in locations where high strength is not a requirement. The theoretically resulting deterministic stiffness profiles improve the minimum safety of the assembly for the functionally graded parts in comparison to the homogeneous parts. On the one hand, this may be used to reduce weight while retaining the safety, on the other hand, the safety-margin can be improved at constant part mass. The latter is pursued here, as keeping the overall part mass constant reduces the need for load bearing changes in the overall assembly due to changes in the part mass, thus further lowering costs.

All configurations involve a structural beam with dimensions $450 \times 60 \times 9$ mm. Each of the three functionally graded beams is designed to meet the changing requirements posed by a different application configuration. For the demonstration, we vary the external loads and the boundary conditions.

- Configuration 1, shown in Fig. 4, is a cantilever beam with a clamping on the left side and the load located on the right side at the free end. An equivalent one-dimensional and homogeneous system exhibits a linear bending moment curve M_B , as marked in the figure with contrasting styling. Designing a material with properties appropriate for the stress decreasing together with the distance from the clamping requires a matching grading of the yield stress. Choosing a linear yield stress curve leads to the largest length-scale considered in this study.
- Configuration 2, shown in Fig. 4, is a cantilever beam with a clamping on the left side and a free tip, which is subject to a line load p . An equivalent homogeneous one-dimensional system exhibits a bending moment curve M_B proportional to the trunk of a parabola, as the contrasting line displays. Designing a material with an according grading of the yield stress necessitates a decreasing yield stress with growing distance from the clamping. The volume fractions are endowed with a medium correlation length to assimilate half of a parabolic curve in the material parameters.
- Configuration 3, shown in Fig. 4, involves a beam with the pinned boundary condition on the left side and a roller bearing at the right end. Subjected to a line load, an equivalent one-dimensional and homogeneous system possesses a parabolic bending moment curve M_B that is plotted with a contrasting color. Designing a material with an according grading of the yield stress requires the maximum yield stress to be at the center between the bearings and the minimum yield stresses to be located at the bearings. Here, the smallest length-scale investigated in this study is appropriate for the described yield stress distribution.

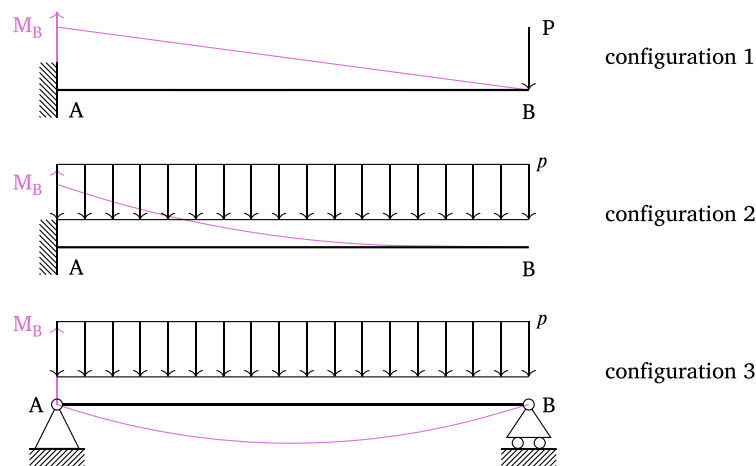


Fig. 4. Part design configurations: For configuration 1, the cantilever beam is clamped on the left side and subject to a load located at the free end on the right. In configuration 2, the cantilever beam is clamped on the left side and subject to a line load acting on the entire domain. In configuration 3, the beam is pinned on the left side and has a roller bearing on the right side. Again, a line load acts on the entire domain.

Table 1

This table lists the characteristics of the exemplary homogeneous material that serves as the material for the baseline parts and thus as a reference for the functionally graded parts. Specifically, the popular additive manufacturing thermoplastic ABS is chosen to be the reference in terms of density and stiffness.

	Homogeneous material
Name	ABS
Young's modulus	3×10^3 MPa
Yield stress	48.3 MPa
Density	1190 kg m^{-3}

As a reference for the virtual functionally graded parts, consider a virtual traditional homogeneous part made of a typical additive manufacturing thermoplastic, see [Table 1](#), whose Young's modulus is expected as 3×10^3 MPa. For the functionally graded parts, consider two materials, of which filament A is less stiff than the baseline material with 2.5×10^3 MPa, while filament B is stiffer than the baseline with 3.5×10^3 MPa. The average stiffness and mass density of filaments A and B are equal to that of the baseline material for the sake of comparability. This in turn necessitates also fictitious filaments, as no existing materials fulfill this equality constraint perfectly (see [Table 2](#)).

3.2.2. Fused deposition modeling

Our academic example is centered around fused deposition modeling, see [Fig. 5](#). Fused deposition modeling is a multi-material additive manufacturing process categorized within material extrusion. Thermoplastic polymers make up the most common stock material for this process. Typically dual nozzle systems are employed, where a separate feed mechanism passes through the extrusion head for each of the two filaments. The building strategy consists of assigning a filament type to each position on the build bed. Consequently, the smoothness of the functional grading at the macro-scale depends on the spatial resolution of the building strategy [29].

For simplicity, we consider the positional volume fractions resulting from the building strategy as the process parameters in this study and assume that their length-scales match those of the compound material parameters.

The building strategy involving filaments A and B tailors the part to the specific application configuration via functional grading. [Figs. 6](#) and [7](#) show possible volume fraction designs for both materials that need to be accomplished by the building strategy for all configurations. Here, the material strength is shifted towards regions with high stresses, while the overall mass stays constant.

In practice, the length-scale is readily estimated by the maximum-likelihood-estimate of the covariance connected to the standard Gaussian process regression equation applied to the volume fractions. A naïve estimate thereof suffices for this demonstration. The variability of the profile for configuration 1 is the smallest, while it increases for configuration 2 and increases further for configuration 3. With this observation, we arrive at the estimated length-scales reported in [Table 3](#). To rule out any errors by length-scale approximation for this study, the ideal stiffness profiles are projected onto the eigenfunctions of a covariance operator parameterized with the length-scales provided in [Table 3](#).

Table 2

This table presents the Young’s modulus, yield stress, and density of the two exemplary materials used in the fused deposition modeling process. Filament A has 5/6 of the homogeneous material’s stiffness and density, while filament B has 7/6 of the homogeneous material’s stiffness and density. Filament A is thus the less stiff and dense component and filament B provides higher stiffness at the drawback of increased density.

	Filament A	Filament B
Young’s modulus	2.5×10^3 MPa	3.5×10^3 MPa
Yield stress	40.3 MPa	56.4 MPa
Density	992 kg m^{-3}	1390 kg m^{-3}

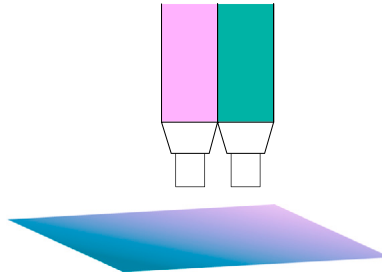


Fig. 5. Sketch of the fused deposition modeling principle. The jet shown at the top of the image is capable of producing a part, which is shown at the bottom, whose material distribution is functionally graded.

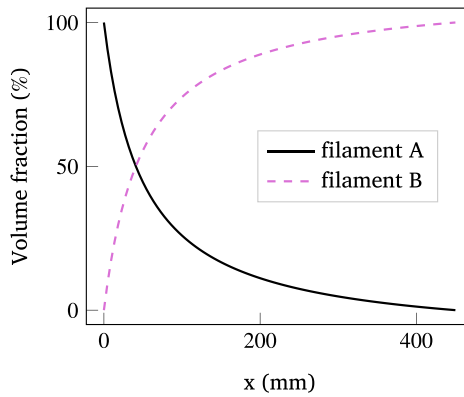


Fig. 6. Configuration 2 (reference): Here, the volume fraction corresponding to filament A decreases hyperbolically, while that of filament B constitutes the remainder. These volume fractions represent the ideal deterministic volume fractions that correspond to the ideal deterministic stiffness profiles and that are not manufacturable in practice.

Table 3

The table lists the naive length-scale estimates for each configuration. The volume fractions’ length-scales pose the optimal choice for the priors on the material parameter length-scales and care should be taken to correctly identify them. For our academic problem, we assume these length-scales to be known by projecting the stiffness profiles onto the eigenfunctions of a covariance function with the respective length-scale.

	configuration 1	configuration 2	configuration 3
Length-scale	$L_1 = 900 \text{ mm}$	$L_2 = 450 \text{ mm}$	$L_3 = 225 \text{ mm}$

3.2.3. Assumption of the manufacturable stiffness profiles as realizations of Gaussian processes

In theory, with a deterministic linear manufacturing process and deterministic materials, the shown material volume fractions translate into Young’s modulus functions over x assuming a linear volumetric Young’s modulus law. Fig. 8 shows the corresponding stiffness profiles for configuration 1, configuration 2, and configuration 3. These present the ideal aggregated stiffness profiles that raise the minimum safety-margin and retain the mass.

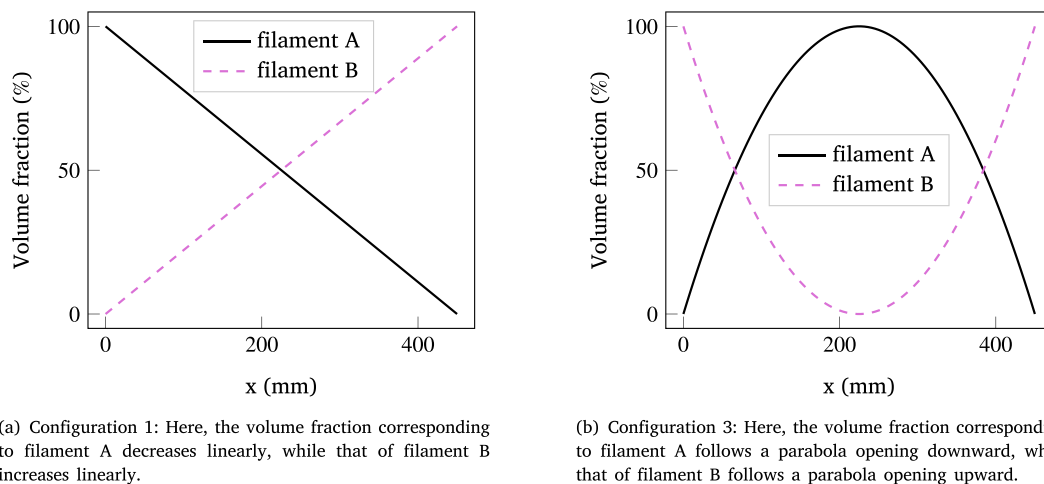


Fig. 7. The figures show the material volume fractions over the beams' x -coordinate for the altered configurations. These volume fractions represent the ideal deterministic volume fractions that correspond to the ideal deterministic stiffness profiles and that are not manufacturable in practice.

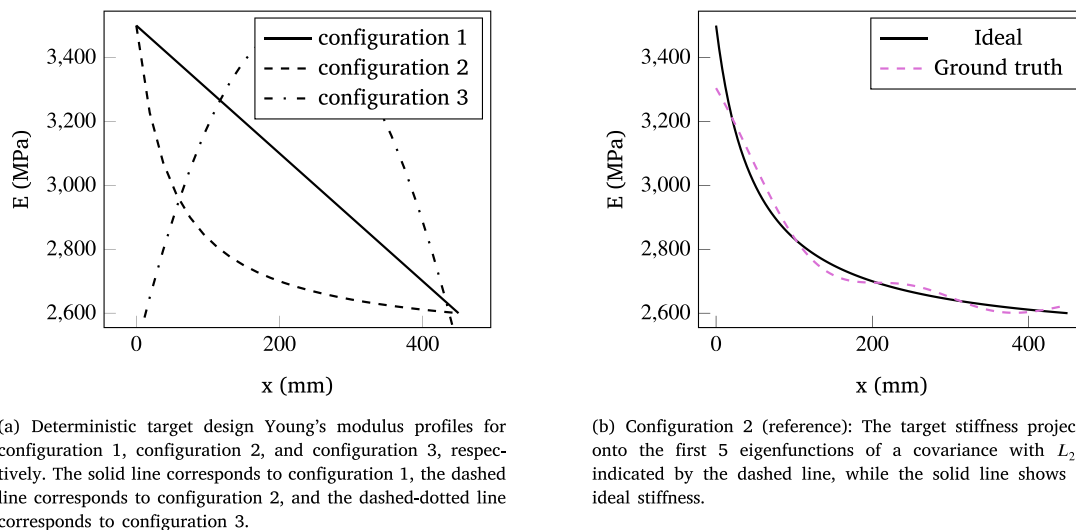
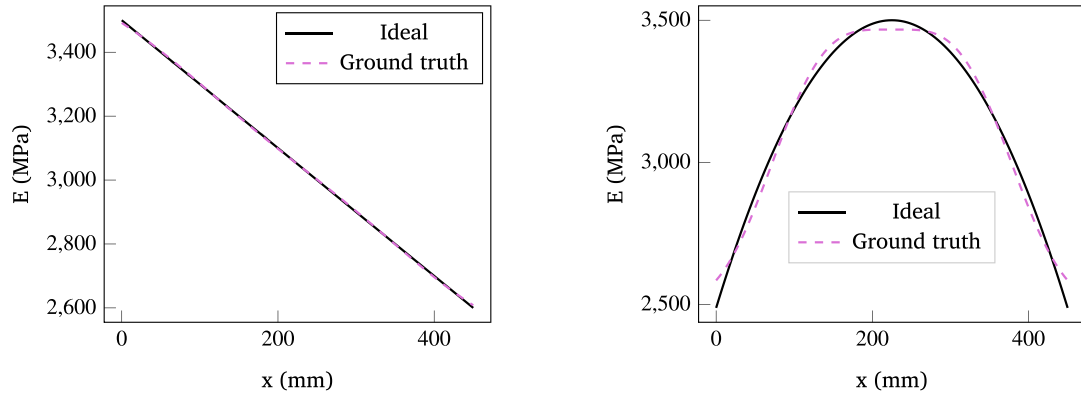


Fig. 8. Deterministic target design Young's modulus profiles for all configurations and ground truth stiffness for the reference configuration.

In practice, the properties of the manufactured parts are not deterministic. Instead, they are subject to uncertainty. We model the manufacturable stiffness profiles as realizations of Gaussian processes. To achieve this, the ideal stiffness profiles are individually approximated with a Karhunen-Loève expansion with a truncation order of $K = 5$, with the covariance from Eq. (19), and the matching length-scales from Table 3. The manufacturable stiffness profiles are considered as the quantity of interest and thus the ground truth for the inverse problem in the following section. Fig. 8 shows the ground truth stiffness profile for the reference configuration, while Fig. 9 shows the corresponding profiles for configuration 1 and configuration 3. The ground truth stiffness for configuration 1 shows a close agreement throughout the beam with the original stiffness, while the ground truth stiffness for configuration 2 fails to capture the desired stiffness peak at the clamping. The chosen random space discretization overestimates the minimum stiffness values at the beam's boundaries for configuration 3. Overall, the characteristics of the ideal profiles are captured well. The approximation of the configuration 1 profile being the most accurate demonstrates that retaining more terms in the Karhunen-Loève expansion would enable the projection to capture even more of the ideal profiles' variance.



(a) Configuration 1: The deterministic target stiffness projected onto the first 5 eigenfunctions of a covariance with L_1 is indicated by the dashed line and the ideal stiffness is marked with a solid line.

(b) Configuration 3: Manufacturable or ground truth stiffness profile subject to uncertainty as the realization of a Gaussian process. The dashed line marks the projection of the deterministic stiffness onto the first 5 eigenfunctions of a covariance function with length-scale L_3 . The solid line indicates the ideal stiffness.

Fig. 9. Ground truth stiffness profiles subject to uncertainty as Gaussian process realizations for configuration 1 and configuration 3.

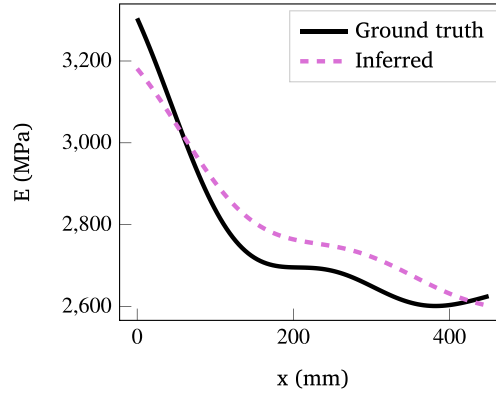


Fig. 10. This figure shows the result of the dimensionality-reduced and generalized polynomial chaos-accelerated inference of the beam's Young's modulus E_x for configuration 2. The beam's first eigenvector at the upper surface area serves as the model response and observation data. The solid line shows the ground truth Young's modulus field M^{true} and the dashed line corresponds to the estimated Young's modulus field \bar{M}_K attained via the maximum a posteriori estimate. Here, the covariance function used to generate the ground truth is employed for training the surrogate and as prior information on the *a priori* unknown spatially varying Young's modulus. The identified field agrees excellently with the ground truth field.

4. Results

4.1. Dimensionality-reduced and generalized polynomial chaos accelerated inference of Young's modulus using mode shape data

Now follow results for the identification of the ground truth stiffness based on mode shape data generated with the same finite element method model as described in Section 3.1 and endowed with the identical signal-to-noise ratio. The surrogate shortens the inversion procedure duration from more than 170 to less than 1.7 s on consumer-grade hardware. Now, the bulk amount of CPU time is spent evaluating the likelihood instead of the model, as is the case when using the full finite element model. The inference results for the Young's modulus E_x using maximum a posteriori estimation agree excellently with the ground truth, see Fig. 10. This clearly demonstrates the efficiency and efficacy of our proposed method for identifying the spatially varying Young's modulus of a structure using mode shape data.

4.2. Surrogate recycling results

This section first presents the effect of using the functionally graded material as opposed to homogeneous material on the safety-margin within static loading. Following this, the spatially varying stiffness identification results obtained from the academic example are shown together with metrics on the computational effort of our methodology.

Table 4

The table compares the homogeneous parts with the functionally graded parts with respect to their minimum safeties for each configuration. The minimum safeties corresponding to the functionally graded parts are higher than those of their homogeneous counterparts throughout the configurations. The increase of the minimum safety is calculated as the relative percentage deviation with the homogeneous configuration as reference.

	configuration 1	configuration 2	configuration 3
Relative increase of s_{\min}	16.7%	16.7%	16.3%

Table 5

Amount of necessary forward model evaluations comparing the proposed framework to conventional surrogate modeling. The surrogate connects η to the beam's first mode shape. Traditionally, the surrogate must be recomputed when the length-scale L changes and consequently, new finite element model evaluations are necessary. With the proposed workflow, no new finite element model evaluations are necessary and one set of evaluations suffices.

Forward model evaluations	configuration 1	configuration 2	configuration 3
Proposed methodology	0	42	0
Conventional surrogate modeling	42	42	42

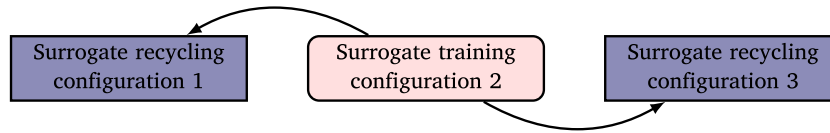
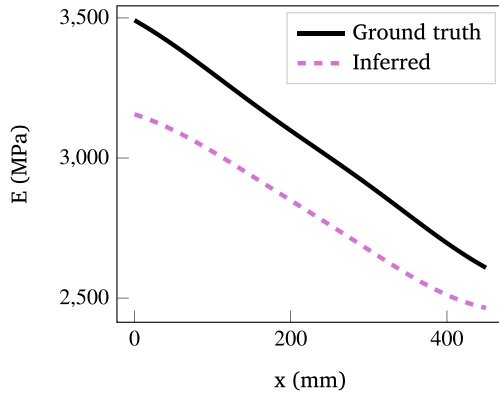


Fig. 11. The generalized polynomial chaos surrogate is trained using finite element model evaluations based on the stiffness covariance belonging to the functionally graded part designed for configuration 2. With the known length-scales L_1 and L_3 , but without new finite element model evaluations using stiffness samples based on these length-scales, the surrogate trained on configuration 2 can be reused for both configuration 1 and configuration 3.

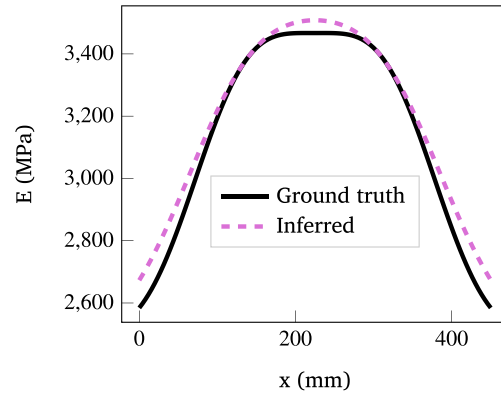
The three configurations undergo static analysis with the finite element method to assess the effect of the functional grading in comparison with the homogeneous material. Here, a three-dimensional volume model of a beam with the same geometry as used in Section 3.1 is created using the commercial finite element method code COMSOL. The discretization using quadratic tetrahedral serendipity elements yields 6327 degrees of freedom. The boundary conditions and loads are applied uniformly across the width of the beam. The yield and von Mises stresses σ_y and σ_{Mises} are computed and the safety-margin s is obtained as $s = \sigma_y / \sigma_{\text{Mises}}$ along the beam coordinate. The safety-margin s is not constant over the beam domain due to the loads and boundary conditions, and the minimum safety s_{\min} signifies the minimum value of s within this region. Table 4 reports the percentage increases in terms of the s_{\min} of the functionally graded material relative to the homogeneous material for all configurations. These results show that the functional grading improves the safety in the critical regions. The functionally graded safety of configuration 1 exceeds that of the homogeneous part at the clamping, where both material configurations exhibit s_{\min} . For configuration 2, the minimum safety lies at the clamping as well, while the minimum safety for configuration 3 is located at the center of the beam. Using the functionally graded material results in a uniform increase in s_{\min} with respect to the homogeneous material throughout the configurations.

Now, the stiffness is assumed as unknown. All configurations consequently undergo non-destructive testing where the aim is to identify the stiffness. For configuration 2, the baseline procedure described in Section 3.1 is applied. The mean value of the stiffness is assumed as 3×10^3 MPa. The Young's modulus is modeled as homogeneous in y and z direction and only varies along the x -coordinate. The length-scale for the Karhunen-Loève expansion of the inference is chosen as L_2 in accordance with Table 3. Here, the Karhunen-Loève truncation order is set to 5. The finite element model is evaluated for random field realizations connected to the length-scale of configuration 2 $L_2 = 450$ mm. The generalized polynomial chaos surrogate is trained using these finite element model evaluations. Presenting one of the main contributions of this study, the stiffness identifications for configuration 1 and configuration 3 use a transformed version of the surrogate connected to configuration 2. No additional finite element model evaluations are necessary. Merely the Karhunen-Loève expansion must be recomputed with the appropriate length-scale from Table 3 in order to obtain the projection coefficients from Eq. (10) for the surrogate transformation described in Section 2.4. The transformed surrogates following the scheme shown in Fig. 11 can now be used for the inference. Table 5 lists the amount of high-fidelity finite element forward model evaluations that are necessary for each inference. This study uses twice the number of necessary model evaluations as given by Eq. (9) to augment the amount of equations for the generalized polynomial chaos expansion least squares problem and thus improve it. Note that only surrogate model evaluations are necessary for the inference involving configuration 1 and configuration 3 with our proposed procedure. The inference is carried out using maximum a posteriori estimation.

Fig. 12 shows the agreement of the identified Young's moduli with the *a priori* unknown ground truth stiffness. The unknown ground truth stiffness is plotted using a solid line and the estimated stiffness uses a dashed style. For configuration 1, the estimation based on the recycled surrogate correctly identifies the trend and character of the ground truth stiffness. However, there is an offset throughout the beam domain of order of magnitude 1×10^2 MPa. The estimation using the surrogate trained on L_2 correctly identifies the trend and character of the ground truth stiffness belonging to configuration 2. However, the inversion underestimates the beam stiffness near the clamping and overestimates it at $x > 100$ mm. Finally, the estimation for configuration 3 based on the



(a) Configuration 1: Result of the inference procedure using a recycled surrogate model compared to the *a priori* unknown ground truth stiffness.



(b) Configuration 3: Result of the inference procedure using a recycled surrogate model (dashed) compared to the *a priori* unknown ground truth stiffness (solid).

Fig. 12. Bayesian inference results for the non-reference configurations: The *a priori* unknown ground truth stiffness (solid) and the estimated stiffness (dashed) are compared with each other.

recycled surrogate correctly identifies the trend and character of the ground truth stiffness. The maximum stiffness at the center and the minimum stiffness values at the bounds are overestimated by the order of magnitude 1×10^1 MPa. Overall, the lowest error is achieved here.

Overall, the estimations agree well with the reference values. The shapes are excellently approximated for all configurations, while the maximum errors at the respective x -coordinates lie in the range of $1 \times 10^1 - 1 \times 10^2$ MPa. The smallest error over the beam domain is achieved for configuration 3 and the largest error over the domain is attributed to configuration 1. The error for configuration 2 lies in between the error connected to configuration 1 and configuration 3. This is an unexpected result, as no surrogate recycling occurs here. Indeed, the error is proportional to the magnitude of the first two ground truth Karhunen-Loève coefficients and thus depends on the application.

Accuracy assessment. The errors of the inference procedure clearly depend on the chosen application, the measurement noise, and the optimization algorithm used to identify the maximum a posteriori estimate. Errors arising from the use of individual components within the methodology are well-documented in the literature. Specifically, the convergence of the generalized polynomial chaos expansion is scrutinized by Ernst et al. [34], while Huang et al. [35] study the truncation error of the Karhunen-Loève expansion. The expected errors connected to our setup are shown in Fig. 13. Several ground truth samples drawn from a Karhunen-Loève expansion with target correlation length L are inferred based on surrogates using reference correlation lengths {225, 360, 450, 900} mm. We deliberately choose Karhunen-Loève expansion samples here to avoid any unwanted influence of Karhunen-Loève expansion order errors as studied by Huang et al. [35] on the desired assessment of the error resulting from the surrogate recycling procedure. Nonetheless, the ratio of covered variance exceeds 95% for all configurations. The inference results are averaged over all samples and compared to results from the conventional procedure, where $l' = L$.

The error when using recycled surrogates increases with shortening ground truth correlation lengths L . This effect is more pronounced for large reference length-scales l' . This leads to the recommendation of using the smallest possible l' . However, this entails a computational complexity trade-off, as higher Karhunen-Loève expansion orders are required if the variance coverage is to be kept constant and higher expansion orders in turn necessitate more forward model evaluations due to the increased number of generalized polynomial chaos inputs.

Note that the quality of results obtained using recycled surrogates depends on the quality of the reference surrogate. To this aim, a worst-case curve is plotted for $l' = 360$ mm, where the accuracy of the conventional method is lower compared to other L . Thus confirming the accuracy of the surrogate before recycling it is prudent. Again, the convergence of the generalized polynomial chaos expansion is application specific and has been extensively studied in the literature [34].

5. Discussion and conclusions

5.1. Discussion

Scrutinizing the results reveals that the proposed stiffness identification procedure succeeded in identifying the stiffness in a mean sense for configuration 2 and configuration 3 with reasonable accuracy, but failed to identify the stiffness correctly in the mean sense for configuration 1. One way of identifying an erroneous offset in the identification results is to carry out a brief cross-check between the mean of the identified stiffness and an experimentally determined eigenfrequency.

The proposed methodology cannot be applied when the geometry or the boundary conditions of the tested structure change. Other methods must be developed to cover these application areas.

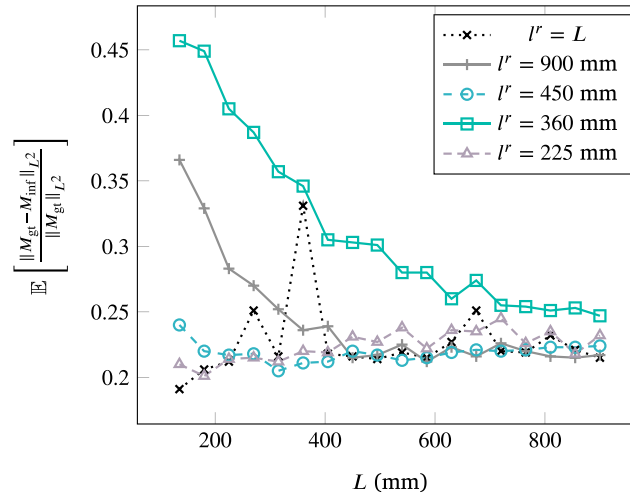


Fig. 13. Accuracy assessment for our methodology, where the ratio of covered variance exceeds 95% for all parameter study configurations. The graph shows the statistically expected error, where M_{gt} represents the unknown quantity of interest and M_{inf} results from its inference. The dotted line corresponds to the conventional inference strategy using the generalized polynomial chaos surrogate, whereas the remaining curves are connected to our approach.

Further, there exist scenarios, where employing the proposed method is not necessary. The advantages thrive when forward model evaluations are computationally expensive. This is especially the case for complex geometries and the necessity of fine discretization. If a computationally affordable and sufficiently accurate model exists, the construction of surrogates may not be necessary.

Our academic example uses only three different length-scales. However, the proposed methodology provides more value when many process parameter length-scales are deployed during manufacturing. The computational cost for constructing the reference surrogate can be viewed as fixed cost in this context. Further, the fixed cost may be increasingly offset by inference procedures where the reference surrogate is recycled. Within this analogy, the computational overhead, mainly consisting of Karhunen-Loève expansion computations and likelihood evaluations, corresponds to variable cost.

5.2. Conclusions

This study used an accelerated method for non-destructively identifying the multi-dimensional spatially varying stiffness while considering its uncertainty. Here, the structure's mode shapes served as data. We conclude that

- the method delivers excellent results over the entire structure's domain.
- the method exhibits a significant computational time speedup when compared with procedures evaluating the finite element model at each inference step.

Furthering the state of the art, we formulated a novel methodology for recycling the surrogate model for the use in theoretically unlimited follow-up inference procedures. This methodology was based on the estimation of the random field length-scale of filament volume fractions and an assumption of the equivalence to the material property length-scales. We conclude that

- the methodology delivers excellent results when recycling a surrogate model.
- the methodology scales well for an increasing number of process parameter length-scales and thus delivers significant further computational cost saving potential for large-scale applications.
- the reference length-scale shall be chosen as small as possible while considering computational cost constraints.

Future research should produce a database with process-structure-property relations, where correlations between the parameters may be extracted such that our method can be employed with more confidence and the cumbersome integrated computational materials engineering framework may be avoided.

CRediT authorship contribution statement

Karl-Alexander Hoppe: Conceptualization, Methodology, Software, Validation, Formal analysis, Investigation, Resources, Writing – original draft, Writing – review & editing, Visualization, Supervision, Project administration. **Kevin Josef Li:** Methodology, Software, Formal analysis, Investigation, Data curation, Visualization. **Bettina Chocholaty:** Resources, Writing – review & editing. **Johannes D. Schmid:** Resources, Writing – review & editing. **Simon Schmid:** Conceptualization, Writing – review & editing. **Kian Sepahvand:** Validation. **Steffen Marburg:** Writing - review & editing, Supervision, Funding acquisition.

Declaration of competing interest

The authors declare that they have no known competing financial interests or personal relationships that could have appeared to influence the work reported in this paper.

Data availability

Data will be made available on request.

Acknowledgments

The authors gratefully acknowledge the discussions with Suhaib Koji Baydoun-Hidding that led to the tangible fused deposition modeling application as a demonstrator.

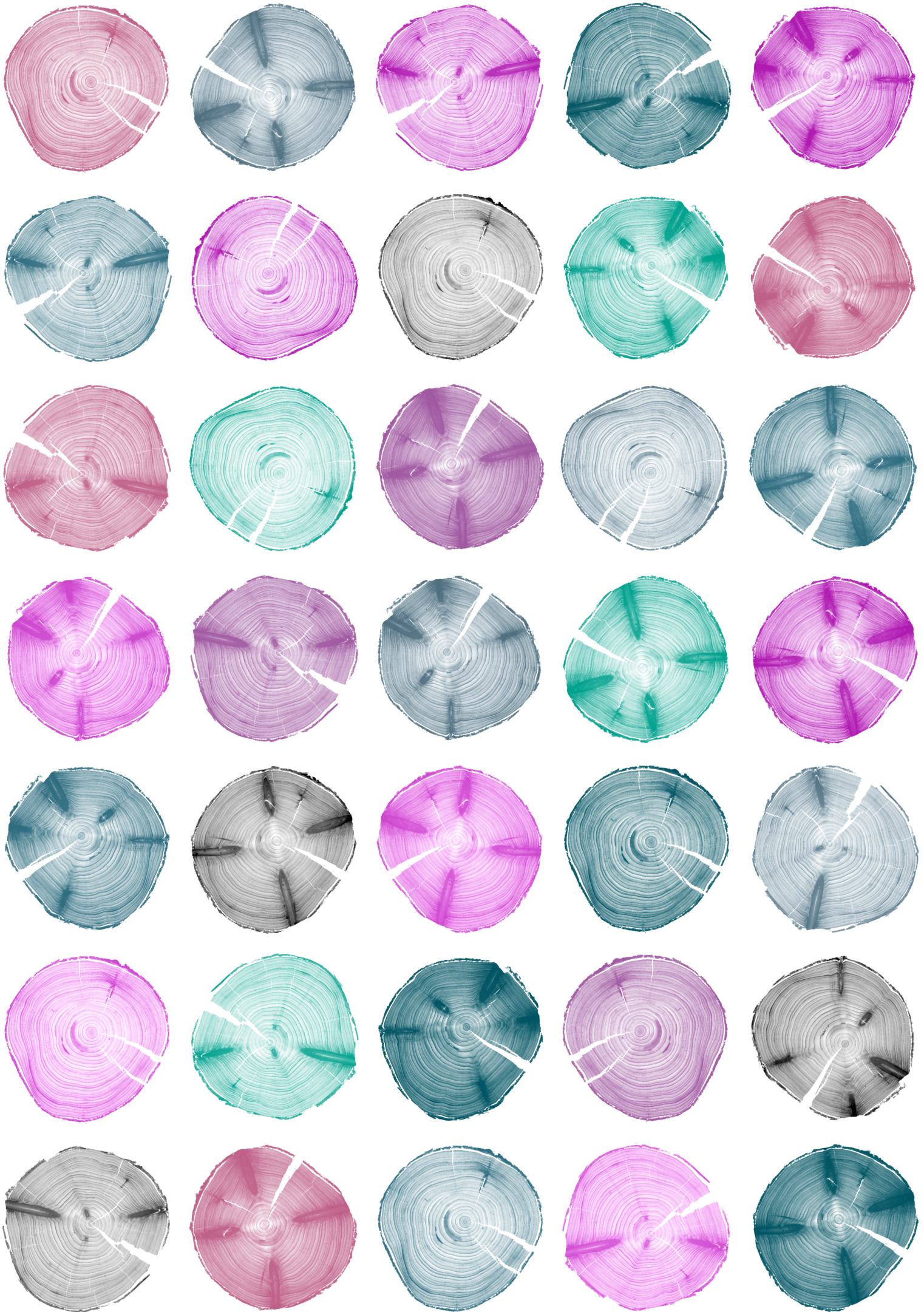
Funding

This study was financially supported by the German Federal Ministry of Food and Agriculture through the Fachagentur Nachwachsende Rohstoffe e.V. (FNR) (grant number 22009817).

References

- [1] H.N. Gupta, R.C. Gupta, A. Mittal, *Manufacturing Processes*, New age international (P) Ltd., New Delhi, 2009.
- [2] D. Garcia, M.E. Jones, Y. Zhu, Z.Y. Hang, Mesoscale design of heterogeneous material systems in multi-material additive manufacturing, *J. Mater. Res.* 33 (1) (2018) 58–67, <http://dx.doi.org/10.1557/jmr.2017.328>.
- [3] Y.M. Marzouk, H.N. Najm, Dimensionality reduction and polynomial chaos acceleration of Bayesian inference in inverse problems, *J. Comput. Phys.* 228 (6) (2009) 1862–1902, <http://dx.doi.org/10.1016/j.jcp.2008.11.024>.
- [4] F. Uribe, I. Papaioannou, W. Betz, D. Straub, Bayesian inference of random fields represented with the Karhunen–Loève expansion, *Comput. Methods Appl. Mech. Engrg.* 358 (2020) 112632, <http://dx.doi.org/10.1016/j.cma.2019.112632>.
- [5] N. Sundararajan, T. Prakash, M. Ganapathi, Nonlinear free flexural vibrations of functionally graded rectangular and skew plates under thermal environments, *Finite Elem. Anal. Des.* 42 (2) (2005) 152–168, <http://dx.doi.org/10.1016/j.finel.2005.06.001>.
- [6] K.-A. Hoppe, M.G.T. Kronthaler, K. Sepahvand, S. Marburg, Identification of a cantilever beam's spatially uncertain stiffness, *Sci. Rep.* 13 (2023) 1169:1–1169:13, <http://dx.doi.org/10.1038/s41598-023-27755-5>.
- [7] L. Mehrez, A. Doostan, D. Moens, D. Vandepitte, Stochastic identification of composite material properties from limited experimental databases, Part II: Uncertainty modelling, *Mech. Syst. Signal Process.* 27 (2012) 484–498, <http://dx.doi.org/10.1016/j.ymsp.2011.09.001>, URL <https://www.sciencedirect.com/science/article/pii/S0888327011003694>.
- [8] S. Debruyne, D. Vandepitte, D. Moens, Identification of design parameter variability of honeycomb sandwich beams from a study of limited available experimental dynamic structural response data, *Comput. Struct.* 146 (2015) 197–213, <http://dx.doi.org/10.1016/j.compstruc.2013.09.004>.
- [9] A. Batou, C. Soize, Stochastic modeling and identification of an uncertain computational dynamical model with random fields properties and model uncertainties, *Arch. Appl. Mech.* 83 (6) (2013) 831–848, <http://dx.doi.org/10.1007/s00419-012-0720-7>.
- [10] I. Sraj, O.P. Le Maître, O.M. Knio, I. Hoteit, Coordinate transformation and polynomial chaos for the Bayesian inference of a Gaussian process with parametrized prior covariance function, *Comput. Methods Appl. Mech. Engrg.* 298 (2016) 205–228, <http://dx.doi.org/10.1016/j.cma.2015.10.002>.
- [11] A. Siripatana, O. Le Maître, O. Knio, C. Dawson, I. Hoteit, Bayesian inference of spatially varying Manning's n coefficients in an idealized coastal ocean model using a generalized Karhunen–Loève expansion and polynomial chaos, *Ocean Dyn.* 70 (8) (2020) 1103–1127, <http://dx.doi.org/10.1007/s10236-020-01382-4>.
- [12] S.M. Hashemi, S. Parvizi, H. Baghbanijavid, A.T. Tan, M. Nematollahi, A. Ramazani, N.X. Fang, M. Elahinia, Computational modelling of process–structure–property–performance relationships in metal additive manufacturing: A review, *Int. Mater. Rev.* 67 (1) (2022) 1–46, <http://dx.doi.org/10.1080/09506608.2020.1868889>.
- [13] T. Gatsos, K.A. Elsayed, Y. Zhai, D.A. Lados, Review on computational modeling of process–microstructure–property relationships in metal additive manufacturing, *JOM* 72 (1) (2020) 403–419, <http://dx.doi.org/10.1007/s11837-019-03913-x>.
- [14] W. Gao, Y. Zhang, D. Ramanujan, K. Ramani, Y. Chen, C.B. Williams, C.C. Wang, Y.C. Shin, S. Zhang, P.D. Zavattieri, The status, challenges, and future of additive manufacturing in engineering, *Comput. Aided Des.* 69 (2015) 65–89, <http://dx.doi.org/10.1016/j.cad.2015.04.001>.
- [15] E. Louvis, P. Fox, C.J. Sutcliffe, Selective laser melting of aluminium components, *J. Mater. Process. Technol.* 211 (2) (2011) 275–284, <http://dx.doi.org/10.1016/j.jmatprotec.2010.09.019>.
- [16] C. Ward, *Materials genome initiative for global competitiveness*, in: 23rd Advanced Aerospace Materials and Processes (AeroMat) Conference and Exposition, Vol. 202, ASM International, OH, 2012.
- [17] P. Fratzl, R. Weinkamer, Nature's hierarchical materials, *Prog. Mater. Sci.* 52 (8) (2007) 1263–1334, <http://dx.doi.org/10.1016/j.pmatsci.2007.06.001>.
- [18] G. Gronau, S.T. Krishnaji, M.E. Kinahan, T. Giesa, J.Y. Wong, D.L. Kaplan, M.J. Buehler, A review of combined experimental and computational procedures for assessing biopolymer structure–process–property relationships, *Biomaterials* 33 (33) (2012) 8240–8255, <http://dx.doi.org/10.1016/j.biomaterials.2012.06.054>.
- [19] J. Song, J. Shangvi, P. Michaleris, Sensitivity analysis and optimization of thermo-elasto-plastic processes with applications to welding side heater design, *Comput. Methods Appl. Mech. Engrg.* 193 (42–44) (2004) 4541–4566, <http://dx.doi.org/10.1016/j.cma.2004.03.007>.
- [20] S.W. Cranford, M.J. Buehler, Shaky foundations of hierarchical biological materials, *Nano Today* 6 (4) (2011) 332–338, <http://dx.doi.org/10.1016/j.nantod.2011.07.001>.
- [21] B. Patham, P.H. Foss, Thermoplastic vibration welding: Review of process phenomenology and processing–structure–property interrelationships, *Polym. Eng. Sci.* 51 (1) (2011) 1–22, <http://dx.doi.org/10.1002/pen.21784>.
- [22] W. Yan, S. Lin, O.L. Kafka, Y. Lian, C. Yu, Z. Liu, J. Yan, S. Wolff, H. Wu, E. Ndip-Agbor, et al., Data-driven multi-scale multi-physics models to derive process–structure–property relationships for additive manufacturing, *Comput. Mech.* 61 (5) (2018) 521–541, <http://dx.doi.org/10.1007/s00466-018-1539-z>.
- [23] T. Moges, G. Ameta, P. Witherell, A review of model inaccuracy and parameter uncertainty in laser powder bed fusion models and simulations, *J. Manuf. Sci. Eng.* 141 (4) (2019) <http://dx.doi.org/10.1115/1.4042789>.

- [24] M.M. Francois, A. Sun, W.E. King, N.J. Henson, D. Tourret, C.A. Bronkhorst, N.N. Carlson, C.K. Newman, T. Haut, J. Bakosi, et al., Modeling of additive manufacturing processes for metals: Challenges and opportunities, *Curr. Opin. Solid State Mater. Sci.* 21 (4) (2017) 198–206, <http://dx.doi.org/10.1016/J.COSSMS.2016.12.001>.
- [25] M.F. Horstemeyer, S. Sahay, *Integrated Computational Materials Engineering (ICME) for Metals*, John Wiley & Sons, Ltd, Hoboken, 2018, <http://dx.doi.org/10.1002/9781119018377>.
- [26] S. Ghosh, Predictive modeling of solidification during laser additive manufacturing of nickel superalloys: recent developments, future directions, *Mater. Res. Express* 5 (1) (2018) 012001, <http://dx.doi.org/10.1088/2053-1591/aaa04c>.
- [27] S.-H. Ahn, M. Montero, D. Odell, S. Roundy, P.K. Wright, Anisotropic material properties of fused deposition modeling ABS, *Rapid Prototyp. J.* 8 (4) (2002) 248–257, <http://dx.doi.org/10.1108/13552540210441166>.
- [28] R. Setter, F. Riedel, W. Peukert, J. Schmidt, K. Wudy, Infiltration behavior of liquid thermosets in thermoplastic powders for additive manufacturing of polymer composite parts in a combined powder bed fusion process, *Polym. Compos.* 42 (10) (2021) 5265–5279, <http://dx.doi.org/10.1002/pc.26221>.
- [29] M. Rafiee, R.D. Farahani, D. Therriault, Multi-material 3D and 4D printing: A survey, *Adv. Sci.* 7 (12) (2020) 1902307, <http://dx.doi.org/10.1002/advs.201902307>.
- [30] T.J. Sullivan, *Introduction to Uncertainty Quantification*, Vol. 63, Springer International Publishing, Cham, 2015, <http://dx.doi.org/10.1007/978-3-319-23395-6>.
- [31] M. Alnæs, J. Blechta, J. Hake, A. Johansson, B. Kehlet, A. Logg, C. Richardson, J. Ring, M.E. Rognes, G.N. Wells, The fenics project version 1.5, *Arch. Numer. Softw.* 3 (100) (2015) <http://dx.doi.org/10.11588/ans.2015.100.20553>.
- [32] C.E. Rasmussen, C.K.I. Williams, *Gaussian Processes for Machine Learning*, The MIT Press, Cambridge, MA, 2005, <http://dx.doi.org/10.7551/mitpress/3206.001.0001>.
- [33] M. Abramowitz, I.A. Stegun, *Handbook of Mathematical Functions with Formulas, Graphs, and Mathematical Tables*, Dover Publications Inc., New York, 1965.
- [34] O.G. Ernst, A. Mugler, H.-J. Starkloff, E. Ullmann, On the convergence of generalized polynomial chaos expansions, *ESAIM Math. Model. Numer. Anal.* 46 (2) (2012) 317–339, <http://dx.doi.org/10.1051/m2an/2011045>.
- [35] S.P. Huang, S.T. Quek, K.K. Phoon, Convergence study of the truncated Karhunen–Loève expansion for simulation of stochastic processes, *Internat. J. Numer. Methods Engrg.* 52 (9) (2001) 1029–1043, <http://dx.doi.org/10.1002/nme.255>.



Appendix V

Paper D

Predicting the elastic properties of Norway spruce by its morphology

Karl-Alexander Hoppe^{*}, Pablo Francisco Ramírez Hönack, Simon Schmid, Jochen Kollofrath, Bettina Chocholaty, Iason Papaioannou, and Steffen Marburg

This publication is reprinted in accordance with its open access license [CC BY 4.0](#).

^{*}orcid.org/0000-0002-3048-8284



Contents lists available at ScienceDirect

International Journal of Mechanical Sciences

journal homepage: www.elsevier.com/locate/ijmecsci

Predicting the elastic properties of Norway spruce by its morphology

Karl-Alexander Hoppe^{a,*}, Pablo Francisco Ramírez Hönack^a, Simon Schmid^c,
Jochen Kollofrath^c, Bettina Chocholaty^a, Iason Papaioannou^b, Steffen Marburg^a^a Technical University of Munich, TUM School of Engineering and Design, Department of Engineering Physics and Computation, Chair of Vibroacoustics of Vehicles and Machines, Boltzmannstraße 15, Garching bei München, 85748, Bavaria, Germany^b Technical University of Munich, TUM School of Engineering and Design, Department of Civil and Environmental Engineering, Engineering Risk Analysis Group, Theresienstraße 90, München, 80333, Bavaria, Germany^c Technical University of Munich, TUM School of Engineering and Design, Department of Materials Engineering, Chair of Non-destructive Testing, Franz-Langinger-Straße 10, München, 81245, Bavaria, Germany

ARTICLE INFO

Keywords:

Wood
Material model
Curvature
Knots
Spiral grain
Homogenization

ABSTRACT

Models for the elastic material properties of wood aim to predict the mechanical response of wooden structures to external loading. Traditionally, the variability of these properties in trees is described by a taxonomy of growth defects that is typically based on visual indicators in the material. This includes curvature, knots, and spiral grain models. Existing meso- and macro-scale models fail to describe the uncertainty connected to the local heterogeneity of the material. In this paper, we propose a novel meso-scale model that describes the natural variability of Norway spruce morphology and material properties based on random field theory. Our approach removes the need for a taxonomy of growth defects and enables uncertainty quantification of the stiffness and density in a straightforward fashion using simulations. This may enhance confidence for stiffness-graded applications, where the dynamic resonant behavior of wood structures is relevant and growth anomalies are present. Further, our stochastic models can generate images that realistically mimic wood patterns, which is relevant for applications like synthetic wood panels and flooring.

1. Introduction

Developing models for the mechanical behavior of wood [1] is a challenging research field due to the natural variation of this material. Walley and Rogers [2] review elastic models for wood and find that many models attempt to mimic the observed behavior but are not based on theoretical considerations related to the natural growth of the material wood. The insufficient prediction of the behavior is partly due to a lack of understanding of the mechanical behavior of wood [2], but is also related to a lack of available data [3]. The material properties are governed by uncertainty, which is due to geometric variability resulting from natural growth, and uncertainty in effects like moisture and reaction wood.

As wood is a non-homogeneous material, multi-scale or hierarchical modeling is often necessary to predict its macroscopic behavior. Bengtsson et al. [4] investigate how the structure of softwood affects the elastic properties across the scales. Gambarelli and Ožbolt [5] formulate a meso-scale model for mechanical damage processes and find that these significantly influence the macroscopic behavior of wood.

Knots, as well as the local grain angle resulting from tapering, curvature, and spiral growth represent those growth features of wood with the most significant impact on the strength and modulus of elasticity [6]. The following briefly reviews the pertinent literature.

The radial growth observed in a tree over the course of the year is subject to phases. The terms earlywood and latewood very broadly refer to such phases. Due to differences in density, moisture, chemical composition, and other factors, the appearance changes between phases, and thus, annual rings can be made out. Annual ring models consider the density profile over the radial coordinate or the cross-section's shape. The growth layer surface [7] is generally non-circular with anisotropic radii. Recently, surface annual rings and the pith location are being identified using neural-network-based black box models [8,9].

Knots are sections of branches that are encompassed by the trunk, and they receive significant attention within the literature, see Collins and Fink [10]. Kandler et al. [11] approximate knot properties using the distance to the pith and the fiber directions at the surface. Huber et al. [12] estimate, among other properties, the knot geometry together with the adjacent fiber directions by X-ray scans. Guindos and

* Corresponding author.

E-mail address: alexander.hoppe@tum.de (K.-A. Hoppe).<https://doi.org/10.1016/j.ijmecsci.2024.109570>

Received 20 February 2024; Received in revised form 11 July 2024; Accepted 12 July 2024

Available online 19 July 2024

0020-7403/© 2024 The Author(s). Published by Elsevier Ltd. This is an open access article under the CC BY license (<http://creativecommons.org/licenses/by/4.0/>).

Guaity [13] point out the analogy of laminar flow around an obstacle and the fiber alignment around wood knots. Pyörälä et al. [14] employ terrestrial laser scanning to identify branch parameters, while Kantola et al. [15] confine their study to the diameter of branches over the height of trees.

Taper describes the decrease in trunk or bole diameter over the growth direction. Taper models continue to evolve within the literature. While polynomial models are being considered [16], most models are based on the modified Brink's function [17], which scales and shifts a superposition of exponential terms. Popular predictor variables include tree height, age and the number of rings, the mean stand diameter and basal area, and the bole diameter at breast height [18,19], typically 1.3 m from the ground. Kantola et al. [15] integrate taper modeling of Norway spruce with an adapted version of their holistic growth process model.

Curvature is the subject of several studies. Khaloian Sarnaghi et al. [20] quantify the pronounced curvature of beech using a surface scan and note that a custom board cutting scheme is necessary to reduce the waste to a level comparable to that of trunks with less significant curvature. The bow height and crook of a Norway spruce stud [21] and log [22] are identified in the literature, while the corresponding statistics for 56 logs are identified by Edlund and Warensjö [23].

Spiral grain results from the twisting growth of fibers about the pith. To predict shrinkage and twist among other defects, Bäckström and Johansson [24] develop a deterministic analytical model for spiral grain angle variation. Bossu et al. [25] study the influence of growth mechanisms at the tissue level and find extreme grain angle variations. Gjerdrum and Bernabei [26] refine the knowledge on the transition from left-handed grain in the juvenile wood in radial proximity of the pith to subsequent right-handed spiraling over the growth direction. Säll [27] finds that the slope of the grain angle is statistically barely significant in the average sense between butt and middle logs. They do, however, report individual specimens with large grain angles. Finally, Brémaud et al. [28] confirm that the grain angle not only affects the strength but also the vibrational properties of wood.

To model the effect of the local fiber directions, their identification is necessary. Indeed, validation approaches exist for model predictions of the grain angle: Sepúlveda et al. [29] deem predicting the spiral grain angle based on commercially accessible X-ray scans possible. Olsson et al. [30] identify the local fiber orientation on the surface using laser scanning and Hu et al. [31] repeat this around a branch within a wood volume using CT scan data, while Hu et al. [32] quantify the fiber direction of Norway spruce boards using the tracheid effect. Foley [33] locally predicts the orientation of the orthotropic material considering knots. The influence of the local grain angle on the Young's modulus is studied in the literature. Purba et al. [34] find that their stiffness predictions are significantly sensitive towards the microfibril and grain angles and that taking into account for them reduces the model error.

To ultimately predict the modulus of elasticity, a link needs to be established between grain angle and stiffness. Astley et al. [35] formulate the micro-scale orthotropic stiffness as a function of the microfibril angle. Olsson et al. [30] calculate the local Young's modulus from the identified fiber directions. Lukacevic [36] model the stiffness of benign knots based on surface fiber directions. Hu et al. [37] model the local bending stiffness using a fiber direction description within the board volume. In contrast to the expression in terms of the fiber directions, the direct identification of the Young's modulus within an object is cumbersome to achieve. One approach is to use digital volume correlation if a sufficient speckle pattern is present. While the Young's modulus identification at the surface is more accessible, e.g., Hu et al. [38] use digital image correlation for surface imaging of the heterogeneous Young's modulus of wood. However, it does not capture the complete three-dimensional characteristics of the material. Kandler et al. [39] apply their stochastic engineering framework

that considers the non-homogeneous stiffness of boards as random to laminated timber.

To summarize the classical modeling of the material properties of wood, many investigations of the global grain angle or local Young's modulus do not develop a deductive model; see Denzler et al. [40]. Contrary to this, our study operates on an abstraction level comparable to the whorl level of the growth process models in an interpretable and intuitive manner. To this aim, we develop a meso-scale morphological description of Norway spruce based on the annual ring pattern and grain angle as induced by curvature, taper, and spiral grain. Our taper description additionally takes into account the effect of branches. The basis functions and the structure of our model may be tailored to specific wood species. The input parameters to the model are unique for each specimen.

Our morphological model generates heterogeneous fiber directions and heterogeneous density. Using these intermediate results, the local Young's modulus is obtained whilst accounting for earlywood and latewood elasticity of Norway spruce provided in the literature [41]. To validate the stiffness predictions similar to the identification of elastic material parameters from vibration measurements [42], we obtain the morphological parameters from a CT scan of a Norway spruce specimen and then compare its experimental and numerical vibration response.

Statistically predicting wood quality from the morphology of trees and identifying key predictors is a research trend that is rapidly gaining interest, see Lenz et al. [43]. Many papers attempt to fit parameters from large data sets to identify causal relationships and significant predictor variables, see Riesco Muñoz [44]. Unfortunately, the crucial interpretability is commonly overlooked here. Examples of such data-driven approaches to predict curvature and twist consider the grain angle, growth stresses, compression wood, the annual ring width, the relative ring width difference, drying, the board position within the trunk, knots, density, and age, see [45–47].

Data-driven prediction of the Young's modulus of Norway spruce is primarily accomplished in the literature based on CT scan data. Johansson et al. [48] and Oja et al. [49,50] predict the stiffness of Norway spruce boards using data extracted from CT scans. That data includes density, log diameter and taper, and knot volume and occurrence.

While effort is poured into developing deterministic empirical equations for spiral grain and taper, these existing models are not flexible enough to account for the stochastic natural variability of the organic material wood. Likewise, reviews on multi-scale and hierarchical modeling papers that begin at the microstructure reveal that most of these contributions fail to capture the natural variability at the macro- over even the meso-scale [51,52]. Nonetheless, collections of the statistics of macro-scale material properties of wood exist [53]. The natural growth process induces variability in the wood properties [47]. The important task of modeling this growth process is accomplished by hierarchical models operating at the stand, tree, whorl, and branch levels, see [15]. These types of models are complemented by wood formation models [54] and tree information models [55]. However, they often lack the depth and flexibility to incorporate spatial uncertainty within the tree. Specifically, probabilistic models for the longitudinal and circumferential distribution of knots as a function of the longitudinal direction would be valuable.

Indeed, González-Rodrigo et al. [56] observe trends for the variation of wood properties throughout the tree. Finally, Kandler et al. [57] interpret wood material properties as random fields. This perspective is attractive because it can potentially eliminate the need for several defect taxonomies, most prominently those related to curvature like bow and crook. If Gaussian random fields are used to describe the spatial variability, it is completely defined by their second-order statistics. Particularly, the spatial variability is described by the covariance function [58]. Once the covariance function is identified, the description of, say, curvature can be reduced to as little as two variables, namely variance and length-scale.

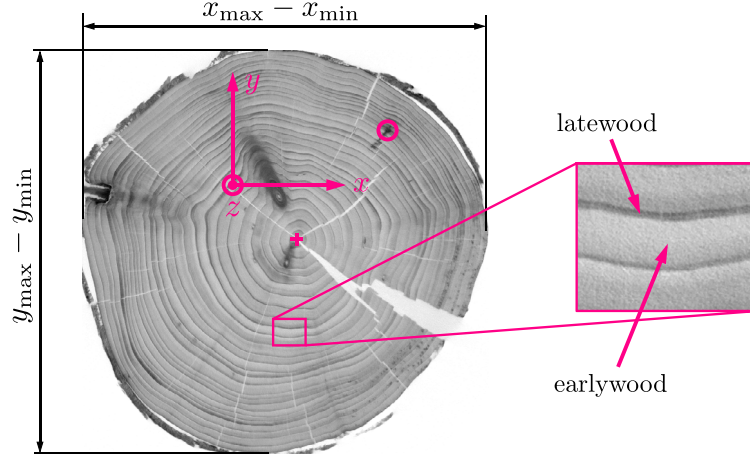


Fig. 1. Wood cross-section as obtained by a CT scan of the specimen with the used coordinate system. Here, the '+' symbol marks the pith location, while the 'o' marker refers to the resin streak. Next to the probe boundaries, exemplary earlywood and latewood locations are annotated in the figure.

Our study considers the curvature, taper, and spiral grain descriptors as stochastic. All stochastic parameters entail a one-dimensional random field defined on z , as defined in Fig. 1. Taper and spiral grain additionally contain trend components, and the taper model is endowed with a stochastic arrival process model for the local effect of branches on the taper. We identify the statistics of these shape parameters for the morphological model from a CT scan of a Norway spruce specimen and data from the literature to cover inter-specimen variability. The parameter uncertainty is propagated through a numerical homogenization routine, which is a standard procedure in the literature [4]. This way, drawing samples from the stochastic model produces the stochastic Young's modulus to predict the homogenized stiffness in the z direction of a cutout. This presents a main outcome of our study.

This paper is organized as follows: Section 2 presents the novel morphological model for Norway spruce logs and the associated material model. The material model validation using modal analysis follows. Section 3 considers stochastic inputs to the model and how this uncertainty propagates to the homogenized Young's modulus of a small specimen. Section 4 discusses the model and evaluates the uncertainty quantification results. Finally, conclusions pertinent to the application of the model and relevant for timber stakeholders are drawn in Section 5.

2. Model development and validation

The following aims to develop a meso-scale description for the heterogeneous Young's modulus of Norway spruce. The meso-scale properties are shown to be relevant in the literature [30], and their consideration is becoming increasingly accessible due to the continuing development of computational resources. This motivates our approach.

Fig. 1 introduces the coordinate system used during the remainder of the paper along with some significant features of the specimen for reference.

Following the scheme shown in Fig. 2, this section describes the morphological model comprised of the shape parameters and an annual ring approximation, see Section 2.1. Its outputs, namely heterogeneous fiber directions and density, feed into the material model, see Section 2.2, which computes the heterogeneous stiffness. To validate the morphological model and the material model, see Section 2.3, numerical modal analysis is carried out based on the heterogeneous stiffness generated using shape parameters identified from a CT scan of a Norway spruce log. These results are compared with the results of an experimental modal analysis of the specimen.

2.1. Morphological model

We base the novel meso-scale material model on an intuitive morphological model that predicts the local fiber direction Φ and density ρ of wood. The morphological model utilizes three simple shape parameters that are described in the following to achieve this. These shape parameters $\theta(z) = \{\Delta(z), \zeta(z), \alpha(z)\}$, where Δ is the offset parameter, ζ is the stretching parameter and α is a rotation parameter, are defined as functions of the z -coordinate running in the out-of-plane direction, see Fig. 1. They have an effect on the xy -plane orthogonal to z . For ease of notation, we omit explicitly noting the z -dependency of these parameters from now on.

Density model. Consider the annual ring pattern of wood modeled by a deterministic function over the radial coordinate. Step functions, sawtooth functions, or sinusoidal functions represent some candidates for such a model. The application should dictate the choice of function, as the density transitions from earlywood to latewood and from latewood to earlywood vary. None of the candidates presents noteworthy advantages with respect to its peers for our application. Because the sinusoid function's character acceptably mimics the general annual ring pattern and because it is readily modified, we proceed with it. Such a sinusoid ρ can be represented as

$$\rho(\delta, T, \theta) = \frac{1}{2} \left(\sin \left(\frac{2\pi}{T} \delta(\theta) \right) + 1 \right) \in [0, 1], \quad (1)$$

where

$$\delta = \sqrt{\tilde{x}^2 + \tilde{y}^2} \quad (2)$$

and T is the thickness of an annual ring. Now, the first two shape parameters $\Delta = [\Delta_x, \Delta_y]^T$ and $\zeta = [\zeta_x, \zeta_y]^T$ can be used to manipulate the reference Cartesian coordinates $[x, y]^T$ shown in Fig. 1 and obtain the morphed coordinates

$$\begin{bmatrix} \tilde{x} \\ \tilde{y} \end{bmatrix} = \begin{bmatrix} \frac{1}{\zeta_x} (x - \Delta_x) \\ \frac{1}{\zeta_y} (y - \Delta_y) \end{bmatrix}. \quad (3)$$

Firstly, Δ describes the x and y -offset of the pith from the reference coordinate system, see Fig. 3. Δ can be used to model various manifestations of curvature, such as bow or crook. Secondly, ζ describes the change in annual ring thickness in the x and y directions, see Fig. 3. ζ is suitable for modeling the taper along z , local distortions due to branches, and longitudinal as well as basic circumferential variability in the annual ring thickness. Setting $\zeta_x \neq \zeta_y$ creates an elliptic instead of a circular annual ring pattern.

Here, ρ from Eq. (1) is related to the material density ρ ; low ρ are associated with earlywood and high ρ are connected to the location

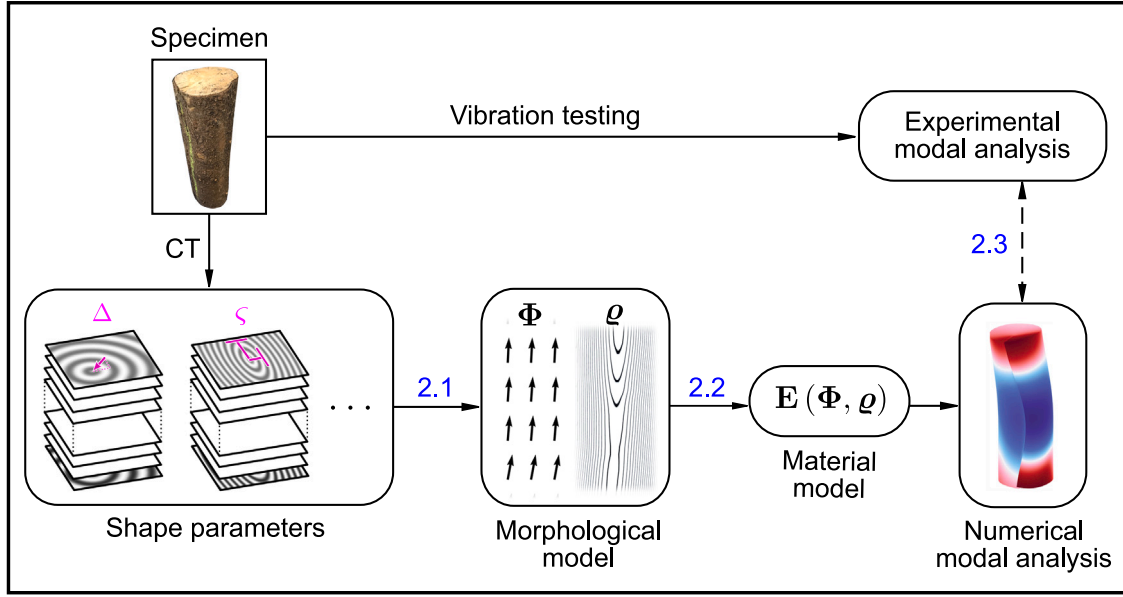


Fig. 2. Model development and validation: The figure shows the development scheme for the morphological and material model for wood based on CT scans. How the shape parameters that are identified from CT data are related to the models is covered in the annotated sections. To validate the models, the generated heterogeneous Young's modulus E as a function of the fiber directions Φ and the density ρ is applied in a numerical modal analysis of the Norway spruce specimen. Ultimately, the simulation results for the natural frequency f are compared with those from the experimental modal analysis.

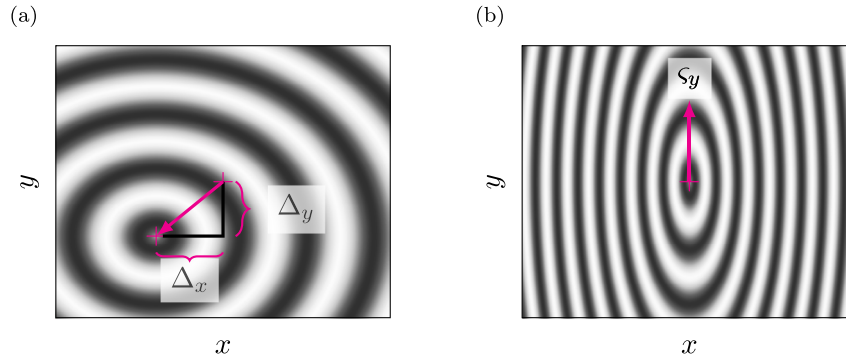


Fig. 3. Panel (a) shows the offset parameter Δ components. It describes the offset of the pith from the center. Panel (b) depicts the influence of the stretching parameter ζ . Its components ζ_x and ζ_y can scale the annual ring thickness in the respective directions to create taper with circular cross-sections or also elliptic cross-sections.

of latewood. Following this analogy, stacking ρ along the z -direction yields a discrete three-dimensional scalar field of density-like values

$$P = [\rho_{z_0}, \rho_{z_1}, \rho_{z_2}, \dots, \rho_{z_n}]^T \quad (4)$$

that may be interpreted as a tree trunk.

Fiber direction. The local fiber direction model incorporates the third and final shape parameter, namely α . α can be interpreted as a rotation about the pith, as marked in blue in Fig. 4, and is linked to the spiral grain angle, which in turn is colored red there.

The fiber directions from one z -layer to another are derived from the relative positions of early- and latewood annual rings at the respective layer. This is owed to the fiber directions not being inherently encoded in the annual ring pattern at one single z position. Therefore, considering the z -coordinates $Z = \{z_i < z_j < z_k\}$ with $j-i = k-j = 1$, it must be assumed that the fiber direction vector field at z_j is the average of the fiber direction field from z_i to z_j and from z_j to z_k , respectively. Since this is not possible for z_0 and z_n , the fiber directions at these locations are set to the second and penultimate ones, respectively.

To this aim, the transformed coordinates $[x'_i, y'_i]^T$ and $[x'_k, y'_k]^T$ are obtained using the transformation function χ employing a rotation

$$x' = \chi(x, \theta, \theta') = \cos(\alpha' - \alpha) \frac{\zeta'_x}{\zeta_x} x - \sin(\alpha' - \alpha) \frac{\zeta'_y}{\zeta_y} y + (\Delta'_x - \Delta_x) \quad (5)$$

$$y' = \chi(y, \theta, \theta') = \sin(\alpha' - \alpha) \frac{\zeta'_y}{\zeta_y} y + \cos(\alpha' - \alpha) \frac{\zeta'_x}{\zeta_x} x + (\Delta'_y - \Delta_y) \quad (6)$$

as $[x'_i, y'_i]^T = [\chi(x_j, \theta_j, \theta_i), \chi(y_j, \theta_j, \theta_i)]^T$ and $[x'_k, y'_k]^T = [\chi(x_j, \theta_j, \theta_k), \chi(y_j, \theta_j, \theta_k)]^T$. Here, $[x_j, y_j]^T$ can be set to the reference coordinates due to the relative nature of Eqs. (5) and (6). Note that no manipulation of z_i and z_k occurs. Now, using the upper and lower fiber directions Φ

$$\Phi_{ij} = \begin{bmatrix} x_j \\ y_j \\ z_j \end{bmatrix} - \begin{bmatrix} x'_i \\ y'_i \\ z_i \end{bmatrix} \in \mathbb{R}^3 \quad (7)$$

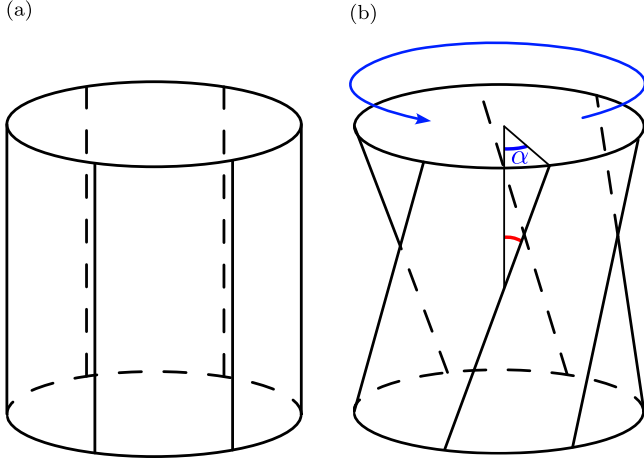


Fig. 4. Effect of spiral grain on the fiber directions: Consider the abstract sketch of a log in panel (a), where the vertical black lines represent fibers. Now, panel (b) shows the effect of the spiral grain angle annotated in red on the fiber directions along the circumference. This study instead uses an absolute rotation angle of each cross-sectional plane marked α in blue color in the figure. The fiber directions are ultimately obtained using the relative rotation angle between two planes in conjunction with the height difference.

and

$$\Phi_{jk} = \begin{bmatrix} x'_k \\ y'_k \\ z_k \end{bmatrix} - \begin{bmatrix} x_j \\ y_j \\ z_j \end{bmatrix} \in \mathbb{R}^3, \quad (8)$$

the fiber directions Φ_j at z_j are approximated as

$$\Phi_j \approx \Phi_{ik} = \frac{\Phi_{ij} + \Phi_{jk}}{2} \quad \forall j \in [1, 2, \dots, n-2, n-1], \quad (9)$$

where $\|\Phi_{ij}\|_2$ denotes the Euclidean norm of Φ_{ij} .

Due to the CT scan resolution available for this study, individual fibers cannot be traced along the growth direction [31], and the fiber direction error cannot be assessed quantitatively. Automatic procedures that may be helpful when high-fidelity CT data are available include triggering on a rising edge to identify transitions from earlywood to latewood and image processing methods such as template matching or also sparse optical flow. A commercial option for automatic fiber tracing is given by the XFiber extension to Avizo.¹ Fig. 5 now showcases a qualitative comparison between an overlay of the first and last plane of the CT scan on the one hand and the predicted fiber direction fields on the other hand to validate the fiber direction model. The fiber directions are based on an evaluation of the morphology at the longitudinal bottom of the CT scan of the trunk (pink color) and of the morphological parameters at the longitudinal top of the CT scan (teal color). The arrows correspond to a normalized displacement from the top (teal) to the bottom (pink). The prediction is evaluated on a regular square grid, i.e. any arrows originating beyond the teal surface have no physical implications. Accounting for only Δ yields a uniform displacement field. Additionally incorporating ζ in Fig. 5(a) produces a small improvement of the displacement prediction. This tapering effect would be more pronounced for longer logs but is nonetheless visible here as the top-left arrow length is greater than the bottom-right arrow length. Including α , and thus completing θ , results in a pronounced improvement. Only now is the counter-clockwise rotation of the log cross-section about the bottom-left properly accounted for. This agrees well with the observations gained from a z -sequential animation of all CT scan cross-sections.

2.2. Material model

The material model represents a modification to the standard orthotropic material used for wood, where the tangential (index t), radial (index r), and longitudinal (index l) components are considered. Corresponding literature values are aggregated in Table 1. The orthotropic stiffness entries are gathered in ν as

$$\nu = [E_t, E_r, E_l]. \quad (10)$$

First, the longitudinal stiffness E_l is projected onto the fiber directions Φ in the Cartesian reference coordinates, yielding

$$\begin{bmatrix} E_{x,l} \\ E_{y,l} \\ E_{z,l} \end{bmatrix} = \begin{bmatrix} E_l \frac{|\Phi_x|}{\|\Phi\|_2} \\ E_l \frac{|\Phi_y|}{\|\Phi\|_2} \\ E_l \frac{|\Phi_z|}{\|\Phi\|_2} \end{bmatrix}. \quad (11)$$

Next, a link between the morphology and the radial as well as tangential components needs to be established. As the circular annual ring pattern cross-section $\zeta_x = \zeta_y$ is a special case, an elliptic distortion of the orthotropy needs to be considered. The simplification of real growth layer cross-sections to be ellipse-shaped is justified as a trade-off between model complexity and accuracy. The local ellipse slope angle τ is needed to orient the radial and tangential vectors correctly. The semi-major axis a and semi-minor axis b related to the standard ellipse centered on the origin with width $2a$ and height $2b$ are obtained as

$$a = \sqrt{(x - \Delta_x)^2 + \frac{(y - \Delta_y)^2 \zeta_x^2}{\zeta_y^2}} \quad (12)$$

and

$$b = a \frac{\zeta_y}{\zeta_x}, \quad (13)$$

assuming that the semi-major axis corresponds to the x direction and the semi-minor axis corresponds to the y direction, thus $\zeta_x \geq \zeta_y$. This is based on the standard shifted ellipse equation $(x - \Delta_x)^2/a^2 + (y - \Delta_y)^2/b^2 = 1$. Note that if $\zeta_x \geq \zeta_y$ does not hold, a change of variables is required. Now, the eccentric anomaly connected to the parametric representation of an ellipse is obtained as

$$t = \begin{cases} \tan^{-1} \frac{y - \Delta_y}{-\sqrt{b^2 - (y - \Delta_y)^2}} & \forall x \leq \Delta_x \\ \tan^{-1} \frac{y - \Delta_y}{\sqrt{b^2 - (y - \Delta_y)^2}} & \forall x > \Delta_x. \end{cases} \quad (14)$$

This leads to the tangent slope $-b/a \cot t$, whose angle is finally found as

$$\tau = \tan^{-1} \left(-\frac{b}{a} \frac{1}{\tan t} \right). \quad (15)$$

Using τ , the tangential stiffness is oriented in parallel to the ellipse slope, while the radial stiffness is oriented orthogonally on the ellipse slope. Essentially, τ provides the correct orientation to the otherwise fiber-direction-agnostic orthogonal stiffness entries with this mapping. The heterogeneous Cartesian stiffness

$$\begin{bmatrix} E_x \\ E_y \end{bmatrix} = \begin{bmatrix} E_{x,l} + E_r \sin(|\tau|) + E_t(1 - \sin(|\tau|)) \\ E_{y,l} + E_t \sin(|\tau|) + E_r(1 - \sin(|\tau|)) \end{bmatrix} \quad (16)$$

is updated accordingly and appropriately scaled to

$$\mathbf{E} = \sqrt{\frac{\|\nu\|_2^2}{E_x^2 + E_y^2 + E_{z,l}^2}} \begin{bmatrix} E_x \\ E_y \\ E_{z,l} \end{bmatrix} \quad (17)$$

using ν .

To arrive from a description of the overall stiffness to accounting for the stiffness disparity between earlywood (index ew) and latewood (index lw), corresponding compensation coefficients

$$\zeta_{lw} = \frac{E_{l,lw}}{E_l} \quad \text{and} \quad (18)$$

¹ Thermo Fisher Scientific, Waltham, Massachusetts, USA.

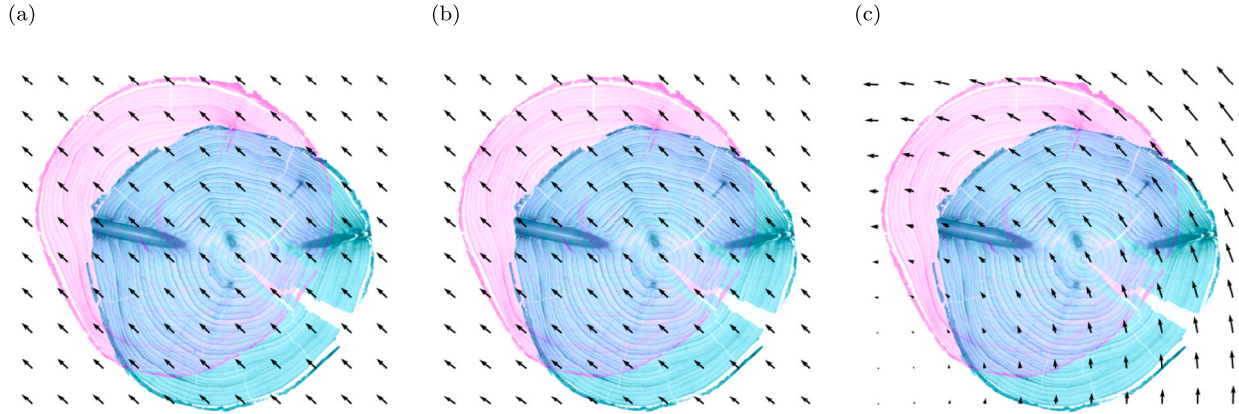


Fig. 5. Fiber direction prediction plotted over an overlay of the first and last CT scan plane of the specimen: panel (a) shows the prediction using Δ , panel (b) shows the prediction considering Δ and ζ , and panel (c) displays the fiber direction prediction accounting for all shape parameters $\theta = \{\Delta, \zeta, \alpha\}$.

Table 1

Literature values for spruce orthotropic material parameters. The density is taken from [59]. The Young's modulus data is taken from [35]. Literature values for shear moduli and Poisson's ratios are collected from [6]. Here, it is assumed that $G_{ij} = G_{ji}$, see [60].

ρ	E_t	E_r	E_l	G_{tr}/E_t	G_{rt}/E_t	G_{tl}/E_t	ν_{tr}	ν_{rl}	ν_{tl}
440 kg m ⁻³	0.43 MPa	0.68 MPa	10.8 MPa	.003	.064	.061	.245	.04	.025

Table 2

Spruce log dimensions.

Cartesian coordinate	Min. probe dimension	Max. probe dimension
x	295 mm	324 mm
y	302 mm	323 mm
z	1015 mm	1040 mm

$$\zeta_{ew} = \frac{E_{l,ew}}{E_l} \quad (19)$$

need to be computed. They need to be determined individually for each considered wood species, as the ratio of earlywood to latewood stiffness is one of the species-specific parameters affecting the stiffness properties. Influences such as the wood's chemical composition or changes in micro-structure are neglected within this study. $\zeta_{lw} = 1.91$ and $\zeta_{ew} = 0.694$ are found for Norway spruce using literature values for the longitudinal stiffness of earlywood $E_{l,ew} = 7.5 \times 10^9$ Pa and of latewood $E_{l,lw} = 20.6 \times 10^9$ Pa [41]. A density threshold γ shall be tuned to accommodate for the specific relative thicknesses of early- and latewood, where increasing values of γ reflect a decreasing portion of latewood. Finally, applying the stiffness ratio coefficients above and below γ yields the final material model M

$$M(\Phi, \rho) = \begin{cases} \zeta_{lw} \mathbf{E} & \forall \rho > \gamma \\ \zeta_{ew} \mathbf{E} & \forall \rho \leq \gamma \end{cases} \quad (20)$$

as an implicit function of the fiber directions Φ and the density-equivalent ρ that are obtained using θ .

2.3. Model validation

To validate the final material model, the result of the numerical modal analysis of the Norway spruce log based on the novel model is compared to its experimental equivalent. To this aim, the shape parameters θ and annual ring thickness are identified from a CT scan of the specimen with the dimensions that are given in Table 2. Then, the morphological model's early- and latewood location predictions are compared qualitatively to the CT scan. Using these predictions, the material model yields the heterogeneous stiffness approximation, which is finally used for the numerical modal analysis.

Identification of morphological descriptors – CT. A Yxlon precision scanner refurbished by Diondo is employed to scan the specimen. The detector comprises 2048×2048 pixels, with a pixel pitch of 200 μ m. The scan is carried out using a voltage of 140 kV and a current of 700 μ A, with an integration time of 990 ms. The resulting projections are reconstructed using the Feldkamp–Davis–Kress (FDK) reconstruction technique, see Feldkamp et al. [61], utilizing cube-shaped voxels with an edge length 0.142 mm. The raw generated voxel volume spans $3888 \times 3888 \times 6430$ pixels. Subtracting the buffer volume of air, a total of 824 mm in terms of the trunk's length can be captured by the scan of the specimen due to packaging constraints.

The shape parameters θ are identified manually from the CT scans using the dimensions and locations marked in Fig. 1 for a set of longitudinal coordinates. Here, the width and height of the log cross-section are determined, excluding bark and branches, to obtain the stretching parameter ζ . Tracking the coordinates of the pith along the height of the trunk represents the offset parameter Δ . The identification of the rotation parameter α is not simple with the CT scan resolution available for this study. If a finer resolution were available, individual cells or fiber paths along the growth direction could be identified. By following fibers from bottom to top, their local spiral grain angle could easily be computed. However, individual fibers are not discernible with the CT scan at hand. Thus, unique features along the height of the trunk are necessary for an estimation of the fiber direction at those locations. Specifically, a second, consistently identifiable feature apart from the pith is necessary to calculate the rotation about the pith. Conveniently, a distinct resin streak is visible in the CT data throughout the entire z-range and the resin streak coordinates are used together with those of the pith to obtain the angle of the connecting slope and thus α . Note that the identified shape parameter data is extrapolated using constant values for the last 216 mm of the specimen that cannot be captured by the CT scans due to geometrical restrictions. Finally, the parameters are gathered into θ such that each longitudinal coordinate corresponds to a vector with five scalar entries.

Numerical modal analysis. The numerical modal analysis is carried out with the finite element method implemented in COMSOL using a three-dimensional model with free boundary conditions. A linear material model serves as an approximation for the elastic behavior. The stiffness obtained from Eq. (20) is evaluated on a grid with a density exceeding



Fig. 6. The measurement setup for the experimental modal analysis is shown in panel (b). The laser Doppler vibrometer captures the vibrations of the log, which is excited by the shaker via a stinger and is suspended using bungee straps. Bark is locally removed to enable the attachment of the stinger with adhesive, which is shown in panel (a). Panel (c) shows the crack along the height of the log, and panel (d) shows the geometry approximation within the simulation model with the crack modeled as a wedge.

twice that of the finite element mesh to avoid aliasing. Subsequently, the stiffness is linearly interpolated from this grid to the mesh vertices. The shear moduli are considered as functions of the heterogeneous stiffness in accordance with Table 1. Here, $G_{xy} = G_{lr}$, $G_{yz} = G_{rl}$, $G_{xz} = G_{rl}$. This analysis considers the material density and Poisson's ratios as homogeneous as given in Table 1, where $\nu_{xy} = \nu_{lr}$, $\nu_{yz} = \nu_{rl}$, $\nu_{xz} = \nu_{rl}$. Special care is taken that the bounds on Poisson's ratio are complied with at each location [62].

Now, the geometry of the numerical wood log model is described. Fig. 6 shows the real and virtual structures side-by-side with the prominent crack facing forward. The geometry approximation is not straightforward, and it is an interesting task connected to the simulation of the wood log. Miniscule benign holes, deviations, and imperfections cause attempts at any direct translation of the CT data into a finite element method geometry to fail. Thresholding the CT data and drawing a three-dimensional contour plot of the outcome proves helpful here. The outer surface of the obtained volume is well approximated by the truncation of an eccentric cone. An appropriately sized slanted, wedge-shaped cutout mimics the dominant crack and is aligned to the latter's radially inner- and outermost positions at the top and bottom of the log.

The displacement field discretization comprises quadratic serendipity shape functions. A structured mesh using 100 triangular prism elements over the log diameter in the radial direction and 40 elements along the growth direction yields more than 4.8×10^6 degrees of freedom. The high mesh density orthogonal to z is needed to capture the annual ring pattern within the heterogeneous material. As the annual ring pattern changes morphology over z , additional elements are required here. An analysis of the expected transitions from earlywood to latewood along z yields 19 transition cycles over the domain in this direction. Thus, 40 elements are chosen here to avoid aliasing.

Experimental modal analysis. Similar to the longitudinal natural frequency elasticity measurement found in the literature [63–65], vibration measurements of the log are conducted to experimentally validate the model; see Fig. 6. Two rubber-coated cables support the bottom part of the log at the nodal lines of the first global bending mode. Bungee straps suspend this setup to mimic free boundary conditions. A B&K² modal exciter type 4284 produces white noise excitation and is attached to the log's bottom part in the radial direction via a stinger glued to a bark-free part of the surface. A B&K DeltaTron type 8230 force transducer records the exerted force to facilitate frequency response functions. Using the PSV-500³ scanning laser Doppler vibrometer with

a PSV-I-500 scanning head, the PSV-500-3D-H controller captures the structure's surface velocities at points where no bark is present or where the truncated onset of a branch protrudes through it. An average of 10 measurements is obtained for the frequency data. Using the software ME'scope to carry out the corresponding experimental modal analysis with the complex mode indication function applied to the real part of the data for peak counting and subsequent polynomial curve fitting serves to identify the natural frequency connected to the first global bending mode shape.

Results. The spruce log belongs to the Norway spruce (*Picea abies*) species. Its CT data shows that it exhibits 27 annual rings and that the average latewood thickness amounts to 0.53 mm. To tune the ratio of earlywood to latewood thickness within the model correctly, the modified sine function resulting from Eq. (1) that ranges from 0 to 1 needs to be discretized, such that areas above a certain value are associated with latewood, and those below it are connected to earlywood. Applying the average latewood thickness of 0.53 mm from the experimental data leads to a density model threshold for earlywood-latewood discrimination within the material model of $\gamma = 0.967$ for Eq. (1). This is obtained by optimizing the threshold for the sine function such that the thickness of the values above the threshold equals its experimental equivalent. Prior to this, the period for the sine function must be chosen in accordance with the experimental specimen.

Fig. 7 presents the shape parameters obtained from the CT scan. Note that Δ is considerably smoother than the remaining shape parameters. We observe that both components of ζ exhibit a comparable shape and that they contain kinks. Scrutinizing the CT scan at the corresponding z -coordinates shows that these kinks are caused by branches emerging from the trunk. The curve identified for α appears to possess a linear trend. A deviation from this trend is visible in proximity to the z -coordinate of one of the branch kinks; however, due to the lack of consistency with respect to other branch locations, this deviation is deemed insignificant.

Using the identified shape parameters, we evaluate the density model and use γ to calibrate both the earlywood and the latewood thickness. The simulation results agree excellently with the experimental CT data; see the density model validation shown in Fig. 8. The model captures the closed annual ring contours at the bottom and the leaning towards the left at the top perfectly. Especially within the top third of the figures, the spacing between latewood contours is approximated very well. The L_2 norm of the difference between the measurement and simulation at the arbitrarily chosen position of $x = 29.3$ mm serves as a quantitative error measure for the density model. Normalizing the continuous CT scan and the discrete model prediction to the interval $[0, 1]$ makes them comparable. Note that the density data on the wood is

² Hottinger Brüel & Kjær GmbH, D-64293 Darmstadt, Germany

³ Polytec GmbH, D-76337 Waldbronn, Germany

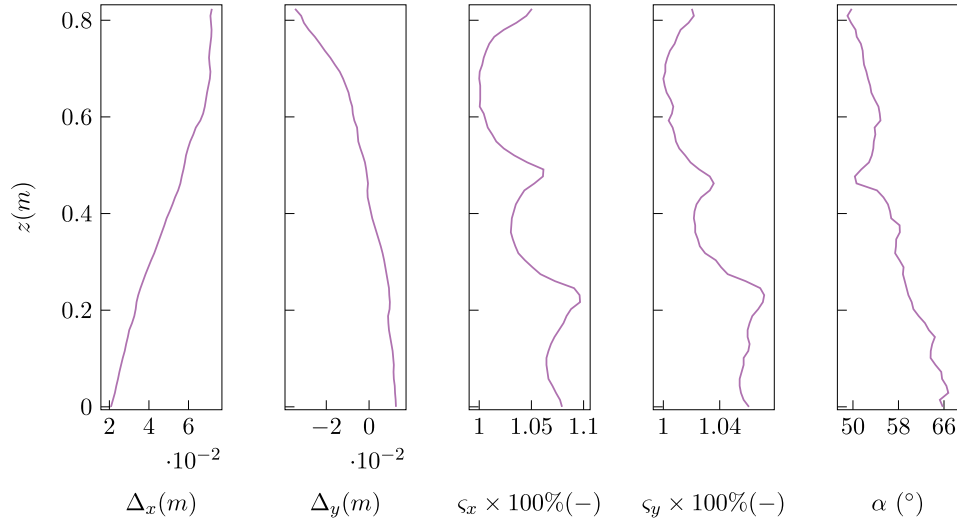


Fig. 7. This figure presents the results for θ as identified from the CT scan of the spruce log. The Δ components exhibit smooth changes over the height z , more so than those of ζ . The kinks within the latter are caused by branches. The identified α appears to have a linear trend. It is mildly noisy, mainly because it is computed from two manually identified features: the pith and resin streak.

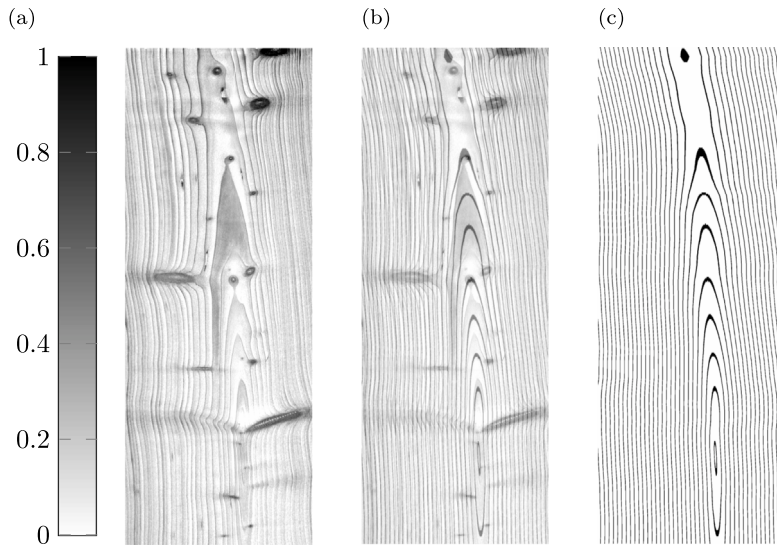


Fig. 8. Density approximation by the morphological model at $x = 29.3$ mm after applying the discrimination between earlywood and latewood. Light shades mark earlywood, while dark shades are connected to latewood. The CT scan excerpt is shown in panel (a) with enhanced contrast. Its data is normalized to the interval $[0, 1]$. The identically normalized model prediction is shown by panel (c) and an overlay of both to facilitate comparison is placed in panel (b).

naturally akin to a discrete step function due to the alternation between early- and latewood and thus additional thresholding is not necessary. The chosen norm yields 5.73×10^{-4} when evaluated on the rectangular area shown in Fig. 8 and normalized on the number of pixels.

The heterogeneous stiffness obtained from the material model cannot be compared directly to the heterogeneous Young's modulus of the spruce log, as no feasible direct measurement method is available. Instead, these two quantities are indirectly compared by means of the corresponding eigenfrequencies connected to the first global bending mode shape shown in Fig. 2. The comparison of the experimental modal analysis and the numerical modal analysis shown in Table 3 represents an outstanding result considering the plethora of involved uncertainties. The discretization fidelity shall be chosen conservatively, especially for comparatively small domain sizes, as the heterogeneity of the wood microstructure has the largest effect on the simulation result here.

Table 3

Experimental and numerical modal analysis comparison: Frequency f of first global bending mode shape and relative percentage error ϵ .

Experimental f_{exp}	Numerical f_{num}	ϵ
832 Hz	845 Hz	$\approx 2\%$

3. Uncertainty quantification

As shown in Fig. 9, this section quantifies the uncertainty of the homogenized Young's modulus of Norway spruce wood. To this aim, Section 3.1 develops a stochastic description for each shape parameter using experimental and literature data. Monte Carlo samples of the corresponding heterogeneous stiffness are drawn and subjected to a numerical (finite element method) homogenization routine in Section 3.2, yielding a sample-based characterization of the Young's modulus probability distribution.

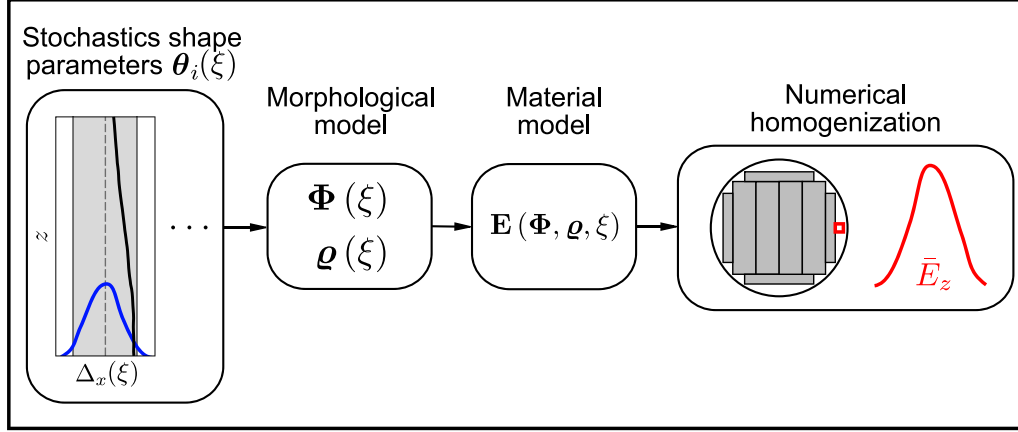


Fig. 9. Uncertainty quantification: this part of the paper develops a stochastic description for the shape parameters θ and identifies the parameters for this stochastic model using the experimental CT data. The uncertainty is then propagated through both the morphological and material model and finally through a numerical homogenization scheme for a small clear wood specimen that is highlighted in red. Ultimately, a distribution of the homogenized Young's modulus for this small cutout is obtained.

Table 4

Overview of additive components for the stochastic model parameters $\theta(\xi)$. The components entail a Gaussian random field $q(z)$, a trend component $\psi(z)$, and a stochastic arrival process $\beta(z)$. A cross signifies that the respective component is being used for a parameter, while a dash means that the component is not used.

	$q(z)$	$\psi(z)$	$\beta(z)$	Full additive model
$\Delta(\xi)$	×	–	–	$\Delta(\xi) = q_\Delta(z)$
$\zeta(\xi)$	×	×	×	$\zeta(\xi) = q_\zeta(z) + \psi_\zeta(z) + \beta(z)^a$
$\alpha(\xi)$	×	×	–	$\alpha(\xi) = q_\alpha(z) + \psi_\alpha(z)^b$

$$^a \psi_\zeta(z) = \vartheta_{\zeta,2} + \vartheta_{\zeta,1}z.$$

$$^b \psi_\alpha(z) = \vartheta_{\alpha,1}z.$$

3.1. Stochastic model

Our shape parameters relate to established quantities used for the description of wood defects. Bow height is connected to the parameter Δ as its maximum deviation from a straight line. Taper describes the narrowing of the trunk with increasing z . In our description, a linear trend of ζ corresponds to a linear tapering of the tree. Finally, spiral grain angle and α are geometrically coupled, as shown in Fig. 4, such that a linear trend in α translates to a constant spiral grain angle.

To explain the variability of the morphological parameters, we pursue a manual analogy to the approach proposed in [66]. To this aim, additive components that cover the variability of the data presented in Fig. 7 in a satisfactory manner are identified empirically; see Table 4. The following describes our approach.

Description of the stochastic parameters. All morphological parameters comprise a zero-mean Gaussian random field using the following correlation kernel r

$$r(z, z') = \exp\left(-\frac{|z - z'|^2}{2h^2}\right), \quad (21)$$

which considers the distance between two spatial points $\{z, z'\}$ and a length-scale h . The x and y components of q_Δ and q_ζ are modeled as uncorrelated random fields with identical variance σ^2 and length-scale h .

The model parameters ζ and α additionally contain a trend component. Including a linear trend component in the model for ζ is sensible because the sections of taper curves corresponding to logs are well-approximated as linear functions [17]. We use the same trend parameters for the x and y components of ζ , as these components exhibit strong dependence, cf. Fig. 7. The choice of adding a linear component to α is based on the data because it shows this trend clearly; see Fig. 7. While the gradient of α has an influence on the mechanical

properties, the intercept of α is irrelevant for the mechanical properties, as it is a cumulative measure of spiral grain. Therefore, the intercept $\vartheta_{\alpha,2}$ is set to zero.

The kinks in ζ caused by branches are modeled using a stochastic arrival process, as the spacing of the kinks does not follow a deterministic pattern. Naturally, we use the same stochastic arrival process to model the branch kinks at the x and y components of ζ . Fig. 10 shows our model for the branch kinks. The z -locations of the kinks are considered the arrival locations of a stochastic arrival process. The inter-arrival distances $(z_{a,i} - z_{a,i-1}) \sim \mathcal{LN}$ are modeled as log-normally distributed. A modified logit-normal function with scale parameter s is empirically found to be a good match for the shape of the branch effect. The composite effect of the branches is described by

$$\beta(z) = \sum_{i \text{ where } z_{a,i} \in \left(z - \frac{h_z}{2}, z + \frac{h_z}{2}\right)} w_i \frac{1}{s\sqrt{2\pi}} \frac{1}{\hat{z}(1-\hat{z})} \exp\left[-\frac{\text{logit}^2(\hat{z})}{2s^2}\right] \quad (22)$$

$$\text{with } \hat{z} = \frac{z - z_{a,i}}{h_z} + \frac{1}{2},$$

where e is the number of arrival events within the considered domain, w_i is the weight of each arrival event, and h_z is the influence height of any single branch. The kink amplitudes w_i are modeled with independent log-normal random variables, as the log-normal distribution was able to best describe the observed data.

Fitting procedure and results. We first describe the fitting of the stochastic arrival process $\beta(z)$ modeling the branch kinks in ζ . This process $\beta(z)$ is fitted using the kinks in the corresponding panels in Fig. 7 that are caused by branches. The locations and the amplitudes of these kinks are manually picked from this data. The z -direction scale s of the logit-normal approximation for the kinks is identified using optimization while assuming a linear residual with respect to the data. The parameters for the log-normal distribution of $(z_{a,i} - z_{a,i-1})$ and w_i are identified jointly for both x and y components using maximum likelihood estimation on the manually picked data.

The trend component and the random field hyper-parameters of the ζ residual are jointly identified using Gaussian process regression with an uninformative prior. The same procedure is used for α from Fig. 7. Specifically, the hyper-parameters σ and length-scale h of each Gaussian random field component $q(z)$ are found by maximum likelihood estimation, i.e., through maximizing the likelihood function

$$f(\mathbf{y}|h, \sigma, \vartheta) = \frac{1}{(2\pi)^{n_y/2} (\sigma^2)^{n_y/2} (|\mathbf{R}(h)|)^{1/2}} \times \exp\left[-\frac{(\mathbf{y} - \mathbf{X}\vartheta)^T \mathbf{R}(h)^{-1} (\mathbf{y} - \mathbf{X}\vartheta)}{2\sigma^2}\right]. \quad (23)$$

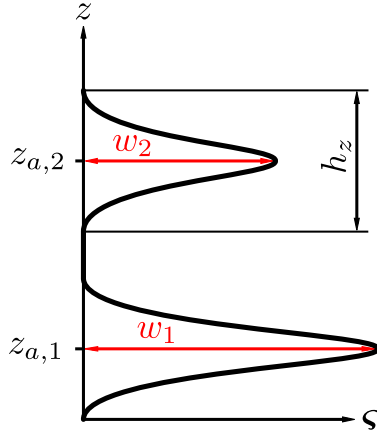


Fig. 10. The exemplary effect of two branches on ζ based on the stochastic arrival process is depicted. All branches are modeled with a modified logit-normal function with the identical scale parameter s and bounded height of influence h_z . The weight w_i of each branch on ζ and the location $z_{a,i}$ are considered random variables and are annotated in the sketch.

Table 5

Identified parameters connected to the stochastic model. Standard deviations are shown in parentheses.

	σ	h	ϑ_1	ϑ_2
Δ	0.086 m	0.75 m	–	–
ζ	$4.67 \times 10^{-3} \%$	1.85×10^{-2} m	9.8 %/m (0.42 %/m) ^a	5.5% (0.205 %) ^a
α	1.27°	1.59×10^{-2} m	20.2 ° m ⁻¹ (1.09 ° m ⁻¹)	–

^a Reference: 295 mm in Table 2

Here, \mathbf{X} is the design matrix and ϑ makes up the trend parameters, while \mathbf{y} is respectively set to θ as identified in Fig. 7. The correlation matrix \mathbf{R} is evaluated through Eq. (21). The expected value and the variance of the trend parameters are obtained as

$$\mathbb{E}[\vartheta|\mathbf{y}] = (\mathbf{X}^T \mathbf{R}^{-1} \mathbf{X})^{-1} (\mathbf{X}^T \mathbf{R}^{-1} \mathbf{y}) \quad (24)$$

and as

$$\mathbb{V}[\vartheta|\mathbf{y}] = \sigma^2 (\mathbf{X}^T \mathbf{R}^{-1} \mathbf{X})^{-1}, \quad (25)$$

respectively. As no trend component is considered for $\Delta(\xi)$, Eq. (23) uses $\mathbf{X}\vartheta = \mathbf{0}$ for this morphological parameter.

Table 5 lists the results for the Gaussian random field component hyper-parameters and the mean slope of the trend component of the stochastic shape parameters. Comparing the standard deviations and length-scales obtained for each parameter, it is obvious that the Gaussian random field component must be interpreted differently for Δ than for ζ and α . The length-scale of Δ is significantly larger than those connected to ζ and α , which in turn may be understood as uncorrelated noise terms.

A log-normal distribution with a mean of 0.208 m and standard deviation of 4.69×10^{-2} m is identified for the inter-arrival distances ($z_{a,i} - z_{a,i-1}$). The branch kinks' amplitudes w are best described by a log-normal distribution with mean $3.83 \times 10^{-3} \%$ and standard deviation $6.39 \times 10^{-3} \%$, while their z -direction scale measures $s = 0.235$ m for an area of influence of $h_z = 0.824$ m.

Since Δ is related to bow, it is of interest to establish a link between these two quantities. Obtaining the bow height in (%) from an individual sample of a random field can be done by connecting the start and end point with a line and measuring the absolute value of the maximum difference between this interpolation line and the sample [23]. This procedure eventually converges to the ensemble bow height estimate with increasing sample size. However, converting from the common description of bow height using (%) in the literature [23] to the corresponding variance of a Gaussian random field is not straightforward.

The conversion in terms of the bow height mean may be accomplished iteratively using optimization.

Evaluating samples of $\Delta(\xi)$ shows that their bow height is well-approximated by a log-normal distribution, see Fig. 11, which is a noteworthy result. The bow height sample mean over 1×10^4 samples evaluates to 2.55 % and 3.50 % for the x and y components of Δ , respectively, while the associated standard deviations are 1.66 % and 2.27 %, respectively.

We remark that in the uncertainty propagation study of Section 3.2, the posterior distribution of the slope $\vartheta_{\zeta,1}$ is truncated to enforce positive values. This ensures that the trunk tapers, i.e., it narrows with increasing height.

Adopted probability distributions. To make our results interoperable, we convert them to bow height, taper, and spiral grain angle. The bow height conversion is described above, the taper is obtained from the identified trend component slope $\vartheta_{\zeta,1}$, and the spiral grain angle is computed using the identified trend component slope $\vartheta_{\alpha,1}$ and the trivial geometrical relation in Fig. 4. Our fitted results are listed in Table 6 together with results from previous studies taken from the literature.

The taper and grain angle results for our spruce log lie within the upper tail of typical literature data. Concerning the taper, this indicates that our specimen might be a butt log close to the bottom of the trunk.

The parameters applied in the uncertainty propagation in Section 3.2 are obtained by combining the fitting results with the parameters from the literature in an attempt to account for inter-specimen variability. The identified uncertainty for Δ as formulated by the bow height overlaps with the range of values from the literature, and therefore, the new results are used for the uncertainty propagation. The trend components for ζ and α are directly related to taper and spiral grain angle. We apply the respective mean and standard deviation values from the literature to capture inter-specimen variability. The uncertainty applied to the trend component $\vartheta_{\zeta,1}$ for ζ is obtained by fitting a log-normal distribution to the taper data from [18], resulting in the log-normal random variable parameters $\mu_{\ln X} = 0.346 \text{ cm m}^{-1}$ and $\sigma_{\ln X} = 0.630 \text{ cm m}^{-1}$. Concerning α , Säll [27] presents extensive information on the spiral grain of Norway spruce. Thus, their results for the pertinent cambial age of 27 are used. Since they do not provide standard deviations, the latter for the Gaussian random variable spiral grain trend component $\vartheta_{\alpha,1}$ is taken from [26].

3.2. Uncertainty propagation

In this section, samples are drawn from the identified stochastic model for the shape parameters θ . Using these shape parameters, the heterogeneous stiffness of a small clear wood specimen is then computed for each sample using the material model M from Eq. (20). Then, the specimen is subjected to a numerical homogenization routine for each stiffness sample, yielding a histogram of the Young's modulus prediction.

A possible cutting scheme is based on the minimum diameter of the Norway spruce specimen. The main yield of the cutting scheme, see Fig. 12, consists of four 50 mm by 200 mm beams, one of the preferred sizes for softwood sawn timber in the EN 1313 standard [67]. The remaining yield of this cutting scheme consists of four 22 mm by 150 mm boards, commonly occurring in Sweden. Our clear specimen dimensions are 20 mm \times 20 mm perpendicular to z and 120 mm long as applied in Aicher and Stapf [68]. This specimen, highlighted in red in Fig. 12, is centered on the symmetry axis of the fictitious cutting scheme and is adjacent to the outermost yield. The motivation for this placement pursues sustainability targets and lies in the investigation of the potential usage of traditionally discarded regions within logs.

To obtain the homogenized stiffness for such a specimen, its static analysis is carried out using the commercial finite element software COMSOL [69] and the linear elastic material assumption. The displacements of all nodes at the bottom surface of the hexahedral volume

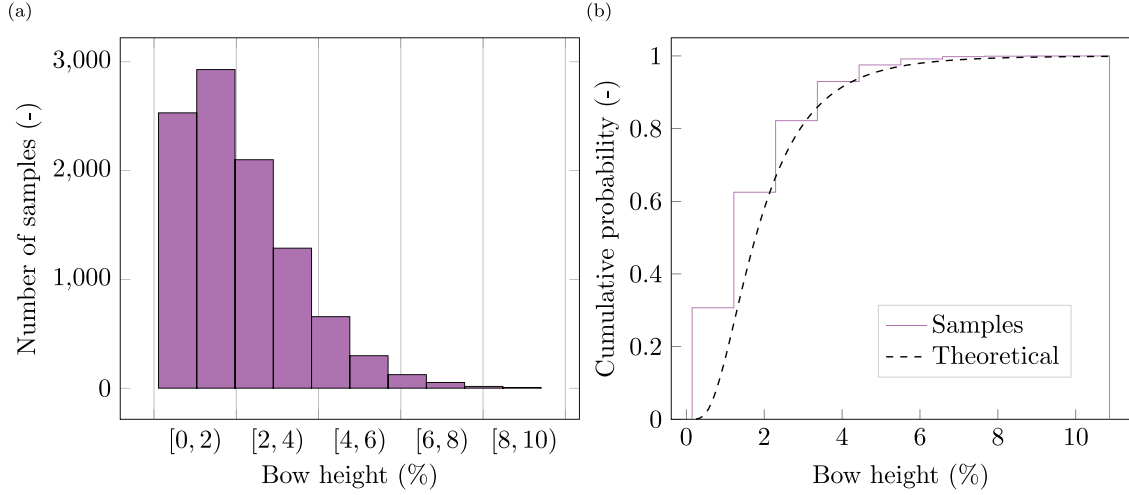


Fig. 11. Bow height distribution of 1×10^4 samples of $\Delta(\xi)$ with a histogram in panel (a) and a cumulative probability distribution in panel (b). The theoretical cumulative distribution function of the log-normal distribution with matching sample statistical moments is shown on the right side for reference.

Table 6

Comparison of new data with literature values. Standard deviations are shown in parentheses.

	Bow height (%)	Taper (cm m ⁻¹)	Spiral grain angle (°)
Fitted results	3.06 (1.98)	2.92 (0.13)	2.17 (0.12)
Literature	0.65 [21], > 2 [22], 1.3 (1) [23]	1.72 (1.2) [18], 1.3 [16]	-0.91 (3.8) [26], 1.77 [Cambial Age 27] [27]
Applied	3.06 (1.98)	1.72 (1.2)	1.77 (3.8)

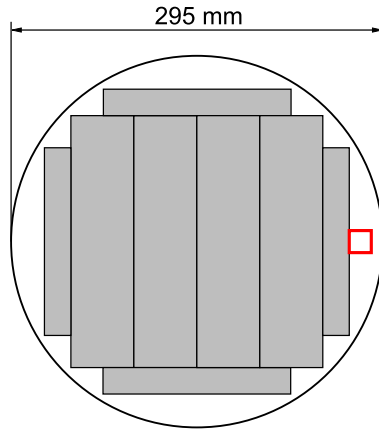


Fig. 12. Potential cutting scheme, where the $20 \times 20 \times 120$ mm clear specimen considered for numerical homogenization is highlighted in red color. This specimen is used for the stiffness uncertainty quantification.

model are set to zero. The vertical displacements of the nodes at the top of the specimen are set to $u_z = 0.1$ mm, see Fig. 13. The structured mesh comprises hexahedral elements with an edge length of 0.5 mm, while the displacement field is discretized using linear polynomials. This discretization is sufficient here, as any occurring bending is negligible. The heterogeneous stiffness is obtained from Eq. (20) on a three-dimensional Cartesian grid with equidistant vertices spaced every 0.25 mm. This stiffness is assigned using linear interpolation at the mesh vertices. Again, the shear moduli are considered as functions of the heterogeneous stiffness in accordance with Table 1. Here, $G_{xy} = G_{tr}$, $G_{yz} = G_{rl}$, $G_{xz} = G_{tl}$. This analysis considers the Poisson's ratios as homogeneous as given in Table 1, where $\nu_{xy} = \nu_{tr}$, $\nu_{yz} = \nu_{rl}$, $\nu_{xz} = \nu_{tl}$. The local bounds on Poisson's ratio are satisfied [62]. The clear specimen is then considered a representative volume element with volume $|V|$. Now, the homogenized stress σ_{ij}^h can be obtained using the

stress σ_{ij}^ε resulting from the static analysis as

$$\sigma_{ij}^h = \frac{1}{|V|} \int \sigma_{ij}^\varepsilon dy, \quad (26)$$

and the homogenized strain ε_{ij}^h is computed analogously as

$$\varepsilon_{ij}^h = \frac{1}{|V|} \int \varepsilon_{ij}^\varepsilon dy, \quad (27)$$

where y refers to the meso-scale, see Charalambakis [70]. Finally, the homogenized stiffness E^h reads as

$$E^h = \frac{\sigma^h}{\varepsilon^h}. \quad (28)$$

Results. After the parameter fitting for the stochastic models, samples can be drawn from the stochastic versions of θ . A few randomly chosen samples of the shape parameters are plotted in Fig. 14 together with the bounding envelopes. Note that the random samples of ζ are normalized on their minimum value for consistency, which implies that $\vartheta_{\zeta,2}$ is chosen deterministically after the sampling of $\vartheta_{\zeta,1}$. Immediately, a different impression arises from these plots when compared to those connected to the spruce log shown in Fig. 7. This is because the z -dimension here is very small in comparison. Among other effects, the branch kinks are not clearly visible as such here. The extreme percentiles for ζ and α appear non-smooth, this is however due to sample size.

Fig. 15 shows five randomly chosen evaluations of the density model, see Eq. (1), after discretization at the clear specimen surface using the stochastic shape parameters. The latewood contours vary heterogeneously in spacing and curvature even on this small domain. These results indicate that the morphological uncertainty is significant and that it needs to be taken into account for accurate simulation results.

Finally, Fig. 16 shows the homogenized Young's modulus in the z -direction for 1477 samples from the stochastic shape parameters that are propagated through the morphological model to the material model and ultimately to the numerical homogenization routine. It is not straight-forward to compare this result to measurements of the longitudinal Young's modulus, where the measurement direction is aligned to the fiber direction [71]. This is because the z -direction explicitly

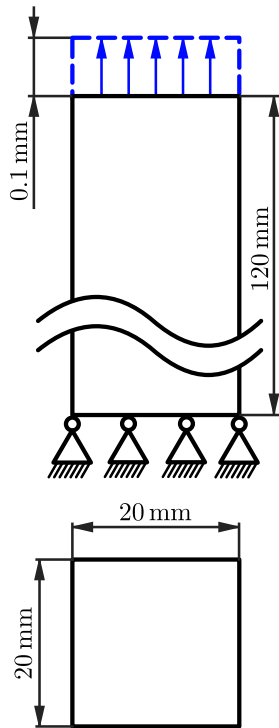


Fig. 13. Visualization of the boundary conditions for the numerical static analysis of the $20 \times 20 \times 120$ mm clear specimen considered for numerical homogenization. The displacement u_z is shown in blue color. Here, the z -direction corresponds to the vertical direction in the figure.

Table 7

Statistical moments of the homogenized Young's modulus of the small clear specimen resulting from uncertainty propagation.

Mean	Coefficient of variation	Skewness coefficient
8.19×10^9 Pa	0.0471	-0.86

does not coincide with the longitudinal one due to the random nature of wood, which our model captures. Nonetheless, the entire range spanned by the histogram is plausible and within the ranges reported in the literature [49]. In fact, the left-skewed distribution of \bar{E}_z , whose statistical moment estimates are given in Table 7, has an intuitive interpretation. The theoretically possible upper limit corresponds to the deterministic case, where the longitudinal direction is parallel to z . The upper bound from the rule of mixtures is not exceeded here [72]. Any distortion of the morphology as induced by any of the stochastic shape parameters reduces \bar{E}_z . Extreme values for the shape parameters evoke particularly low values for \bar{E}_z . Both constitute rare events, thus producing the long left tail of the distribution.

These quantitative results should raise awareness for the variability of wood stiffness, especially at large radial distances from the pith as studied here, due to its naturally random morphology. More importantly, they should inspire confidence in dealing with these inherent uncertainties in practical situations.

4. Discussion

The proposed morphological model has its limitations. Specifically, this study does not consider knots, pith eccentricity, the change in the number of annual rings along the growth direction as proposed by Saint-André et al. [18], it does not consider the radial variability

of annual ring thickness, and it cannot account for tilted ellipse cross-sections, or generalized cross-section shapes. Further, we approximate the spiral grain angle as a linear function of the radial distance from the pith. The material model, in turn, assumes the overall stiffness to stay constant with changing annual ring number, while the Young's modulus as an increasing function of the annual ring number is reported in the literature [73].

Note that an evaluation of the fiber direction errors at the pith and resin pocket would arguably cast the most unfavorable light possible on our results. This is because the displacements along the connection between pith and resin streak are almost parallel to the pith displacement itself, see Fig. 5. If, for instance, evaluation points were available at the left-most or the bottom part of the cross-section, the errors there would decrease significantly with each additionally considered shape parameter. Due to the geometrically restricted maximum probe height within the CT device, 824 mm of the total probe height of 1040 mm is covered by the CT scan, and the shape parameters for the remainder of the domain are found using constant extrapolation.

The numerical modal analysis utilizes homogeneous density and does not account for the influence of moisture. The effect of Poisson's ratio on the natural frequency [74] is less pronounced than that of Young's modulus, and the local fluctuation about the equivalent Poisson's ratio is not considered in this study.

Here, the mesh fidelity is limited by the available amount of memory. This is due to the large domain and usage of quadratic shape functions on the one hand and the eigenvalue problem related to the modal analysis on the other hand.

The validation of the identified distribution for the inter-arrival distances, as well as the shape of the branch kinks, could not be performed within this study due to a lack of findable and accessible data.

The uncertainty in the maximum likelihood estimation of the stochastic shape parameter random field variance and length-scale is high. The gradient of the likelihood with respect to the variance is comparatively shallow in proximity to the maximum. Indeed, the variance connected to Δ is higher than that reported in the literature. However, the distribution identified for the bow height encompasses the range of values found in the literature. Including new specimens and, thus, more samples of the shape parameters in this analysis will significantly enhance the confidence in especially the variance estimates. Additionally, this may provide better insight into both intra- and inter-specimen variability.

5. Conclusions

We have proposed and validated a model for the heterogeneous elastic properties of Norway spruce considering meso-scale geometrical variations. The shape parameters stem from volume scans, but they could be identified from surface scans when assuming a centered pith, fixing the longitudinal direction, and linearly interpolating the spiral grain between the bottom and top. Stochastic descriptions for spiral grain, taper, and curvature effects have been identified for Norway spruce to quantify its uncertainty in Young's modulus. A new probabilistic model for knot distributions in the longitudinal direction has been proposed. Further, a link between empirical descriptions of growth defects like bow height or crook and random fields has been established. In general, our stochastic model can be applied to other wood species after the parameters of the stochastic model are identified for the relevant species. With this model, confidence in using wood with so-called growth defects is enhanced.

A promising practical application of our method lies in generating realistic patterns for synthetic, wood-imitating flooring. Merely a non-linear mapping from our density model to the desired color space is needed here. This relates to existing research on the simulation of lifelike images of wood [8]. Future studies may leverage digital volume correlation to validate the local stiffness directly. They may further

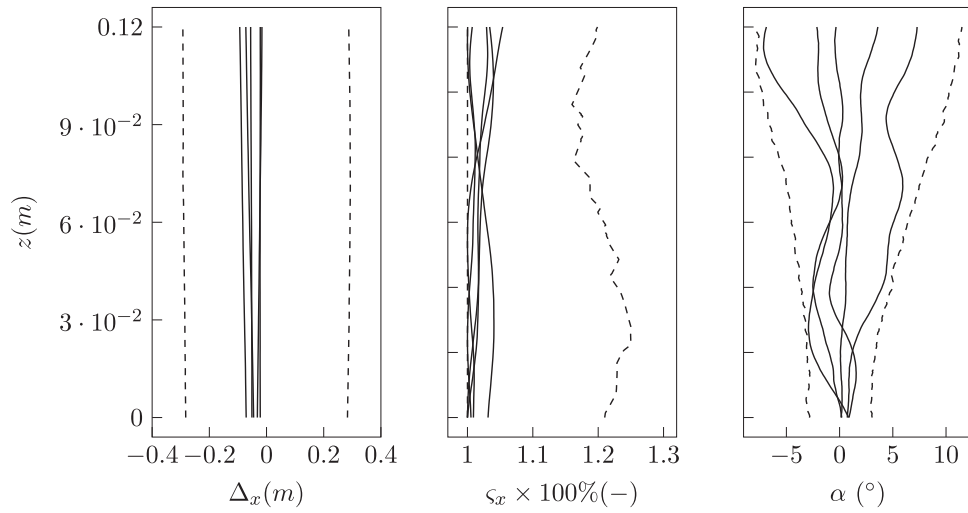


Fig. 14. Four samples of the stochastic shape parameters together with the 1st and 99th percentiles within the Monte-Carlo simulation plotted with a dashed style. Only the samples for one component of both Δ and ζ are shown as the statistics are identical for the components. Note that the ordinate scale is significantly smaller in comparison to that of the shape parameters identified from the CT scan.

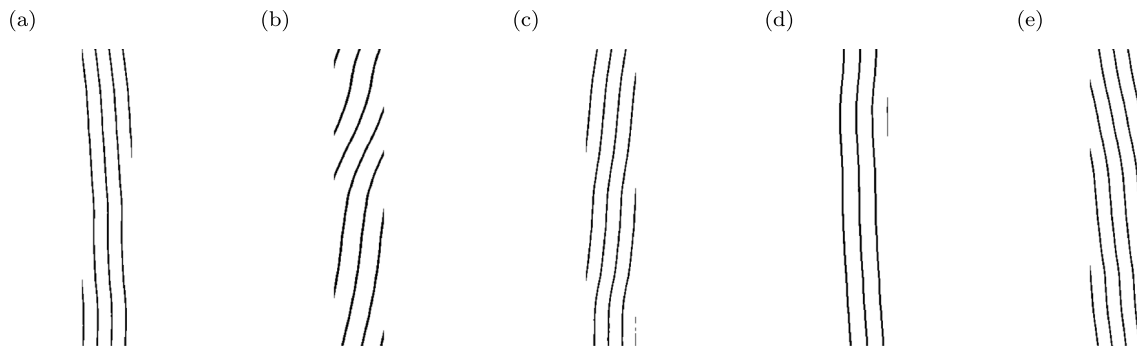


Fig. 15. Annual ring pattern at the clear specimen surface after application of the threshold γ . Each picture represents one sample of $\theta(\xi)$.

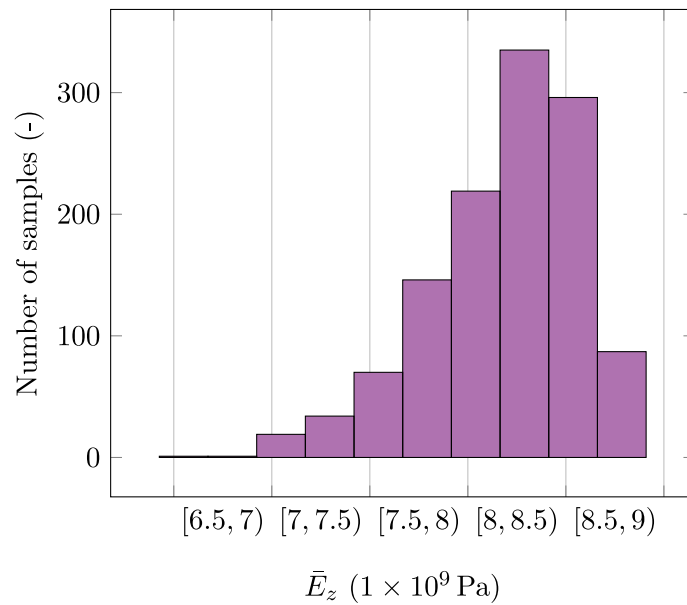


Fig. 16. Homogenized Young's modulus of the clear specimen in the longitudinal direction \bar{E}_z for 1210 random samples of the stochastic shape parameters.

utilize higher resolution CT scans to more extensively validate the local grain angle through applying methods like automatic fiber tracing algorithms as implemented in the XFiber extension to Avizo,⁴ see Hu et al. [31].

CRedit authorship contribution statement

Karl-Alexander Hoppe: Writing – review & editing, Writing – original draft, Visualization, Validation, Supervision, Software, Project administration, Methodology, Investigation, Formal analysis, Data curation, Conceptualization. **Pablo Francisco Ramírez Hönack:** Visualization, Validation, Software, Formal analysis, Data curation. **Simon Schmid:** Writing – review & editing, Writing – original draft, Investigation. **Jochen Kollofrath:** Investigation. **Bettina Chocholaty:** Writing – review & editing, Investigation. **Iason Papaioannou:** Writing – review & editing, Supervision, Formal analysis, Conceptualization. **Steffen Marburg:** Writing – review & editing, Supervision, Resources.

Declaration of competing interest

The authors declare that they have no known competing financial interests or personal relationships that could have appeared to influence the work reported in this paper.

Data availability

Data will be made available on request.

Acknowledgments

The authors gratefully acknowledge the helpful discussions with Ani Khaloian Sarnaghi. The authors express their gratitude towards Ani Khaloian Sarnaghi for providing the spruce specimen. The authors thank Jonas Latz for the interesting and insightful discussions on random fields. The authors thank Dirk Porezag for the valuable comments and corrections for the morphological and material model equations.

References

- [1] Harrigan JJ, Reid SR, Tan P, Yella Reddy T. High rate crushing of wood along the grain. *Int J Mech Sci* 2005;47(4):521–44. <http://dx.doi.org/10.1016/j.ijmecsci.2004.12.013>.
- [2] Walley SM, Rogers SJ. Is wood a material? Taking the size effect seriously. *Materials* 2022;15(15):5403. <http://dx.doi.org/10.3390/ma15155403>.
- [3] Konopka D, Gebhardt C, Kaliske M. Numerical modelling of wooden structures. *J Cult Herit* 2017;27:93–102. <http://dx.doi.org/10.1016/j.culher.2015.09.008>.
- [4] Bengtsson R, Mousavi M, Afshar R, Gamstedt EK. Viscoelastic behavior of softwood based on a multiscale computational homogenization. *Mech Mater* 2023;179:104586. <http://dx.doi.org/10.1016/j.mechmat.2023.104586>.
- [5] Gambarelli S, Ožbolt J. 3D hygro-mechanical meso-scale model for wood. *Constr Build Mater* 2021;311:125283. <http://dx.doi.org/10.1016/j.conbuildmat.2021.125283>.
- [6] Forest Products Laboratory. *Wood handbook—wood as an engineering material. General Technical Report FPL-GTR-282*, Forest Service, U.S. Department of Agriculture; 2021, p. 543.
- [7] Hu M, Briggert A, Olsson A, Johansson M, Oscarsson J, Säll H. Growth layer and fibre orientation around knots in Norway spruce: A laboratory investigation. *Wood Sci Technol* 2018;52(1):7–27. <http://dx.doi.org/10.1007/s00226-017-0952-3>.
- [8] Abdeljaber O, Habite T, Olsson A. Automatic estimation of annual ring profiles in Norway spruce timber boards using optical scanning and deep learning. *Comput Struct* 2023;275. <http://dx.doi.org/10.1016/j.compstruc.2022.106912>.
- [9] Habite T, Abdeljaber O, Olsson A. Automatic detection of annual rings and pith location along Norway spruce timber boards using conditional adversarial networks. *Wood Sci Technol* 2021;55(2):461–88. <http://dx.doi.org/10.1007/s00226-021-01266-w>.
- [10] Collins S, Fink G. Modeling the tensile mechanical properties of silver birch timber boards. *Constr Build Mater* 2022;344:128147. <http://dx.doi.org/10.1016/j.conbuildmat.2022.128147>.
- [11] Kandler G, Lukacevic M, Füssl J. An algorithm for the geometric reconstruction of knots within timber boards based on fibre angle measurements. *Constr Build Mater* 2016;124:945–60. <http://dx.doi.org/10.1016/j.conbuildmat.2016.08.001>.
- [12] Huber JA, Broman O, Ekevad M, Oja J, Hansson L. A method for generating finite element models of wood boards from X-ray computed tomography scans. *Comput Struct* 2022;260. <http://dx.doi.org/10.1016/j.compstruc.2021.106702>.
- [13] Guindos P, Guaita M. A three-dimensional wood material model to simulate the behavior of wood with any type of knot at the macro-scale. *Wood Sci Technol* 2013;47:585–99. <http://dx.doi.org/10.1007/s00226-012-0517-4>.
- [14] Pyörälä J, Liang X, Vastaranta M, Saarinen N, Kankare V, Wang Y, et al. Quantitative assessment of Scots pine (*Pinus sylvestris* L.) whorl structure in a forest environment using terrestrial laser scanning. *IEEE J Sel Top Appl Earth Obs Remote Sens* 2018;11(10):3598–607. <http://dx.doi.org/10.1109/JSTARS.2018.2819598>.
- [15] Kantola A, Mäkinen H, Mäkelä A. Stem form and branchiness of Norway spruce as a sawn timber—predicted by a process based model. *Forest Ecol Manag* 2007;241(1–3):209–22. <http://dx.doi.org/10.1016/j.foreco.2007.01.013>.
- [16] Socha J. A taper model for Norway spruce (*Picea abies* (L.) Karst.). *Electron J Polish Agric Univ* 2002;5(2):3.
- [17] Matović B, Koprivica M, Radonja P. Generalized taper models for Norway spruce (*Picea abies* L. Karst.) in Bosnia and west Serbia. *Allgemeine Forst und Jagdzeitung* 2007;178(7/8):150–5.
- [18] Saint-André L, Hervé J-C, Leban J-M. Modelling the number of rings in individual logs of Norway spruce. *Scandinavian J For Res* 2000;15(1):135–43. <http://dx.doi.org/10.1080/02827580050160574>.
- [19] Pukkala T, Holt Hanssen K, Andreassen K. Stem taper and bark functions for Norway spruce in Norway. *Silva Fennica* 2019;53(3):10187. <http://dx.doi.org/10.14214/sf.10187>.
- [20] Khaloian Sarnaghi A, Rais A, Kovryga A, Gard W, van de Kuilen J. Yield optimization and surface image-based strength prediction of beech. *Eur J Wood Wood Prod* 2020;78:995–1006. <http://dx.doi.org/10.1007/s00107-020-01571-4>.
- [21] Johansson M, Kliger R. Influence of material characteristics on warp in Norway spruce studs. *Wood Fiber Sci* 2002;34(2):325–36.
- [22] Warensjö M. *Compression wood in scots pine and Norway spruce - distribution in relation to external geometry and the impact on the dimensional stability in sawn wood* [Ph.D. thesis], Swedish University of Agricultural Sciences; 2003.
- [23] Edlund J, Warensjö M. Repeatability in automatic sorting of curved Norway spruce saw logs. *Silva Fennica* 2005;39(2):265–75. <http://dx.doi.org/10.14214/SF.388>.
- [24] Bäckström M, Johansson M. Analytical model of twist in Norway spruce (*Picea abies*) timber. *Scandinavian J For Res* 2006;21(1):54–62. <http://dx.doi.org/10.1080/02827580500470271>.
- [25] Bossu J, Lehnebach R, Corn S, Regazzi A, Beauchêne J, Clair B. Interlocked grain and density patterns in Bagassa guianensis: Changes with ontogeny and mechanical consequences for trees. *Trees* 2018;32:1643–55. <http://dx.doi.org/10.1007/s00468-018-1740-x>.
- [26] Gjerdrum P, Bernabei M. Three-dimensional spiral grain pattern in five large Norway spruce stems. *Silva Fennica* 2009;43(3):457–64. <http://dx.doi.org/10.14214/sf.200>.
- [27] Säll H. *Spiral grain in Norway spruce* [Ph.D. thesis], Växjö University Press; 2002.
- [28] Brémaud I, Gril J, Thibaut B. Anisotropy of wood vibrational properties: dependence on grain angle and review of literature data. *Wood Sci Technol* 2011;45(4):735–54. <http://dx.doi.org/10.1007/s00226-010-0393-8>.
- [29] Sepúlveda P, Oja J, Grönlund A. Predicting spiral grain by computed tomography of Norway spruce. *J Wood Sci* 2002;48(6):479–83. <http://dx.doi.org/10.1007/BF00766643>.
- [30] Olsson A, Oscarsson J, Serrano E, Källsner B, Johansson M, Enquist B. Prediction of timber bending strength and in-member cross-sectional stiffness variation on the basis of local wood fibre orientation. *Eur J Wood Wood Prod* 2013;71:319–33. <http://dx.doi.org/10.1007/s00107-013-0684-5>.
- [31] Hu M, Olsson A, Hall S, Seifert T. Fibre directions at a branch-stem junction in Norway spruce: A microscale investigation using X-ray computed tomography. *Wood Sci Technol* 2022;56(1):147–69. <http://dx.doi.org/10.1007/s00226-021-01353-y>.
- [32] Hu M, Olsson A, Johansson M, Oscarsson J, Serrano E. Assessment of a three-dimensional fiber orientation model for timber. *Wood Fiber Sci* 2016;48(4):271–90.
- [33] Foley C. A three-dimensional paradigm of fiber orientation in timber. *Wood Sci Technol* 2001;35(5):453–65. <http://dx.doi.org/10.1007/s002260100112>.
- [34] Purba CYC, Dlouha J, Ruelle J, Fournier M. Mechanical properties of secondary quality beech (*Fagus sylvatica* L.) and oak (*Quercus petraea* (Matt.) Liebl.) obtained from thinning, and their relationship to structural parameters. *Ann For Science* 2021;78(3):1–11. <http://dx.doi.org/10.1007/s13595-021-01103-x>.
- [35] Astley RJ, Stol KA, Harrington J. Modelling the elastic properties of softwood: Part II: The cellular microstructure. *Holz als Roh- und Werkstoff* 1998;56(1):43–50. <http://dx.doi.org/10.1007/s001070050262>.
- [36] Lukacevic M, Kandler G, Hu M, Olsson A, Füssl J. A 3D model for knots and related fiber deviations in sawn timber for prediction of mechanical properties of boards. *Mater Des* 2019;166. <http://dx.doi.org/10.1016/j.matdes.2019.107617>.

⁴ Thermo Fisher Scientific, Waltham, Massachusetts, USA.

- [37] Hu M, Olsson A, Johansson M, Oscarsson J. Modelling local bending stiffness based on fibre orientation in sawn timber. *Eur J Wood Wood Prod* 2018;76(6):1605–21. <http://dx.doi.org/10.1007/s00107-018-1348-2>.
- [38] Hu M, Johansson M, Olsson A, Oscarsson J, Enquist B. Local variation of modulus of elasticity in timber determined on the basis of non-contact deformation measurement and scanned fibre orientation. *Eur J Wood Wood Prod* 2015;73:17–27. <http://dx.doi.org/10.1007/s00107-014-0851-3>.
- [39] Kandler G, Lukacevic M, Zechmeister C, Wolff S, Füssl J. Stochastic engineering framework for timber structural elements and its application to glued laminated timber beams. *Constr Build Mater* 2018;190:573–92. <http://dx.doi.org/10.1016/j.conbuildmat.2018.09.129>.
- [40] Denzler JK, Weidenhiller A, Golser M. Property relationships between spruce logs and structural timber. *Scandinavian J For Res* 2015;30(7):617–23. <http://dx.doi.org/10.1080/02827581.2015.1046479>.
- [41] Lanvermann C, Hass P, Wittel FK, Niemi P. Mechanical properties of Norway spruce: Intra-ring variation and generic behavior of earlywood and latewood until failure. *BioResources* 2014;9(1):105–19.
- [42] Sepahvand K, Marburg S. Identification of composite uncertain material parameters from experimental modal data. *Probab Eng Mech* 2014;37:148–53. <http://dx.doi.org/10.1016/j.probgemch.2014.06.008>.
- [43] Lenz P, Bernier-Cardou M, MacKay J, Beaulieu J. Can wood properties be predicted from the morphological traits of a tree? A canonical correlation study of plantation-grown white spruce. *Canadian J For Res* 2012;42(8):1518–29. <http://dx.doi.org/10.1139/x2012-087>.
- [44] Riesco Muñoz G. Prediction of shear strength parallel to grain in clear wood of oak (*Quercus robur* L.) on the basis of shear plane orientation, density and anatomical traits. *Holzforschung* 2021;75(12):1104–14. <http://dx.doi.org/10.1515/hf-2021-0036>.
- [45] Piispanen R, Heikkinen J, Valkonen S. Deformations of boards from uneven-aged Norway spruce stands. *Eur J Wood Wood Prod* 2020;78:533–44. <http://dx.doi.org/10.1007/s00107-020-01524-x>.
- [46] Leban J-M, Haines DW. The modulus of elasticity of hybrid larch predicted by density, rings per centimeter, and age. *Wood Fiber Sci* 1999;31(4):394–402.
- [47] Johansson M, Ormarsson S. Influence of growth stresses and material properties on distortion of sawn timber—numerical investigation. *Ann For Sci* 2009;66(6):1–10. <http://dx.doi.org/10.1051/forest/2009045>.
- [48] Johansson E, Berglund A, Skog J. Comparing predictability of board strength between computed tomography, discrete X-ray, and 3D scanning of Norway spruce logs. *Wood Mater Sci Eng* 2016;11(2):116–25. <http://dx.doi.org/10.1080/17480272.2015.1022875>.
- [49] Oja J, Grundberg S, Grönlund A. Predicting the stiffness of sawn products by X-ray scanning of Norway spruce saw logs. *Scandinavian J For Res* 2001;16(1):88–96. <http://dx.doi.org/10.1080/028275801300004442>.
- [50] Oja J, Källsner B, Grundberg S. Predicting the strength of sawn wood products: A comparison between X-ray scanning of logs and machine strength grading of lumber. *Forest Prod J* 2005;55(9):55–60.
- [51] Hofstetter K, Gamstedt EK. Hierarchical modelling of microstructural effects on mechanical properties of wood. A review. COST action E35 2004–2008: Wood machining—micromechanics and fracture. *Holzforschung* 2009;63:130–8. <http://dx.doi.org/10.1515/HF.2009.018>.
- [52] Mishnaevsky Jr L, Qing H. Micromechanical modelling of mechanical behaviour and strength of wood: State-of-the-art review. *Comput Mater Sci* 2008;44(2):363–70. <http://dx.doi.org/10.1016/j.commatsci.2008.03.043>.
- [53] Faber M, Vrouwenvelder T. JCSS Probabilistic model code Part 3: Resistance models. (3.5 Properties of timber JCSS-OSTL/DIA/VROU-10-11-2000): Joint Committee on Structural Safety; 2006, p. 1–16.
- [54] Eckes-Shephard AH, Ljungqvist FC, Drew DM, Rathgeber CB, Friend AD. Wood formation modeling—a research review and future perspectives. *Front Plant Sci* 2022;13:265. <http://dx.doi.org/10.3389/fpls.2022.837648>.
- [55] Balestra M, Tonelli E, Vitali A, Urbinati C, Frontoni E, Pierdicca R. Geomatic data fusion for 3D tree modeling: The case study of monumental chestnut trees. *Remote Sens* 2023;15(8):2197. <http://dx.doi.org/10.3390/rs15082197>.
- [56] González-Rodrigo B, Esteban LG, de Palacios P, García-Fernández F, Guindeo A. Variation throughout the tree stem in the physical-mechanical properties of the wood of *Abies alba* Mill. from the Spanish Pyrenees. *Madera y bosques* 2013;19(2):87–107.
- [57] Kandler G, Füssl J, Eberhardsteiner J. Stochastic finite element approaches for wood-based products: theoretical framework and review of methods. *Wood Sci Technol* 2015;49:1055–97. <http://dx.doi.org/10.1007/s00226-015-0737-5>.
- [58] Rasmussen CE, Williams CKI. Gaussian processes for machine learning. Cambridge, MA: The MIT Press; 2005. <http://dx.doi.org/10.7551/mitpress/3206.001.0001>.
- [59] Ågren AR. Wood as a material. Properties of softwood 6, Swedish Forest Industries Federation; 2024.
- [60] Dahl KB, Malo K. Linear shear properties of spruce softwood. *Wood Sci Technol* 2009;43:499–525. <http://dx.doi.org/10.1007/s00226-009-0246-5>.
- [61] Feldkamp L, Davis LC, Kress J. Practical cone-beam algorithm. *J Opt Soc Am* 1984;1(6):612–9. <http://dx.doi.org/10.1364/JOSAA.1.000612>.
- [62] Mentrasti L, Molari L, Fabiani M. Poisson's ratio bounds in orthotropic materials. Application to natural composites: Wood, bamboo and arundo donax. *Composites B* 2021;209. <http://dx.doi.org/10.1016/j.compositesb.2021.108612>.
- [63] Ross RJ, McDonald KA, Green DW, Schad KC. Relationship between log and lumber modulus of elasticity. *For Prod J* 1997;47(2):89–92.
- [64] Denzler JK, Weidenhiller A, Golser M. Property relationships between spruce logs and structural timber. *Scandinavian J For Res* 2015;30(7):617–23. <http://dx.doi.org/10.1080/02827581.2015.1046479>.
- [65] Edlund J, Lindström Ha, Nilsson F, Reale M. Modulus of elasticity of Norway spruce saw logs vs. structural lumber grade. *Holz als Roh- und Werkstoff* 2006;64(4):273–9. <http://dx.doi.org/10.1007/s00107-005-0091-7>.
- [66] Lloyd JR, Duvenaud D, Grosse R, Tenenbaum JB, Ghahramani Z. Automatic construction and natural-language description of nonparametric regression models. In: Proceedings of the twenty-eighth AAAI conference on artificial intelligence, vol. 28, 2014, p. 1242–50. <http://dx.doi.org/10.48550/arXiv.1402.4304>.
- [67] Technical Committee CEN/TC 175 Round and sawn timber. Round and sawn timber - Permitted deviations and preferred sizes - Part 1: Softwood sawn timber. EN 1313-1:2010, DIN Deutsches Institut für Normung e.V., European committee for standardization; 2010, p. 5.
- [68] Aicher S, Stapf G. Compressive strength parallel to the fiber of spruce with high moisture content. *Eur J Wood Wood Prod* 2016;74:527–42. <http://dx.doi.org/10.1007/s00107-015-1004-z>.
- [69] COMSOL multiphysics reference manual. Tech. Rep. CM020005, COMSOL; 2021, p. 1–2026.
- [70] Charalambakis N. Homogenization techniques and micromechanics. A survey and perspectives. *Appl Mech Rev* 2010;63(3). <http://dx.doi.org/10.1115/1.4001911>.
- [71] Keunecke D, Sonderegger W, Pereteau K, Lüthi T, Niemi P. Determination of Young's and shear moduli of common yew and Norway spruce by means of ultrasonic waves. *Wood Sci Technol* 2007;41:309–27. <http://dx.doi.org/10.1007/s00226-006-0107-4>.
- [72] Fan M, Naughton A, Bregulla J. 14 - Fire performance of natural fibre composites in construction. In: Fan M, Fu F, editors. Advanced high strength natural fibre composites in construction. Woodhead Publishing; 2017, p. 375–404. <http://dx.doi.org/10.1016/B978-0-08-100411-1.00014-5>.
- [73] Koponen T, Karppinen T, Häggström E, Saranpää P, Serimaa R. The stiffness modulus in Norway spruce as a function of year ring. *Wood Res Technol* 2005;59(4):451–455. <http://dx.doi.org/10.1515/HF.2005.074>.
- [74] Al-Jumaily A, Jameel K. Influence of the Poisson ratio on the natural frequencies of stepped-thickness circular plate. *J Sound Vib* 2000;234(5):881–94. <http://dx.doi.org/10.1006/jsvi.2000.2905>.